

Nanoscale Transparent Conductive Oxides via Microwave-assisted Polyol Synthesis

Zur Erlangung des akademischen Grades eines

DOKTORS DER NATURWISSENSCHAFTEN

(Dr. rer. nat.)

der Fakultät für Chemie und Biowissenschaften der
Universität Karlsruhe (TH)
vorgelegte

DISSERTATION

von

M.Sc. Elin Hammarberg
aus Uppsala, Schweden

Dekan: Prof. Dr. S. Bräse
Referent: Prof. Dr. C. Feldmann
Korreferent: Prof. Dr. U. Lemmer
Tag der mündlichen Prüfung: 18.12.2008

Zusammenfassung

Transparente leitfähige Oxide (transparent conductive oxides, TCOs) werden typischerweise als transparente Elektroden in Solarzellen oder Flachbildschirmen verwendet. Um den Einsatz von Beschichtungs- oder Drucktechniken, die deutlich billiger als die üblichen Gasphasenabscheidungen sind, zu ermöglichen, werden Suspensionen von TCO-Nanopartikeln benötigt. Das Ziel dieser Arbeit war die Synthese kristalliner, nicht-agglomerierter, redispersierbarer TCO-Nanopartikel mit enger Größenverteilung. Zu diesem Zweck wurde eine mikrowellenunterstützte Polyolsynthese entwickelt. Das verwendete Polyol war Diethylenglykol (DEG), das gleichzeitig als Oberflächenstabilisator und Lösungsmittel fungiert. Das Erhitzen erfolgte mittels Mikrowellenbestrahlung, welche wegen ihrer positiven Auswirkung auf die Kristallinität des Materials eingesetzt wurde.

Suspensionen aus $\text{In}_2\text{O}_3:\text{Sn}$ (ITO) in DEG bestanden aus praktisch nicht-agglomerierten Partikeln mit einer durchschnittlichen Größe von 15-19 nm. Die ITO-Pulver waren nach der Synthese hochkristallin, zeigten demzufolge einen geringen spezifischen Widerstand ($1,1 \cdot 10^{-2} \Omega\text{cm}$) und eine hohe Reflektanz im infraroten Bereich. Dünne Schichten wurden hergestellt indem unbehandelte Suspensionen direkt auf Glasplatten aufgetragen wurden. Nachbehandelte Schichten zeigten im sichtbaren Bereich eine ähnliche Transmittanz wie unbeschichtete Glasplatten und einen geringen spezifischen Widerstand ($1,2 \cdot 10^{-2} \Omega\text{cm}$).

Dotierte ZnO- und SnO_2 -Pulver waren nach der Synthese kristallin, aber nicht leitfähig, obwohl der Einbau von Dotiersubstanzen nachgewiesen werden konnte. Die ZnO-Partikel zeigten eine durchschnittliche Größe von 10-15 nm und einen geringen Agglomerationsgrad. Nachbehandelte ZnO-Partikel wiesen spezifische Widerstände von $2,0 \cdot 10^{-1} \Omega\text{cm}$ (ZnO:In, IZO) und $5,7 \cdot 10^{-1} \Omega\text{cm}$ (ZnO:Al, AZO) auf. Weiterhin wurden transparente, leitfähige ZnO Schichten hergestellt. SnO_2 -Proben beinhaltenen 3-4 nm große Partikel, die kleine Aggregate ausbildeten. Nachbehandelte $\text{SnO}_2:\text{F}$ - (FTO) Pulver wiesen einen spezifischen Widerstand von $1,9 \cdot 10^{-1} \Omega\text{cm}$ auf.

Zusätzlich zu üblichen TCO-Materialien wurden andere binäre und ternäre Oxide nanoskalig dargestellt. Zinn-dotiertes Zink-Indium-Oxid zeigte im Vergleich zu ITO trotz seines deutlich niedrigeren Indiumgehalts nach thermischer Behandlung einen ähnlichen spezifischen Widerstand. Gemäß der berechneten Bandlücke ist Zink-Indium-Oxid im sichtbaren Bereich transparent. Die Kristallstruktur des synthetisierten ternären Oxides ist noch nicht vollständig verstanden. Es stellt dennoch ein hochinteressantes, alternatives TCO-Material dar.

Darüber hinaus wurde die Festkörper-NMR-Spektroskopie zum ersten Mal verwendet um TCO-Nanomaterialien zu untersuchen. Dadurch wurde entdeckt, dass nur ein Teil der zugegebenen Al^{3+} -Dotierungen im kristallinen Kern der AZO-Partikel eingebaut wurde. Zusätzliche Dotierungen wurden in eine amorphe Hülle eingebettet, woraus ein erhöhter spezifischer Widerstand resultierte. Die FTO-Partikel waren dagegen einkristallin und alle F-Dotierungen waren auf O^{2-} -Plätzen in einer Sn^{II} -Umgebung eingebaut. Es wird erwartet, dass die erhaltenen Kenntnisse über die lokale Struktur von Dotiersubstanzen zu einer verbesserten Synthese und dadurch zu verbesserten Leitfähigkeiten beitragen werden.

Schließlich wurde der Umfang der Forschungsarbeit durch die Synthese von unedlen Metallen erweitert, wobei Indium als Fallbeispiel verwendet wurde. Suspensionen von In^0 in DEG bestanden aus kristallinen, nanoskaligen, agglomerierten Partikeln. Durch die Verwendung eines zusätzlichen Oberflächenstabilisators wurde ein Phasentransfer in eine unpolare Phase ermöglicht. Hierbei konnten die Metallpartikel leicht von den gelösten Precursoren abgetrennt werden und transparente, stabile In^0 Suspensionen erhalten werden.

Abstract

Transparent conductive oxide (TCO) materials are typically applied as transparent electrodes in e.g. solar cells or flat panel displays. In order to apply coating or printing techniques, which are significantly cheaper than standard gas-phase deposition processes, suspensions of TCO nanoparticles are required. The goal of this work was the synthesis of crystalline, non-agglomerated, redispersible TCO nanoparticles with a narrow size distribution. To this end, a microwave-assisted polyol synthesis was developed. The utilized polyol was diethylene glycol (DEG), which acts as surface stabilizer as well as solvent. Microwave-assisted heating was applied due to its advantageous effect on material crystallinity.

Suspensions of $\text{In}_2\text{O}_3:\text{Sn}$ (ITO) in DEG contained practically non-agglomerated particles with an average size of 15-19 nm. As-prepared ITO powders turned out to be highly crystalline; as a result they exhibited a low resistivity ($1.1 \cdot 10^{-2} \Omega\text{cm}$) and a high reflectivity in the infrared region. Thin layers were prepared via direct deposition of as-prepared ITO suspensions on glass plates. Post-treated layers displayed a visible transmittance similar to the uncoated glass substrate and a low resistivity ($1.2 \cdot 10^{-2} \Omega\text{cm}$).

As-prepared doped ZnO and SnO_2 powders were crystalline but nonconductive although dopants were evidenced to be inserted. ZnO particles exhibited a mean size of 10-15 nm and a low degree of agglomeration. Post-treated powders showed resistivities of $2.0 \cdot 10^{-1} \Omega\text{cm}$ ($\text{ZnO}:\text{In}$, IZO) and $5.7 \cdot 10^{-1} \Omega\text{cm}$ ($\text{ZnO}:\text{Al}$, AZO). In addition, transparent conductive ZnO thin layers were prepared. SnO_2 samples contained 3-4 nm large particles formed into small aggregates. Post-treated $\text{SnO}_2:\text{F}$ (FTO) powders exhibited a resistivity of $1.9 \cdot 10^{-1} \Omega\text{cm}$.

In addition to standard TCO materials, other binary and ternary oxides were achieved on the nanoscale. Tin-doped zinc indium oxide exhibited a conductivity comparable to ITO subsequent to thermal treatment despite its considerably lower indium content. According to the estimated bandgap of zinc indium oxide, it is transparent in the visible region. The crystal structure of the prepared ternary oxide has not yet been fully determined. Nevertheless, it represents a very interesting alternative TCO material.

Furthermore, solid state NMR spectroscopy was for the first time applied to investigate TCO nanomaterials. It was discovered that only a certain amount of Al^{3+} dopants was inserted in the crystalline core of the AZO particles. Further added dopants were embedded in an amorphous shell, which resulted in an increased resistivity. FTO particles were on the other hand single crystalline with all F^- dopants incorporated at O^{2-} sites, located in a Sn^{II} environment. The gained knowledge of the local structure of dopants is expected to contribute to enhancement of the synthesis and thereby improved conductivities.

Finally, the scope of the research work was extended to less noble elementary metals with indium as a case study. Suspensions of In^0 in DEG contained crystalline, nanoscale, agglomerated particles. With the application of an additional surface stabilizer, a phase transfer into a nonpolar phase could be demonstrated. Hereby, the metal particles were easily separated from dissolved precursors and transparent, stable In^0 suspensions were obtained.

TABLE OF CONTENTS

1	INTRODUCTION.....	1
2	EXPERIMENTAL	3
2.1	MICROWAVE-ASSISTED POLYOL SYNTHESIS OF NANOPARTICLES	3
2.2	EVACUATION/INERT GAS APPARATUS.....	4
2.3	SAMPLE PREPARATION	4
2.4	POST-TREATMENT OF SAMPLES	5
2.5	CHEMICALS	5
3	ANALYTICAL METHODS.....	7
3.1	ELECTRON MICROSCOPY	7
3.1.1	Transmission electron microscopy (TEM).....	9
3.1.2	Scanning electron microscopy (SEM).....	10
3.1.3	Energy dispersive X-ray analysis (EDX).....	11
3.2	X-RAY DIFFRACTION (XRD)	12
3.2.1	X-ray single crystal diffraction	14
3.2.2	X-ray powder diffraction.....	16
3.3	LIGHT SCATTERING TECHNIQUES.....	17
3.3.1	Particle sizing with dynamic light scattering (DLS).....	17
3.3.2	Zeta potential with electrophoretic light scattering.....	19
3.4	NITROGEN ADSORPTION (BET)	20
3.5	THERMAL ANALYSIS (DTA-TG)	21
3.6	FOUR-POINT PROBING.....	22
3.7	ABSORPTION SPECTROSCOPY	25
3.7.1	Fourier transform infrared (FT-IR) spectroscopy	26
3.7.2	Ultraviolet-visible (UV-Vis) spectroscopy	27
3.7.3	Solid state nuclear magnetic resonance (NMR) spectroscopy.....	28
3.7.4	Mössbauer spectroscopy	32
4	RESULTS AND DISCUSSION.....	35
4.1	BINARY OXIDES AND HYDROXIDES.....	35
4.1.1	Indium tin oxide (ITO).....	35
4.1.2	Zinc oxide.....	41
4.1.3	Tin oxide	62
4.1.4	Cerium oxide	78
4.1.5	Lanthanum hydroxide	81
4.2	TERNARY OXIDES	85
4.2.1	Zinc aluminium oxide	85
4.2.2	Zinc gallium oxide	88
4.2.3	Zinc indium oxide	92
4.3	ELEMENTARY METALS	105
4.3.1	Indium	105
5	CONCLUSIONS.....	113
5.1	SUMMARY	113
5.2	OUTLOOK.....	115
6	ACKNOWLEDGEMENTS.....	117
7	REFERENCES	119

8	INDEX OF TABLES AND FIGURES	125
8.1	INDEX OF TABLES	125
8.2	INDEX OF FIGURES	125
9	APPENDIX	131
9.1	CURRICULUM VITAE	131
9.2	PUBLICATIONS.....	133

List of abbreviations

AZO	aluminium-doped zinc oxide
BET	Brunauer, Emmett, and Teller; gas absorption according to
CN	coordination number
CP	cross polarization
DEG	diethylene glycol
DLS	dynamic light scattering
DTA	differential thermal analysis
EDX	energy dispersive X-ray analysis
EtOH	ethanol
FTO	fluorine-doped tin oxide
h	hours
HRTEM	high-resolution transmission electron microscopy
IEP	isoelectric point
IR	infrared
ITO	tin-doped indium oxide
IZO	indium-doped zinc oxide
MAS	magic angle spinning
min	minutes
NMR	nuclear magnetic resonance
SEM	scanning electron microscopy
TCO	transparent conductive oxide
TEM	transmission electron microscopy
TG	thermogravimetry
UV	ultraviolet
Vis	visible
XRD	X-ray diffraction

1 Introduction

Metal oxides that exhibit a high optical transmittance and in addition are highly electrically conductive are referred to as transparent conductive oxides (TCOs).^[1] They can also be described as wide-bandgap oxide semiconductors. Examples of compounds within this material class are CdO, In₂O₃, SnO₂, and ZnO. Since the bandgaps of these materials lie in the ultraviolet wavelength region they do not absorb visible light – as a consequence, they appear transparent to the human eye. If such an oxide is doped with a sufficient amount of suitable ions, high electrical conductivities can be achieved. TCOs are of major technical importance since thin films exhibiting a high electrical conductivity and optical transmittance are needed in, for instance, solar cells, flat panel displays, and electrochromic devices.^[2,3]

Among the transparent conductive oxides, tin-doped indium oxide, also called indium tin oxide (ITO), shows the highest electrical conductivity, which – in combination with its optical transmittance – has granted it a position as the most widely applied TCO material in optoelectronic devices.^[4,5] However, due to the high cost and scarcity of indium metal, intense research to find materials that can replace ITO is conducted, whereby ZnO as well as ternary oxides are regarded as promising alternatives.^[3] On the other hand, fluorine-doped tin oxide (FTO) is the most commonly employed TCO in energy-efficient windows.^[6]

TCO films are commonly produced via vacuum-based gas phase methods, such as magnetron sputtering or chemical vapor deposition.^[3,6] Due to the high crystallinity and compactness of the resulting thin films, excellent conductivities can be achieved. At present, sputtered ITO films with a resistivity around $1 \cdot 10^{-4} \Omega\text{cm}$ are commercially available.^[3] Patterned structures today are normally produced via lithographic etching. This subtractive process includes several fabrication steps and causes a significant waste of preliminarily sputtered TCO material.^[7] Both aspects – sputtering and etching – lead to a time-consuming and cost-intensive process. Here, coating or printing techniques (e.g. dip- or spin-coating, ink-jet, offset, or silk-screen printing) can offer significant advantages when aiming at a facile and low-cost process with a reduced waste of material. Moreover, coating or printing on flexible substrates (e.g. plastics) would be possible.^[8,9] The latter technologies, however, require the availability of a suited suspension or ink, containing crystalline non-agglomerated, TCO nanoparticles with a narrow particle size distribution.

Particles with a diameter of 1-100 nm ($1 \text{ nm} = 10^{-9} \text{ m}$) are referred to as nanoparticles.^[10-12] They are characterized by having a large specific surface area, i.e., they are so small that a substantial part of the atoms that make up the particle are located on its surface. Thus, apart from the application of nanoparticles in functional thin films,^[13] the large specific surface area of nanoparticles is utilized e.g. in catalysis, where especially elementary metal nanoparticles are employed.^[14,15] An interesting feature of nanoparticles is that some material properties have been proven to be size dependent. One example of this is semiconducting nanoparticles 1-20 nm in size (so-called quantum dots), for which the bandgap becomes larger as the particles size decreases.^[16,17] This implies that the wavelength of the light that is absorbed or emitted by these particles can be tuned via particle size.

Chemical synthesis of nanoparticles is already a well-established field of research upon which several books have been written.^[18-21] Liquid phase methods for the preparation of nanoparticles include precipitation,^[11,12] sol-gel synthesis,^[11,22-24] microemulsion techniques,^[11,25] as well as hydrothermal^[11,26] and solvothermal^[11,27] methods. In this work, a precipitation process will be utilized. Although all the previously mentioned synthetic routes in a way include precipitation, here nanoparticles are precipitated from a single phase homogeneous solution without application of high pressure techniques. Agglomeration of

precipitated particles is practically inevitable in the absence of a stabilizer.^[11] In many cases, the organic capping agent normally used to prevent agglomeration can also serve as reducing agent in the synthesis of elementary metal particles. An example of this is the polyol method developed for preparation of metal particles^[28,29] by Fievet *et al.* The polyol method was later extended to include synthesis of colloidal suspensions of oxides.^[30]

The polyol – a multidentate and high-boiling alcohol (e.g. diethylene glycol/DEG, ethylene glycol, glycerin) – acts as surface stabilizer as well as solvent. Since high temperatures are applied, well-crystallized materials can be realized.^[29,31,32] DEG furthermore stabilizes the particle surfaces during nucleation and crystallization, and therefore prevents particle growth and aggregation. This stabilizing effect of the polyols is well known and has been used to prepare a wide range of nanoscale materials, including elemental metals, oxides, sulfides or fluorides.^[28-38] Thus, over time, polyol-mediated synthesis has been proven to be successful for the preparation of nanoscale functional materials. The application of microwave irradiation results in rapid heating of the reaction mixtures and thus rapid and nearly simultaneous precipitation of particles, which leads to very small particle size and narrow size distribution.^[11] Applying microwave-assisted heating of high-boiling solvents such as polyols or ionic liquids has been advantageous with regard to particle morphology and material crystallinity for several described nanomaterials – e.g. Ag, Pt, Au, and CdSe in polyols^[39-41] and Pt, ITO, and LaPO₄ in ionic liquids.^[42-44]

In this work, the above mentioned positive effects of the application of polyols as solvents and microwave irradiation as heat source will be combined and utilized for the preparation of suspensions of transparent conductive oxide nanoparticles. The goal is to achieve non-agglomerated suspensions of crystalline particles with a narrow size distribution, which could find future application as printable inks. Since ITO is known for its superior electrical and optical properties, it will initially be investigated. In addition, the possibility to prepare alternative TCO materials via a microwave polyol approach will be explored. To this end, particle size and crystallinity will be studied via several independent analytical tools. The insertion of dopants in host lattices is of major importance and their effect on the electrical conductivity of particles will be studied. The effects of post-treatment on crystallinity, particle size, and agglomeration are also going to be investigated. Obviously, in addition the transparency and conductivity of as-prepared and post-treated powders and thin layers will be evaluated.

2 Experimental

2.1 Microwave-assisted polyol synthesis of nanoparticles

Nanoparticulate suspensions were prepared in a high-boiling multidentate alcohol – a polyol – by precipitation via hydrolysis (for metal oxides) or reduction (for elementary metals). Diethylene glycol (DEG) has been proven to be an excellent medium for the preparation of nanoscale compounds^[31,32,37] and was therefore chosen as solvent. Agglomeration of precipitated particles is practically inevitable in the absence of a particle surface stabilizer,^[11] however in this case DEG acts as both solvent and chelating agent. Thus, the particles are complexed by DEG directly after nucleation, which hinders further particle growth and prevents agglomeration.^[31,32,37] Since high temperatures can be applied – the boiling point of DEG is 248 °C^[45] – well crystallized materials can be realized.^[29,31,32]

In order to synthesize homogeneous particles with a narrow size distribution, it is necessary to separate the nucleation and growth processes of the particles.^[12] To achieve this, it is imperative that precipitation occurs in a homogeneous solution. Thus, all precursors must be dissolved prior to reaction. Inorganic compounds/salts are often well soluble in polyols due to their high polarities – the dielectric constant of DEG is 32.^[45] As a reference, the dielectric constant of water amounts to 80.^[45] Furthermore, heating of the liquid must be homogeneous, i.e. the solutions must be stirred during reaction. To prevent the solvent from reacting with air – oxidizing – the samples are vented with inert gas.

The application of microwave irradiation results in rapid heating of the reaction mixtures and thus rapid and nearly simultaneous precipitation of particles, which leads to very small particle size and narrow size distribution.^[11] Several studies have confirmed the advantageous effects concerning particle morphology and material crystallinity realized by heating via microwave irradiation.^[39-44,46] Thus, in the studies presented in this thesis, heating was carried out via microwave irradiation. The heating effect of microwave irradiation – so-called dielectric heating – is caused by an interaction of the electromagnetic radiation with the dipole moments in a liquid.^[47,48] Polyols are well-suited for microwave heating due to their high polarities and their ability to form hydrogen bonds, which results in long relaxation times; this in turn results in efficient absorption of microwave energy.^[47,48]

In order to realize well-crystallized, nanoscale, non-agglomerated particles, adjustment of synthesis parameters such as heating time and temperature as well as the concentration of the metal precursors and the base solution and the amount of added water had to be done. In addition, suitable metal precursor had to be found. All chemicals used in this work (see section 2.5) were applied as received.

The precursors were first dissolved in DEG in a three-neck flask through magnetic stirring and heating with a heating mantle at temperatures up to 150 °C. During dissolving, the samples were vented with inert gas (N₂). Precipitation occurred either upon adding distilled water or a base solution to the clear precursor solution, or upon further heating, depending on the synthesized substance. The resulting suspension or solution was heated in a standard laboratory microwave oven (rotaPREP, 1200 W, 2.45 GHz from MLS, Leutkirch, Germany). The experimental set-up is shown in Figure 1. The three-neck flask containing the liquid was attached to a distillation head, through which volatiles could pass out and inert gas (Ar) was introduced. Heat rate, temperature and maximal power are programmable. During operation of the microwave oven, all suspensions were magnetically stirred, while the temperature was measured directly in the liquid via an IR fiber optic cable. Heating was conducted at up to

200 °C, and was maintained for up to 2 h to improve material crystallinity. In accordance with the boiling point of DEG (248 °C),^[45] heating was performed at ambient pressure.



Figure 1. Experimental set-up of microwave-assisted polyol synthesis.

2.2 Evacuation/inert gas apparatus

A combined evacuation/inert gas apparatus, consisting of one evacuation line and one inert gas line, each equipped with several Young valves, was utilized for this work. The apparatus was used to introduce inert gas during synthesis, as well as to dry samples by evacuation. The utilized inert gas was argon (Argon 4.8, from Air Liquide, Paris, France) or nitrogen (technical grade). Before being introduced into the inert gas line of the apparatus, argon and nitrogen were dried by being conveyed through a series of drying towers containing silica gel, potassium hydroxide, molecular sieve (4 Å), and phosphorus pentoxide, respectively. Argon was additionally conveyed through a titanium sponge heated to 600 °C in a LOBA tube furnace from HTM Reetz (Berlin, Germany). This procedure removes impurities such as water or carbon dioxide from the inert gas. Vacuum ($p < 10^{-3}$ mbar) was produced by a rotary vane vacuum pump from Vacuubrand (Wertheim, Germany). A cold trap was inserted between the vacuum pump and the evacuation line to prevent flow of any volatiles other than the inert gas. The pressure was measured with a manometer from Vacuubrand.

2.3 Sample preparation

After microwave-assisted heating, the suspensions were centrifugated at 25 000 rpm with a 3K30 laboratory centrifuge from Sigma (Osterode am Harz, Germany). In order to remove dissolved salts and to keep a fluid phase, the sediment was redispersed in DEG after the centrifugate solution was removed.

To obtain powders, the centrifugated sediments were redispersed in ethanol after the centrifugate solution was removed. The resulting suspensions were then centrifugated again; this washing procedure was repeated three times. Drying was carried out overnight at 70 °C in air in a drying cabinet. The obtained powder was finely rubbed in a mortar. Subsequently, it was placed in a Schlenk tube and dried for 30 min in vacuum at ambient temperature with the evacuation/inert gas apparatus.

Thin layers were prepared by applying suspensions (solids contents of 5-10 wt-%) on glass plates with a Pasteur pipette. The solvents evaporated via infrared light irradiation.

2.4 Post-treatment of samples

In order to burn out remaining DEG adhered to the particle surfaces and in some cases to crystallize materials, powders were placed in α -Al₂O₃ crucibles and heated in air in an M 110 muffle furnace Heraeus (Hanau, Germany) at temperatures up to 800 °C. Thin layers densified by heating in air in the same muffle furnace at temperatures up to 500 °C. Additionally, powders and thin layers were heated in forming gas, H₂/N₂ 10 % (ARCAL F10 from Air Liquide, Paris, France), in a MTF 1200 °C tube furnace from Carbolite (Derbyshire, UK) at temperatures up to 500 °C with the intention to establish charge carriers and thereby enhance conductivity.

2.5 Chemicals

The following chemicals were used in the syntheses presented in this thesis:

substance name	empirical formula	manufacturer	purity
1-methoxy-2-propanol	CH ₃ OCH ₂ CH(OH)CH ₃	Acros Organics	98.5 %
aluminium chloride hexahydrate	AlCl ₃ · 6 H ₂ O	Fluka	≥99.0 %
cerium nitrate hexahydrate	Ce(NO ₃) ₃ · 6 H ₂ O	Acros Organics	99.5 %
diethylene glycol	(HOCH ₂ CH ₂) ₂ O	Acros Organics	99 %
dodecane	CH ₃ (CH ₂) ₁₀ CH ₃	Aldrich	99 %
ethanol	CH ₃ CH ₂ OH	Seulberger	99.9 %
gadolinium nitrate hexahydrate	Gd(NO ₃) ₃ · 6 H ₂ O	Aldrich	99.9 %
gallium nitrate hydrate	Ga(NO ₃) ₃ · x H ₂ O	Aldrich	99.9 %
indium chloride tetrahydrate	InCl ₃ · 4 H ₂ O	ABCR	99.99 %
lanthanum nitrate hexahydrate	La(NO ₃) ₃ · 6 H ₂ O	Aldrich	99.99 %
oleylamine	CH ₃ (CH ₂) ₇ CH=CH(CH ₂) ₇ CH ₂ NH ₂	Fluka	≥70 %
pentane	CH ₃ (CH ₂) ₃ CH ₃	Sigma-Aldrich	98 %
sodium borohydride	NaBH ₄	Riedel-de Haën	95 %
sodium hydroxide	NaOH	Acros Organics	98.5 %
tantalum ethoxide	Ta(OC ₂ H ₅) ₅	Aldrich	99.98 %
tetramethylammonium fluoride tetrahydrate	N(CH ₃) ₄ F · 4 H ₂ O	Aldrich	98 %
tetramethylammonium hydroxide pentahydrate	N(CH ₃) ₄ OH · 5 H ₂ O	Acros Organics	99 %
tin chloride pentahydrate	SnCl ₄ · 5 H ₂ O	Aldrich	98 %
titanium isopropoxide	Ti(OCH(CH ₃) ₂) ₄	Aldrich	97 %
zinc acetate dihydrate	Zn(CH ₃ COO) ₂ · 2 H ₂ O	Acros Organics	98 %

3 Analytical methods

In the following, a short description of the analytical techniques used in this work will be given. Focus will be on the applications relevant for the results presented.

3.1 Electron microscopy

Electron microscopy can be utilized to view and take images of nanoscale objects.^[49-51] In principle, it works in the same way as light microscopy. However, since the limit of magnification is set by the wavelength of the radiation that is used to view the sample, applying an electron beam instead of light makes it possible to study structures smaller than the wavelength of visible light (400-750 nm). Electron microscopy can also be used for elemental analysis of the sample.

The two main advantages of electron microscopy compared to light microscopy are higher resolution and larger depth of field. The *resolution*, r , of a microscope is defined as the minimum distance between two nearby points that is needed to distinguish them as separate objects. Below the resolution limit, two nearby objects will be seen as one entity. Thus, it is possible to observe structures that are smaller than the resolution limit of the microscope. The resolution of a microscope is given by

$$r = \frac{0.61\lambda}{n \sin \theta} \quad (1)$$

where λ is the wavelength of the incident radiation, n is the refractive index of the medium between the object and the objective lens, and θ is the semi-angle between the object and the aperture at the objective lens in radians.

The *depth of field*, h , is defined as the range of object positions for which no change in the sharpness of the image can be detected. The depth of field is related to the resolution by the following expression

$$h = \frac{r}{\tan \theta} \quad (2)$$

Light microscopes have a theoretical resolution limit of around 150 nm ($\lambda = 400$ nm, $n \sin \theta = 1.6$). The depth of field is of about the same magnitude since large apertures (large angles) are used. In an electron microscope, small aperture angles ($\sin \theta \approx \tan \theta \approx \theta$) are used and the medium between object and lens is always vacuum ($n = 1$). Therefore, Equations (1) and (2) can be simplified to

$$r = \frac{0.61\lambda}{\theta}, h = \frac{r}{\theta} \quad (3)$$

Thus, for an angle of e.g. 5 degrees, the depth of field is much larger than the resolution. As a consequence, sharp images of objects with raw surfaces can be viewed with an electron microscope, in contrast to with a light microscope.

The electron source is normally a tungsten tip. The electron microscopes utilized in this work are operated with a *field emission gun (FEG)*. When an extremely high electric field ($>10^9$ V/m) is applied to a metal, electrons in a well-defined energy interval can be obtained through tunneling. To achieve this high field, tungsten is formed as a very sharp tip, and is

held under ultra-high vacuum. The electrons are then accelerated towards an anode, where the wavelength, λ , of the electron beam depends on the acceleration voltage, V , applied in the microscope according to the following relationship

$$\lambda = \frac{h}{\sqrt{2meV}} \quad (4)$$

where m is the electron mass, e is the electron charge, and h is Planck's constant.

Thus, for an acceleration voltage of e.g. 20 kV, a wavelength of ~ 10 pm is obtained. This would lead to a theoretical resolution in the subatomic range according to Equation (3). However, this resolution has not been achieved due to technical issues such as lens aberrations, which affect the electron beam diameter. The resolution also depends on the interaction volume, i.e., the volume of the sample from which detected electrons are coming from.

In an electron microscope, instead of optical lenses, electromagnetic fields are used to focus the electrons. The *condenser* lenses are used to control the size and angular spread of the electron beam that is incident on the sample. The sample chamber is held under vacuum in order to avoid scattering with particles in the chamber atmosphere. As the electron beam hits the sample, a number of interaction processes can take place (Figure 2).

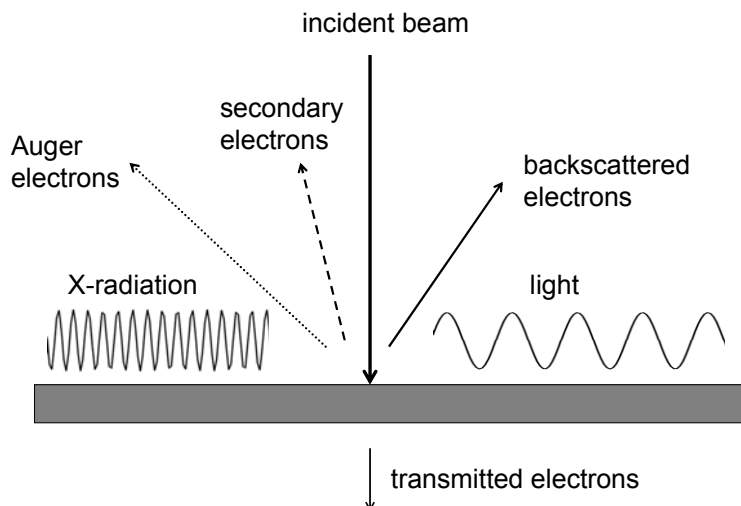


Figure 2. Interaction processes between the incident electron beam and the sample.

When an electron interacts with the sample, it can be scattered either *elastically* (i.e., the scattering does not lead to any change in energy) or *inelastically* (scattering leads to change in energy). The strength of elastic scattering is strongly dependent on the atomic number of the scattering element. An example of inelastic scattering is when the incident electron loses energy by knocking out an electron from a sample atom. The vacancy will then be filled via a transition of an electron from a higher energy level while excess energy is released. If the knocked-out electron is a valence electron, the released energy will be in form of a photon, which may be in the visible range. This effect is referred to as *cathodoluminescence*. If the knocked-out electron is an inner shell electron, the release of excess energy from the filling of the vacancy can be in the form of emission of characteristic X-ray radiation (see section 3.2), or an outer electron, a so-called *Auger electron*, can leave with the excess energy as kinetic

energy. Depending on which of these effects is detected, different information about the sample can be obtained.

There are two main types of electron microscopy: *transmission electron microscopy (TEM)* and *scanning electron microscopy (SEM)*. Some SEM and TEM instruments have an additional feature with which the emitted X-rays can be analyzed. As the X-ray radiation is characteristic for each element, this makes an elemental analysis of sample composition possible.

3.1.1 Transmission electron microscopy (TEM)

TEM makes use of the electrons that go through the sample and have been elastically scattered (diffracted).^[49,51] In a transmission electron microscope, electrons are accelerated to a voltage of typically 100 to 300 kV and sent through the sample. Sample thickness should be less than ~ 200 nm to avoid complete absorption. The size of the sample area illuminated by the electron beam can be controlled by an aperture between the condenser lenses. Electrons transmitted through the sample then pass through a sequence of lenses – objective, intermediate and projector – and finally arrive on a viewing screen. Photographs can be taken using photographic film or charged-coupled device (CCD) array cameras.

Depending on the settings of an intermediate lens between the objective lens and the following projector lenses, either a diffraction pattern or a magnified image of the sample is obtained as a final result (Figure 3).

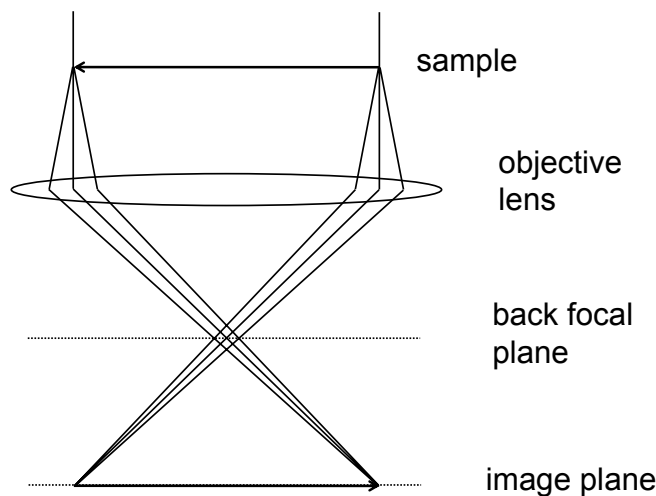


Figure 3. Sample, objective lens, and back focal and image plane in TEM.

In the image mode, the intermediate lens (not shown in the figure) is focused on the image plane of the object. The image is then magnified by the following projector lenses. Normally, a large sample area is illuminated by the electron beam. With *high resolution TEM (HRTEM)* it is possible to achieve a resolution of ~ 2 Å. Thereby, the lattice planes of a crystalline material can be directly observed. Since the strength of scattering is dependent on atomic number, different phases can be separated through intensity differences. Overview images can also be made, however the upper practical working limit of TEM is ~ 100 nm.

In the diffraction mode, the intermediate lens is focused on the back focal plane of the object. In this case, the diffraction pattern is then magnified by the projector lenses. The electron

diffraction pattern can, similarly to an X-ray diffraction pattern (see section 3.2), be used to characterize the crystal structure of the investigated specimen. A smaller sample area is normally illuminated by the electron beam in order to analyze only a selected part of the sample.

In this work, TEM was utilized to take overview and high resolution images of nanoparticles in order to study particle size and crystallinity. High resolution images were used for measuring lattice plane distances in order to confirm the crystal structure. TEM samples were prepared by ultrasonic nebulization of dispersions on holey or lacey-film Cu grids. The TEM images presented in this thesis were taken by Dipl. Phys. W. Send (ITO and SnO₂:F) and Dr. R. Popescu (ZnO:In and In) in the research group of Prof. Dr. D. Gerthsen, Laboratory for Electron Microscopy, University of Karlsruhe (TH).

3.1.2 Scanning electron microscopy (SEM)

SEM mainly makes use of electrons that have been inelastically scattered (reflected) off the sample.^[49,50] In a scanning electron microscope, acceleration voltages of 1 to 30 kV are employed. After being focused to a diameter of 2-10 nm by the condenser lens system, the electron beam is digitally scanned systematically over the sample. Sample thickness is unimportant, since only the surface is studied. As the beam hits the sample, scattering processes occur, whereby most electrons are brought to a halt within the solid. The penetration distance of the electrons is called interaction volume. The electrons that escape the sample make up the SEM image, which is displayed on a computer screen. The magnification of the image is done without any additional lenses and depends merely on the ratio between the scanned sample size and the size of the screen. The reflected electrons are divided into two types; *secondary electrons* and *back-scattered electrons*.

Secondary electrons are defined as having energy less than 50 eV. These low-energy electrons can be detected by an *Everhart-Thornley* detector, which consists of a scintillator-photomultiplier system and is placed on the side of the sample or within the focusing condenser lens system. Most secondary electrons have been inelastically scattered within a short distance of the primary beam, i.e. their interaction volume is small. However, some electrons escape the sample after multiple scattering processes and can also be detected. Electrons that have been scattered many times have a large interaction volume, which decreases the resolution of the image. However, multiple-scattered electrons are in clear minority. The higher-energy back-scattered electrons have been elastically scattered and can be detected by a *Robinson* detector. Since the strength of elastic scattering is dependent on atomic number, detection of back-scattered electrons gives an image of the elemental distribution in the sample.

The ratio between incident primary electrons and reflected secondary and back-scattered electrons is called the electron yield. At typical working voltages, the electron yield is less than unity, i.e., there are more electrons hitting the sample than leaving it. As a consequence, charges are built up, which, if they are not conducted to earth, repel the incident electrons and cause them to deviate. The deviations would cause image distortions and in order to prevent this, non-conducting samples are usually coated with a thin layer of metal. Scanning electron microscopes can be used over a much wider magnification range than transmission electron microscopes. With the SEM, structures over a range from $\sim 10^2$ to $\sim 10^{-2}$ μm can be studied. On one end of the scale, SEM complements optical microscopy for studying surface features of powders or solid pieces. On the other end of the scale, particle sizes and shapes, texture, and surface detail can be studied under high magnification.

In this work, SEM was utilized to take images of nanoparticles and thin layers thereof in order to study particle size, morphology, and agglomeration. SEM images were also used for statistical evaluation of particle size and size distribution. The instrument used was a Supra 40 VP microscope from Zeiss (Oberkochen, Germany) operated at 10 kV with a working distance of 3 mm. Statistical analysis was performed based on the software package Scandium 5.0 from Soft Imaging Systems. Samples were prepared by depositing suspensions in DEG or ethanol on silicon wafers, which were applied on aluminium sample carriers (Plano, Wetzlar, Germany), evaporated, and sputtered with Pt. Glass plates coated with thin layers were cut, applied on aluminium sample carriers, and sputtered with Pt.

3.1.3 Energy dispersive X-ray analysis (EDX)

Energy dispersive X-ray analysis can be carried out in a TEM or a SEM instrument.^[49-51] The energy of the X-rays that can be generated through inelastic scattering is characteristic for the energy levels of the elements present in the sample. By scanning the energy of the emitted X-rays, it is thus possible to identify the elements present in the sample. The smallest volume that can be analyzed with EDX in a SEM instrument is $\sim 1 \mu\text{m}^3$ since the interaction volume of X-rays is much larger than the electron interaction volume.

If the electron beam knocks out an inner shell electron of a sample atom, the vacancy is filled by an outer electron, and the excess energy is released as X-ray radiation. The allowed transitions are characteristic of the energy levels of the element (Figure 4). The transitions are named K-series, L-series, etc. after the shell of the knocked-out electron.

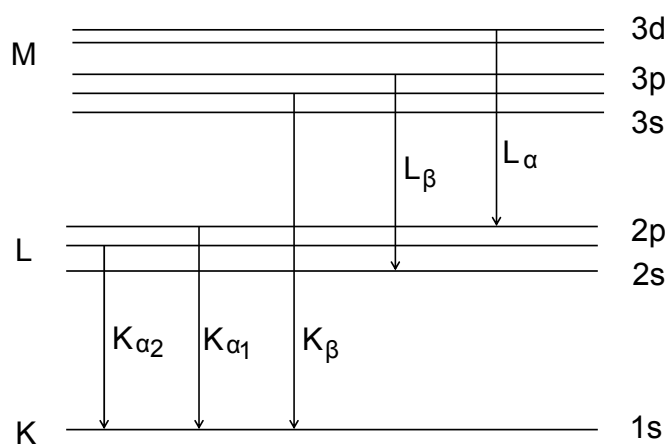


Figure 4. Some of the allowed transitions resulting in emission of characteristic X-rays.

The most efficient production of X-rays generally occurs when the bombarding electrons have energy of about three times as much as the generated X-ray radiation. Fortunately, all elements have at least one strong X-ray line with energy less than 10 keV, thus there is no problem to carry out EDX with an SEM instrument operating at 25-30 keV. Along with the characteristic peaks, there is also a significant amount of background in the spectrum, consisting of *bremstrahlung*, i.e., braking radiation, which is generated in the sample without ionization and can be of all wavelengths.

The emitted X-rays are detected by a semiconductor (normally Si or Ge) crystal, which is cooled to liquid nitrogen temperature (77 K). To avoid condensation of contaminants from the

sample chamber on the cold surface of the detector, it must be covered by a protective film. The protective film inevitably absorbs a part of the incident radiation, and thereby sets a limit for the energy of the elements that can be analyzed. If a very thin polymer film is used, it is possible to detect all elements with an atomic number equal to or larger than boron. The element concentration in the sample must be at least around 0.1 % in order for the emission peak of the characteristic X-ray radiation to be separable from the background of bremsstrahlung X-rays.

EDX can also be used for quantitative elemental analysis of the sample if a suitable calibration procedure has been adopted. However, due to inevitable differences between sample and calibration standard, the accuracy of quantitative EDX is relatively low. Since calibration standards consist of pure elements, whereas investigated samples normally are compounds, corrections of atomic number (Z), absorption (A), and fluorescence (F) effects must be carried out (so-called ZAF correction). Different elements generate X-rays with different efficiencies and also absorb them with different efficiencies, which can lead to inaccuracies if elements with large differences in atomic number are present in the sample. On the other hand, if elements with similar atomic number are present, X-rays generated by one element can excite X-rays from another element, which is known as fluorescence. The ZAF correction is done automatically by the instrument software.

In this work, elemental analyses of samples were carried out via EDX with a Supra 40 VP microscope from Zeiss (Oberkochen, Germany). The applied acceleration voltage was 15 kV and the working distance 8 mm. Samples were prepared by application of powders on conductive carbon adhesive tape adhered on aluminium sample carriers, both from Plano (Wetzlar, Germany).

3.2 X-ray diffraction (XRD)

The main application of X-ray diffraction (XRD) is to determine the crystal structure of a material.^[52-54] For already known structures, this is done by comparison with database records, whereas for unknown structures, this must be done by calculations.

X-rays are electromagnetic radiation of wavelength $\sim 1 \text{ \AA}$, i.e., of the same order of magnitude as the interatomic distances in solid state matter. Therefore, when X-rays fall on a crystalline material, they are diffracted. Modern X-ray diffraction experiments employ monochromatic X-rays, which can be produced by accelerating an electron beam coming from a heated tungsten filament through a high voltage of typically 40 - 60 kV. When the electrons strike a metal target, e.g. copper, characteristic X-ray radiation is emitted (see section 3.1.3). The X-ray radiation used in most diffraction experiments is the $\text{Cu-K}_{\alpha 1}$ radiation, which has a wavelength of 1.54 \AA and originates from the transition $2p \rightarrow 1s$ in copper. Radiation of other wavelengths originating from bremsstrahlung and other transitions can be removed by insertion of filters or monochromators in the beam path before the beam hits the sample.

When X-rays are incident on a periodic structure of lattice planes, they are scattered by the electrons of the lattice atoms (Figure 5), whereby scattering strength increases with increasing atomic number.

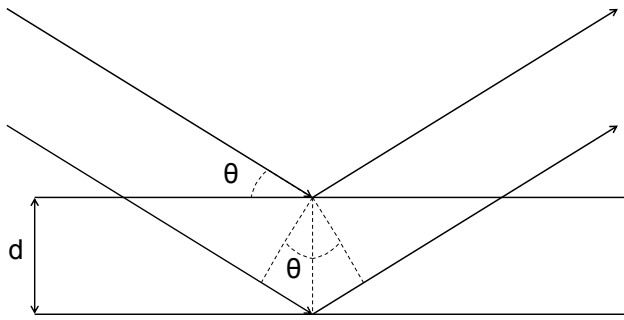


Figure 5. Diffraction of electromagnetic radiation according to Bragg's law.

The angle of incidence is denoted θ and the lattice plane distance is referred to as d . The electromagnetic waves scattered from two adjacent planes interfere according to Bragg's law

$$2d \sin \theta = n\lambda \quad (5)$$

where n is an integer and λ the wavelength of the incident radiation.

Thus, there is constructive interference between scattered waves when the optical path difference between them is equal to an integer multiple of the wavelength of the incident radiation. When the lattice plane distance is in the same order of magnitude as the wavelength of the incident radiation, individually resolved diffraction peaks of order $n = 1, 2, 3, \dots$, etc. can be observed. In every crystal, there are many sets of lattice planes upon which X-rays are diffracted. Each plane is characterized by its *Miller indices*, which are given in the form (hkl) .

Depending on the form of the sample, namely, if the sample consists of a large (tens of a millimeter in size) single crystal, or many small crystals (micrometers and below in size), the diffraction pattern generated is rather different. The diffraction pattern of a single crystal consists of spots of varying intensity in a periodic pattern (Figure 6 a). In a polycrystalline powder, the many small crystals are oriented in all different directions. This causes the spots of the separate crystals to expand into concentric circles (Figure 6 b). These two cases make out the two main X-ray diffraction methods – single crystal methods (see section 3.2.1) and powder methods (see section 3.2.2).

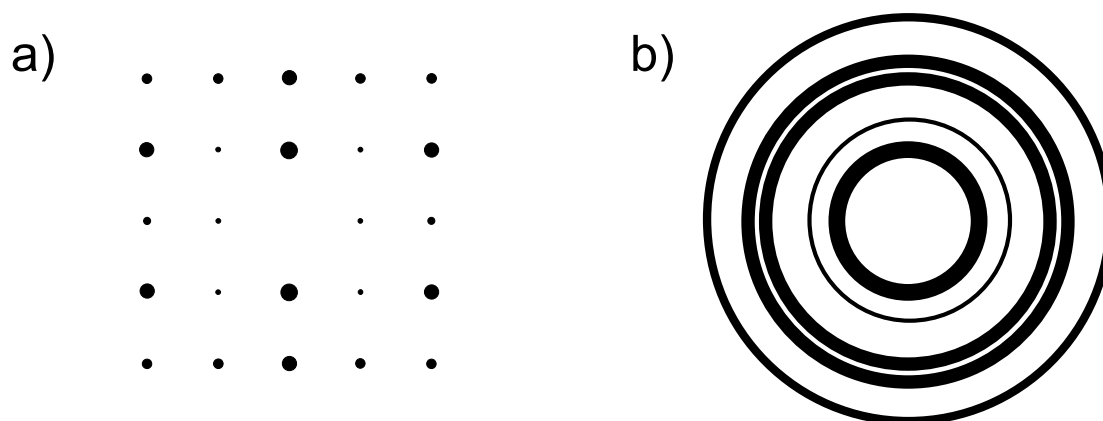


Figure 6. Diffraction pattern from a) single crystal and b) polycrystalline powder.

Rearrangement of Equation (5) and setting $n = 1$ gives

$$\sin \theta = \left(\frac{\lambda}{2} \right) \times \left(\frac{1}{d_{hkl}} \right) \quad (6)$$

The distance of each spot or circle from the center of the diffraction pattern is proportional to $\sin \theta$ and hence to $1/d_{hkl}$. Thus, there is a reciprocal geometrical relationship between a crystal lattice and its diffraction pattern. For example, if the d_{hkl} is increased due to incorporation of larger ions in the lattice, the reflections are shifted to smaller θ .

Diffraction patterns can be recorded either with a photographic film or a detector, which converts the incident X-rays into a digital signal. There are small movable counter detectors as well as larger position sensitive area detectors, such as CCD systems or image plates.

3.2.1 X-ray single crystal diffraction

X-ray single crystal diffraction is applied to determine the crystal structure of samples in the form of single crystals.^[52-54] In an ideal single crystal the unit cells are all aligned in the same orientation, so that they scatter cooperatively to give a clear diffraction pattern. In all real crystals, however, there is a slight misalignment creating a mosaic structure. In a good quality single crystal, the misalignment is only a fraction of a degree. For a randomly oriented crystal, the Bragg equation will be satisfied for only very few reflections. Therefore, the crystal must be rotated around different axes during measurement.

The unit cell geometry (side lengths a , b , and c , angles α , β , and γ) and preliminary symmetry information can be determined from a subset of the complete diffraction pattern. This is done by assigning the correct hkl indices to each of the observed reflections. From these and the measured Bragg angle for a few reflections, the six unit cell parameters can be calculated from Bragg's law. The subset can be recorded within minutes when an area detector is used and the calculations are done by a computer. Recording the full diffraction pattern (consisting of thousands of reflexes) including intensities can take days.

The intensity, I , of a reflection in a crystal diffraction pattern is equal to the square of the amplitude of a diffracted wave F , which can be expressed as

$$F = |F|(\cos \varphi + i \sin \varphi) \quad (7)$$

where $|F|$ is the amplitude and φ the phase of the diffracted wave.

The diffraction pattern and the arrangement of atoms in the unit cell of the crystal structure are related to each other by Fourier transformation: the diffraction pattern is the Fourier transform of the electron density of the crystal and the electron density is itself the Fourier transform of the diffraction pattern. However, during detection, an important piece of information is lost – only the intensity of the diffracted radiation is recorded. Thus, the information about the phase is lost and the structure cannot be determined by simply Fourier transforming the recorded diffraction pattern. This is referred to as the *phase problem* and is a fundamental challenge of crystal structure determination. Due to the phase problem, solving a crystal structure involves a significant amount of trial-and-error.

The measured intensities are converted to observed structure amplitudes, $|F_o|$, and each amplitude has a standard uncertainty, $\sigma(F_o)$, associated with it, which is a measure of the quality of the measurement. The first step of solving the full structure is to identify a part of the structure, i.e. the positions of some of the atoms. Since scattering is proportional to atomic number, heavy atoms contribute to a large part of the pattern and if only few heavy atoms are present, they can be easily identified. Sometimes certain atomic groups are known to be present and can be identified or the symmetry can be considered. When some atom positions have been identified, a Fourier transform of this first model structure is carried out, which results in a set of calculated structure factors F_c , consisting of amplitude $|F_c|$ and phase φ_c . Now, the two sets of values are compared in various ways, e.g. with the *residual factor* R defined as

$$R = \frac{\sum ||F_o| - |F_c||}{\sum |F_o|} \quad (8)$$

R is thus a measure of how well the pattern calculated from the model structure fits the real (observed) pattern. Now, a reverse Fourier transform is carried out with the observed amplitudes $|F_o|$ and the calculated phases φ_c as parameters. If the errors in the calculated phases are not too large, an electron density map including the first model structure and some additional atoms not already known is obtained from the reverse Fourier transform. If the reverse Fourier transform is carried out with the difference $|F_o| - |F_c|$ as parameter instead of just $|F_o|$, the already known atoms do not appear and the new atoms stand out more clearly, which makes the procedure more effective. Then, a forward Fourier transform gives new calculated $|F_c|$ and φ_c and the process can be repeated until no more new atoms are found. When all atoms are found, all structure parameters are refined with least-squares methods. There are commonly nine parameters per independent atom to be refined (x , y , z , and six displacement parameters due to vibrations of the atom). However, there are normally many more reflections than independent parameters, thus the refinement problem is over-determined.

In this work, single crystal XRD was applied with the intention to determine the crystal structure of crystals. Measurements were conducted with a STADI-4 four-circle diffractometer from STOE & CIE (Darmstadt, Germany).

3.2.2 X-ray powder diffraction

X-ray powder diffraction is applied to determine the crystal structure of powder samples and is mainly used for qualitative identification of crystalline phases or compounds.^[52-54] Impurities in form of separate crystalline phases can be determined with a limit of detection in the range 1 to 5 per cent.

The sample is a finely powdered substance consisting of small crystals, which ideally are randomly arranged in all directions. For each set of lattice planes, some crystals will be oriented at the Bragg angle, θ , to the incident beam and diffraction will occur for these planes and crystals. The resulting diffracted beam will appear as a cone with semi-angle 2θ (Figure 7). The diffracted beam may be detected by surrounding the sample with a strip of photographic film, or by using a movable detector. Each cone intersects the film as two short arcs that appear as lines on the detector surface. In modern instruments, a convergent, intense incident beam, which improves the resolution of lines, is obtained by placing a bent single crystal between the X-ray source and the sample. A beam stop is inserted between the sample and the detector to prevent the highly intensive transmitted beam, corresponding to $n = 0$ in Equation (5), from hitting the detector.

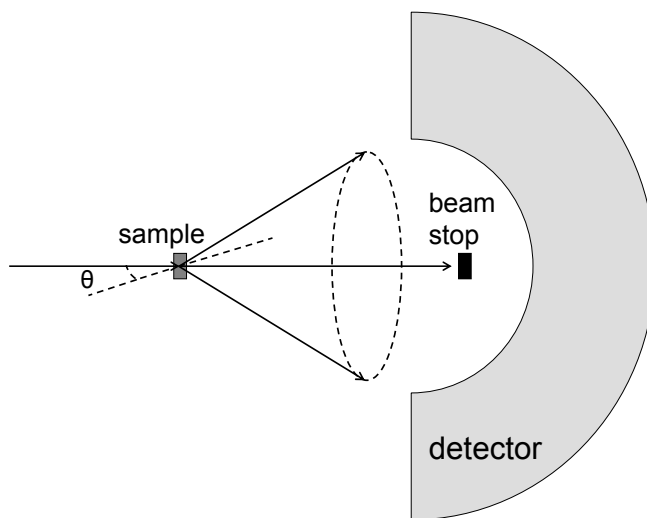


Figure 7. Schematic set-up of a powder diffractometer.

The resulting powder diffraction pattern is plotted as intensity versus angle. The lines in a powder diffraction pattern are of finite width, and if the sample consists of very small single-crystalline domains (crystallites), the lines are extra broadened. The line broadening increases with decreasing crystallite size, and as a result, X-ray powder diffraction may also be used to estimate the average crystallite diameter, D , in a powdered sample. This is usually done using Scherrer's formula

$$D = \frac{0.89\lambda}{FWHM \cdot \cos\theta} \quad (9)$$

where λ is the wavelength of the incident X-ray radiation, θ is the diffraction angle, and $FWHM$ stands for the full width at half maximum of the diffraction peak in question.

If the crystallite diameter is in the range of roughly 20 to 100 Å, the lines become so broad that it is impossible to distinguish them from the background radiation, and thus Scherrer's formula cannot be applied any more.

Powder XRD was in this work carried out with a STADI-P diffractometer from STOE & CIE (Darmstadt, Germany), operating with Ge-monochromatized Cu-K α radiation with a wavelength of 1.54 Å. The measured diffractograms were evaluated with the program Win-XPOW by comparison with the International Centre for Diffraction Data (ICDD) data base. Samples were prepared by applying a thin film of powder on a piece of adhesive tape. Radiation was detected within an angle interval of $-69^\circ \leq \theta \leq 69^\circ$.

3.3 Light scattering techniques

3.3.1 Particle sizing with dynamic light scattering (DLS)

Dynamic light scattering (DLS) measures the time-dependent fluctuations of the intensity of light scattered from particles in a suspension.^[55-59] From these data, the diffusion coefficient of the particles can be determined, from which the particle size then can be estimated. The terms quasielastic light scattering (QELS) or photon correlation spectroscopy (PCS) are sometimes used instead of dynamic light scattering.

The Brownian motion of dispersed particles causes fluctuations in the total intensity of scattered light which are related to the velocity of the particles. In a system where the Brownian motion is not interrupted by sedimentation or particle-to-particle interactions, the movement of particles is random. However, when the intensity of scattered light is measured twice within a short time interval, the observed values will be correlated. The correlation decreases as the time interval increases. The correlation decreases faster if the particles are smaller, since smaller particles move apart from each other faster. The autocorrelation function, $G_2(\tau)$, is defined as the average value of the product of the scattered intensity at an arbitrary time, t , and the intensity at a later time, $t + \tau$:

$$G_2(\tau) = \langle I(t)I(t + \tau) \rangle \quad (10)$$

The autocorrelation function is related to the electric field autocorrelation function $g_1(\tau)$

$$G_2(\tau) = A + Bg_1^2(\tau) \quad (11)$$

where A is the background scattering and B is an instrument-depending factor.

The ratio B/A is regarded as a quality factor, or the signal-to-noise ratio, of the measurement. For a monodisperse system of particles in Brownian motion, the electric field autocorrelation function is an exponential decay

$$g_1(\tau) = \exp(-\Gamma \tau) \quad (12)$$

where Γ is the decay constant, given by

$$\Gamma = Dq^2 \quad (13)$$

where D is the diffusion coefficient and q is the modulus of the scattering vector

$$q = \frac{4\pi n}{\lambda} \sin(\theta/2) \quad (14)$$

where n is the refractive index of the dispersion medium, θ is the scattering angle, and λ the wavelength of the incident light.

The particle size, d , is often obtained from the Stokes-Einstein equation for the diffusion coefficient D

$$D = \frac{kT}{3\pi\eta d} \quad (15)$$

where k is Boltzmann's constant, T is the absolute temperature, and η the viscosity.

For a reliable determination of the particle size, T must be kept constant within ± 0.1 °C. Stokes-Einstein equation is only valid for non-interacting, spherically shaped, smooth, and rigid particles, and is only an approximation for other cases. In addition, for polydisperse samples, the autocorrelation function has to be extended to an integral

$$g_1(\tau) = \int_0^{\infty} C(\Gamma) \exp(-\Gamma \tau) d\Gamma \quad (16)$$

where $C(\Gamma)$ represents the distribution of decay rates.

Since this equation has no definite solution, several different distribution curves will fit the measured autocorrelation function, and exact intensity distributions cannot be obtained. The obtained intensity distributions are converted to volume distributions. For particles where d/λ is smaller than 1/20 ($d \sim 30$ nm), the volume distribution can be obtained via Rayleigh scattering theory. Here, the intensity-size dependency is shown in the following equation

$$I = \frac{8\pi^4 d^6}{r^2 \lambda^4} \left(\frac{n^2 - 1}{n^2 + 2} \right)^2 (1 + \cos^2 \theta) \quad (17)$$

where r is the distance from the particle to the detector.

For larger particles, the volume distribution can be obtained via so-called Mie theory.^[60] Mie theory is relatively complex, because here the proportionality between intensity and size depends on the ratio d/λ . However, Mie theory is valid for spherical particles of arbitrary size and is therefore used for calculations in DLS instruments. Finally, the obtained volume distribution can simply be converted to number distributions via the volume of a sphere ($4\pi r^3/3$). Despite the complicated and inexact theory, dynamic light scattering has the advantage of being a fast, non-invasive method, which gives an approximate size distribution of a suspension within minutes.

In this work, DLS was applied to determine the particle average size and size distribution in a suspension. DEG suspensions were measured in polystyrene cuvettes with a Nanosizer ZS from Malvern Instruments (Herrenberg, Germany). The light source was a 4.0 mW He-Ne laser with a wavelength $\lambda = 633$ nm. Measurements were conducted of suspensions enough diluted to deter particle-to-particle interactions, which was determined through a dilution series. Measurements of suspensions with solids contents of 10 wt-% were also carried out.

3.3.2 Zeta potential with electrophoretic light scattering

The *zeta potential* is a measure of the electrostatic potential at the hydrodynamic plane of shear between a stationary liquid and a charged surface made up of a moving particle and the ions moving together with it.^[55,56] This potential determines the net interparticle forces and is therefore an important property when investigating colloidal stability. It is normally measured as a function of pH or amount of added surface stabilizer. The point where the zeta potential and thus the net interparticle forces are zero is called the *isoelectric point (IEP)*, or *point of zero charge (PZC)*.

The movement of a charged particle relative to a stationary liquid under the influence of an applied electric field is called *electrophoresis*, whereas *electroosmosis* refers to the motion of a liquid relative to a stationary charged surface. The velocity v of a particle in electrophoretic motion is given approximately by

$$v = \frac{\varepsilon \zeta E}{f \pi \eta} \quad (18)$$

where ε is the dielectric constant of the dispersion medium, ζ is the zeta potential, E is the electric field at the particle, f is a shape factor, and η is the viscosity of the medium. The ratio v/E is termed the electrophoretic mobility.

For nonconductive particles where the extent of the ionic double layer around them is small relative to the radius of the particle, the applied electric field lines conform to the shape of the particles. In this case, the shape factor $f=4$ according to Smoluchowski. For particles with conductivity equal to the bulk liquid, which are much smaller than the thickness of the ionic double layer, the applied field lines run straight between the electrodes, without conforming to the shape of the particles. In this case, the shape factor $f=6$ according to Hückel.

When measuring the electrophoretic velocity of a dispersion, electroosmotic effects also have to be taken into account, since the electroosmotic flow is superimposed on the electrophoretic movement of the particles in the cell. At a certain point or level in the suspension – the stationary level – the resultant velocity of the osmotic flow is zero. Here, the electrophoretic mobility can be accurately measured. Another solution is to apply an alternating field of sufficiently high frequency to suppress electroosmotic flows. Colloidal particles respond to the electric field much faster than the time it takes for the electroosmotic flows to develop. Hence the mobility of particles can be measured within a short time interval before the electroosmosis has started.

The electrophoretic velocity is measured with the laser Doppler method and utilizes electrophoretic light scattering (ELS). The output of a laser is split into two coherent beams which are cross-focused in the cell to illuminate the sample. The light scattered by the particle, together with the reference beam, is detected by a photomultiplier. Since the Doppler shift often is too small to detect due to the slow motion of the particles, the phase shift is instead detected.

In this work, measurements of the zeta potential of aqueous suspensions as a function of the pH value were performed with a Nanosizer ZS from Malvern Instruments (Herrenberg, Germany). Titration was performed by a MPT2 Autotitrator, also from Malvern Instruments. Samples were prepared by redispersing powders in H₂O via ultrasound. During measurement, the suspensions were vigorously stirred.

3.4 Nitrogen adsorption (BET)

The specific surface of a substance can be measured via gas adsorption with the *Brunauer-Emmett-Teller (BET)* type of method.^[61-64] When adsorption occurs on a solid, the solid is referred to as the *adsorbent* and the adsorbed material the *adsorbate*. Adsorption is a spontaneous, exothermic process. Because of its exothermic nature, the adsorption will decrease with increasing temperature. Molecules and atoms can adsorb on surfaces either physically (*physisorption*) or chemically (*chemisorption*).

In physisorption processes, only weak, but long ranging van der Waal interactions take place between surface and adsorbate. The heat of adsorption, E_{Ads} , is in the same order of magnitude as the heat of condensation, E_L of the adsorbate. Physisorption requires no activation energy and is therefore a reversible process for which equilibrium will be reached quickly. Multiple layers of adsorbate can form. In chemisorption processes, a chemical bond, usually covalent, is formed between adsorbent and adsorbate. E_{Ads} is here much larger than in the case of physisorption. Chemisorption processes in general have activation energy and may therefore be much slower than physisorption processes. They may also be non-reversible, i.e., they may exhibit hysteresis. Chemisorption is limited to the formation of a monolayer of adsorbate. The general relationship between the amount of gas (volume V) adsorbed by a solid at a constant temperature (T) and as a function of the gas pressure (P) is defined as its adsorption isotherm.

Langmuir isotherms apply in the case of chemisorption, where the adsorbed volume reaches a limiting value, corresponding to attainment of monolayer coverage. The assumptions of the Langmuir isotherm model are: adsorption cannot exceed monolayer coverage, adsorption is localized to specific sites (where interactions are solely between the site and a specific molecule), and the heat of adsorption is independent of the amount of material adsorbed. The rate of adsorption (rate constant k_A) is assumed to be proportional to the partial pressure of the adsorbate, p , and the number of unoccupied adsorption sites, $N - n$, where N is the total number of adsorption sites and n the number of occupied sites. The rate of desorption (rate constant k_D) is proportional to n . At equilibrium, the rates of adsorption and desorption are equal, which gives the following relationship

$$k_A p(N - n) = k_D n \quad (19)$$

The equilibrium constant K_{eq} of the process is given by

$$K_{eq} = \frac{k_A}{k_D} = \exp\left(\frac{-E_{Ads}}{RT}\right) \quad (20)$$

where R is the gas constant and T the temperature.

From Equations (19) and (20), the Langmuir equation can be stated

$$\frac{1}{n} = \frac{1}{N} + \frac{1}{K_{eq} N p} \quad (21)$$

Plotting n^{-1} versus p^{-1} should be linear if the Langmuir model applies.

BET isotherms apply in the case of physisorption. After monolayer coverage, the adsorbed volume continues to increase, corresponding to multilayer coverage. The BET model assumes that the Langmuir equation applies for each layer of adsorption and that the heat of adsorption

for the first layer has a characteristic value, E_{Ads} , whereas it for all subsequent layers is equal to the heat of condensation, E_L . These assumptions lead to the *BET equation*

$$\frac{p}{V(p_0 - p)} = \frac{1}{V_m c} + \frac{(c-1)}{V_m c} \frac{p}{p_0} \quad (22)$$

where p is the partial pressure of the adsorbate, p_0 is the saturated vapor pressure of the adsorbate, V is the adsorbed volume, V_m is the monolayer volume, and the BET constant c is given by

$$c \approx \exp\left(\frac{E_{Ads} - E_L}{RT}\right) \quad (23)$$

The BET isotherm fits experimental observations moderately well over restricted pressure ranges, but it errs by underestimating the extent of adsorption at low pressures and by overestimating it at high pressures. However, plotting $p/V(p_0 - p)$ versus p/p_0 usually gives a straight line in the range $0.05 \leq p/p_0 \leq 0.35$ having a slope s and intercept i

$$s = \frac{c-1}{V_m c}, \quad i = \frac{1}{V_m c} \quad (24)$$

From Equation (24), the monolayer volume V_m can be calculated and the specific surface area A_{BET} then equals

$$A_{BET} = \frac{V_m N_A A}{M_V} \frac{1}{\text{sample weight}} \quad (25)$$

where N_A is Avogadro's number, A is the area per adsorbate molecule, and M_V the adsorbate molar volume.

Assuming that the particles are rigid spheres, the mean particle size, D , can be estimated from the BET specific area A_{BET} using the following relationship:

$$\frac{D}{6} = \frac{1}{A_{BET} \cdot \rho} \quad (26)$$

where ρ is the bulk density.

In this work, BET analyses of powder samples were carried out with a BELSORP-mini II instrument from BEL Japan (Osaka, Japan) in order to determine their specific surfaces. The applied adsorbate was gaseous N_2 , therefore the sample was cooled with liquid N_2 to a temperature of 77 K. Measurements were done according to a volumetric method while correcting for saturated vapor pressure and dead volume.

3.5 Thermal analysis (DTA-TG)

The term thermal analysis is used to describe measurement of endothermic and exothermic effects caused by thermal processes in materials.^[52,65] Material properties such as enthalpy, heat capacity, weight, and coefficient of thermal expansion, can be determined as a function

of temperature. Thermal analysis can be conducted in order to study e.g. solid state reactions, thermal decompositions, and phase transitions.

Thermogravimetry (TG) measures the change in weight of a substance as a function of temperature or time. Thereby, the sample weight is recorded as the sample is heated at constant rate to a specific temperature. Thermogravimetry is normally carried out at the same time as *differential thermal analysis (DTA)* or *differential scanning calorimetry (DSC)*. *Differential thermal analysis (DTA)* measures the difference in temperature, ΔT , between a sample and an inert reference material as a function of temperature. Sample and reference are placed side by side in a heating block which is either heated or cooled at a constant rate. Each is connected to a thermocouple, which are connected back to back. Initially, sample and reference have the same temperature, thus the net output of the thermocouples is zero. As a thermal event takes place in the sample, the sample temperature either lags behind (endothermic process) or leads (exothermic process) the reference temperature. The temperature difference between sample and reference, ΔT , is detected by the net voltage of the two thermocouples. A third thermocouple is used to monitor the temperature of the heating block.

In this work, DTA-TG was performed with a STA 409C instrument from NETZSCH (Selb, Germany), applying $\alpha\text{-Al}_2\text{O}_3$ as crucible material as well as reference sample. The samples were heated under N_2 flow to up to 800 °C with a heat rate of 10 K/min.

3.6 Four-point probing

Four-point probing is a method to measure the electrical resistivity of thin samples, typically semiconductors.^[66-68]

The electrical resistivity, ρ , of a material is the inverse of the conductivity, σ , which is the product of the number of charge carriers, N , (free electrons and holes), their mobility, μ , and the elementary charge, e , according to the following expression

$$\rho = \frac{1}{\sigma} = \frac{1}{eN\mu} \quad (27)$$

The mobility is a measure of how strongly the drift velocity v of a charge carrier is influenced by an applied electric field E

$$v = -\mu E \quad (28)$$

The charge carrier velocity, and thereby the mobility, is decreased by different scattering processes. The two main scattering mechanisms influencing the mobility are lattice scattering and impurity scattering; both of which are temperature dependent. Lattice scattering increases with increasing temperature, whereas impurity scattering decreases with increasing temperature. For lightly doped samples, the mobility will be dominated by lattice scattering for all temperatures, whereas the impurity scattering will be dominating at low temperatures for heavily doped samples. The number of charge carriers N is temperature independent for metals but is exponentially dependent of the temperature for semiconductors. For example, for an intrinsic semiconductor, N is given by

$$N = \sqrt{N_c N_v} \exp(-E_g / 2k_B T) \quad (29)$$

where E_g is the energy band gap, k_B is Boltzmann's constant, T is the temperature, and N_c and N_v are the effective density of states in the conduction and valence band, respectively.

The four-point probing method is the most common method to determine the resistivity of a thin material. As shown in Figure 8, the resistivity of a sample is measured using four electrodes, where the current I is applied to the two outer electrodes. The resulting voltage V is measured between the two inner electrodes while drawing either no or very little current. This procedure eliminates the problem with probe and contact resistance, which would be part of the measured resistance if two electrodes were used.

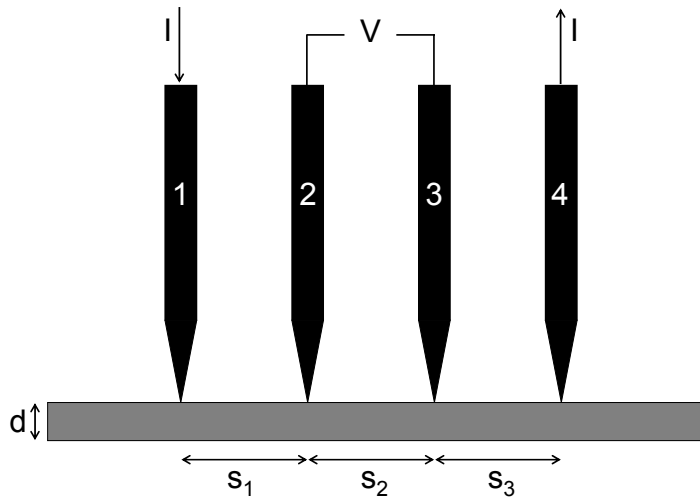


Figure 8. Schematic set-up of the four-point probing method.

The potential, V , at a distance, r , from an electrode carrying a current, I , in a material of resistivity, ρ , is given by the relationship

$$V = \frac{\rho I}{2\pi r} \quad (30)$$

For probes resting on a semi-infinite medium with current entering probe 1 and leaving through probe 4, the voltage V_0 , measured with respect to zero reference potential, becomes

$$V_0 = \frac{\rho I}{2\pi} \left(\frac{1}{r_1} - \frac{1}{r_4} \right) \quad (31)$$

where r_1 and r_4 are the distances from probes 1 and 4, respectively.

For probe spacings s_1 , s_2 , and s_3 , the voltages V_2 at probe 2 and V_3 and probe 3 are given by

$$V_2 = \frac{\rho I}{2\pi} \left(\frac{1}{s_1} - \frac{1}{s_2 + s_3} \right), \quad V_3 = \frac{\rho I}{2\pi} \left(\frac{1}{s_1 + s_2} - \frac{1}{s_3} \right)$$

With equal probe spacings $s_1 = s_2 = s_3$, the measured voltage $V = V_2 - V_3$ becomes

$$V = \frac{\rho I}{2\pi s} \quad (32)$$

The resistivity can easily be determined from Equation (32). However, this relation is only valid for semi-infinite geometries; for finite geometries a correction factor, F , is introduced, so that

$$\rho = 2\pi s F \frac{V}{I} \quad (33)$$

For thin samples, where the distance s between the electrodes is much larger than the thickness d of the sample ($d \ll s$), F is given by

$$F = \frac{d}{s} \frac{1}{2 \ln(2)} \quad (34)$$

Now, the sheet resistance R_s of a homogeneous sample is defined as

$$R_s = \frac{\rho}{d} \quad (35)$$

From Equations (33), (34), and (35) a useful expression for the sheet resistance is gained

$$R_s = \frac{\pi}{\ln(2)} \frac{V}{I} \quad (36)$$

Thus, from the measured voltage, V , and the measured current, I , the sheet resistance can be obtained. The resistivity is then obtained by multiplying the sheet resistance with the sample thickness.

In this work, the sheet resistances of pellets and thin layers were measured via four-point probing using a Keithley system (485 Autoranging Picoammeter, 199 System DMM/Scanner, 230 Programmable Voltage Source). The measuring station was constructed by Dr.-Ing. A. Weber in the research group of Prof. Dr.-Ing. E. Ivers-Tiffée, Institute of Materials for Electrical Engineering, University of Karlsruhe (TH). The electrodes were placed in a row at a distance of 1.0 mm from each other. To calculate the sheet resistance of pellets and thin layers, a geometrical correction factor equal to $\pi/\ln 2$ was applied.^[68]

In order to minimize the influence of grain boundaries when evaluating the electrical resistance, pellets were prepared by pressing 50-100 mg powder with an IR pressing tool for 15 min at 50 kN (stainless steel pressing tool, 13 mm in diameter; hydraulic laboratory press, both from Specac, Orpington, UK). The thickness of the pellets was calculated from the substance weight and density.

3.7 Absorption Spectroscopy

With absorption spectroscopy, the amount of absorption in a substance is analyzed as a function of the energy of incident electromagnetic radiation.^[61] Absorption occurs when energy provided to the sample causes a transition between two energy levels in the sample; thus, the energy levels of the sample are characterized with spectroscopy.

Energy is provided in the form of electromagnetic radiation and can, if in the right amount, lead to a transition between two energy states in the sample. In general, the absorbed energy, i.e., the energy difference, ΔE , between the two states associated with the transition, can be expressed in terms of the frequency, ν , or the wavelength, λ of the incident radiation:

$$\Delta E = h\nu = h\frac{c}{\lambda} \quad (37)$$

where c is the speed of light and h is Planck's constant.

The absorbance, A , of a substance is defined as:

$$A = \frac{\text{intensity of absorbed radiation}}{\text{intensity of incident radiation}} \quad (38)$$

The radiation that is not absorbed can be either transmitted through or reflected off the sample. The transmittance, T and the reflectance, R , are defined similarly as the absorbance:

$$T = \frac{\text{intensity of transmitted radiation}}{\text{intensity of incident radiation}} \quad (39)$$

$$R = \frac{\text{intensity of reflected radiation}}{\text{intensity of incident radiation}} \quad (40)$$

The sum of the three quantities is always equal to unity.

$$T + R + A = 1 \quad (41)$$

The absorbance can never be directly measured, but must be calculated from Equation (41). In many cases, however, either the reflectance or the transmittance can be assumed to be zero, which simplifies calculation of A . For cases where $R = 0$, Lambert-Beer's law can be applied:

$$T = \exp(-\alpha d) \quad (42)$$

where α is the absorption coefficient, d is the thickness of the sample, and A is given by $A = \alpha d$.

What type of absorption process is involved depends on which spectral region the incident electromagnetic radiation lies in, which will be explained in more detail in the following sections.

3.7.1 Fourier transform infrared (FT-IR) spectroscopy

Infrared (IR) radiation has a wavelength of about $1\text{-}10^4\ \mu\text{m}$ and can excite molecular vibrations and rotations. Many functional groups in organic molecules show characteristic absorptions in the IR region, and can thus be identified with IR spectroscopy.^[69,70]

IR absorption spectra are normally plotted as transmitted intensity versus *wavenumber* $\tilde{\nu} = 1/\lambda$ (cm^{-1}), since this quantity is proportional to the absorbed energy, in contrast to the wavelength.

$$\Delta E = h \frac{c}{\lambda} = hc \tilde{\nu} \quad (43)$$

IR radiation can excite motions – vibrational and rotational – of molecules or atomic groups via interaction with their dipole moments. The type of vibration occurring in an atom group can be either *stretching* or *deformation*. Stretching vibrations, denoted ν , alter the bond length, whereas deformation vibrations, denoted δ , alter the bond angles while the bond length is mainly unchanged. Rotational motions always occur together with vibrational motions. However, rotational motions can normally only be observed as well-resolved absorption bands for gaseous molecules.

IR spectra are most often used for straightforward identification of specific functional groups through comparison with tables or data base records. In inorganic solids, covalently bonded linkages such as hydroxyl groups, trapped water and oxyanions – carbonate, nitrate, sulphate etc. give rise to intense IR peaks. Peaks associated with the vibrational modes of covalently bonded groups such as oxyanions, usually occur at relatively high frequencies above $300\ \text{cm}^{-1}$. At lower frequencies in the far infrared region, lattice vibrations give rise to peaks, e.g. alkali halides have bands in the region 100 to $300\ \text{cm}^{-1}$.

The main type of modern commercial spectrometer is the *Fourier transform infrared* (FT-IR) instrument based on interferometric measurement. Here, before hitting the sample, the beam is sent through an interferometer with movable mirror positions. The intensity signal from the detector, as a function of the change of the optical pathlength is called an interferogram. Adding several interferograms improves the signal-to-noise ratio. The obtained interferograms are converted into the spectrum by Fourier transformation. FT spectrometers have several advantages over dispersive spectrometers; since all wavelengths are measured at the same time, measurements can be carried out faster, or, when measurement time is the same, FT spectrometers achieve a higher signal-to-noise ratio. The wavelength stability of FT spectrometers is also superior that of dispersive spectrometers, due to the integration of a He-Ne laser used for wavelength calibration of every measurement.

In this work, FT-IR spectra were recorded with a Vertex 70 FT-IR spectrometer from Bruker Optics (Ettlingen, Germany). The instrument applies a Globar (a silicon carbide rod) as radiation source and a pyroelectric detector. The transmittance of pellets consisting of 1 mg substance powder and 300 mg KBr was measured in a wavenumber interval of $7000\text{-}370\ \text{cm}^{-1}$. The instrument was flowed with N_2 during measurement.

3.7.2 Ultraviolet-visible (UV-Vis) spectroscopy

Electromagnetic radiation in the ultraviolet (UV) wavelength interval (10-400 nm) and in the interval visible (Vis) to the human eye (400-750 nm) can excite electrons, in particular valence electrons, in a sample. As a result, UV-Vis spectroscopy can be used to characterize different types of electronic transitions in a sample.^[52,70,71]

The various types of electronic transitions that can occur and may be detected spectroscopically include (Figure 9):

- I) Transition of an electron from a localized orbital on one atom to a higher energy but still localized orbital on the same atom (e.g. d-d or f-f transitions).
- II) Transition of an electron from a localized orbital on one atom to a higher energy but still localized orbital on an adjacent atom (charge transfer transitions).
- III) Transition of an electron from a localized orbital on one atom to a delocalized energy band (the conduction band).
- IV) Transition of an electron from the valence band to the conduction band.

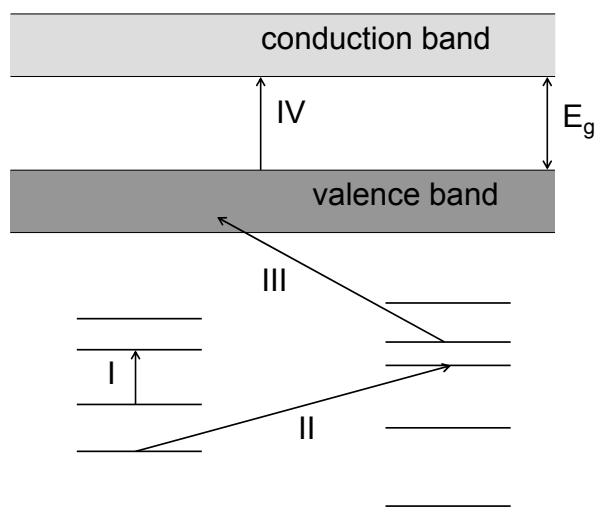


Figure 9. Possible electronic transitions that can be detected with UV-Vis spectroscopy.

Transition of electrons from the valence band to the conduction band (IV in Figure 9) is the mechanism that causes conductance in semiconductors. The energy difference of the valence band and the conduction band is referred to as the *band gap* energy, E_g . Standard semiconductors such as Si and Ge absorb in the near infrared, and are thus non-transparent for visible light. Some oxides, such as indium oxide, zinc oxide and tin oxide, absorb in the UV when doped with suitable ions, and are thus transparent to visible light. They are known as *transparent conductive oxides* (TCOs).

The band gap energy, E_g of a semiconductor with a direct band gap can be calculated from UV-Vis spectra when combining Equation (42), Lambert-Beer's law, with the formula given by Tauc^[72]

$$\alpha h\nu = C\sqrt{(h\nu - E_g)} \quad (44)$$

where C is a constant and $h\nu$ is the energy of the incident radiation.

As radiation source for visible light, many spectrometers use thermal radiation from tungsten lamps, filled either with inert gas, such as argon or nitrogen, or with a halogen gas. In contrast to IR spectrometers, most UV-Vis spectrometers separate light of different wavelengths with a monochromator, which consists mainly of a diffraction grating and a set of mirrors. The wavelength interval of interest is then scanned through via different settings of the monochromator.

In this work, optical spectra in the UV-Vis wavelength interval of powders and films were recorded in a wavelength interval of 250-800 nm with a Cary 100 spectrometer from Varian (Palo Alto, USA) equipped with a DRA-CA-30I integrating sphere from Labsphere (North Sutton, USA). The UV-light source was a Deuterium lamp and the visible light source was a quartz halogen lamp.

3.7.3 Solid state nuclear magnetic resonance (NMR) spectroscopy

Nuclear magnetic resonance (NMR) spectroscopy utilizes radiofrequency electromagnetic radiation to induce nuclear spin transitions of nuclei which are exposed to a strong magnetic field.^[70,73-75] The magnitude of the energy change depends not only on the particular element involved but also on its near chemical environment. Therefore, NMR is an important tool for structural analysis, complementary to, e.g. XRD.

NMR applies to all nuclei with an odd number of protons and neutrons, i.e., a nonzero spin quantum number I (also called nuclear spin quantum number). Table 1 shows some examples of the spins of certain nuclei.

Table 1. Some examples of spin quantum numbers of nuclei.

nucleus	1_1H	2_1H	${}^{12}_6C$	${}^{13}_6C$	${}^{16}_8O$	${}^{19}_9F$	${}^{27}_{13}Al$	${}^{119}_{50}Sn$
spin I	1/2	1	0	1/2	0	1/2	5/2	1/2

The *Zeeman interaction* affects all nuclei with nonzero spin that are located in a magnetic field. The nuclear magnetic energy splits into different levels, depending on how the nuclear spins are aligned with the applied magnetic field. At resonance, spin inversion takes place, whereby the population difference between the energy levels becomes zero. This condition is referred to as *saturation*. However, after some time, the nuclei return to their equilibrium orientation through *relaxation*. There are two kinds of relaxation processes by which equilibrium can be restored: *spin-lattice relaxation* (T_1) and *spin-spin relaxation* (T_2). The Zeeman interaction is dependent on nuclear type and the strength of the magnetic field, and thus determines the resonance frequency of nuclei. It is, however, independent of the chemical environment of a nucleus, and can therefore not be utilized for structural analysis.

In addition to the Zeeman interaction, all samples are affected by the magnetic *shielding interaction* (σ) and the *indirect spin-spin coupling interaction* (J). The magnetic shielding interaction is dependent on the electron distribution around the nucleus, which in turn depends on the bonding to other nearby nuclei (with or without magnetic moment). It can thus be

utilized to investigate which nucleus is bonded to which. The shielding of the nucleus affects the magnetic field around it, and thus its resonance frequency. Thereby, the peak position in the absorption spectrum is shifted. In liquids, the magnetic shield interaction consists of an averaged isotropic part. In solids, there is also an anisotropic part with an angular dependence of $(3\cos^2\theta - 1)$. The indirect, or electron-coupled, spin-spin interaction is an interaction between neighboring nuclei with magnetic moment. The J-coupling gives rise to splitting of energy levels, so-called fine structure, due to the differences in the relative orientation of the nuclear spins and the surrounding electron spins. It is dependent on the electron density around the nucleus, and thus on the chemical bonding. It is, however, independent of the applied field and has no spatial dependence. Normally, the spin-spin coupling is too weak to be observed in solids.

The effect of the Zeeman interaction is removed from the spectrum by measuring against a reference standard containing nuclei of the same element as in the investigated sample. The shift of the resonance frequency caused by magnetic shielding and the splitting of the peaks into doublets or, generally, multiplets, caused by spin-spin coupling, are the main features of an NMR spectrum of a liquid. The x-axis of a one-dimensional NMR spectrum is normally the *chemical shift*, δ , which is defined as the change in the magnetic field around the nucleus caused by magnetic shielding. The chemical shift is conventionally expressed in terms of the difference between the resonance frequency of the nucleus in question and that of a reference standard, ν^0 , see Equation (45). Due to the term 10^6 , the chemical shift is conventionally given in units of parts per million (ppm).

$$\delta = \frac{\nu - \nu^0}{\nu^0} \times 10^6 \quad (45)$$

In addition to the above mentioned interactions, solids are affected by the *direct dipole-dipole interaction (D)*. D-coupling occurs between the magnetic moment of neighboring nuclei, either of different types (heteronuclear) or of the same type (homonuclear). The interaction takes place via a classical dipolar field, where the strength of the interaction depends on a factor $1/r^3$, where r is the distance between the two magnetic moments. In liquids, the D-interaction averages to zero, and in solids it has an angular dependence of $(3\cos^2\theta - 1)$. Furthermore, nuclei with spin $I > 1/2$ have a quadrupole moment, i.e., they have a non-spherical charge distribution, and are thus affected by the *quadrupole-field interaction (Q)*. Electric field gradients are present in most solid state samples and originate from the valence electrons of the nucleus, and from surrounding atoms and ions. If $I > 1/2$, there are more than two possible values of the nuclear magnetic moment, m , and thereby more than two possible energy levels. The quadrupole coupling causes a shift of the energy levels in absolute values and also relative to each other. In liquid samples, the interaction averages to zero, while it in solids has a complex angular dependence.

NMR spectra of liquids as well as solids are carried out via a pulsed Fourier transform (PFT) technique. With the PFT technique, all nuclei of a particular type in a sample are excited simultaneously by an intense radiofrequency pulse. The effect of a so-called $\pi/2$ pulse is depicted in Figure 10. The net macroscopic magnetic moment, \mathbf{M} , is made up of all individual magnetic moments, m , that precess around the applied magnetic field (aligned along the z-axis). The electromagnetic pulse is characterized by a circular polarization in the xy -plane, a magnetic field magnitude of $2B_1$ and a frequency of (or around) the Larmor (resonance) frequency of the investigated nucleus. If the coordinate system is changed from the stationary laboratory frame (xyz) to a frame rotating in the xy -plane at the Larmor frequency ($x'y'z'$), the field along the x' -axis felt by an individual nucleus is constant with a magnitude B_1 . As a

consequence, it starts to precess around the x' -axis. The net effect on \mathbf{M} is that it is tipped, or rotated, away from its equilibrium position along the z -axis, giving it a component in the xy -plane. The angle θ from the z -axis depends on the pulse width, T_p , see Equation (46). A pulse which tips \mathbf{M} with an angle of 90° is referred to as a $\pi/2$ pulse (Figure 10).

$$\theta = \gamma B_1 T_p \quad (46)$$

Seen from the stationary laboratory frame, \mathbf{M} now precess in the xy -plane, giving rise to an electric signal. After the pulse, the nuclei return to their equilibrium positions through relaxation. The decay of signal from the transverse magnetization – known as the free induction decay (FID) – is then measured. As soon as the relaxation is complete, a new pulse can be applied. The procedure is repeated until the signal-to-noise ratio is satisfactory. The NMR spectrum is then obtained via Fourier transformation. A sequence of pulses can be applied to manipulate the spin further and so acquire more information, for example two-dimensional spectra. Here, the signal is a function of the evolution time, t_1 , and the detection time, t_2 . The evolution time – the time between the first pulse of a chosen pulse sequence and the start of data acquisition – is systematically varied and the detected signal thus becomes a function of t_1 and t_2 . Fourier transformation gives a two-dimensional plot, where off-diagonal peaks show couplings between nuclei.

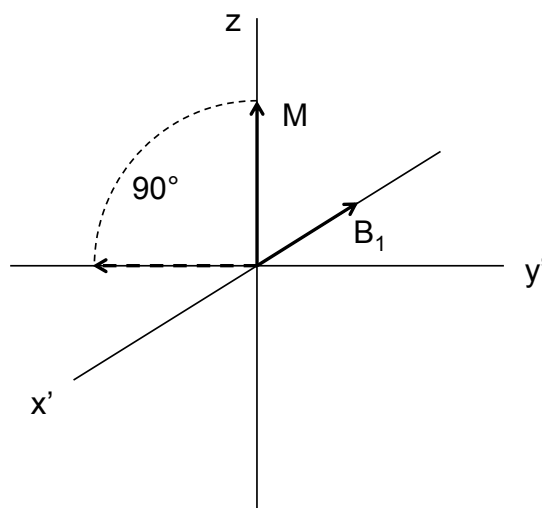


Figure 10. A $\pi/2$ pulse rotates \mathbf{M} from the z -axis with 90° .

The relaxation times T_1 and T_2 can also be measured by applying pulse sequences. The longitudinal relaxation time T_1 is a measure of the time it takes for M_z to return to equilibrium. Thus, \mathbf{M} is first rotated 180° to the negative z -axis by a π -pulse. It is now left to return to equilibrium during a relaxation period, τ . As there is no xy -component, only longitudinal relaxation occurs. The remaining part of \mathbf{M} is then rotated 90° by a $\pi/2$ -pulse and the FID is measured. By systematic variation of τ , T_1 can be obtained. The transversal relaxation time T_2 is a measure of the time it takes for M_x and M_y to return to equilibrium. Simply applying a $\pi/2$ -pulse does not give T_2 , but rather the effective T_2^* , due to inhomogeneities in the magnetic field.

The true T_2 can be measured by a technique called *spin echo*, where a simple pulse sequence – $\pi/2, \tau, \pi$ – is applied. \mathbf{M} is first rotated to the y' -axis and during τ , relaxation takes place in the $x'y'$ -plane. Due to phase incoherence, some individual magnetic moments travel faster than

others. The effect of the π -pulse is a rotation around the y' -axis and the magnetic moments now travel back towards the y' -axis. Thus, the further each magnetic moment had moved before the pulse, the further it now has to move back. At a time 2τ , the spins are refocused at the y' -axis and the FID signal reaches a maximum (spin echo). By systematic variation of τ , T_2 can be obtained.

Conventional NMR measurements on solid samples give broad featureless bands which are of little use for structural work. However, line-narrowing refinements can make the broad bands collapse to reveal fine structure. The main approach for obtaining high-resolution NMR spectra of solid samples is the so-called magic angle spinning (MAS) technique, which is normally combined with other techniques. Here, the powder samples are tilted at an angle of 57.74° and rotated (Figure 11). At this angle, the term $(3\cos^2\theta-1)$ equals zero. Consequently, by spinning at the magic angle, the D-coupling becomes zero and the σ -coupling becomes isotropic. These effects cause significant line-narrowing but require that the spinning speed is larger than the magnitude of the coupling constant. For couplings including protons, this is not yet realizable. MAS is often combined with other techniques to obtain high-resolution spectra. These techniques are rather different depending on what interactions – heteronuclear dipolar coupling, homonuclear dipolar coupling, and quadrupole coupling – occur in the sample.

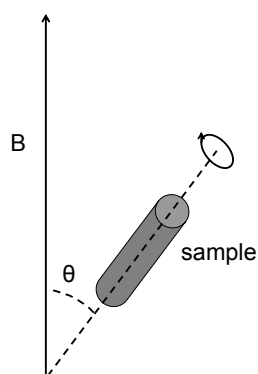


Figure 11. Magic angle spinning of sample in solid state NMR.

For nuclei with *heteronuclear dipolar coupling*, the interaction can be decoupled by constantly applying pulses that rotate the nuclear spin between its two states (parallel and antiparallel to the applied field). The average orientation of the protons is then zero, and the dipolar coupling is essentially averaged away. *Cross polarization (CP)* improves the sensitivity by making use of the high polarization and short relaxation time of protons compared to other nuclei. Here, two RF fields are applied simultaneously. Each field is tuned to the resonance frequency of one of the nuclei. The two spins can now be rotated independently and so be brought into contact. The magnetization can then flow from the highly polarized protons to the lower polarized other nuclei, which increases the signal from the other nuclei. The process can be repeated as soon as the protons return to equilibrium, which means more scans can be made during a given time. Two-dimensional NMR spectra showing the correlation between the chemical shifts of protons and another type of nuclei are referred to as *HETCOR (heteronuclear correlation)*. The dipolar coupling can, when of interest, be reintroduced into the system by a recoupling technique referred to as *REDOR (rotational echo double resonance)*. Dipolar coupling can e.g. be utilized to measure internuclear distances due to its dependence on the term $1/r^3$. The effect of REDOR is to partially undo the effect of MAS, which averages the dipolar coupling to zero over time. By

applying two π -pulses tuned to the resonance frequency of one of the nuclei during each rotation period, the time average is no longer zero and can be measured. This way, about 70 % of the dipolar coupling can be recovered.

For nuclei with *homonuclear dipolar coupling*, the interaction cannot be decoupled as described above for heteronuclear coupling, since they have the same resonance frequency. However, a sequence of $\pi/2$ pulses flips \mathbf{M} around the axes of the coordinate system so that it in average is oriented at the magic angle 57.74° from the z-axis – an angle at which the dipolar coupling is known to be zero. This technique is called *WAHUHA*, after its inventors. The dipolar coupling can be reintroduced with multipulse techniques such as *DRAMA* (*dipolar recovery at the magic angle*). DRAMA works similarly as REDOR, but applies $\pi/2$ -pulses and can recover about 45 % of the dipolar coupling.

For nuclei with *quadrupole coupling* ($I > 1/2$), the angular dependence is more complicated than that for dipolar coupling, since the principal axis of the electric field gradient does not in general coincide with the z-axis of the applied B field. The first-order part of the coupling is dependent on the term $(3\cos^2\theta - 1)$ and can thus be removed by MAS. The second-order part of the angle dependence of the quadrupole coupling can be removed by rotation at a second angle, where the second-order part becomes zero. Rotation at the two angles can either be done simultaneously by the *double rotation (DOR)* technique or sequentially by the *dynamic angle spinning (DAS)* technique. Another approach makes use of the shift of the energy levels due to the quadrupole coupling. In general, there are $2I + 1$ spin states and thus $2I$ detectable transitions. For example, for ${}^2_1\text{H}$ with $I=1$, there are three energy levels. Since its quadrupole constant, Q , is small, it is mainly affected by the first order term. Although the first order term shifts all three energy levels, the relative difference between the $m = 1$ and $m = -1$ remains the same and double quantum excitation can be applied. For nuclei with higher spins, such as ${}^{27}_{13}\text{Al}$ with $I=5/2$, multiple quantum excitations can be applied sequentially to average away the second-order term with the multiple quantum MAS technique known as *MQMAS*.

The solid state NMR spectra presented in this thesis were measured and interpreted by Yamini Avadhut and Dr. Jörn Schmedt auf der Günne in the research group of Prof. Dr. W. Schnick, Department of Chemistry and Biochemistry, Munich University (LMU).

3.7.4 Mössbauer spectroscopy

Mössbauer spectroscopy, also called nuclear gamma resonance spectroscopy, uses radiation produced by the decay of radioactive elements to study the local structure of a solid material containing atoms similar to those responsible for the emission.^[75]

Through the change in population of energy levels in a radioactive nucleus, a highly monochromatic beam of γ -rays originates. Only few isotopes can be induced to emit γ -rays suitable for Mössbauer work; among them, ${}^{57}_{26}\text{Fe}$ and ${}^{119}_{50}\text{Sn}$ are the most widely used. Therefore, most investigated samples have been substances containing Fe or Sn. Absorption of γ -rays involves transitions between two different energy levels in the nucleus, the ground state and the first excited state, which means a change of the spin, I . As could be observed in Table 1, ${}^{119}_{50}\text{Sn}$ has a spin $I = 1/2$, thus, excitation would imply a transition to $I = 3/2$.

The energy transitions within the nucleus depend on the density and arrangement of the surrounding electrons. Mössbauer spectroscopy can therefore provide information about properties such as oxidation state, coordination number, electronic configuration, bond character, and symmetry site distortions of the absorbing atom. The energy of the γ -radiation

from the source can be modified by making use of the Doppler effect. The sample is placed in a fixed position and the γ -ray source is moved at a specific velocity either towards or away from the sample. This way, the energy of the incident γ -rays is either increased or decreased. The energy, E , perceived by the sample is given by

$$E = E_{\gamma} \left(1 + \frac{v}{c} \right) \quad (47)$$

where v is the applied velocity, c is the speed of light, and E_{γ} is the energy of a stationary source.

The spectrometer sweeps through a range of velocities and the absorption of γ -rays by the sample is monitored as a function of energy (source velocity). The x-axis of a Mössbauer spectrum is usually expressed in units of mm/s. and a spectrum is obtained which usually consists of a number of poorly resolved peaks. When sample and emitter are identical, the resonant absorption peak occurs when the source is stationary, whereas when they are not identical, the absorption peak is shifted to a certain velocity.

This chemical shift, δ , is a result of variations in nuclear energy levels of the absorbing atoms, which originates from changes in the extra-nuclear density distribution. In particular, the chemical shift depends on the electron density at the nucleus. Since only s -electrons have a finite probability of being located at the nucleus, the chemical shift is in principle a measure of the difference in valence s -orbital electron populations of the Mössbauer atom between the sample and the reference. Valence s -electrons populations are controlled by oxidation state, coordination number, and type of bonding.

For those nuclei that have a nuclear spin quantum number $I > 1/2$, the distribution of positive charge inside the nucleus is non-spherical and a quadrupole moment, Q , results. This causes splitting of the nuclear energy levels, and hence splitting of the peaks in the Mössbauer spectrum. The separation of the doublets, known as quadrupole splitting, Δ , is, like the chemical shift, δ , sensitive to local structure and oxidation state.

The Mössbauer spectrum presented in this thesis was measured and interpreted by I. Schellenberg and Prof. Dr. R. Pöttgen, Institut für Anorganische und Analytische Chemie, Universität Münster.

4 Results and discussion

4.1 Binary oxides and hydroxides

4.1.1 Indium tin oxide (ITO)

Thin films exhibiting a high electrical conductivity and optical transmittance are of major technical importance, for instance in solar cells, flat panel displays, and electrochromic devices.^[1] The required combination of properties can be realized by degenerate doping of wide-bandgap oxide semiconductors, such as In_2O_3 , SnO_2 , or ZnO .^[2,3] Among these, tin-doped indium oxide, also called indium tin oxide (ITO), shows the highest electrical conductivity, which – in combination with its optical transmittance - has granted it a position as the most widely applied transparent conductive oxide (TCO) in optoelectronic devices.^[4,5] Due to its high reflectivity in the infrared, ITO is also employed in energy-efficient windows.^[76]

Liquid phase synthesis of ITO nanoparticles has been carried out with sol-gel, hydrothermal, and solvothermal methods as well as in microemulsions and ionic liquids.^[43,77-82] In order to establish a certain conductivity, however, annealing of as-prepared powders is most often necessary till now, either to crystallize the material or to remove organic surfactants. Furthermore, particle size distribution and degree of agglomeration of as-prepared ITO have been barely addressed. To this end, Ba *et al.* have prepared ITO nanocrystals in benzyl alcohol.^[81] Here, pellets of as-prepared powders exhibited a resistivity of $3.9 \cdot 10^{-1} \Omega\text{cm}$; subsequent to annealing of as-prepared powders a value of $1.9 \cdot 10^{-2} \Omega\text{cm}$ was measured. However, the size distribution and degree of agglomeration of the material were not verified. Furthermore, Bühler *et al.* have prepared ITO nanocrystals with a narrow size distribution in an ionic liquid.^[43] Here, the resistivity of pellets of as-prepared powders was measured to $3 \cdot 10^{-2} \Omega\text{cm}$.

Suspensions of ITO particles in diethylene glycol (DEG) were prepared via microwave irradiation.^[83,84] In a typical recipe, 2.4 mmol $\text{InCl}_3 \cdot 4 \text{H}_2\text{O}$ and 0.12 mmol $\text{SnCl}_4 \cdot 5 \text{H}_2\text{O}$ were dissolved in 25 ml DEG. The molar ratio Sn:In was thus 5 %. At 80 °C the solution was added to a solution of 25 ml DEG containing 12.0 mmol $\text{N}(\text{CH}_3)_4\text{OH} \cdot 5 \text{H}_2\text{O}$ and 1.4 ml deionized H_2O . Immediate precipitation of a colorless solid was observed. To crystallize the particles, the resulting suspension was heated for 2 h at 200 °C in a laboratory microwave oven (Ar atmosphere, magnetic stirring).

As-prepared suspensions of ITO in DEG are colloidal stable for weeks and exhibit a transparent appearance with a bright blue color (Figure 12a). Qualitatively, this finding already hints to the presence of sufficiently doped In_2O_3 :Sn nanocrystals. Subsequent to centrifugation and drying, as-prepared In_2O_3 :Sn can be separated from the suspension and was yielded as a blue powder in quantities of 92 %. The size and size distribution of as-prepared ITO suspensions were quantified by dynamic light scattering (Figure 12a). According to DLS measurements, the average diameter of as-prepared ITO particles in DEG amounts to 19(1) nm (Figure 12). As a consequence, ITO suspensions exhibit an almost monodisperse size distribution. Thereafter, scanning electron microscopy of diluted DEG suspensions is applied to obtain a direct view of as-prepared ITO nanocrystals (Figure 13).

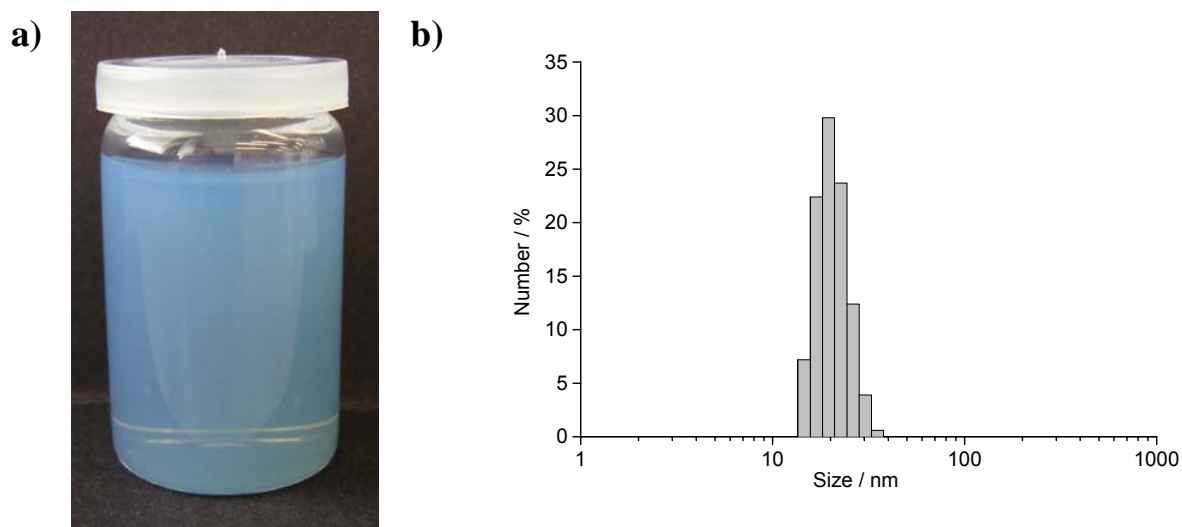


Figure 12. a) Photograph of ITO nanocrystals in DEG (solids content: 0.62 wt-%), and b) Particle size distribution thereof, measured with dynamic light scattering.

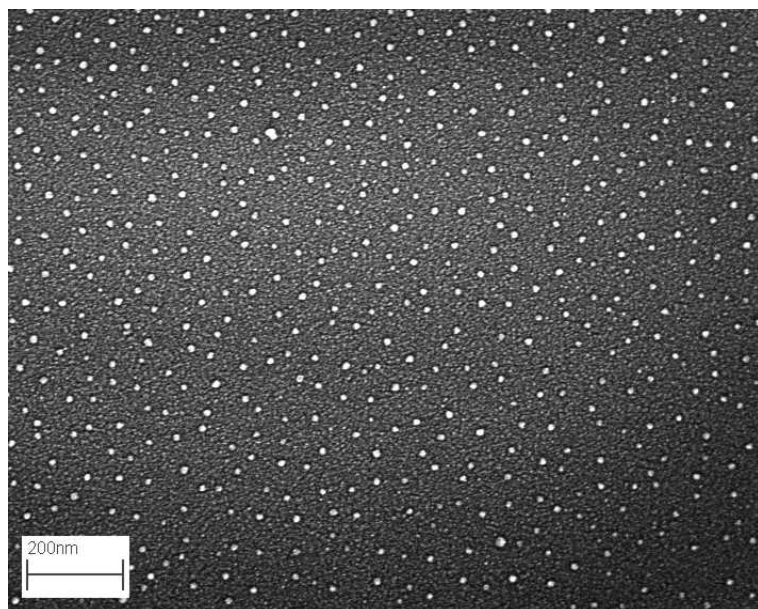


Figure 13. SEM image of as-prepared ITO nanocrystals.

Characteristic SEM images reveal as-prepared ITO particles to be non-agglomerated and of spherical and very uniform morphology (Figure 13). SEM images were also used for a statistical evaluation of particle diameter and size distribution. To this end, a mean diameter was deduced based on 320 particles and amounts to 15(1) nm. This value is in very good agreement with DLS analysis, considering an enlarged hydrodynamic diameter in the latter case. Finally, nitrogen absorption measurements of powder samples were performed according to the BET type of method. Herein, a specific surface of $56.1 \text{ m}^2 \text{ g}^{-1}$ was measured. Assuming spherical and non-porous ITO particles with a density of bulk In_2O_3 (7.1 gcm^{-3}),^[45] this value corresponds to a particle diameter of 15 nm, which is again in accordance with SEM and DLS analysis.

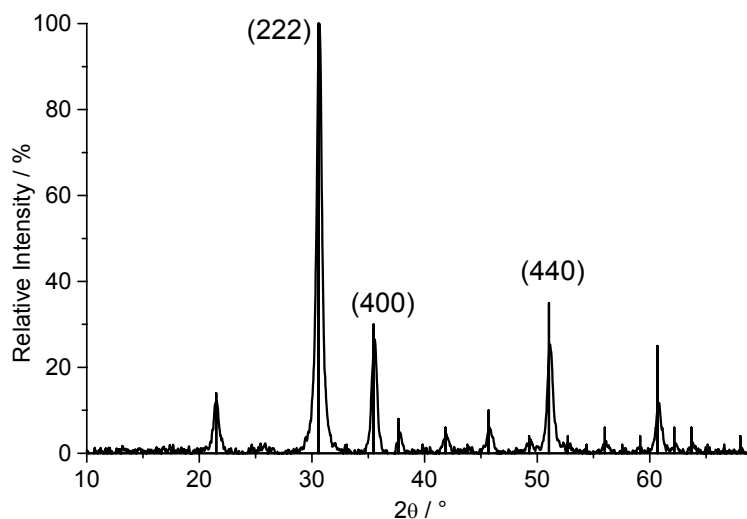


Figure 14. XRD pattern of as-prepared nanocrystalline ITO (reference: In_2O_3 – ICCD No. 6-416) with diffraction peaks (222), (400), and (440) denoted.

The crystallinity of as-prepared ITO is evidenced based on X-ray diffraction as well as with high-resolution transmission electron microscopy. The powder diffraction pattern of as-prepared nanocrystalline ITO is presented in Figure 14. XRD evidences the presence of cubic In_2O_3 ,^[85] i.e. powder samples crystallize with a CaF_2 -defect type superstructure. Even more important, the hexagonal In_2O_3 phase, which is expected – according to the step rule by Ostwald^[86] – for a liquid-phase approach turned out to be completely absent. The absence of the hexagonal phase is expected to be advantageous with concern to the conductivity of prepared samples, since the cubic phase is known for its superior conductivity.^[2,3,76] Via Scherrer's formula (see Equation (9)), powder diffraction patterns can also be used to calculate the crystallite size. From the three most intensive Bragg diffraction peaks – (222), (400), and (440) – an average crystallite size of 18 nm was obtained. Taking the particle diameter stemming from DLS and SEM analysis into account, this confirms the single crystallinity of the as-prepared ITO particles.

This view is further confirmed by high resolution transmission electron microscopy images (Figure 15). Representative HRTEM images display ITO nanoparticles with highly ordered lattice fringes, indicating that even areas close to the particle surface are well crystallized. Two lattice plane distances were identified from HRTEM images by direct measurement: 2.93 Å and 2.54 Å. This again proves the presence of cubic In_2O_3 (lattice plane (222) with 2.92 Å and (400) with 2.53 Å).^[85] Thus, the crystallinity of as-prepared ITO nanoparticles is confirmed by means of two independent analytical tools; X-ray powder diffraction and transmission electron microscopy.

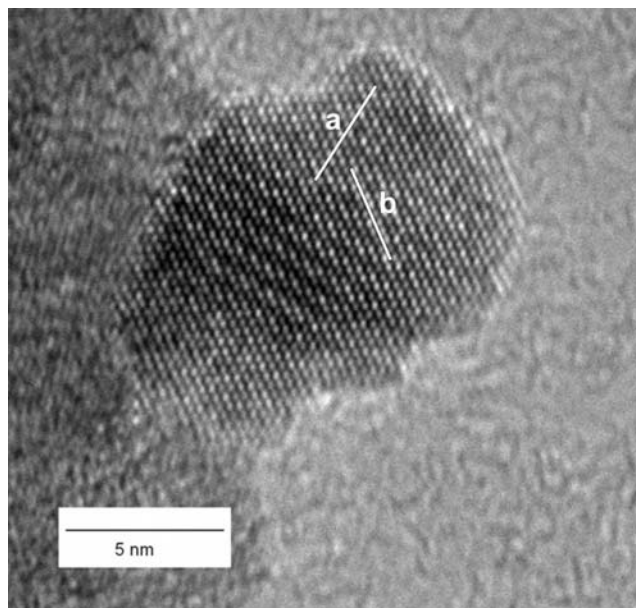


Figure 15. HRTEM image of as-prepared ITO nanocrystal with lattice plane distances denoted, where a corresponds to 10 lattice planes with a distance of 2.93 \AA and b to 10 lattice planes with a distance of 2.54 \AA .

The particle sizes obtained via investigations based on DLS, SEM, BET, and XRD are summarized in Table 2. Here it can be seen that the investigations of particles sizes based on several analytical tools resulted in a very good agreement of a particle size of 15-19 nm. Moreover, microwave-assisted heating turned out to be essential. If a conventional resistance heating (e.g. with heating mantle) is performed at similar temperature and time of heating, ITO remained amorphous.

Table 2. Comparison of particle sizes of as-prepared ITO evidenced with various analytical tools.

DLS	SEM	BET	XRD
19 nm	15 nm	15 nm	18 nm

Former investigations addressing a polyol-mediated synthesis have shown that the polyol as a coordinating, and thereby stabilizing agent is adhered on the particle surface. Even washed and dried powder materials contain the multidentate alcohol in quantities of a monolayer.^[87,88] Since this monolayer might hinder the particle-to-particle electron transfer, prior to electrical conductivity the surface conditioning is investigated. To this concern, FT-IR spectra of as-prepared ITO powder were recorded (Figure 16). According to FT-IR spectra, the transmittance of as-prepared ITO powders is very low in the wavenumber interval of $7000\text{-}2000 \text{ cm}^{-1}$. This is expected due to a high IR reflectivity, which implies a large number of free carriers.^[76] Thus, the conductivity of as-prepared ITO particles should be high. Vibration bands are visible at 1084 , 610 , and 500 cm^{-1} (Figure 16). Hereof, the two at lower wavenumber can be ascribed to phonon absorptions of the In_2O_3 lattice.^[89] The absorption at 1084 cm^{-1} is attributed to the valence vibration $\nu(\text{C-O})$ ^[70] of diethylene glycol adhered on the particle surface.

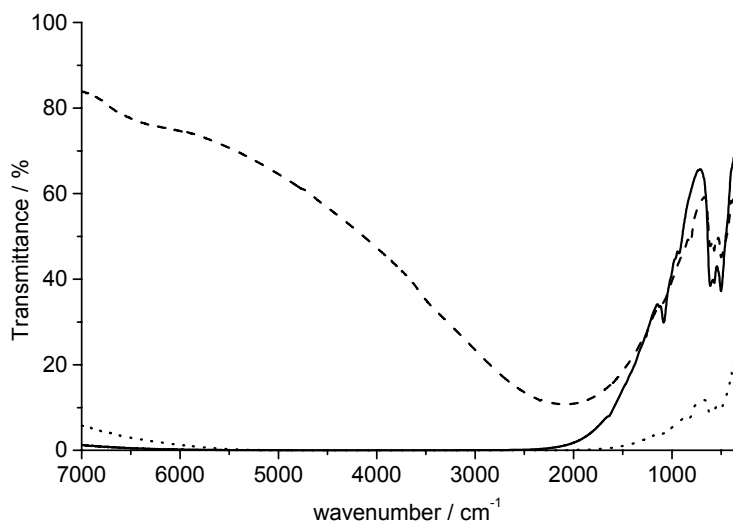


Figure 16. FT-IR spectra of ITO powder sample: as-prepared (solid), after thermal treatment in air at 500 °C (dashed), and after reduction with forming gas at 300 °C (dotted).

In addition, DTA-TG analysis was carried out to quantify the amount of DEG on the particle surface. Thermogravimetry resulted in a weight loss of 0.3 % between 200 and 400 °C (Figure 17). Considering the boiling point of DEG, this weight loss can be related to DEG, although it is considerably lower than a monolayer coverage obtained from other investigations.^[28,87,88] Taking both – the specific surface and the low weight loss of as-prepared ITO – into account, a significant influence on the conductivity of powder samples is not to be expected.

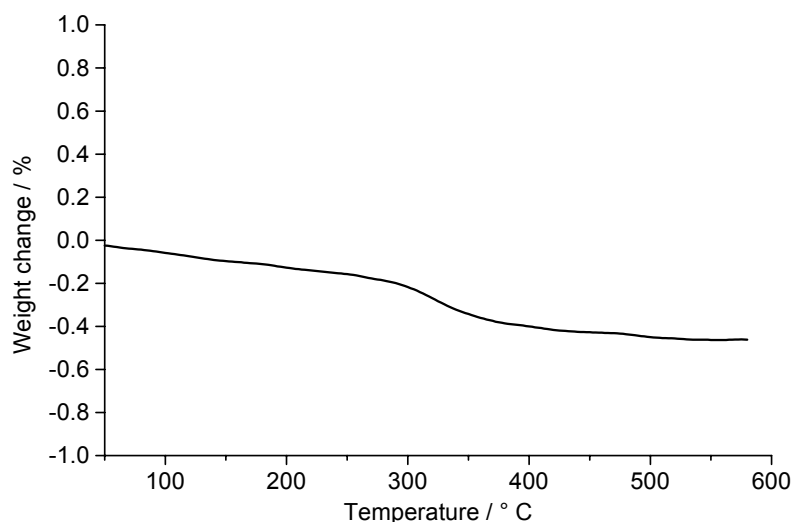


Figure 17. TG analysis of as-prepared ITO powder.

In order to reduce the influence of the grain boundaries and to initiate a close particle-to-particle contact, the nanocrystalline ITO powder was pressed to form dense pellets. Via four-point probing, a sheet resistance of $4.0 \Omega \square$ was measured. Considering a pellet thickness of 26 μm , this corresponds to a resistivity of $1.1 \cdot 10^{-2} \Omega\text{cm}$. Thus, it can be concluded that as-

prepared $\text{In}_2\text{O}_3:\text{Sn}$ (5 mol-%) powders show a considerable conductivity. This is even more surprising since in contrast to literature neither a thermal nor a chemical post-treatment is required (e.g. to remove all hydroxyl contents, to burn out organic residues, to reduce lattice defects, or to establish a sufficient carrier concentration).^[2,3,77-82] Furthermore, the conductivity of as-prepared ITO is slightly better than as-prepared ITO prepared in an ionic liquid, although the temperature applied here was lower.^[43] In addition, DEG has the advantage of being a readily available solvent, in contrast to ionic liquids.

Aiming at thin layers on transparent substrates, as a proof of concept $\text{In}_2\text{O}_3:\text{Sn}$ (5 mol-%) nanocrystals suspended in DEG and 1-methoxy-2-propanol were spread and dried on glass plates. The suspensions were applied here without any further optimization of, for instance, viscosity, solids content, type of solvent, or substrate pre-conditioning. In contrast to pressed pellets, the resulting films only showed a minor conductivity. Considering the high conductivities exhibited by as-prepared powder pellets, the low conductivity of as-prepared thin layers is attributed to their incompactness. With the intention to increase the particle-to-particle contact, as-deposited films were firstly treated thermally in air (500 °C, 1 h) and secondly treated with forming gas (H_2/N_2 10 %, 300 °C, 2 h). For comparison, this treatment was also carried out on powder samples.

According to FT-IR spectra, ITO powders that have been heated in air exhibit a considerably increased transmittance above 2000 cm^{-1} in comparison with as-prepared samples (Figure 16). This is due to a filling of lattice defects with oxygen and in correspondence with a significantly reduced number of free carriers.^[2,3,76] To repopulate the level of free carriers, ITO was partly reduced with forming gas as a second step. Reduced ITO powder show a reestablished and partly even further decreased IR transmittance in comparison with as-prepared samples (Figure 16). Consequently, the relevant lattice defects were recreated, and the free carrier concentration should thus be re-increased, too.^[2,3,76]

In the case of ITO coated glass plates, the described post-treatment resulted in a sheet resistance of $295\ \Omega\Box$. The layer thickness was estimated to 400 nm from SEM images. As a consequence, a resistivity of $1.2 \cdot 10^{-2}\ \Omega\text{cm}$ was obtained without applying any correction factor for porosity. Since as considerable porosity can be assumed, the resistivity of the particles themselves will be even lower. The high conductivity of post-treated layers implies that the low conductivity of as-prepared layers is indeed due to insufficient particle-to-particle contact. Finally, in order to investigate the optical properties of post-treated ITO layers on glass, UV-Vis spectra were recorded. UV-Vis measurements show that the transmittance of post-treated, ITO-coated glass plates is above 80 % in the whole visible wavelength interval and similar to the uncoated glass plate in the main part of the spectrum (Figure 18). The transmittance is equal to 91.6 % in the middle of the visible interval (550 nm). Thus, the applied thin ITO layers exhibit a very high optical transmittance.

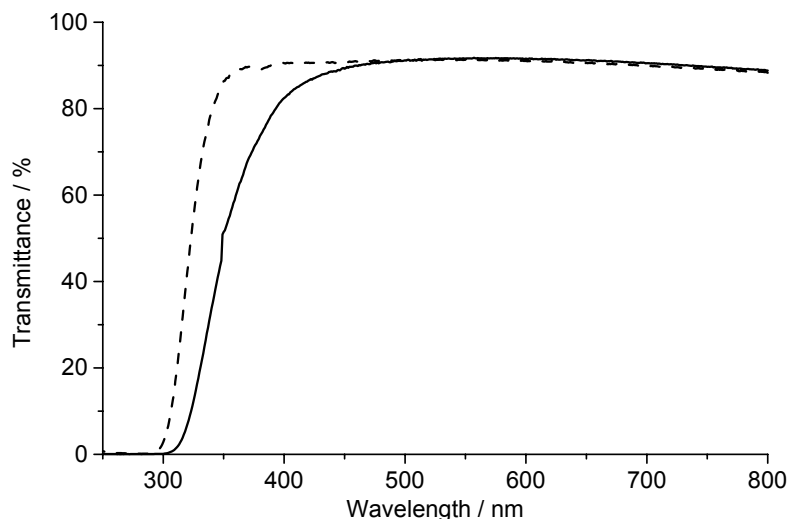


Figure 18. UV-Vis spectra of ITO-coated (solid) and uncoated glass plate (dashed).

In summary, microwave-assisted synthesis of ITO in DEG results in transparent, blue, colloiddally stable suspensions. Nanoscale ITO is realized with high yields, and in principle accessible in large quantities, while applying less harmful chemicals and solvents throughout. Particle size is evidenced via dynamic light scattering, scanning electron microscopy, Brunauer-Emmett-Teller analysis, and X-ray powder diffraction. The various methods show a very good agreement and the mean particle diameter equals 17 nm. X-ray diffraction and HRTEM images evidence as-prepared ITO to be highly crystalline. As-prepared powder samples exhibit a low resistivity ($1.1 \cdot 10^{-2} \Omega\text{cm}$) and a high reflectivity in the infrared. Consequently, as-prepared ITO nanopowders indeed exhibit a sufficient concentration of free charge carriers. Microwave-assisted heating turned out to be advantageous with concern to particle size, size distribution as well as regarding the crystallinity of nanoscale ITO.

As a proof of concept, a simple layer formation process via direct deposition of as-prepared ITO suspensions on glass plates is carried out. Due to the incompactness of these layers, here thermal post-treatment is necessary in order to initiate close particle-to-particle contacts. Subsequent to heating in air and reduction with forming gas, the resulting layers are with a visible transmittance similar to the uncoated glass substrate and a comparably low resistivity ($1.2 \cdot 10^{-2} \Omega\text{cm}$). Based on this proof of concept significantly improved layers (e.g. with concern to homogeneity and density), and thereby increased conductivities are to be expected while applying professional printing technologies.

4.1.2 Zinc oxide

Zinc oxide is a wide-bandgap semiconductor with a direct bandgap of about 3.4 eV.^[90] When ZnO is doped with ions such as Al^{3+} or In^{3+} , it becomes a transparent conductive oxide (TCO). This makes it a promising and significantly cheaper alternative to ITO ($\text{In}_2\text{O}_3:\text{Sn}$) for all applications that require a transparent electrode.^[2,3,6,91] Liquid phase preparation of transparent conductive IZO and AZO nanocrystals is nowadays dominated by sol-gel techniques.^[92-99] In 1998, Hilgendorff *et al.* realized a sheet resistance of $150 \Omega\Box$ after a first coating step, and $20 \Omega\Box$ after two subsequent infiltration steps for IZO and AZO ($2 \mu\text{m}$, $4 \cdot 10^{-3} \Omega\text{cm}$).^[92] Since then, different groups employing sol-gel methods have reported resistivities ranging from $6 \cdot 10^{-4} \Omega\text{cm}$ ^[97] to $1 \cdot 10^{-2} \Omega\text{cm}$,^[94,96] whereby the reason for this

variation is not clearly understood. In general, only the deposited sol-gel films are subject to investigation; not the sol itself. Thus, in these studies, particle size distribution, degree of agglomeration, and redispersibility of liquid phase as-prepared AZO and IZO have not been addressed at all.

Suspensions of IZO and AZO nanoparticles with different solids contents were prepared in DEG.^[84,100] As a reference, non-doped ZnO was synthesized similarly. Sample IZO-1 and AZO-1 exhibit solids contents of 0.7 wt-% and were prepared according to the following recipe: 4.56 mmol of $\text{Zn}(\text{CH}_3\text{COO})_2 \cdot 2 \text{H}_2\text{O}$ was dissolved in 50 ml DEG together with 0.23 mmol of $\text{InCl}_3 \cdot 4 \text{H}_2\text{O}$ or $\text{AlCl}_3 \cdot 6 \text{H}_2\text{O}$. The molar ratios Al:Zn and In:Zn are thus 5 %. Subsequently, 1 ml deionized H_2O was added. Sample IZO-2 and AZO-2 have solids contents of 8.7 and 9.2 wt-%, respectively, and were scaled up accordingly. Solutions were heated at 200 °C in a laboratory microwave oven (Ar atmosphere, magnetic stirring). To improve material crystallinity, the temperature was maintained for 30 min.

As-prepared suspensions of IZO and AZO in DEG with different solids contents are colloiddally stable for months. AZO suspensions exhibit a slight bluish shade (Figure 19 a), whereas IZO suspensions are bright blue (Figure 20 a). Qualitatively, this finding already hints to the incorporation of the dopants in the ZnO lattice. Subsequent to centrifugation and drying, as-prepared IZO and AZO powders can be separated from the suspension and were yielded in quantities of about 90 % for all samples.

In the following, characterization and properties are presented for four samples – all with an introduced doping concentration of 5 mol-% – with low as well as high solids contents: IZO-I (0.7 wt-%), IZO-II (8.7 wt-%), AZO-I (0.7 wt-%), and AZO-II (9.2 wt-%). In order to determine the particle size distribution in the liquid phase, dynamic light scattering (DLS) was employed. All suspensions were diluted with DEG prior to DLS measurement in order to exclude concentration artifacts. Figure 19 b shows the results for AZO-I and Figure 20 b the results for IZO-I.

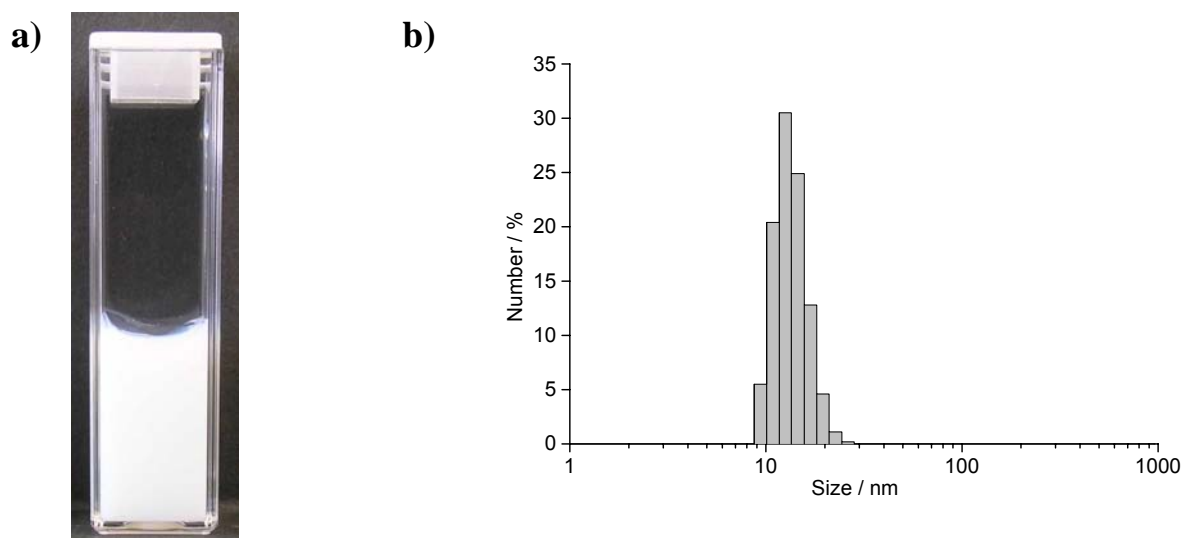


Figure 19. a) Photograph of AZO-I nanocrystals in DEG (solids content: 10 wt-%), and b) Particle size distribution thereof, measured with dynamic light scattering.

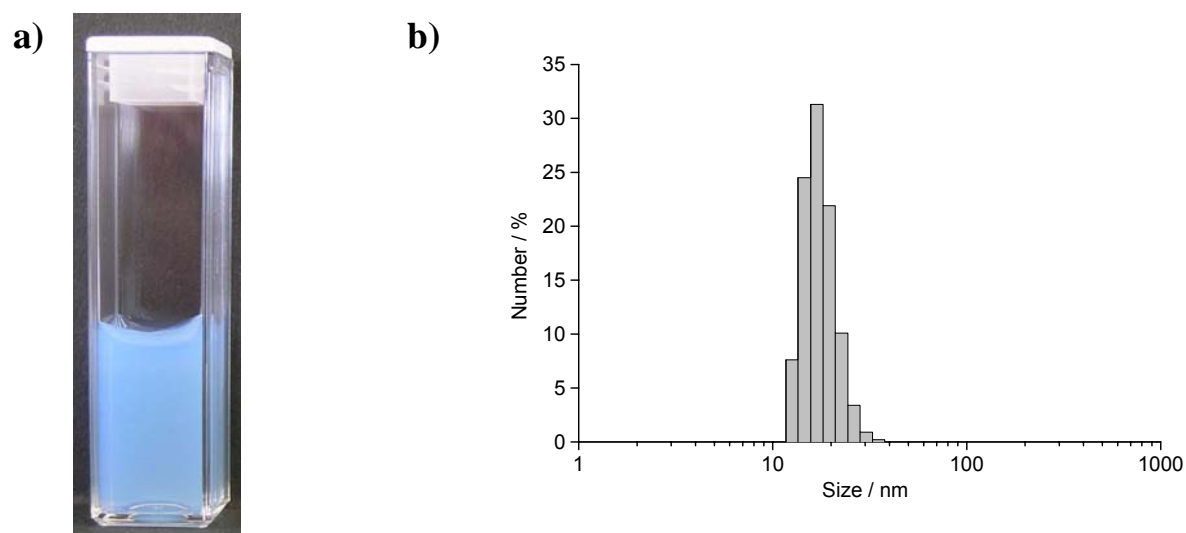


Figure 20. a) Photograph of IZO-I nanocrystals in DEG (solids content: 10 wt-%), and b) Particle size distribution thereof, measured with dynamic light scattering.

According to DLS, the resulting average hydrodynamic diameters are 15(1) nm and 12(1) nm for IZO-I and AZO-I, respectively. Hence, IZO and AZO particles are of similar size and have an almost monodisperse particle size distribution. DLS measurements of IZO-II and AZO-II after dilution resulted in an average hydrodynamic diameter of 16(1) nm and 13(1) nm, respectively. Thus, the particle size is only weakly affected by the solids content of the suspension. In addition to diluted suspensions, DLS measurements were conducted of suspensions with solids content of 10 wt-% (Table 3). The resulting average hydrodynamic diameters range from 29(2) nm (IZO-I) to 79(3) nm (AZO-II). These values can be interpreted as the mean agglomerate size at a particular concentration. Obviously, free Brownian motion of individual particles is hampered in concentrated suspensions. However, this finding is not related to formation of hard aggregates since the hydrodynamic diameter drops to the value of primary particles after dilution. Note also that even concentrated suspensions are colloiddally stable and with hydrodynamic diameters clearly below 100 nm.

Table 3. Comparison of particle sizes of IZO and AZO evidenced with various analytical tools.

Sample		DLS (diluted)	DLS (10 wt-%)	SEM	BET	XRD
IZO-I	0.7 wt-%	15 nm	29 nm	12 nm	10 nm	8 nm
AZO-I	0.7 wt-%	12 nm	52 nm	10 nm	22 nm	12 nm
IZO-II	8.7 wt-%	16 nm	50 nm	13 nm	13 nm	14 nm
AZO-II	9.2 wt-%	13 nm	79 nm	12 nm	21 nm	12 nm

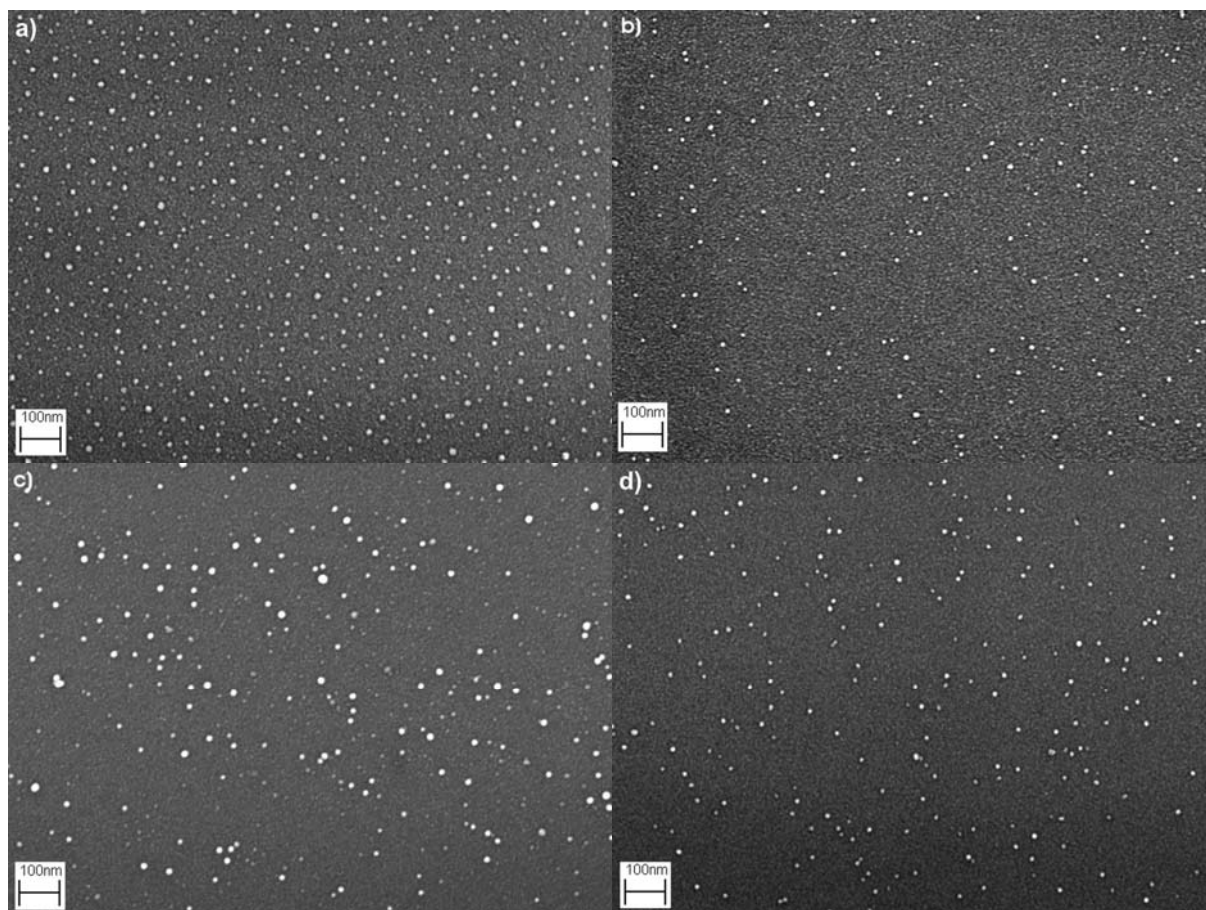


Figure 21. SEM images of as-prepared nanocrystals of a) IZO-I, b) AZO-I, c) IZO-II, and d) AZO-II.

Scanning electron microscopy of diluted DEG suspensions is applied to obtain a direct view of as-prepared nanocrystals. Characteristic images of IZO-I, AZO-I, IZO-II, and AZO-II are exhibited in Figure 21. SEM investigations of diluted suspensions in DEG reveal as-prepared particles of all samples to be non-agglomerated and of spherical and very uniform morphology (Figure 21). SEM images were also used for statistical evaluation of the particle diameter. Calculations were based on more than 400 particles per sample. The resulting mean diameters compiled in Table 3 exhibit a very good agreement with the particle size obtained from DLS analysis.

In addition, nitrogen absorption measurements were performed according to the BET type of method aiming at the size and degree of agglomeration of dried powder samples. Here, specific surfaces of 110 and 82 m²g⁻¹ were measured for IZO-I and AZO-I, respectively. Assuming the presence of spherical and non-porous particles with ZnO bulk density (5.6 gcm⁻³),^[45] these values correspond to particle diameters of 10 nm (IZO-I) and 22 nm (AZO-I). BET measurements of IZO-II and AZO-II show similar results (Table 3). Taking the accuracy of the diameter stemming from BET analysis into account, these values are in sufficient agreement with those from SEM and DLS analysis. Altogether, IZO and AZO particles appear to be practically non-agglomerated. Transmission electron microscopy (TEM) investigations are performed with IZO and AZO redispersed in ethanol without adding any additional surface-active agent. Figure 22 shows characteristic overview and high-resolution images of as-prepared IZO.

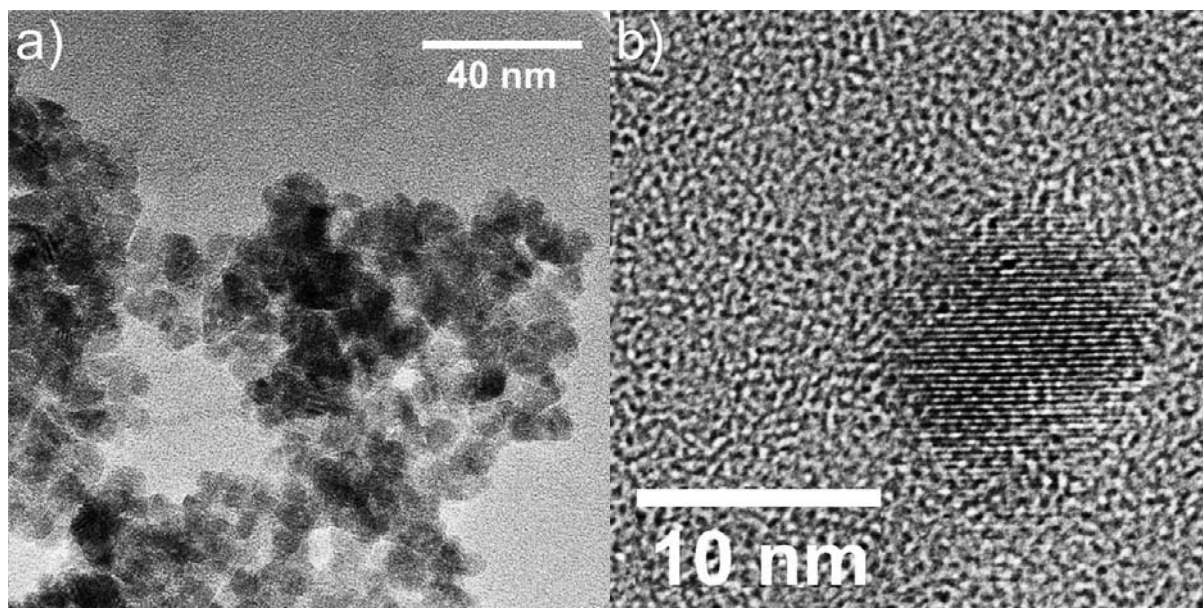


Figure 22. TEM images of as-prepared IZO nanocrystals: a) overview image and b) HRTEM image.

Overview TEM images (Figure 22 a) exhibit homogenous, but agglomerated, IZO particles with a diameter around 10 nm. In HRTEM images (Figure 22 b), nanoparticles with highly ordered lattice fringes can be observed. This indicates that even areas close to the particle surface are well crystallized. From Figure 22 b, a lattice plane distance of $2.84 \pm 0.08 \text{ \AA}$ was identified. This distance agrees well with the lattice plane (100) of hexagonal ZnO (2.81 \AA).^[101] Furthermore, the crystallinity of as-prepared IZO and AZO is confirmed by X-ray diffraction (XRD). The resulting powder diffraction patterns of IZO and AZO are presented in Figure 23.

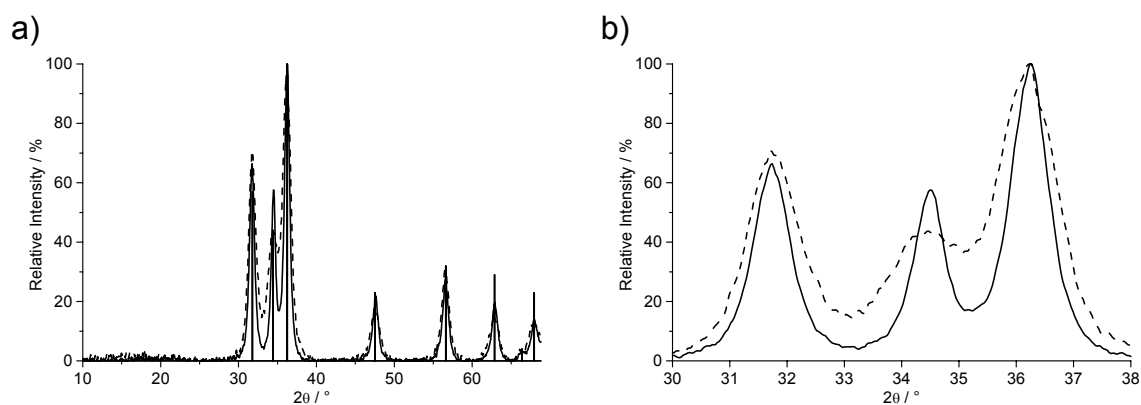


Figure 23. a) XRD patterns of as-prepared nanocrystalline AZO (solid) and IZO (dashed) (reference: ZnO – ICDD No. 36-1451), and b) magnification of the three most intensive diffraction peaks (100), (002), and (101).

According to XRD measurements, as-prepared IZO and AZO crystallize in the hexagonal wurtzite-type structure^[101] and are phase pure (Figure 23). Considering the comparably broad Bragg peaks of the nanoscale materials, a significant shift of diffraction patterns is neither expected nor observed although the radii of the zinc ions in the host lattice and the dopant ions are different (Table 4). Nevertheless, the peak width can also be used to calculate the

crystallite size via Scherrer's formula (see Equation (9)). From the most intensive Bragg diffraction peaks (100) and (101), average crystallite sizes of 8 nm and 12 nm are obtained for IZO-I and AZO-I, respectively (Table 3).

Table 4. Radii of metal ions in doped ZnO.^[45]

ion	CN	radius
Zn ²⁺	4	0.60 Å
Al ³⁺	4	0.39 Å
In ³⁺	4	0.62 Å

Consequently, IZO and AZO nanocrystals have been successfully prepared via microwave-assisted heating in a polyol medium. Primary particle size and degree of agglomeration of as-prepared IZO and AZO particles have been investigated based on several independent analytical tools, leading to very comparable results. To this concern, the primary particle size is not influenced by the solids content of the suspension and was determined to be 10 to 15 nm in average based on DLS, SEM, TEM, BET and XRD analysis. IZO samples are practically non-agglomerated; AZO samples exhibit a low degree of agglomeration. Thus, the microwave-polyol process turns out to be advantageous with regarding to particle size and size distribution of nanoscale IZO and AZO.

Furthermore, to confirm the presence and amount of dopants, as-prepared powders were pressed to pellets and used to perform EDX analysis. This resulted in an In:Zn molar ratio of 6 % for IZO and an Al:Zn molar ratio of 3 % for AZO. Although EDX is not very precise for low amounts of elements incorporated in a sample, the presence of dopants is evidenced with about the same amount as introduced in the synthesis. To validate the incorporation of the dopants in the host lattice, electrical measurements via four-point probing were carried out. Again, as-prepared powders were pressed to pellets to reduce the influence of grain boundaries and initiate a close particle-to-particle contact. Nevertheless, pellets of as-prepared IZO and AZO showed a sheet resistance in the MΩ range although the particles are highly crystalline and – taking the bluish color into account – free charge carriers seem to be present. However, DEG as a stabilizer which is adhered on the particle surface might hinder the particle-to-particle electron transfer and therefore cause a low conductivity. In fact, several studies aiming at a polyol-mediated synthesis have reported the nanomaterials to contain the multidentate alcohol in quantities of a monolayer even in washed and dried powder materials.^[87,88]

In order to illuminate the surface conditioning of as-prepared IZO and AZO, FT-IR spectra as well as TG data were recorded. In Figure 24, FT-IR spectra of as-prepared and thermally treated (see below) AZO are presented. According to FT-IR spectra of as-prepared AZO powders, DEG is indeed indicated by weak vibrations below 1500 cm⁻¹ ($\nu(\text{C-O})$, $\delta(\text{CH}_2)$)^[70]. An additional vibration around 500 cm⁻¹ is ascribed to phonon absorptions of the ZnO lattice.^[102] Between 4000 cm⁻¹ and 1500 cm⁻¹, IR transmission is relatively low, which could be due to free charge carriers.^[2,3,6,90,91] However, if the FT-IR spectrum of as-prepared AZO is compared with ITO spectra (Figure 16), it can be seen that even the oxidized ITO sample showed a dip in the IR transmittance, and that the transmittance of as-prepared ITO was much lower than that of as-prepared AZO. FT-IR spectra of IZO were also measured, but they did not show any large differences from AZO spectra.

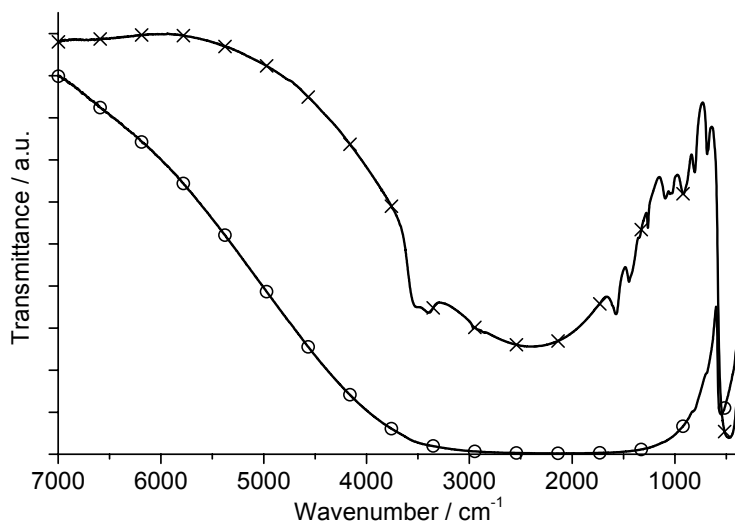


Figure 24. FT-IR spectra of AZO powder: as-prepared (cross) and after thermal treatment (circle).

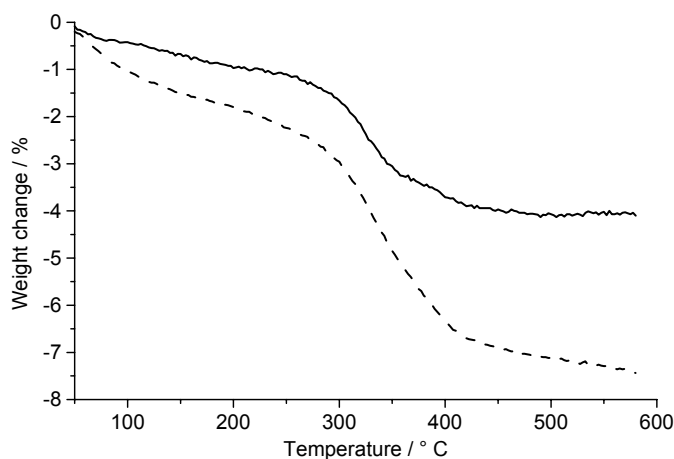


Figure 25. TG analysis of as-prepared AZO (solid) and IZO (dashed).

To quantify the amount of diethylene glycol adhered on the particle surface, DTA-TG measurements were carried out. TG analysis of IZO and AZO resulted in a certain weight loss between 200 and 400 °C for both samples (Figure 25). The weight losses amount to 5.3 % for IZO and 2.6 % for AZO and can be related to DEG.^[28,87,88] Thus, about the double amount of DEG is adhered to the surface of IZO particles. This observation is in accordance with the low degree of agglomeration in IZO suspensions. Interestingly, IZO as well as AZO exhibit a much larger amount of DEG adhered to the surface in comparison to our previous results addressing ITO nanocrystals.^[83] In contrast to doped ZnO, ITO – gained via very similar measures – shows an excellent conductivity immediately after synthesis, which is ascribed to the very small amount of DEG adhered to the surface of ITO particles.

In addition, zeta potential measurements were conducted to verify surface conditioning and colloidal properties of as-prepared IZO and AZO (Figure 26). To this end, powders were redispersed in water and titrated from the neutral pH range to alkaline and back to acidic pH

by addition of NaOH and HCl while measuring the zeta potential (Figure 26). As a result, isoelectric points (IEP) of 8.9 for IZO and 8.5 for AZO were deduced. These values are close to the IEP of undoped ZnO (around pH 9).^[103] Thus, the IEP is only weakly affected by doping; only the more acidic Al^{3+} seems to shift the IEP to a lower pH. Right after redispersion, aqueous IZO and AZO suspensions show pH values of 7.2 and 7.5. Since these values are rather close to the IEP, water-based suspensions are of limited colloidal stability (up to some hours).

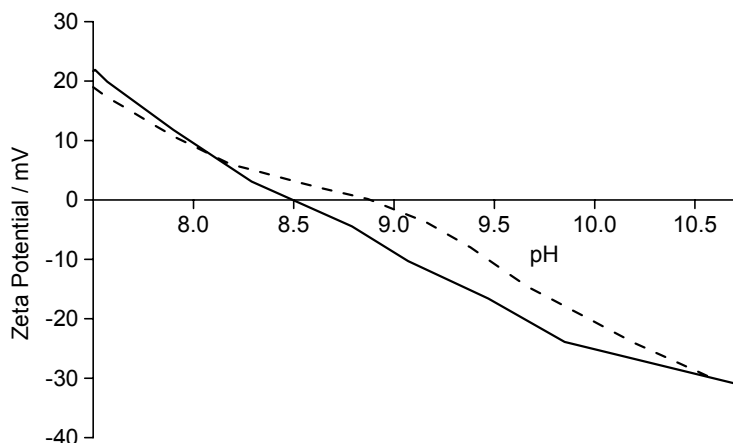


Figure 26. Zeta Potential of as-prepared AZO (solid) and IZO (dashed) redispersed in water.

Aiming at conductive IZO and AZO, as-prepared samples were treated thermally in order to, first, burn-out DEG in air and, second, to reestablish charge carriers by forming gas processing. Since TG analysis showed DEG to be removed below 400 °C, this temperature was chosen for oxidative treatment. After heating in air at 400 °C for 30 min, powders were reduced in forming gas for 60 min at the same temperature.

Subsequent to this treatment, FT-IR spectra of AZO showed DEG to be absent and the transmittance to be decreased (Figure 24). Furthermore, after reduction with forming gas IZO and AZO pellets showed a bright blue color and a sheet resistivity of now 60 $\Omega\Box$ and 170 $\Omega\Box$, respectively. Considering a pellet thickness of 34 μm , this corresponds to specific resistivities of $2.0 \cdot 10^{-1} \Omega\text{cm}$ and $5.7 \cdot 10^{-1} \Omega\text{cm}$ for IZO and AZO. Non-doped ZnO thermally treated likewise as a reference did not show any measurable conductivity at all, which confirms that the low resistivities of IZO and AZO samples indeed is an effect of successful doping.

For optical characterization, the reflectance of IZO, AZO and non-doped ZnO powders was measured via UV-Vis spectroscopy (Figure 27 a). Based on measured UV-Vis spectra, the bandgap was calculated as the energy corresponding to the wavelength where the first derivative of the reflectance is at maximum.^[104,105] For undoped ZnO, this resulted in a wavelength of 383 nm (Figure 27b) and a bandgap energy of 3.24 eV. This is in accordance with values obtained by other groups using reflectance measurements to determine the bandgap.^[104,105] For as-prepared IZO and AZO, bandgap energies of 2.95 eV and 3.18 eV were deduced (Figure 27b). While heating in air the bandgaps were decreased to 2.85 eV (IZO) and 2.91 eV (AZO). After the forming gas process, the bandgap with 3.17 eV for both samples exceeded even the value of the as-prepared materials. Thus, a bandgap shift of +0.3 eV between insulating oxidized samples and conductive reduced samples occurs. This finding is in accordance with the expectation and ascribed to the higher concentration of free charge carriers in reduced samples. The resulting partial filling of the conductance band is

well-known as the Moss-Burstein effect.^[106,107] In fact, in comparison to non-doped ZnO an even larger bandgap energy of the doped samples would have been expected. Thus, a bandgap as large as 3.7 eV has been reported for AZO by some groups utilizing gas-phase deposition methods.^[108,109] For nanocrystalline sol-gel AZO samples, bandgaps of 3.3 to 3.5 eV have been reported.^[92,97,98] For IZO, bandgaps of 3.3-3.5 eV have been reported for sol-gel as well as for gas-phase deposition synthesis.^[92,110-112] However, all these results are based on transmission measurements of thin layers, which might not be directly comparable with the diffuse reflectance of powders recorded here.

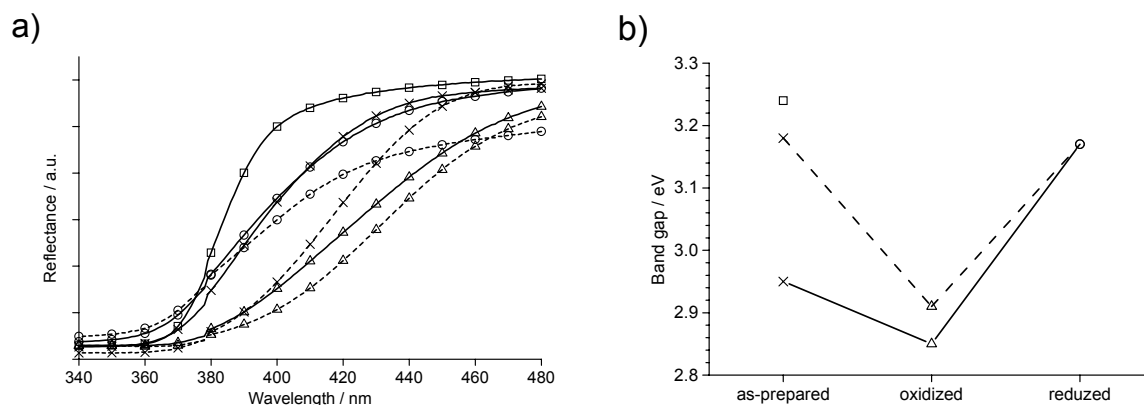


Figure 27. a) UV-Vis spectra and b) bandgap energy of powders of AZO (solid) and IZO (dotted): as-prepared (cross), after annealing in air (400 °C, 30 min, triangle), and after forming gas process (400 °C, 60 min, circle) in comparison to as-prepared ZnO (square).

As a proof of concept, IZO and AZO suspensions with solids contents of 10 wt-% were spin-coated on glass plates without any further optimization of, for instance, viscosity, solids content, type of solvent, or substrate preconditioning. In order to increase the particle-to-particle contact and conductivity, as-deposited films were first treated thermally in air (500 °C, 1 h), and secondly treated with forming gas ($H_2/N_2 = 10\%$, 500 °C, 2 h).

Characteristic SEM images of post-treated IZO and AZO layers are presented in Figure 28 a and b. According to SEM analysis, post-treated thin layers appear quite homogenous (Figure 28). However, the primary particles seen in SEM images of diluted DEG suspensions (Figure 21) are not observable. Instead, small agglomerates can be observed. IZO and AZO thin layers exhibit agglomerates of 40-60 nm and 70-100 nm in diameter, respectively.

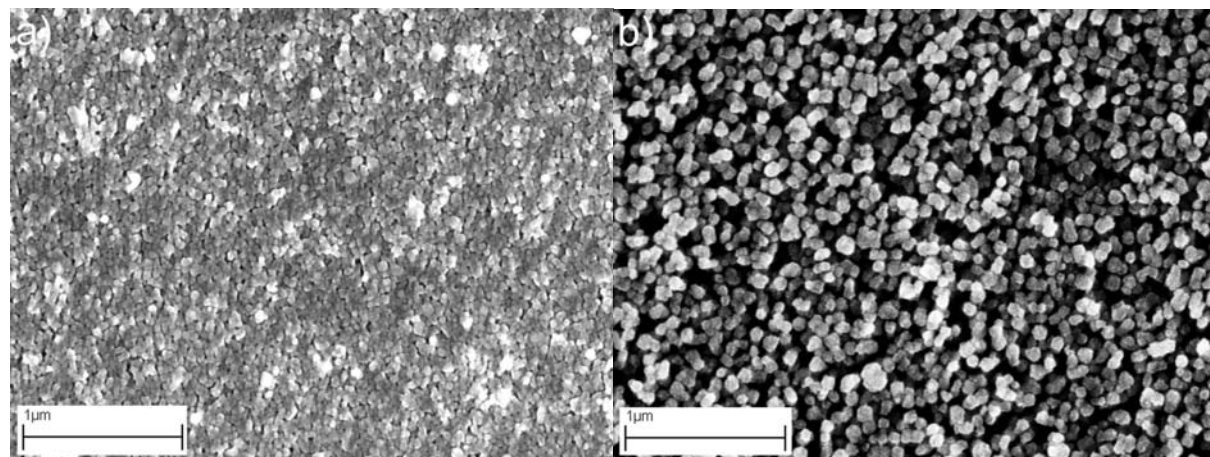


Figure 28. SEM Images of thin layers of a) IZO and b) AZO on glass plates.

Four-point probing of IZO layers results in a sheet resistance of $2.6 \text{ k}\Omega\Box$. With a layer thickness of 800 nm (estimated from SEM images), a resistivity of $2.1 \cdot 10^{-1} \Omega\text{cm}$ was gained without applying any correction factor for porosity. Thus, for IZO the resistivity of post-treated powder pellets and thin layers is very similar. While synthesis and resistivity of IZO samples is very reproducible, AZO as a thin layer showed a considerable variance in its electrical properties. Best results were obtained by increasing the Al:Zn molar ratio to 20 % in synthesis, instead of 5 % as described above. With thin layers made from these suspensions, a sheet resistance of $3.2 \text{ k}\Omega\Box$ and a resistivity ($2.6 \cdot 10^{-1} \Omega\text{cm}$) could be gained. The obvious difficulties in case of AZO are ascribed to the large difference in ionic radii between Zn^{2+} and Al^{3+} (Table 4). As a consequence, incorporation of Al^{3+} into the ZnO lattice is more difficult and can be incomplete, depending on slight variations of the experimental conditions (e.g. exact temperature at solutions, precursor addition, nucleation; exact concentration of precursors and solvents; exact temperature, placement of crucibles, gas flow velocity inside the furnace during thermal post-treatment). Altogether, nanocrystalline IZO and AZO samples show high conductivities.

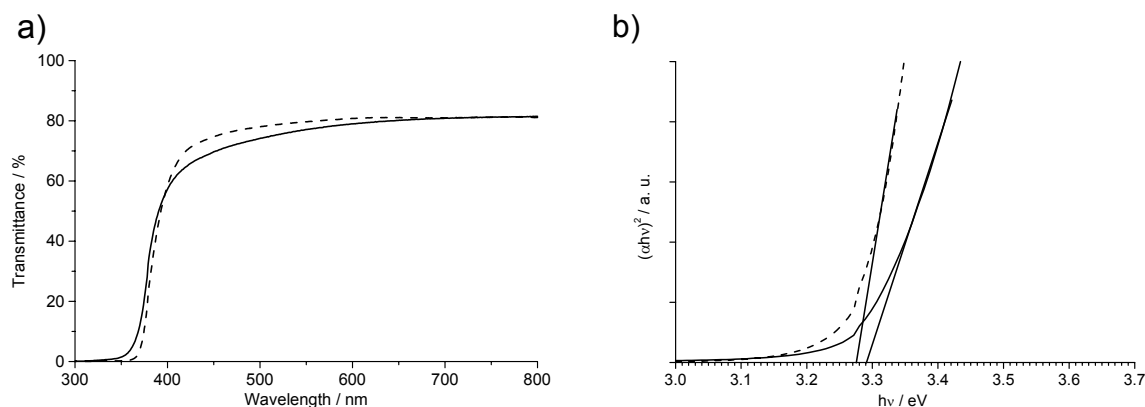


Figure 29. a) UV-Vis spectra of AZO (solid) and IZO (dotted) layers on glass plates and b) estimation of the bandgap of these layers.

Beside the electrical properties of IZO and AZO thin films, UV-Vis spectra of conductive films on glass plates were recorded to determine the optical properties (Figure 29). Although the transmittance at 400 nm is only 60 %, above 420 nm, the transmittance is over 70 %. Thus, considering a non-optimized film quality, the transmittance in the visible wavelength interval is relatively high (Figure 29 a). In the middle of the visible wavelength interval, the transmittance is equal to 79.7 % for IZO and 77.1 % for AZO (both at 550 nm and with a transmittance of the uncoated glass plate of 91.3 %).

The optical absorption coefficient α was calculated from transmission spectra using the relation given by Lambert-Beer's law: $T = \exp(-\alpha d)$ (see Equation (42)). The bandgap energy E_g was then estimated with the assumption of a direct bandgap and the equation given by Tauc *et al.*: $\alpha h\nu = A(h\nu - E_g)^{1/2}$ (see Equation (44)).^[72] Extrapolating the linear part of the curves $(\alpha h\nu)^2$ as a function of the energy $h\nu$ to intercept the energy axis (at $\alpha = 0$.) resulted in bandgap energies of 3.27 eV (IZO thin film) and 3.29 eV (AZO thin film) (Figure 29 b). These values are higher than those values stemming from measuring diffuse reflectance of powders, and are indeed in good agreement with literature data of IZO and AZO thin films.^[92,97,98,108-112]

In conclusion, the incorporation of dopants and the resulting electrical and optical properties have been evidenced by EDX, UV-VIS and four-point probing. Due to adhesion of DEG as

stabilizer on the particle surface, as-prepared powder samples exhibited high resistivities. Subsequent to burn-out of DEG in air (400 °C, 30 min) as well as forming gas processing (400 °C, 60 min), resistivities of $2.0 \cdot 10^{-1} \Omega\text{cm}$ and $5.7 \cdot 10^{-1} \Omega\text{cm}$ were obtained for IZO and AZO powder samples. As a proof of the concept, a simple layer formation process via solvent evaporation of as-prepared IZO and AZO suspensions on glass plates was carried out. Subsequent to thermal treatment, the resulting layers exhibited a visible transmittance of about 80 % and a comparably low resistivity (IZO: $2.1 \cdot 10^{-1} \Omega\text{cm}$, AZO: $2.6 \cdot 10^{-1} \Omega\text{cm}$). The bandgaps of post-treated powders and thin layers were calculated to 3.2 eV and 3.3 eV, respectively.

Moreover, the effect of the Al^{3+} doping concentration was studied in more detail. To this concern, a series of AZO samples was prepared, in which Al:Zn molar ratios of 1 %, 5 %, and 20 % were introduced during synthesis. First, the crystallinity of as-prepared samples was verified via X-ray diffraction (Figure 30).

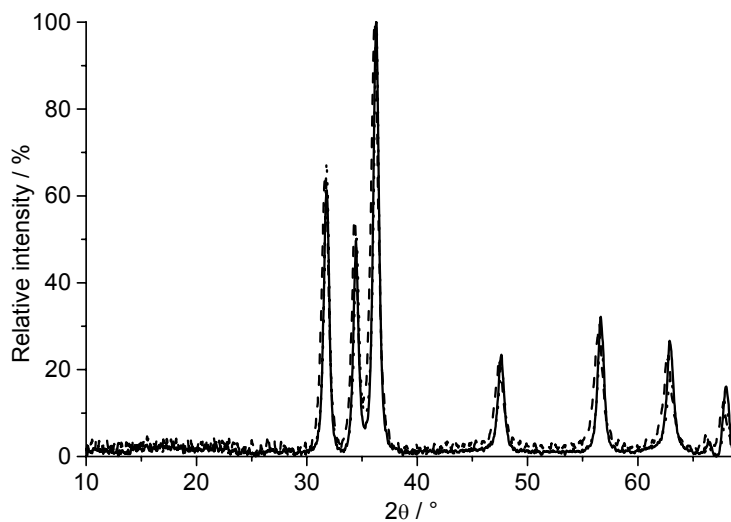


Figure 30. XRD patterns of as-prepared AZO samples with introduced Al:Zn molar ratios of 1 % (solid), 5 % (dashed), and 20 % (dotted).

The powder diffraction patterns of the three AZO samples are very similar, and even the AZO (20 mol-%) sample is evidenced to be phase pure and crystallize in the hexagonal wurtzite-type structure (Figure 30).^[101] Due to the broad Bragg diffraction peaks, no significant shift of diffraction patterns can be observed, as discussed above. According to Scherrer's formula (see Equation (9)), the average crystallite sizes of the as-prepared AZO samples are 17, 13, and 18 nm (Table 5).

Further, nitrogen absorption measurements of as-prepared samples were performed according to the BET type of method. Calculations based on BET measurements resulted in mean particle diameters of 25, 25, and 32 nm for as-prepared AZO, thus being in relatively good agreement with XRD analysis and confirming the trend of observed for previous 5 mol-% samples (AZO-I and AZO-II), where slightly higher particles sizes were obtained from BET measurements in comparison to from XRD and SEM analysis. As-prepared AZO powders with introduced doping concentrations of 1 mol-%, 5 mol-%, and 20 mol-% were redispersed in ethanol with ultrasound and investigated via scanning microscopy analysis (Figure 31).

Table 5. Mean diameters of as-prepared and post-treated AZO samples with varying Al:Zn molar ratios deduced via SEM, XRD, and BET analysis.

Sample		SEM	XRD	BET
AZO (1 mol-%)	as-prepared	250-350 nm	17 nm	25 nm
AZO (1 mol-%)	air (400 °C, 0.5 h)	250-350 nm	18 nm	52 nm
AZO (1 mol-%)	air (400 °C, 0.5 h) + forming gas (400 °C, 1 h)	250-350 nm	18 nm	55 nm
AZO (1 mol-%)	air (800 °C, 0.5 h)	250-350 nm	30 nm	160 nm
AZO (5 mol-%)	as-prepared	60-100 nm	13 nm	25 nm
AZO (5 mol-%)	air (400 °C, 0.5 h)	60-100 nm	16 nm	38 nm
AZO (5 mol-%)	air (400 °C, 0.5 h) + forming gas (400 °C, 1 h)	60-100 nm	16 nm	49 nm
AZO (5 mol-%)	air (800 °C, 0.5 h)	60-100 nm	23 nm	102 nm
AZO (20 mol-%)	as-prepared	60-100 nm	18 nm	32 nm
AZO (20 mol-%)	air (400 °C, 0.5 h)	60-100 nm	21 nm	27 nm
AZO (20 mol-%)	air (400 °C, 0.5 h) + forming gas (400 °C, 1 h)	60-100 nm	20 nm	38 nm
AZO (20 mol-%)	air (800 °C, 0.5 h)	60-100 nm	30 nm	82 nm

According to SEM analysis, primary particles of 15-20 nm are observable in all three as-prepared samples (Figure 31). However, aggregates of different sizes have been formed. AZO (1 mol-%) exhibits agglomerates 250-350 nm in size (Table 5), whereas the agglomerates in AZO (5 mol-%) and AZO (20 mol-%) samples have diameters of 60-100 nm (Table 5) which is in agreement with the observations from SEM images of AZO thin layers (Figure 28). Thus, a higher concentration of acidic Al³⁺ ions during synthesis resulted in smaller aggregate sizes. However, the effect seems to be limited to an introduced doping concentration of 5 mol-%. If the doping concentration exceeds this value, aggregate sizes do not decrease further.

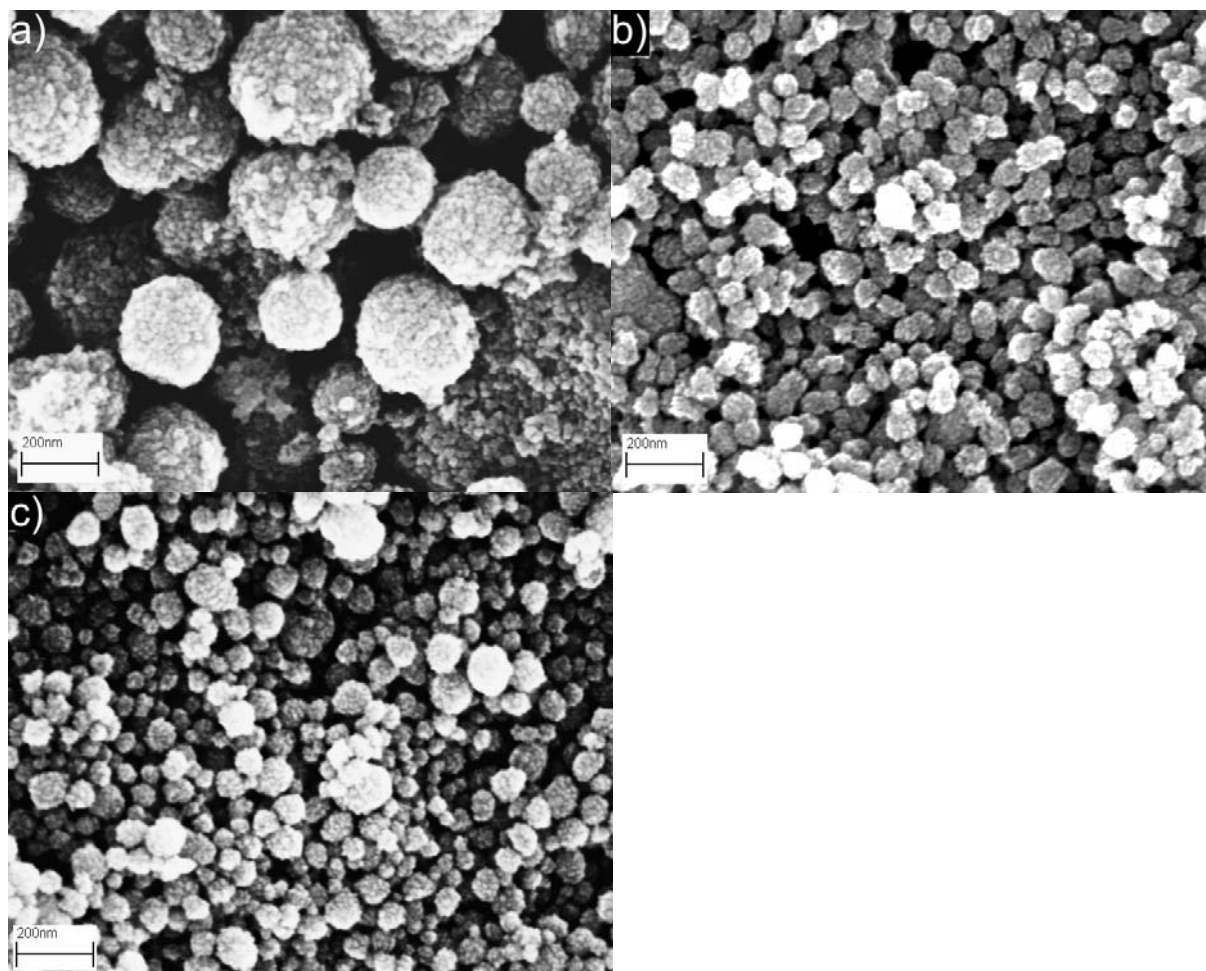


Figure 31. SEM images of as-prepared AZO samples with Al:Zn molar ratios of a) 1 %, b) 5 %, and c) 20 %; powders redispersed in ethanol.

Thereafter, AZO samples were post-treated as described above, i.e., heated in air at 400 °C for 30 min and processed in forming gas for 60 min at the same temperature. In addition, samples were heated in air at 800 °C for 30 min. The effects of this post-treatment on particle sizes were investigated via XRD, SEM and BET; the results are summarized in Table 5. As representative examples, the powder diffraction patterns of as-prepared and post-treated AZO (1 mol-%) are presented in Figure 32.

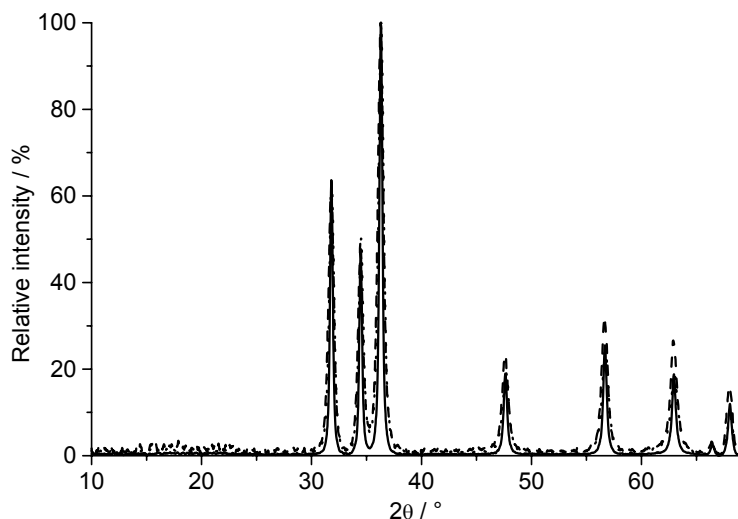


Figure 32. XRD patterns of AZO (1 mol-%): as-prepared (dashed), after heating in air and forming gas at 400 °C (dotted), and after heating in air at 800 °C (solid).

XRD measurements of as-prepared and post-treated AZO (1 mol-%) (Figure 32) show that peak width and thereby crystallite size are hardly affected by thermal treatment at 400 °C. The crystallite size – calculated from Scherrer's formula – of as-prepared AZO (1 mol-%) equals 17 nm and after heating in air and forming gas at 400 °C it amounts to 18 nm. The same trend is observed for AZO (5 mol-%) and AZO (20 mol-%) samples (Table 5). In addition, it is notable that XRD patterns of partially reduced samples treated in forming gas show no additional peaks, thus, no observable reduction of Zn^{II} or Al^{III} has occurred. This further verifies that the conductivity of samples originates from the incorporation of dopants in the ZnO host lattice. For samples heated in air at 800 °C, the peak width decreases slightly (Figure 32) and the crystallite size thus increases somewhat, whereby the calculated crystallite size of AZO (1 mol-%) treated at 800 °C is 30 nm. Accordingly, post-treatment at 800 °C has caused a certain sintering of AZO nanoparticles, although the melting point of bulk ZnO is 1974 °C.^[45] However, sintering of nanoparticles at low temperatures is a well-known effect, which is caused by their higher reactivity due to their high surface areas.^[113]

As representative examples of the morphological effects on the samples due to post-treatment, SEM images of AZO (1 mol-%) and AZO (20 mol-%) samples processed in air and forming gas at 400 °C as well as processed in air at 800 °C are shown in Figure 33. Samples were prepared by redispersing powders in ethanol with ultrasound.

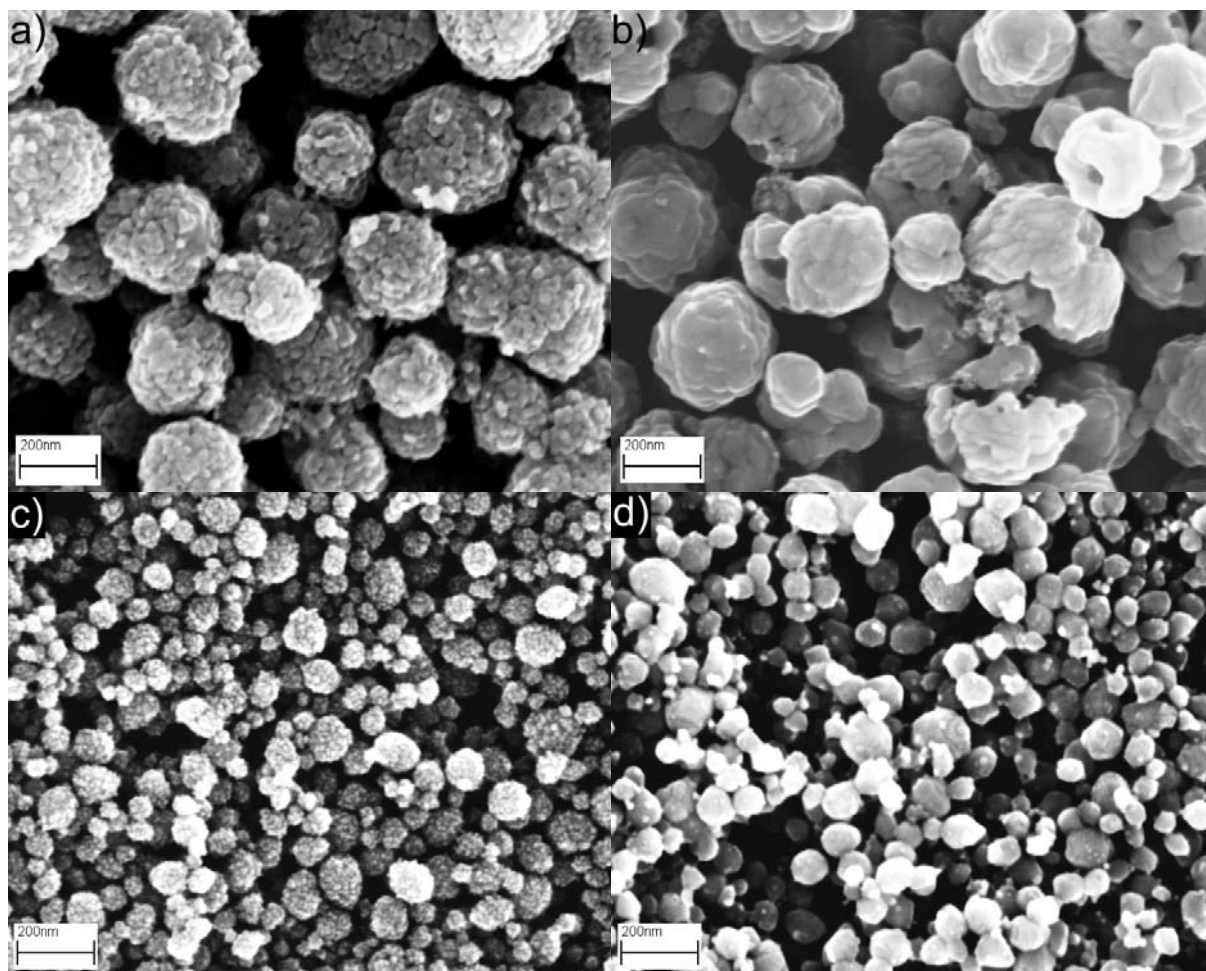


Figure 33. SEM images of thermally treated AZO powders redispersed in ethanol: AZO (1 mol-%) at a) 400 °C and b) 800 °C; AZO (20 mol-%) at c) 400 °C and d) 800 °C.

According to SEM analysis, all post-treated samples exhibit aggregates of the same sizes as in as-prepared samples, i.e., post-treated AZO (1 mol-%) contains aggregates of 250-350 nm in size while the aggregate size of post-treated AZO (5 mol-%) and AZO (20 mol-%) amounts to 60-100 nm, independent of post-treatment temperature (Figure 33). However, whereas SEM images of samples processed at 400 °C still exhibit aggregates consisting of smaller primary particles, the aggregates of samples heated at 800 °C show less internal structure and appear melted together. This is in accordance with the partial sintering observed via XRD.

The same tendency is seen in particle sizes obtained from calculations based on BET measurements of post-treated AZO, where the calculated mean diameter increases with processing temperature and time (Table 5), due to the decreasing surface area accessible to adsorbate gas molecules. Thus, as-prepared samples are highly porous since the aggregate sizes obtained via SEM analysis are much larger than the particle sizes calculated from BET measurements of the specific surface area (Table 5). For samples thermally treated at 400 °C, the values remain essentially the same and the porosity is thus still high. On the other hand, samples heated at 800 °C exhibit low porosities, considering that the aggregate sizes obtained via SEM analysis and the particle sizes calculated from BET surface areas are similar. The aggregates are not, however, completely sintered since calculations based on XRD measurements resulted in crystallite sizes much smaller than the aggregate sizes (Table 5).

Furthermore, the amount of aluminium present in the samples and the effect of doping concentration on the conductivity were studied. In order to investigate how much of the

aluminium that was introduced during synthesis is actually present in the prepared AZO particles, AZO samples treated in air and forming gas were investigated via EDX and quantitative analysis. Quantitative analysis was carried out by Mikroanalytisches Labor Pascher, Remagen, Germany. A comparison of the Al:Zn molar ratios introduced during synthesis and evidenced via EDX and quantitative analysis is presented in Table 6.

Table 6. Al:Zn molar ratios of AZO samples treated in air and forming gas: introduced and evidenced via EDX and quantitative analysis.

introduced	EDX	quantitative analysis
1 %	0.8 %	1.0 %
5 %	1.0 %	1.8 %
20 %	5.3 %	4.6 %

EDX and quantitative analysis show similar results; it is clear that the difference between the introduced and evidenced doping concentrations increases as the introduced doping concentration increases. In AZO (1 mol-%), the introduced and evidenced doping concentrations are essentially the same. However, in AZO (5 mol-%) and AZO (20 mol-%) the evidenced doping concentration is only a fraction of the introduced concentration, which implies that the rest of the aluminium that was introduced during synthesis remains in solution. Comparing these results with the first AZO (5 mol-%) sample, for which a doping concentration of 3 mol-% was evidenced via EDX, it is clear that the reproducibility of the doping concentration present in the particles is comparably poor. The difficulty in inserting Al^{3+} in ZnO is expected due to the large difference in ionic radii between Zn^{2+} and Al^{3+} (Table 4). However, it should be noted that the evidenced doping concentration is not the same as the amount of dopants that are actually inserted in the ZnO crystal lattice. As EDX and quantitative analysis do not give any structural information, it is possible that, e.g. amorphous Al_2O_3 is also present. In order to determine the amount of Al^{3+} dopants inserted in the ZnO crystal lattice, the local structure of the particles would need to be studied.

Moreover, the conductivities of AZO samples were evaluated via four-point probing. The sheet resistances of AZO samples with an introduced Al:Zn molar ratio of 1 %, 5%, and 20 % samples treated in air and forming gas were measured to 160, 170, and 340 $\Omega\Box$, respectively. Thus, apparently, when the introduced doping concentration is low, the exact amount of introduced dopant does not have a large influence of the resistivity of the samples. This indicates that only a certain amount of aluminium is actually inserted in the ZnO lattice. In addition, it seems that the resistivity increases when the introduced doping concentration is too high. This effect has also been observed in other works, where e.g. minimum resistivities have been reported at 1-1.5 mol-% introduced doping concentration in studies where the sol-gel method was employed.^[94,97,98] This also indicates that only a certain amount of dopants are actually inserted in the lattice.

Thus, for AZO samples, there is no apparent benefit of adding large amounts of dopants during synthesis. Comparing the two samples with lower doping concentrations, AZO (5 mol-%) offers a combination of low resistivity and small aggregate size, whereas AZO (1 mol-%) exhibits a low resistivity but a large aggregate size. Considering the relatively poor reproducibility of the evidenced doping concentration in AZO (5 mol-%) samples, this could be a reason why the AZO (20 mol-%) powder sample shows a higher resistivity than AZO (1 mol-%) and AZO (5 mol-%), whereas AZO (20 mol-%) thin layers prepared from another suspension (presented above) showed the lowest resistivity.

In conclusion, the effects of post-treatment and introduced Al^{3+} doping concentration in AZO samples have been studied via SEM, XRD, BET, four-point probing, EDX, and quantitative analysis. It has been evidenced that the crystallinity and the primary particle size are hardly affected by the doping concentration while the aggregate size is smaller for higher doping concentrations. Post-treatment of samples at 400 °C did not result in a change of primary particle size; however, as expected, samples were more agglomerated. Four-point probing of samples treated in air and forming gas at 400 °C resulted in similar resistivities for AZO (1 mol-%) and AZO (5 mol-%) and a higher resistivity for AZO (20 mol-%). EDX and quantitative analysis showed that only a fraction of the doping concentration introduced during synthesis was actually present in AZO (5 mol-%) and AZO (20 mol-%). Samples treated in air at 800 °C were partially sintered but exhibited the same aggregate sizes as other samples. The effect of doping concentration was not studied for IZO samples. However, due to the similarity of ionic radii of Zn^{2+} and In^{3+} (Table 4) it is expected that In^{3+} is inserted in the ZnO lattice to a higher degree.

Finally, solid state NMR spectroscopy of as-prepared and post-treated AZO samples with introduced Al:Zn molar ratios of 1 %, 5 %, and 20 % was carried out.^[114] In Figure 34, one-dimensional ^{27}Al single pulse NMR spectra of as-prepared and post-treated AZO (5 mol-%) are presented.

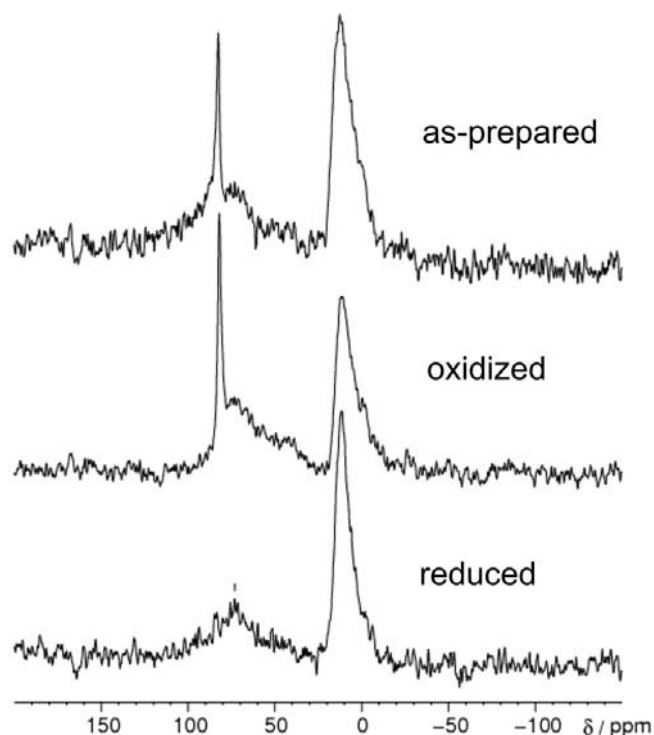


Figure 34. 1D ^{27}Al single pulse NMR spectra of AZO (5 mol-%): as-prepared, oxidized by heating in air (400 °C, 30 min), and reduced via forming gas processing (400 °C, 60 min).

The spectrum of as-prepared AZO (5 mol-%) exhibits two well-resolved peaks for which the observed peak maxima occur at isotropic chemical shifts of $\delta = 82.6$ ppm and 12.6 ppm. In addition, a very broad peak between 30 and 80 ppm is visible. Thus, the presence of aluminium in AZO samples is again confirmed. The left peak ($\delta = 82.6$ ppm) corresponds to fourfold coordinated aluminium in an oxygen environment.^[115] The narrow line width of the peak implies that the fourfold coordinated aluminium ions are located in a crystalline structure. Thus, these Al^{3+} ions are incorporated in the zinc oxide lattice, which has a hexagonal crystal structure with fourfold coordination. The right peak ($\delta = 12.6$ ppm)

corresponds to sixfold coordinated aluminium in an oxygen environment.^[115] The sixfold coordinated Al^{3+} ions are assumed to be located in an amorphous environment due to the broad line width of the corresponding peak. These results are consistent with a model of AZO particles that consist of a single crystalline core in which aluminium is integrated in the zinc oxide lattice and an amorphous shell in which aluminium is coordinated to DEG (Figure 35). Since TEM images exhibited single crystalline ZnO particles (Figure 22), the shell is assumed to be thin in comparison to the diameter of the particles. The broad peak at 30-80 ppm peak is suggested to belong to four- or fivefold coordinated aluminium in the boundary between the crystalline core and the amorphous shell.

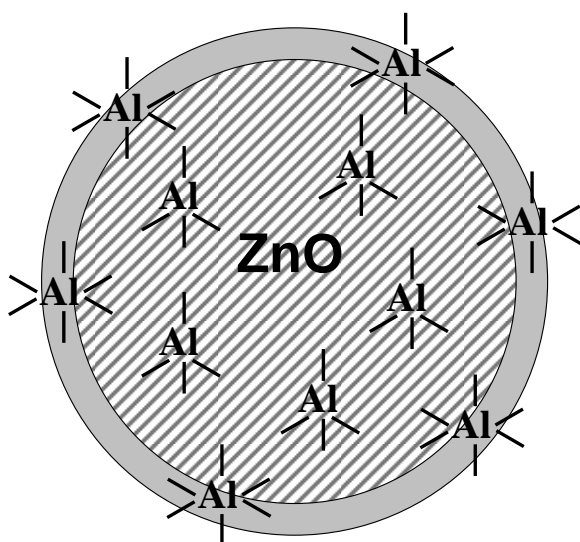


Figure 35. Core-shell model of AZO particles consisting of a single crystalline core with fourfold coordinated Al^{3+} ions inserted in the ZnO lattice and an amorphous shell with sixfold coordinated Al^{3+} .

The spectrum of AZO (5 mol-%) oxidized by heating in air (400 °C, 30 min) shows no significant changes (Figure 34). Thus, sixfold coordinated Al is still present in the sample after heating in air. In addition, two-dimensional ^{27}Al - ^1H NMR was applied to further characterize the oxidized AZO (5 mol-%) sample (Figure 36). The presence of an off-diagonal peak at about 3 ppm in the spectrum indicates that sixfold coordinated aluminium couples to hydrogen. This peak can be assigned to CH_2 in DEG. This assignment is confirmed via ^{13}C - ^1H CP-MAS measurements. From these findings, it is concluded that DEG is still present in the sample. However, DTA-TG analysis (Figure 25) led to the assumption that DEG adhered on the surface is burned out at 400 °C, which confirms the assumption of an amorphous shell in which aluminium is bonded to DEG, since the shell is not expected to burn out. Furthermore, the line width of the peak corresponding to sixfold coordinated Al is still broad (Figure 34), which implies that the crystallinity of the shell does not change during heating in air (400 °C, 30 min).

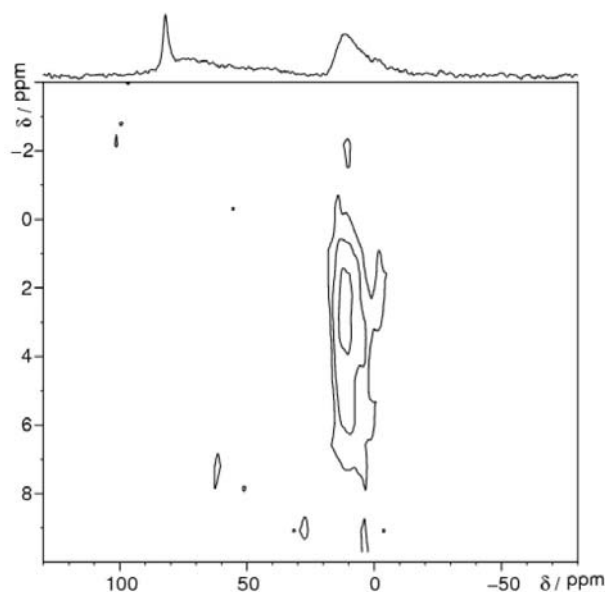


Figure 36. 2D ^{27}Al - ^1H NMR spectrum of AZO (5 mol-%) heated in air (400 °C, 30 min).

After the AZO (5 mol-%) sample had been processed in forming gas (400 °C, 60 min), NMR measurements showed that the peak corresponding to sixfold coordinated aluminium ($\delta = 11.4$ ppm), as well as the weak, very broad peak, were still present in the spectrum (Figure 34). However, subsequent to reduction in forming gas, the peak corresponding to fourfold coordinated aluminium has vanished. This is in accordance with the expectation for a highly conductive sample, for which a Knight shift and/or efficient relaxation are expected to shift and broaden the peak. Thus, the conductivity of post-treated AZO is verified also via NMR. However, since a highly intensive peak corresponding to fourfold coordinated aluminium is visible for as-prepared AZO (5 mol-%) in contrast to the reduced sample, as-prepared samples are evidenced not to be conductive. This contradicts the initial assumption that as-prepared AZO particles are conductive but that the particle-to-particle conductivity is hampered by a coating of DEG. This is in contrast to as-prepared ITO particles, which are highly conductive directly after synthesis (see section 4.1.1).

Thus, it seems that the dip in IR transmittance seen for as-prepared AZO (Figure 24) does not originate from free charge carriers. Considering the results of XRD measurements of as-prepared and post-treated AZO, the crystallinity of samples heated at 400 °C (Table 5, Figure 32) showed only a slight improvement in comparison to as-prepared samples. It is therefore assumed that the low conductivities of as-prepared AZO samples do not depend on insufficient crystallinity. A possible reason for the low conductivity could be that the Al^{3+} ions are not homogeneously incorporated in the ZnO lattice, but that they rather form clusters, which leads to an insufficient number of charge carriers in areas where no Al clusters are present. As earlier discussed, the difficulty of homogeneously inserting aluminium ions in ZnO is expected due to the large difference in ionic radii between Al^{3+} and Zn^{2+} (Table 4). In fact, it seems that a fortunate arrangement of charge carriers in AZO is achieved only after treatment in forming gas.

Furthermore, spin echo measurements were conducted in order to improve the signal-to-noise ratio of the broad peaks in the ^{27}Al NMR spectra. In Figure 37, spin-echo measurements of as-prepared, oxidized and reduced AZO (1 mol-%) and AZO (5 mol-%) are presented (note the difference in the x-axis scale). Finally, in Figure 38, a comparison of AZO samples with introduced doping concentrations of 1 mol-%, 5 mol-%, and 20 mol-% treated in forming gas is shown. With the application of a spin-echo method, an additional, extremely broad peak

with an observed maximum around 130 ppm (dashed line) was revealed for all reduced samples (Figure 38). This broad peak occurs for the same reason as why the peak corresponding to fourfold coordinated aluminium vanished in the single pulse experiment (Figure 34). Via application of spin-echo measurement, it was also possible to observe that all reduced samples still show a weak peak corresponding to fourfold coordinated aluminium. The reason for the existence of this peak is not yet clarified; however, it is believed to signify that the conductivity of the crystalline core could be further optimized. This might be achieved by applying longer microwave-assisted heating times during synthesis. Doped zinc oxide were only heated in DEG at 200 °C for 30 min, whereas ITO, which was conductive directly after synthesis, was heated in DEG at the same temperature for 2 h (see section 4.1.1). Thus, although 30 min heating was clearly sufficient for the preparation of crystalline ZnO, it might not have been sufficient for a successful, homogeneous insertion of Al³⁺ ions in the zinc oxide lattice.

NMR spectra of samples with different doping levels are compared in Figure 38. All measurements were conducted under the same conditions. The absolute intensity of the broad peak located at about 130 ppm (dashed line) is about the same for all samples. Thus, the ratio of sixfold to fourfold coordinated aluminium increases as the introduced doping concentration increases. This implies that only a certain amount of aluminium is integrated in the crystalline core of the particle during the chosen experimental conditions. If more aluminium is introduced during synthesis, it is simply added to the amorphous shell. The overall conductivity of the particles is expected to be improved if the amorphous core is as thin as possible, which was seen to be the case for the lowest introduced doping concentration (1 mol-%). Thus, by introducing a doping concentration lower than 1 mol-%, the shell will possibly become yet thinner which could improve the conductivity. Comparing with AZO thin films prepared via sol-gel synthesis, minimum resistivities have been reported at 1-1.5 mol-% introduced doping concentration.^[94,97,98] However, in these works, the doping concentrations actually present in the samples were not evidenced. It is also expected that the optimal doping concentrations can depend on the preparation process. For example, for pulsed laser deposition, the optimal introduced Al:Zn ratio was reported to be 2 %.^[109]

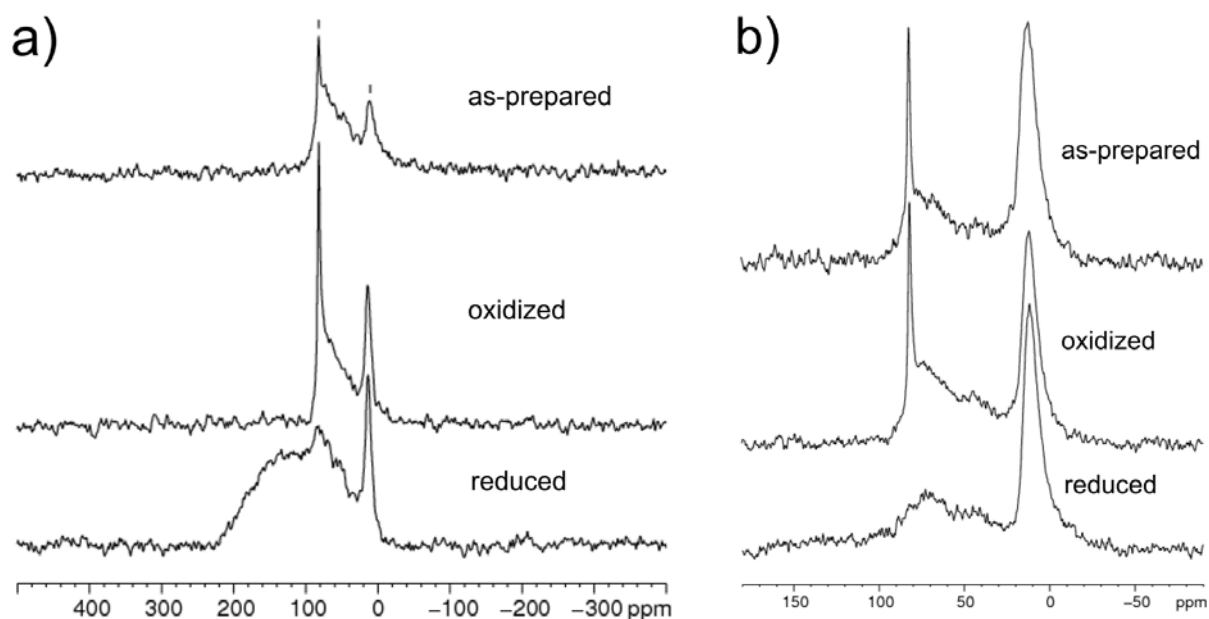


Figure 37. ²⁷Al NMR spectra of as-prepared and post-treated a) AZO (1 mol-%), and b) AZO (5 mol-%) using echo experiment.

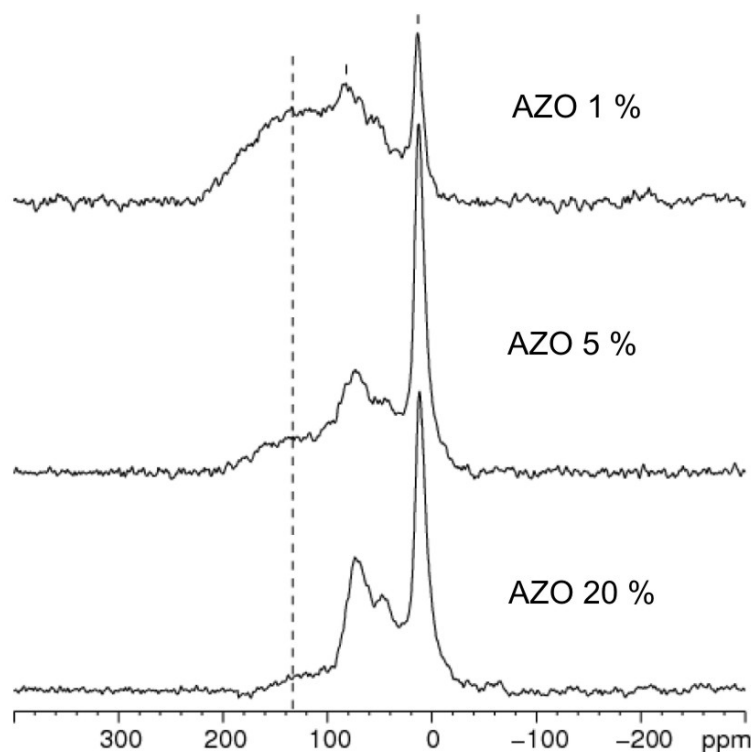


Figure 38. ^{27}Al NMR spectra of AZO samples with Al:Zn molar ratios of 1 %, 5 %, and 20 % reduced in forming gas (400 °C, 60 min) using echo experiment.

In this work, solid state NMR spectroscopy was for the first time applied as an analytical tool for the investigation of TCO nanomaterials. Solid state NMR has proved to offer a unique understanding of the local structure of TCO nanoparticles, which is essential for improving the conductivity. Here, with the aid of solid state NMR spectroscopy, a model for AZO particles prepared via a microwave-assisted polyol process could be set up. According to this model, AZO particles consist of a crystalline core in which Al is integrated in the ZnO lattice with fourfold coordination and an amorphous shell in which Al is bonded to DEG with sixfold coordination. It was observed that the core-shell structure did not change as a result of post-treatment of AZO. As-prepared samples and samples oxidized by heating in air (400 °C, 30 min) were evidenced to be non-conductive, whereas the conductivity of AZO treated in forming gas (400 °C, 60 min) was confirmed. Furthermore, it was also revealed that the ratio of sixfold to fourfold coordinated aluminium increased as the introduced doping concentration increased, which implies that only a certain amount of aluminium was inserted in the crystalline core of the particle. The rest of the aluminium was added to the amorphous shell – when too much Al was added, the amorphous shell caused the particle conductivity to decline. From these findings, improved synthesis conditions, such as longer heating times and introduction of lower amounts of aluminium, can be considered. Finally, it should be noted that further solid state measurements of AZO nanoparticles, as well as realization of optimized syntheses are in progress. However, this is beyond the scope of this work.

4.1.3 Tin oxide

Doped tin oxide is, like doped indium oxide and zinc oxide, a well-known transparent conductive oxide.^[3] The maximum charge carrier concentration, and thereby maximum conductivity of doped SnO₂ is lower in compared to ITO and AZO, which, however, makes it better suited for application in energy-efficient windows.^[6] At present, fluorine-doped tin oxide (FTO) is the most commonly employed TCO in energy-efficient windows.^[6] Antimony-doped tin oxide is known as ATO and other less commonly applied dopants include Ta and Nb.^[3]

Liquid phase preparation of SnO₂:F (FTO) has been achieved by utilizing the sol-gel method, with which resistivities of 0.7-0.8 Ωcm have been achieved for powders.^[116,117] For sol-gel thin films, resistivities of 0.1-1 Ωcm have been reported.^[118,119] In these works, no studies of particle size in the liquid phase were carried out. There are very few reports of liquid phase preparation of SnO₂:Ta. However, Kurz *et al.* applied the sol-gel method to prepare SnO₂:Ta thin films and determined the resistivity of a post-treated film to be $3.9 \cdot 10^{-2}$ Ωcm (film thickness: 52 nm).^[120] The particle size was not investigated at all – neither of the film nor of the sol.

In this work, suspensions of SnO₂:F and SnO₂:Ta particles with different introduced doping concentrations were prepared in diethylene glycol (DEG) via microwave irradiation.^[84] As a reference, non-doped SnO₂ was synthesized similarly. In a typical recipe, 5.7 mmol SnCl₄ · 5 H₂O was dissolved in 50 ml DEG. In the case of FTO samples, 0.57 mmol N(CH₃)₄F · 4 H₂O was dissolved together with SnCl₄ · 5 H₂O, whereas in the case of SnO₂:Ta samples, a solution of 0.38 mmol Ta(OC₂H₅)₅ dissolved in absolute EtOH was added to the SnCl₄ · 5 H₂O solution. At 80 °C the solution was added to a solution of 50 ml DEG containing 28.5 mmol N(CH₃)₄OH · 5 H₂O and 2 ml deionized H₂O. Upon adding the solutions, no precipitation occurred. As the solutions were heated at 200 °C in a laboratory microwave oven (Ar atmosphere, magnetic stirring), precipitation was observed. To improve material crystallinity, the temperature was maintained for 1 h.

As-prepared FTO and SnO₂:Ta suspensions are colloiddally stable for months. They exhibit a transparent appearance and a slight bluish shade (Figure 39 b and Figure 42 b). Qualitatively, this finding already hints to the incorporation of the dopants into the SnO₂ lattice. Subsequent to centrifugation and drying, powders can be separated from the suspensions and are yielded in quantities of 80-90 %.

First, the size and size distribution of as-prepared SnO₂:Ta (7 mol-%) in DEG were determined via dynamic light scattering (Figure 39 a). According to DLS analysis, the average hydrodynamic diameter of SnO₂:Ta amounts to 13(1) nm. Thus, the particle size distribution is almost monodisperse. Scanning electron microscopy was applied to obtain a direct view of as-prepared SnO₂:Ta (Figure 40 a).

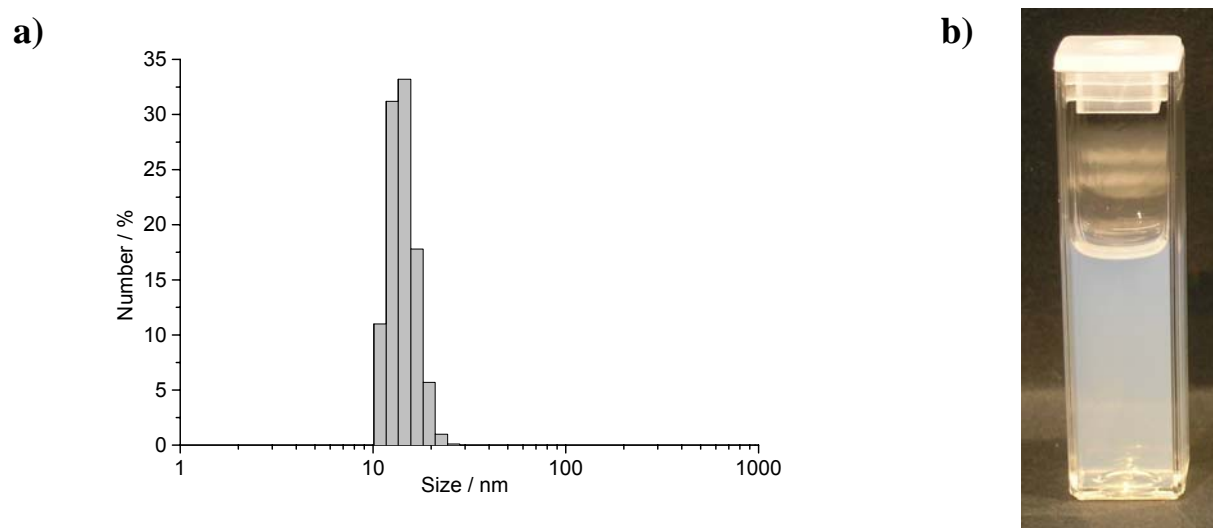


Figure 39. a) Particle size distribution of as-prepared $\text{SnO}_2:\text{Ta}$ in DEG measured with dynamic light scattering and b) photograph of $\text{SnO}_2:\text{Ta}$ in DEG (solids content: 1 wt-%).

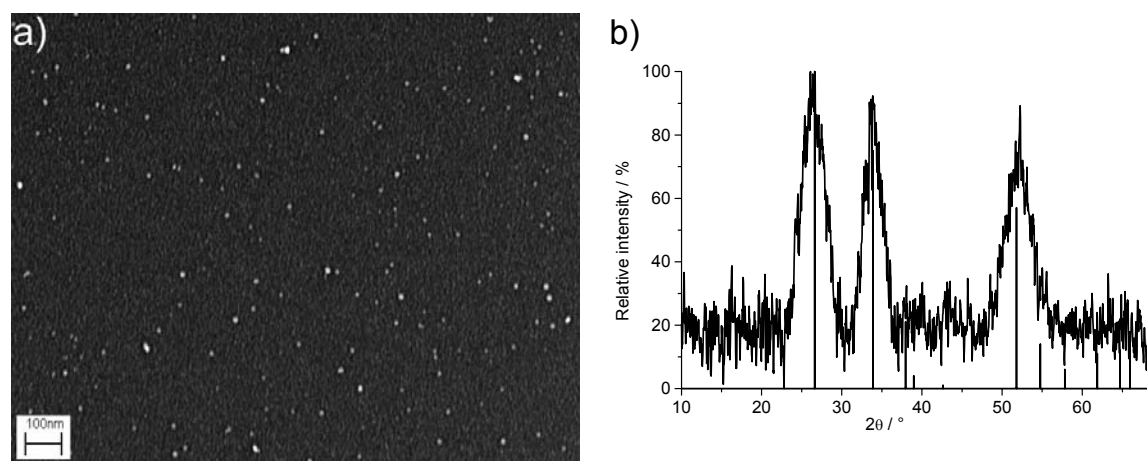


Figure 40. a) SEM image and b) XRD pattern of as-prepared $\text{SnO}_2:\text{Ta}$ (reference: SnO_2 – ICCD No. 41-1445).

SEM investigations of suspensions diluted with DEG show as-prepared particles to be non-agglomerated and of spherical and very uniform morphology (Figure 40 a). Statistical evaluation of the particle diameter based on SEM images was carried out and resulted in a mean diameter of 12 nm calculated from 450 particles, which is in very good agreement with DLS analysis.

Furthermore, the crystallinity of as-prepared $\text{SnO}_2:\text{Ta}$ was investigated via X-ray diffraction (Figure 40 b). XRD evidences the presence of crystalline tetragonal SnO_2 of cassiterite-type structure.^[121] The crystallite size was calculated from the peak width of the powder diffraction pattern via Scherrer's formula (see Equation (9)). From the Bragg diffraction peaks (110), (101), and (211) an average crystallite size of 4 nm was obtained, which is not in agreement with particle size data obtained via DLS and SEM analysis. As the crystallite size is clearly smaller than the particle size, as-prepared $\text{SnO}_2:\text{Ta}$ particles might not to be single crystalline. Alternatively, the particle sizes obtained via DLS and SEM analysis correspond to small agglomerates of single crystalline particles.

4.1.3 Tin oxide

Subsequently, FTO with F:Sn molar ratios of 1 and 10 % were investigated. Via DLS, the particle size distribution of FTO suspensions was determined. Measurements were conducted of the reaction suspensions, as well as of suspensions where particles had been redispersed in DEG and EtOH. The particle size distributions of FTO (1 mol-%) suspensions are exhibited in Figure 41 and those of FTO (10 mol-%) are presented in Figure 42 a. The resulting mean hydrodynamic diameters are compiled in Table 7.

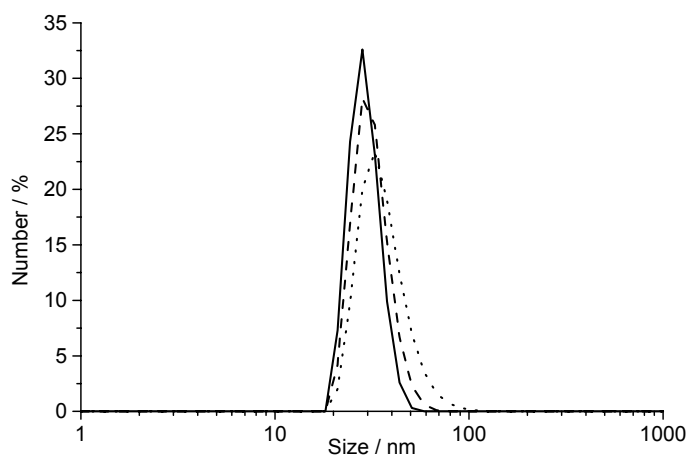


Figure 41. DLS measurement of particle size distribution of FTO (1 mol-%): reaction suspension (solid), redispersed in DEG (dashed), and redispersed in EtOH (dotted).

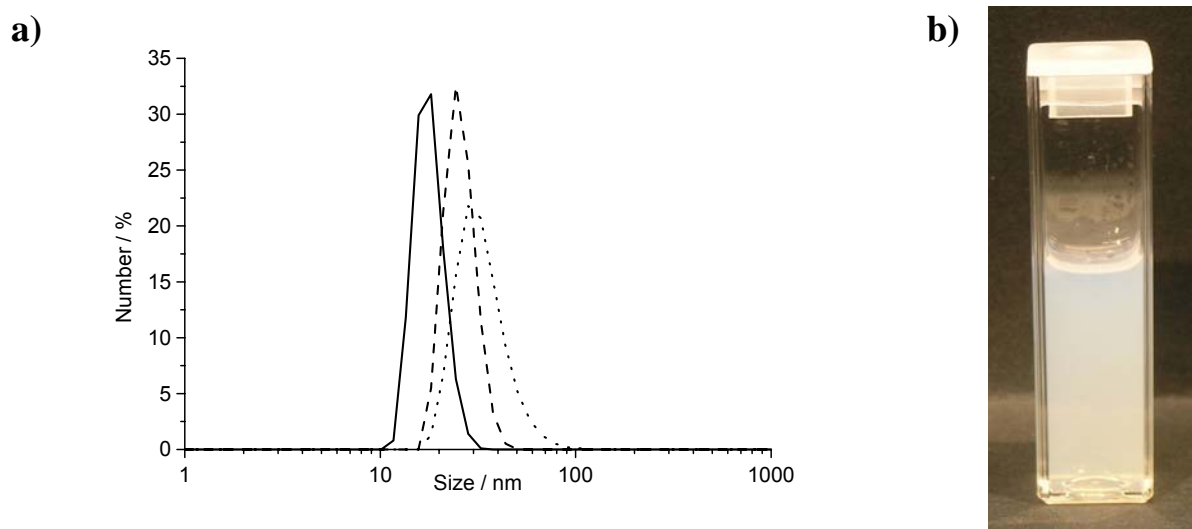


Figure 42. a) DLS measurement of particle size distribution of FTO (10 mol-%): reaction suspension (solid), redispersed in DEG (dashed), and redispersed in EtOH (dotted) and b) photograph of FTO (10 mol-%) suspension in DEG (solids content: 1 wt-%).

Table 7. Mean particle diameters of as-prepared FTO (1 mol-%) and FTO (10 mol-%) suspensions measured via dynamic light scattering.

	reaction suspension	redispersed in DEG	redispersed in EtOH
FTO (1 mol-%)	29 nm	32 nm	36 nm
FTO (10 mol-%)	18 nm	26 nm	34 nm

The mean particle diameters of the reaction suspensions were measured to 29 nm for FTO (1 mol-%) and 18 nm for FTO (10 mol-%). Thus, the particle size of the FTO (1 mol-%) reaction suspension is almost the double of the diameter obtained for FTO (10 mol-%), indicating that a higher introduced concentration of F^- dopants leads to a smaller particle size, or alternatively, a smaller agglomerate size. Samples redispersed in DEG exhibit slightly larger diameters than the reaction suspensions and, in turn, the measured particle sizes of samples redispersed in EtOH are slightly larger than those of samples redispersed in DEG. FTO (1 mol-%) and FTO (10 mol-%) exhibit similar mean diameters – of less than 40 nm – when redispersed in ethanol. It is noteworthy that samples redispersed in EtOH exhibit such small particle sizes without the addition of any surface stabilizer. Thus, the redispersibility of as-prepared $SnO_2:F$ in ethanol is very good.

In addition, as-prepared FTO samples are studied via scanning electron microscopy. In order to directly compare SEM and DLS data of samples redispersed in ethanol, SEM samples were prepared from ethanolic suspensions. Characteristic SEM images of as-prepared FTO particles with introduced F:Sn molar ratios of 1 % and 10 % are presented in Figure 43.

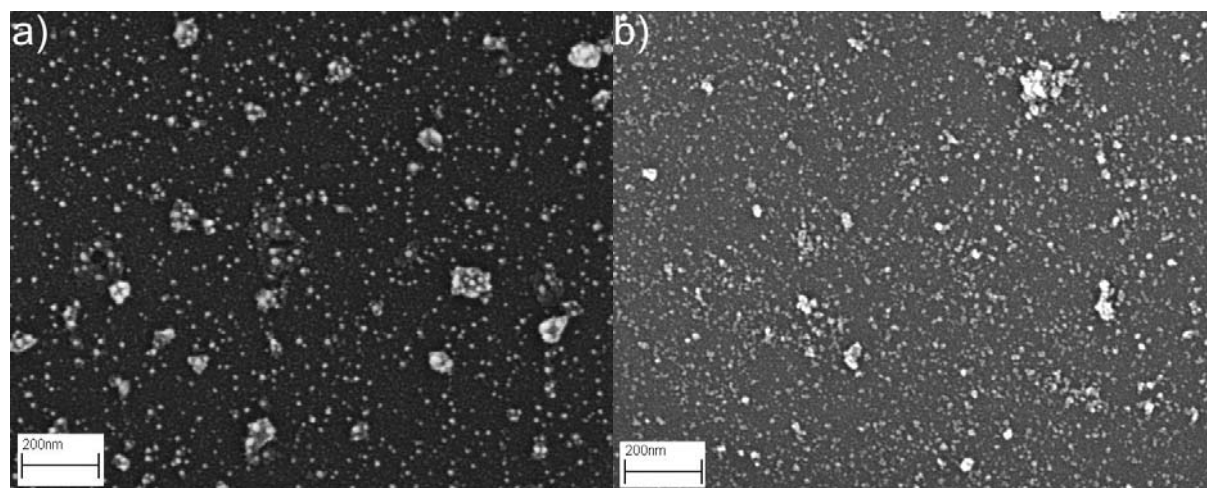


Figure 43. SEM images of as-prepared a) FTO (1 mol-%) and b) FTO (10 mol-%) redispersed in ethanol.

According to SEM analysis (Figure 43), as-prepared FTO particles redispersed in ethanol have a spherical and very uniform morphology. Some aggregates are also observable, which however, are smaller than 100 nm in size. SEM images of as-prepared FTO with F:Sn molar ratios of 1 % and 10 % were used for statistical evaluation of the particle diameter. Calculations were based on more than 1500 particles per sample. The resulting mean diameter of as-prepared FTO (1 mol-%) was calculated to 15 nm and that of FTO (10 mol-%) was determined to 12 nm. Thus, according to SEM analysis, the particle sizes of the two FTO samples are very similar.

Comparing the results of SEM analysis with DLS data for samples redispersed in ethanol, SEM analysis give rise to much smaller particle sizes for both samples. A reason for this could be that primary particles have formed loose aggregates in the liquid phase, which are then separated when the suspension is applied on heated SEM sample carriers. In addition, the method of dynamic light scattering cannot correctly differentiate particle sizes of too similar values into separate peaks. Comparing DLS data of DEG reaction suspensions with the data obtained from SEM analysis, there is good agreement for the FTO (10 mol-%) sample, especially when considering that DLS measures an enlarged hydrodynamic diameter. However, DLS measurements of DEG reaction suspension of FTO (1 mol-%) resulted in a

mean diameter twice as large as the size obtained via SEM analysis. Thus, the FTO (1 mol-%) reaction suspension seems to contain more loose aggregates than the FTO (10 mol-%) reaction suspension.

Moreover, the crystallinity of as-prepared $\text{SnO}_2\text{:F}$ was evaluated via XRD and TEM. Powder diffraction patterns of as-prepared FTO samples with introduced doping concentrations of 1 mol-% and 10 mol-% were recorded and are presented in Figure 44.

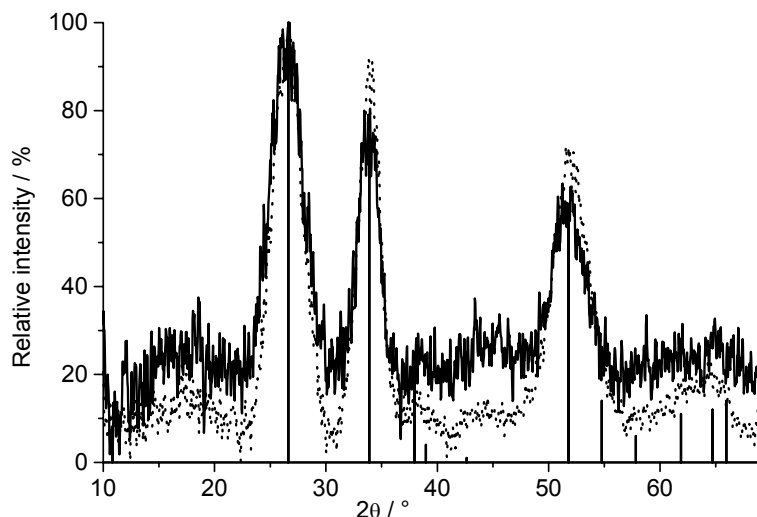


Figure 44. XRD patterns of as-prepared FTO (1 mol-%) (solid) and FTO (10 mol-%) (dotted) (reference: SnO_2 – ICCD No. 41-1445).

The powder diffraction patterns of as-prepared FTO (Figure 44) are very similar to that of as-prepared $\text{SnO}_2\text{:Ta}$ (Figure 40 b). Also here, crystalline SnO_2 of cassiterite-type structure^[121] was evidenced and calculations based on Scherrer's formula resulted in an average crystallite size of 4 nm. This implies that as-prepared powders are not single crystalline, or alternatively, that the particle sizes obtained via DLS and SEM analysis correspond to small agglomerates of single crystalline particles. In order to investigate which of these alternatives is valid, the crystallinity and size of as-prepared FTO (10 mol-%) samples were further investigated via transmission electron microscopy (Figure 45).

Characteristic TEM images of as-prepared FTO (10 mol-%) applied on lacey-film covered Cu grids exhibit agglomerated single crystalline areas 3-4 nm in size (Figure 45 a). This value is in good agreement with the crystallite size that was calculated via the peak width in XRD patterns. In addition, if particles on the edges of the carbon film are studied (Figure 45 b), it can be observed that no amorphous areas are present. Thus, it can be concluded that as-prepared $\text{SnO}_2\text{:F}$ particles are single crystalline. However, in the liquid phase, they are formed into small agglomerates. In SEM images, these agglomerates were visible as single, spherical particles because the primary particles are of approximately the same size as the resolution limit of the microscope.

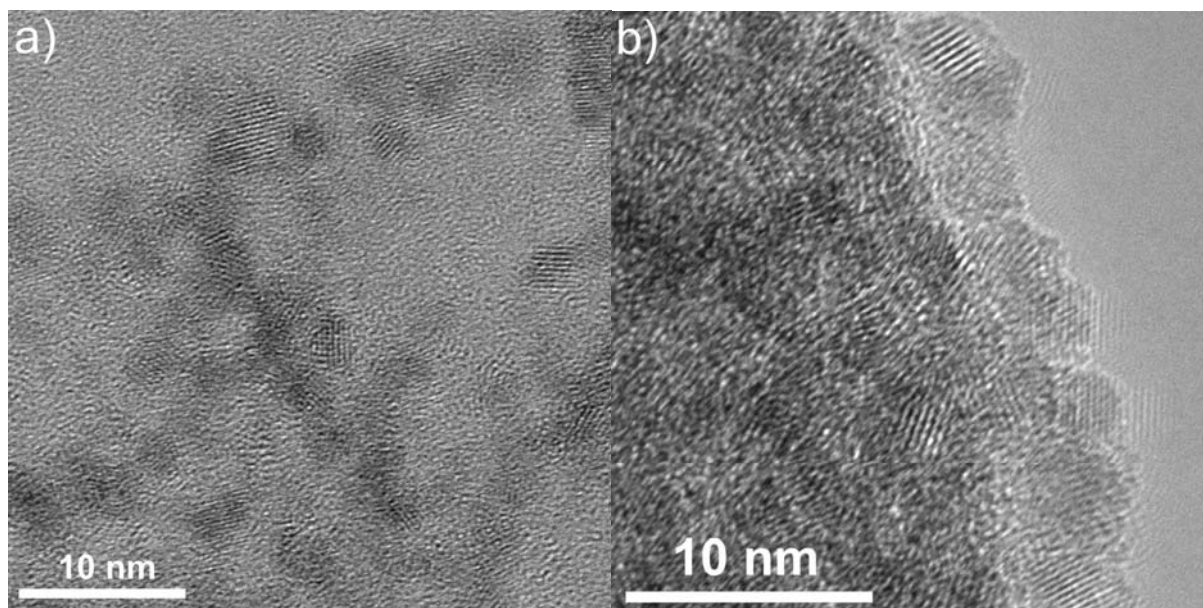


Figure 45. HRTEM images of as-prepared FTO (10 mol-%) in ethanol.

Furthermore, nitrogen absorption measurements of as-prepared FTO were performed according to the BET type of method. Here, specific surface areas of 63 and 116 m^2g^{-1} were measured for $\text{SnO}_2\text{:F}$ with introduced doping concentrations of 1 mol-% and 10 mol-%, respectively. Assuming the presence of spherical and non-porous particles with a density of bulk SnO_2 (6.9 gcm^{-3}),^[45] the measured surface areas correspond to particle diameters of 14 nm for FTO (1 mol-%) and 7 nm for FTO (10 mol-%). Thus, the calculated size of as-prepared FTO (10 mol-%) particles are half the size of as-prepared FTO (1 mol-%). The same relationship between particle sizes was obtained via DLS analysis, which thus confirms the lower degree of agglomeration of FTO (10 mol-%).

Furthermore, DTA-TG analysis of an as-prepared FTO (5 mol-%) sample was carried out; the results are presented in Figure 46.

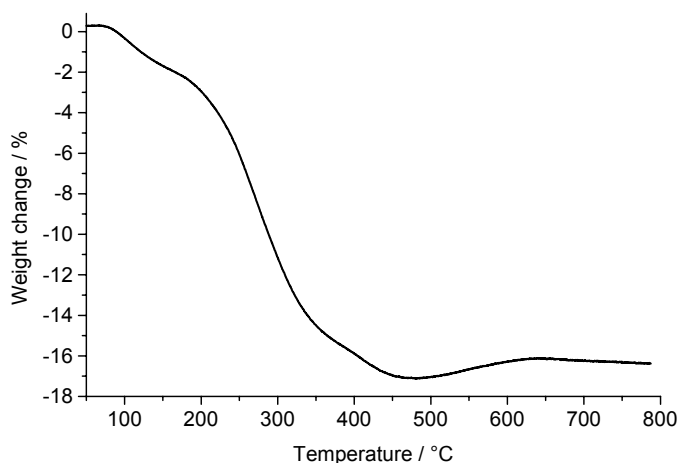


Figure 46. TG analysis of as-prepared FTO (5 mol-%).

To quantify the amount of diethylene glycol adhered on the particle surface, DTA-TG measurements were carried out. Thermogravimetry indicates a weight loss of 12.9 % between 200 and 400 °C for as-prepared FTO (Figure 46). According to previous studies, this weight

loss can be related to DEG adhered to the particle surface.^[28,87,88] The large amount of surface-bound DEG is in agreement with the excellent redispersibility of as-prepared samples in ethanol. Comparing the obtained weight loss of FTO with that gained for ZnO presented above (Figure 25), FTO samples lost more than twice as much weight. This is however expected for particles less than half the size, which have a higher surface area. Thus, more DEG is adhered to the FTO sample in total, which causes a larger weight loss while heating the sample.

Four-point probing of pellets of as-prepared powders was carried out in order to investigate the conductivity of as-prepared samples. Accordingly, as-prepared SnO₂:Ta as well as SnO₂:F samples exhibited no measurable conductivity at all. This is attributed to the large weight loss according to TG analysis and also the fact that as-prepared particles are not single crystalline.

In summary, SnO₂ nanocrystals doped with Ta⁵⁺ and F⁻ have been successfully prepared via microwave-assisted heating in a polyol medium. Primary particle size, degree of agglomeration, and crystallinity of as-prepared SnO₂:Ta and FTO samples were evaluated via DLS, SEM, XRD, TEM, and BET. SEM analysis resulted in mean particle diameters of 10-15 nm, whereby DLS data were in relatively good agreement. However, XRD and TEM analysis showed that primary particles are 3-4 nm in size. Thus, as prepared tin oxide samples are formed into small agglomerates. As-prepared FTO (1 mol-%) is about twice as agglomerated as FTO (10 mol-%) and SnO₂:Ta (7 mol-%). TG analysis showed that as-prepared particles are coated with large amounts of DEG, which is confirmed by an excellent redispersibility of as-prepared particles in DEG as well as ethanol. This is a probable reason for the low conductivity of as-prepared samples.

Aiming at conductive powders, as-prepared samples were thermally treated in order to, first, burn out DEG and other possible organic rests in air and second, to reestablish charge carriers by forming gas processing. Based on the results of thermogravimetry, as-prepared samples were heated in air at 500 °C for 2 h. Subsequently, powders were reduced with forming gas at 250 °C for 1 h. In order to study the effect of heating at higher temperatures, FTO samples were also heated in air at 800 °C for 0.5 h. The structural and morphological effects on FTO samples with introduced F:Sn molar ratios of 1% and 10 % due to this post-treatment were studied via XRD, SEM, and BET. In Figure 47, the powder patterns of post-treated FTO (1 mol-%) are presented as a representative example of the effect on crystallinity due to post-treatment of doped tin oxide samples.

According to X-ray powder diffraction, post-treated samples all consist of cassiterite-type SnO₂ (Figure 47).^[121] All samples are phase pure and there are thus no traces of e.g. elemental tin originating from the reduction in forming gas. Also here, calculations of crystallite size based on Scherrer's formula were carried out. The average crystallite size of powders treated in air (500 °C, 2 h) was calculated to 11 nm for FTO (1 mol-%); for FTO (10 mol-%) it amounts to 10 nm. Thus, the crystallite size has significantly increased compared to as-prepared samples, which indicates that sintering has taken place at 500 °C, although the melting point for bulk tin oxide is 1630 °C.^[45] Sintering at temperatures considerably lower than the melting point was also observed for zinc oxide (see section 4.1.2) and is a well-known effect for nanoparticles.^[113] The smaller size of tin oxide particle in comparison to zinc oxide particles results in a higher reactivity, and thus sintering at even lower temperatures can be expected.^[113] Notably, the crystallite sizes obtained subsequent to heating in air (500 °C, 2 h) are in good agreement with the agglomerate sizes attained via SEM analysis for as-prepared samples. Thus, these agglomerates appear to have become single crystalline. The calculated crystallite sizes of further post-treated FTO samples are shown in

Table 8. As expected, processing in forming gas (250 °C, 1 h) has no effect on the crystallite size. On the other hand, samples treated at higher temperatures in air (800 °C, 0.5 h) exhibit crystallite sizes of 21 and 19 nm, implying that further sintering of the particles has taken place.

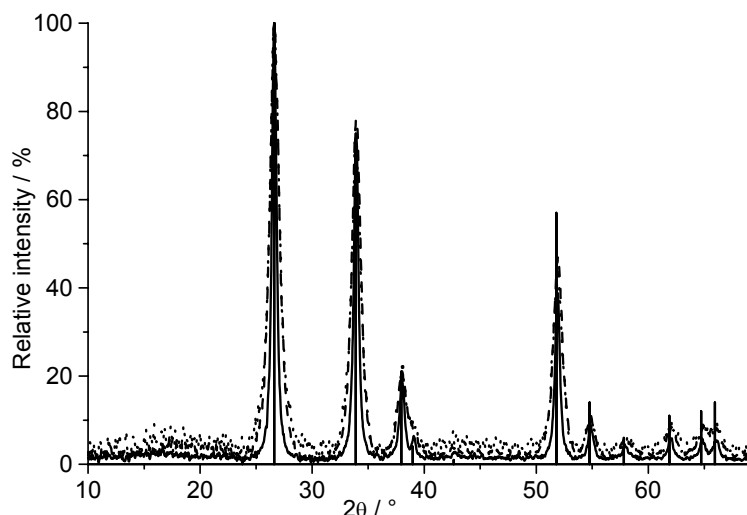


Figure 47. XRD patterns of post-treated FTO (1 mol-%) processed in air (500 °C, dashed), in air (500 °C) and forming gas (250 °C, dotted), and in air (800 °C, solid).

Furthermore, scanning electron microscopy was applied to investigate post-treated powder samples redispersed in ethanol with ultrasound. As representative examples, characteristic SEM images of post-treated FTO (1 mol-%) samples – one sample treated in air (500 °C, 2 h) and forming gas (250 °C, 1 h) and one sample as treated at a higher temperature in air (800 °C, 0.5 h) – are shown in Figure 48.

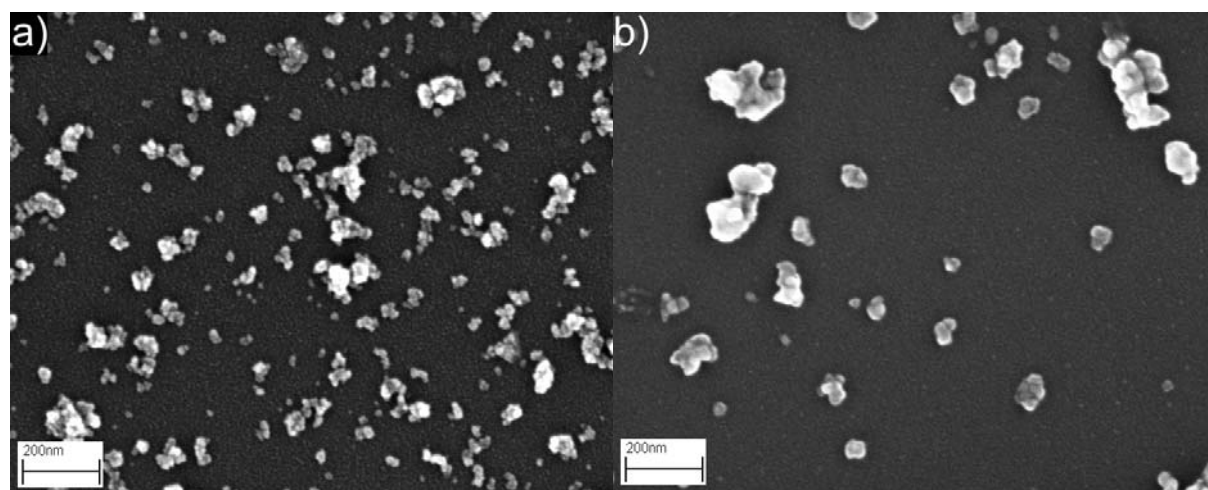


Figure 48. SEM images of FTO (1 mol-%) processed in a) air 500 °C and forming gas 250 °C and b) air 800 °C; powders redispersed in ethanol.

4.1.3 Tin oxide

Table 8. Mean diameters of as-prepared and post-treated FTO (1 mol-%) and FTO (10 mol-%) samples deduced via SEM, XRD, and BET analysis.

Sample		SEM	XRD	BET
FTO (1 mol-%)	as-prepared	15 nm	4 nm	14 nm
FTO (1 mol-%)	air (500 °C, 2 h)	51 nm	11 nm	25 nm
FTO (1 mol-%)	air (500 °C, 2 h) + forming gas (250 °C, 1 h)	59 nm	11 nm	25 nm
FTO (1 mol-%)	air (800 °C, 0.5 h)	64 nm	21 nm	74 nm
FTO (10 mol-%)	as-prepared	12 nm	4 nm	7 nm
FTO (10 mol-%)	air (500 °C, 2 h)	85 nm	10 nm	21 nm
FTO (10 mol-%)	air (500 °C, 2 h) + forming gas (250 °C, 1 h)	87 nm	9 nm	22 nm
FTO (10 mol-%)	air (800 °C, 0.5 h)	85 nm	19 nm	58 nm

According to SEM analysis, samples treated in air (500 °C, 2 h) and forming gas (250 °C, 1 h) exhibit particles/agglomerates 10-20 nm in size as well as many slightly larger aggregates (Figure 48 a). The smallest particles are of the same sizes as the agglomerates visible in SEM images of as-prepared samples, which now have become sintered. Samples treated at higher temperatures in air (800 °C, 0.5 h) show aggregates of about the same size as particles treated at 500 °C, but with less internal structure (Figure 48 b). Statistic evaluation of particle diameters based on SEM images of post-treated samples was conducted: the results are compiled in Table 8. Calculations were based on more than 200 particles per post-treated sample. Here, it is seen that the sizes obtained via SEM analysis of post-treated samples are clearly larger than those obtained for as-prepared samples. However, subsequent to processing at 500 °C in air, the sizes do not change much after further post-treatment. BET analysis (Table 8) of post-treated particles show that samples heated in air at 500 °C are porous, since the particle sizes corresponding to the measured surface areas are much smaller than the aggregate size obtained via SEM analysis. Calculations based on BET measurements of samples treated at higher temperatures (800 °C, 0.5 h) resulted in particle sizes of similar values as the aggregates observed in SEM images. This confirms the presence of dense agglomerates, which however, are only partially sintered as crystallite size obtained via XRD analysis are much smaller than the aggregate size. Finally, it can be noted that the aggregate sizes determined via SEM and BET does not exceed 100 nm for any sample at any investigated temperature.

Moreover, the electrical conductivities of post-treated samples were evaluated. To this concern, four-point probing of pellets of SnO₂:Ta and FTO samples treated in air (500 °C, 2 h) and forming gas (250 °C, 1 h) was conducted. As a reference, undoped SnO₂ synthesized and post-treated the same way was also investigated. The resulting sheet resistances and specific resistivities are compiled in Table 9.

Table 9. Resistance and resistivity of post-treated doped and undoped tin oxide samples according to four-point probing measurements.

	SnO₂:Ta (7 mol-%)	FTO (1 mol-%)	FTO (10 mol-%)	SnO₂
sheet resistance	100 Ω□	60 Ω□	13 Ω□	700 Ω□
resistivity	1.5 · 10 ⁰ Ωcm	8.8 · 10 ⁻¹ Ωcm	1.9 · 10 ⁻¹ Ωcm	1.4 · 10 ¹ Ω

According to four-point probing, all doped tin oxide samples exhibit low resistivities. Comparing doped and undoped SnO₂, there is a clear reduction of the resistivity for doped samples. Thus, introduction of dopants has caused a significantly improved conductivity, which implies that introduced dopants are, in fact, incorporated in the SnO₂ lattice. In addition, FTO samples show a lower resistivity for samples doped with 10 mol-% F⁻ compared to samples doped with 1 mol-% F⁻. Thus, introduction of a higher dopant concentration is evidenced to be beneficial with respect to the conductivity of FTO samples. This is in contrast to previously studies AZO samples (see section 4.1.2), for which an increased resistivity was measured for samples with a higher introduced doping concentration.

However, as was observed for the doped ZnO samples presented above, the introduced and actually present doping concentrations can be rather different. To this concern, samples were investigated via EDX in order to determine the amount of dopants present in synthesized tin oxide samples. EDX analysis resulted in an evidenced Ta:Sn molar ratio of 4 % for as-prepared as well as post-treated SnO₂:Ta (7 mol-%) samples. Thus, Ta dopants were evidenced to be present in SnO₂:Ta samples in about the same amount as introduced in synthesis. However, as was revealed via solid state NMR investigations of AZO particles, the presence of dopants in the synthesized particles does not necessarily mean that they are inserted in the crystal host lattice. EDX analysis of FTO samples resulted in F:Sn molar ratios of around 10 mol-% for both samples. Thus, the presence of F⁻ ions in FTO samples could be verified via EDX. However, the accuracy of EDX is relatively low, especially for light elements. For a more accurate determination of the amount of fluorine present in FTO, quantitative analysis was carried out. Quantitative analysis was carried out by Mikroanalytisches Labor Pascher, Remagen, Germany. A comparison of the F:Sn molar ratios introduced during synthesis and evidenced via quantitative analysis is presented in Table 10.

Table 10. F:Sn molar ratios of FTO samples treated in air and forming gas: introduced and evidenced via quantitative analysis.

introduced	quantitative analysis
1 %	0.4 %
10 %	1.2 %

Thus, quantitative analysis clearly shows the presence of fluorine in FTO samples. However, only a fraction of the amount of dopants introduced during synthesis is actually also present in the samples. In addition, analogous to the results of quantitative analysis of AZO samples, it is seen that if a higher doping concentration is introduced, the difference between introduced and evidenced concentrations becomes larger.

Comparing the resistivities of FTO samples with literature data, the resistivity of the FTO (1 mol-%) sample is similar to reported resistivity values measured on powders synthesized via the sol-gel method,^[116,117] while, on the other hand, the resistivity of the FTO (10 mol-%) sample is clearly lower than that of sol-gel synthesized powders.^[116,117] and almost as high as a sol-gel film prepared by Biswas *et al.*^[119] Thus, considering a liquid-phase synthesis of FTO nanoparticles, the polyol method offers an advantage over the sol-gel method with respect to conductivity. In addition, the sol-gel powders were prepared using metal-organic compounds as precursors, whereas the presented polyol synthesis applies simple salts as precursors, which adds another benefit of the polyol method in comparison to the sol-gel method.

If the resistivity of post-treated, undoped SnO₂ (Table 9) is compared with the resistivity of post-treated, undoped ZnO presented above, undoped SnO₂ exhibits a relatively low resistivity, whereas the resistivity of undoped ZnO was not even measurable. This difference is not expected to originate from the presence of elemental tin, because no diffraction peaks for Sn were observable in powder diffraction patterns (Figure 47) and elemental metals are normally highly crystalline.

Hence, the effects of post-treatment and introduced doping concentration on doped SnO₂ samples have been studied via SEM, XRD, BET, four-point probing, EDX, and quantitative analysis. According to SEM, the primary particle size does not change as an effect of post-treatment at 500 °C. However, aggregate sizes of post-treated samples are larger than those of as-prepared samples. According to XRD measurements, the crystallite sizes of samples treated at 500 °C are larger than those of as-prepared particles and of similar size as primary particles observed in SEM images. Thus, it is concluded that particles treated at 500 °C are single crystalline. Four-point probing of samples treated in air (500 °C, 2 h) and forming gas (250 °C, 1 h) resulted in relatively low resistivities for all samples. Comparing the resistivities of doped and undoped SnO₂, introduction of dopants resulted in a significantly improved conductivity. In addition, an increased doping concentration in FTO samples was evidenced to improve the conductivity. Quantitative analysis showed that only a fraction of the introduced doping concentration during synthesis is also present in the powder samples. Samples treated in air at 800 °C were partially sintered but exhibited the same aggregate sizes as other samples.

In order to study the local structure of as-prepared and post-treated SnO₂:F samples, Mössbauer and NMR spectroscopy were applied.^[122] First, a Mössbauer spectrum of FTO (10 mol-%) treated in air (500 °C, 2 h) and forming gas (250 °C, 1 h) was recorded in order to study the valency and bonding character of tin present in the sample (Figure 49).

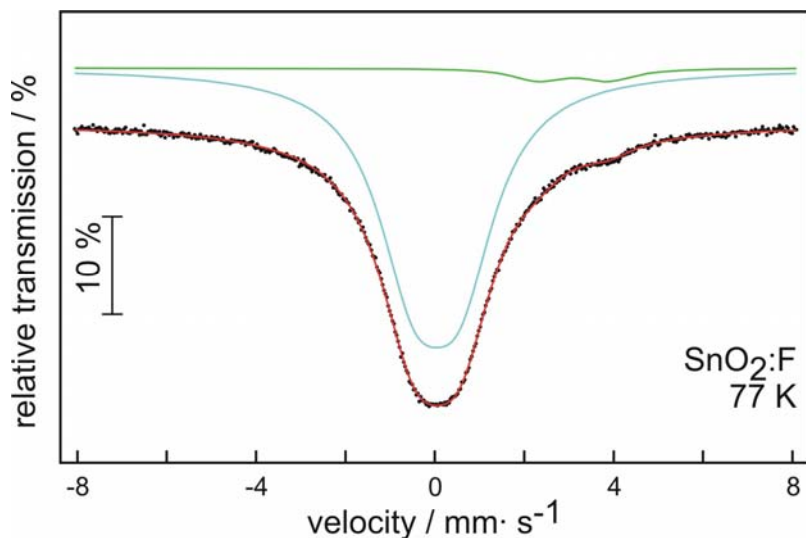


Figure 49. Experimental and simulated ¹¹⁹Sn Mössbauer spectra of FTO (10 mol-%) processed in air (500 °C, 2 h) and forming gas (250 °C, 1 h).

In Figure 49, the measured ¹¹⁹Sn Mössbauer spectrum is presented together with transmission integral fits. The spectrum is composed of one main component at an isomer shift of $\delta = 0.04(2)$ mm/s and an experimental line width of $\Gamma = 1.97(8)$ mm/s, subject to quadrupole splitting of $\Delta E_Q = 1.01(4)$ mm/s. This signal contributes to 95.6(2) % to the total intensity of the Mössbauer spectrum. The shoulder at higher velocity accounts for the second signal at an

area of 4.4(2) %. The latter signal has an isomer shift of $\delta = 3.09(2)$ mm/s, and experimental line width of 1.36(7) mm/s and a quadrupole splitting parameter of $\Delta E_Q = 1.58(3)$ mm/s.

The main contribution can certainly be ascribed to tetravalent tin of SnO₂, cassiterite, which itself has an isomer shift close to zero,^[123,124] similar to the stannate source used for the experiment. The slightly enhanced line width along with the quadrupole splitting parameter can be ascribed to the O / F disorder in the local Sn^{IV} environment. The isomer shift of the second spectroscopic contribution ($\delta = 3.09(2)$ mm/s) is far away from the isomer shift of divalent tin fluoride SnF₂ ($\delta \approx 3.5$ mm/s)^[125,126] and SnO (2.7 mm/s).^[123,124] From this it can be concluded that there is a divalent tin species with a mixed oxygen / fluorine coordination within the sample. These findings are in excellent agreement with the ¹¹⁹Sn Mössbauer spectra obtained for reaction products of partial oxidation of SnF₂ in air ($\delta = 3.11$ -3.15 mm/s for the Sn^{II}, O/F site)^[127] and for the oxide fluoride Sn₂O₂F₂ ($\delta = 3.07$ for Sn1 and 3.12 mm/s for Sn2).^[128] Based on the course of the isomer shift, similar to the comparison made by Fournès *et al.*^[128] for Sn₂O₂F₂ (based on an empirical approach),^[129,130] a significant *p*-character of the Sn-(O/F) bonds can be concluded.

Thus, Mössbauer spectroscopy confirms that fluorine has indeed been incorporated in the SnO₂ lattice of investigated FTO particles. No trace of Sn of zero valency was observable, confirming the results of powder diffraction analysis. However, although the main part of tin present in the sample was tetravalent, significant amounts of divalent tin were evidenced. Mössbauer studies of SnO₂:F powder prepared via sol-gel synthesis did not show any presence of divalent tin.^[116,117] However, these samples were only heated in air, thus this was not unexpected. The presence of divalent tin could be an important factor causing the relatively low resistivity of undoped SnO₂ and could, logically, also have an effect of the resistivity of doped tin oxide samples. Other effects of the presence in divalent tin in FTO samples remain to be investigated. In addition, it is not certain what effect the described post-treatment will have on thin layers.

Interestingly, treatment of FTO thin films deposited via spray pyrolysis in forming gas atmosphere has been reported to result in a significant increase of the film resistivity in comparison to as-deposited films.^[131] Here, processing in forming gas was performed at 830 °C. On the other hand, Jagadish *et al.* treated spray pyrolyzed FTO films in hydrogen atmosphere at temperatures between 200 and 400 °C and found that the resistivity increased with increasing temperature.^[132] Thus, processing in forming gas at moderate temperatures as described in this study appears to be an excellent option for the preparation of conductive SnO₂:F.

Finally, solid state NMR spectroscopy of FTO samples with introduced F:Sn molar ratios of 1% and 10 % was carried out. According to one-dimensional ¹¹⁹Sn NMR measurements of as-prepared FTO (10 mol-%), a single peak with an isotropic chemical shift $\delta = -604.7$ ppm can be observed (Figure 50). This value is in good agreement with earlier results of Sn^{IV} in crystalline SnO₂.^[133] In contrast to Mössbauer spectroscopy, Sn^{II} cannot be directly evidenced via solid state NMR spectroscopy. This is, however, in accordance with the expectation, since divalent tin exhibits an extremely broad line width of the isotropic chemical shift.^[134] According to one-dimensional ¹⁹F NMR measurements of FTO (10 mol-%), a single peak with a chemical shift $\delta = -114.0$ ppm can be observed (Figure 51). Thus, the presence of F⁻ in the synthesized FTO (10 mol-%) sample could be confirmed via NMR measurements. The chemical shift of the ¹⁹F peak is close to previous results for SnF₂ (-110.4 ppm).^[115] Furthermore, ¹⁹F NMR measurements of as-prepared FTO (1 mol-%) were carried out. However, here the signal intensity was unfortunately too low and no peak could be observed, even though a spin-echo method was applied.

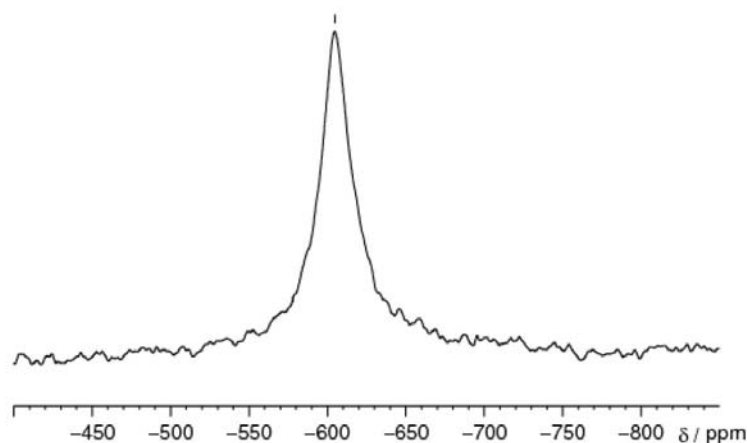


Figure 50. 1D ^{119}Sn NMR spectrum of as-prepared FTO (10 mol-%).

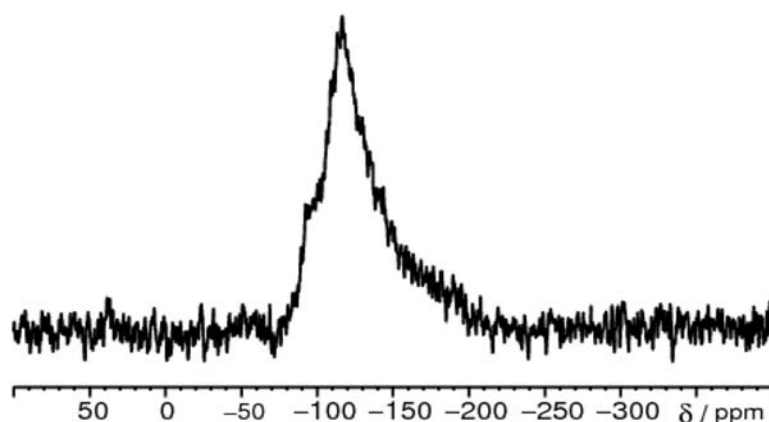


Figure 51. 1D ^{19}F NMR spectrum of as-prepared FTO (10 mol-%).

The coupling between the inserted dopant and the lattice can be studied in fluorine-doped tin oxide samples, since both F and Sn are sensitive to NMR. In addition, the coupling to DEG can be studied via hydrogen coupling. This was done by means of cross polarization measurements of ^{119}Sn - ^{19}F and ^{119}Sn - ^1H , respectively, while applying varying contact times. ^{119}Sn - ^{19}F CP-MAS NMR measurements of as-prepared FTO (10 mol-%) resulted in two different peaks corresponding to two different Sn environments while applying varying contact times (Figure 52). Peak A appears at longer contact times and has a chemical shift of $\delta = -604.7$ ppm. This peak is assigned to Sn in an oxygen environment, i.e., in crystalline SnO_2 .^[133] The reason for this is that longer contact times correspond to longer Sn-F distances. Peak B with $\delta = -639.0$ ppm is thus assigned to Sn in a fluorine environment. Thus, insertion of fluorine in the tin oxide lattice of as-prepared FTO particles is again confirmed by NMR. On the other hand, ^{119}Sn - ^1H CP-MAS NMR measurements did not show any peak shift at different contact times. Thus, there is no coupling between Sn and H apart from at the particle surface, i.e., no hydrogen is present inside the FTO particles. Hence, as opposed to AZO samples, the investigated FTO particles are assumed not to exhibit a structure consisting of a crystalline core and an amorphous shell, but rather a single crystalline structure doped with F⁻ ions. Considering these results, DEG is concluded to be present only on the particle surface.

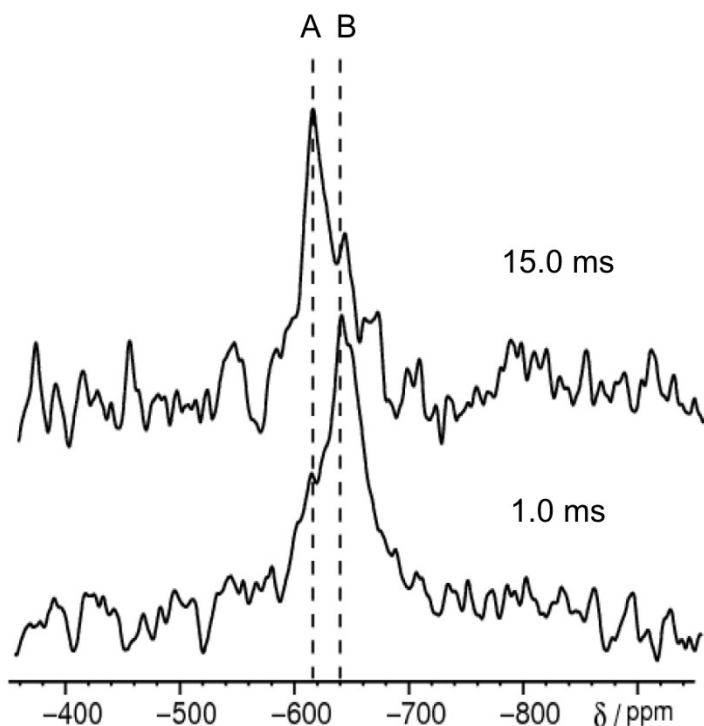


Figure 52. ^{119}Sn - ^{19}F CP-MAS NMR spectra of FTO (10 mol-%) measured with contact times 15.0 ms and 1.0 ms, respectively.

Furthermore, the issues of fluorine localization and charge balance to compensate the charge of fluorine ions were considered. In principle, several alternatives are possible:

- I) H^+ - F^- pairs inserted on interstitial sites.
- II) F^- inserted on O^{2-} sites and on interstitial sites.
- III) F^- inserted on interstitial sites; occurrence of O^{2-} vacancies.
- IV) F^- inserted on O^{2-} sites; O^{2-} inserted on interstitial sites.
- V) F^- inserted on O^{2-} sites; occurrence of Sn^{4+} vacancies.
- VI) F^- inserted on O^{2-} sites; Sn^{2+} on Sn^{4+} sites.

Alternative I) can be ruled out since ^1H - ^{119}Sn CP-MAS NMR measurements indicated that no hydrogen was inserted into the particles. If alternative II) is valid, at least two local fluorine environments must be present in the particles. However, one-dimensional ^{19}F NMR measurements of as-prepared FTO (10 mol-%) resulted in a single peak (Figure 51), which means that FTO particles exhibit only one type of local fluorine environment. Thus, the insertion of fluorine at oxygen vacancy sites and simultaneously at interstitial sites (alternative II) can also be excluded. Alternative III) can be disproved via REDOR experiments. According to ^{119}Sn - ^{19}F CP-REDOR NMR measurements, the distance of the ^{119}Sn - ^{19}F dipole-dipole interaction is in accordance with the Sn-O bond distance of 205.2 pm in SnO_2 .^[135] Thus, it can be concluded that fluorine is inserted on oxygen sites and that there is no occurrence of F^- as an interstitial, which suggests that one of the alternatives IV-VI must be valid. If alternative IV would apply, there should be at least two different oxygen positions, which would create different local environment for fluorine as well as for tin. Since 1D ^{119}Sn and ^{19}F NMR measurements both result in a single peak, there is no evidence for the occurrence of oxygen as an interstitial. In addition to one-dimensional spectra, two-

dimensional ^{19}F exchange spectra were recorded in order to study the coupling between fluorine ions (Figure 53).

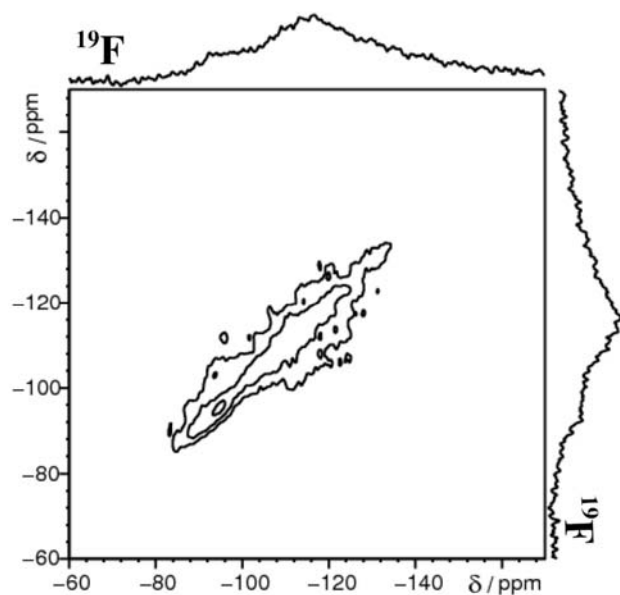


Figure 53. 2D ^{19}F exchange NMR spectrum of as-prepared FTO (10 mol-%) measured with mixing time 100 ms.

Due to the lack of off-diagonal peaks in the exchange spectrum, it can be concluded that there is no dipolar exchange between F^- ions. Firstly, this confirms the results of one-dimensional ^{119}Sn NMR measurements from which it was concluded that there is only one type of local fluorine environment present. The reason for this is that if fluorine is present at O^{2-} sites as well as at interstitials, a dipolar exchange is expected due to the attraction of defect and interstitial sites caused by coulomb interaction. Furthermore, if alternative V) is valid, i.e. if the extra charge from F^- is balanced by the existence of Sn^{4+} vacancies, there would also be dipolar exchange between F^- ions since they would become directly connected around the Sn^{4+} vacancy sites. Thus, the remaining possibility is that the extra charge generated by insertion of F^- on O^{2-} sites is balanced by Sn^{2+} on Sn^{4+} sites. Hence, although divalent tin as stated earlier cannot be directly observed via NMR, alternative VI) is the most likely alternative for creation of charge balance. The results of solid state NMR spectroscopy of FTO particles are consistent with a model of single crystalline SnO_2 particles in which F^- ions are inserted on oxygen sites and a partial reduction of some Sn^{4+} ions to Sn^{2+} has taken place.

Mössbauer measurements clearly evidenced the presence of divalent tin in the FTO (10 mol-%) sample processed in air (500 °C, 2 h) and forming gas (250 °C, 1 h). NMR measurements were also carried out on post-treated FTO samples; however, the signal intensities in ^{19}F NMR were unfortunately too low and no peaks could be observed with the application of a spin-echo method. It is still interesting to compare the amount of fluorine evidenced by quantitative analysis (1.2 mol-%) with the amount of divalent tin (4.4 mol-%) quantified via Mössbauer analysis, which were measured on the same, reduced FTO (10 mol-%) sample. According to expectation, if the F:Sn molar ratio 1.24 %, only 0.62 % Sn^{II} is needed to compensate for the charge generated by insertion of fluorine. Thus, there is an excess of divalent tin in comparison with the expected amount due to charge balancing of fluorine ions. The difference in the results of the two analytic techniques is too large to be explained by measurement accuracy differences, although quantitative analysis is expected to be more accurate. Thus, the charge generated by the presence of divalent tin in

reduced samples must be balanced in an additional way, e.g. by occurrence of oxygen vacancies or insertion of H^+ ions during treatment in forming gas.

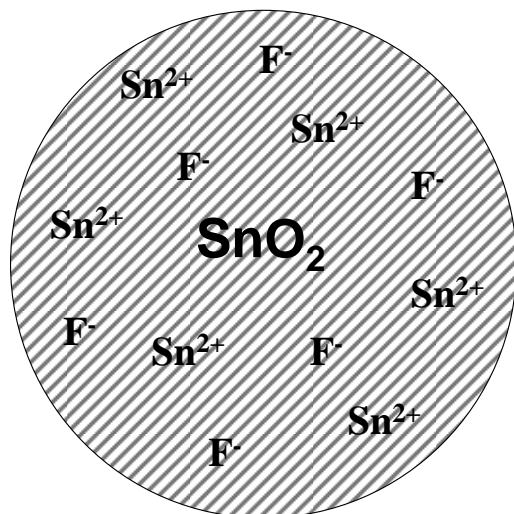


Figure 54. Model of FTO particles consisting of single crystalline SnO_2 in which F^- ions are inserted on oxygen sites and a partial reduction of some Sn^{4+} ions to Sn^{2+} has taken place.

Taking the results of solid state NMR spectroscopy into account, improved synthesis conditions can be considered. Since NMR measurements evidenced all fluorine ions to be inserted on oxygen sites in the SnO_2 host lattice, trying to insert a higher amount of dopants will certainly be worthwhile. This could be done by introducing a higher F:Sn molar ratio while applying the same precursors ($SnCl_4 \cdot 5 H_2O$ and $N(CH_3)_4F \cdot 4 H_2O$). However, as it was revealed that fluorine ions inserted on oxygen sites were located in a Sn^{II} environment, it is possible that application of a Sn^{II} -containing precursor such as SnF_2 would result in a higher inserted doping concentration.

In this work, solid state NMR spectroscopy was for the first time applied as an analytical tool for the investigation of TCO nanomaterials. Solid state NMR has proved to offer a unique understanding of the local structure of TCO nanoparticles, which is essential for improving the conductivity. Here, with the aid of solid state NMR spectroscopy, a model for FTO particles prepared via a microwave-assisted polyol process could be set up. In contrast to the model of AZO particles, the results of solid state NMR spectroscopy are consistent with single crystalline FTO particles without an amorphous shell. According to the model of FTO particles, all fluorine ions present in the particles are inserted on oxygen sites. In addition, a charge balance is created by Sn^{2+} at Sn^{4+} sites. From these findings, improved synthesis conditions such as higher introduced doping concentration and application of Sn^{II} -containing precursors can be considered. Comparing the amount of F^- evidenced by quantitative analysis with the amount of Sn^{II} resulting from Mössbauer spectroscopy of FTO (10 mol-%) processed in air (500 °C, 2 h) and forming gas (250 °C, 1 h), a larger amount of divalent tin than would be needed to balance the charge of F^- was found. Clearly, Mössbauer investigations of as-prepared FTO as well as of post-treated undoped SnO_2 are expected to bring more light on the issues of how the charge is balanced in as-prepared FTO and how the amount of divalent tin in FTO depends on the presence of fluorine dopants. In addition, the presence of oxygen vacancies could be studied via two-dimensional ^{119}Sn exchange spectra. Finally, it should be noted that further solid state measurements of FTO nanoparticles, as well as realization of optimized syntheses are in progress. However, this is beyond the scope of this work.

4.1.4 Cerium oxide

Gadolinium-doped cerium oxide is a well-known ionic conductor that e.g. can be applied as an electrolyte in solid oxide fuel cells (SOFC).^[136] In contrast to the previously presented transparent conductive oxides, CeO₂:Gd is a p-doped material. Liquid phase preparation of nanoscale ceria is often carried out in aqueous solutions.^[137-141] A common problem with water-based synthesis is the formation of poorly crystalline, agglomerated particles. The crystallinity of cerium oxide nanoparticles has however been improved by hydrothermal treatment^[137,141] as well as by the application of a semi-batch reactor.^[139] In addition, nanoscale crystalline CeO₂:Gd has recently been prepared in organic solvents.^[142] In these works, however, the particle size in the liquid phase was not determined.^[137-142]

Here, suspensions of gadolinium-doped cerium oxide particles were prepared in diethylene glycol (DEG) via microwave irradiation. In a typical recipe, 2.3 mmol Ce(NO₃)₃ · 6 H₂O and 0.23 mmol Gd(NO₃)₃ · 6 H₂O were dissolved in 50 ml DEG. The introduced Gd:Ce molar ratio was thus 10 %. At 80 °C, the solution was added to a solution of 50 ml DEG containing 4.6 mmol N(CH₃)₄OH · 5 H₂O and 2 ml deionized H₂O. Upon adding the solutions, no precipitation occurred. As the solutions were heated at 200 °C in a laboratory microwave oven (Ar atmosphere, magnetic stirring), precipitation was observed. To improve material crystallinity, the temperature was maintained for 10 min.

Subsequent to centrifugation and drying, as-prepared gadolinium-doped cerium oxide can be separated from the suspension and was yielded as an ochre colored powder in quantities of 55 %. The yield is thus considerably lower than the yield previously obtained for ITO and doped ZnO and SnO₂. The particle size and size distribution of as-prepared CeO₂:Gd suspensions were quantified by dynamic light scattering. According to DLS measurements, the average diameter of as-prepared gadolinium-doped cerium oxide particles in DEG amounts to 11(1) nm (Figure 55). As a consequence, CeO₂:Gd suspensions exhibit an almost monodisperse size distribution. Thereafter, scanning electron microscopy of diluted DEG suspensions was applied to obtain a direct view of as-prepared nanocrystals.

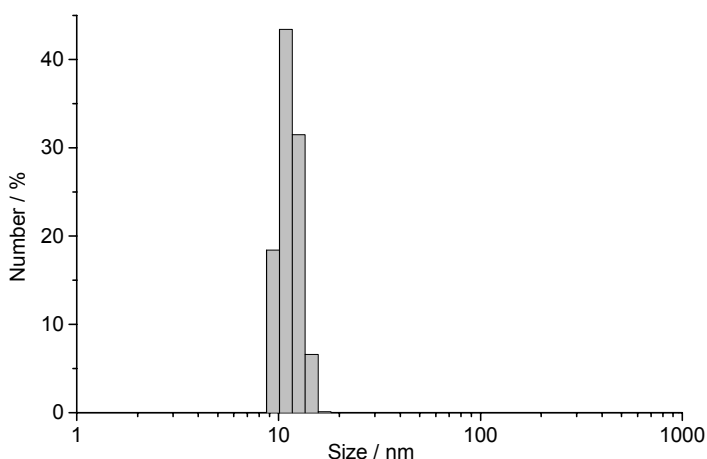


Figure 55. DLS measurement of particle size distribution of as-prepared CeO₂:Gd nanocrystals in DEG.

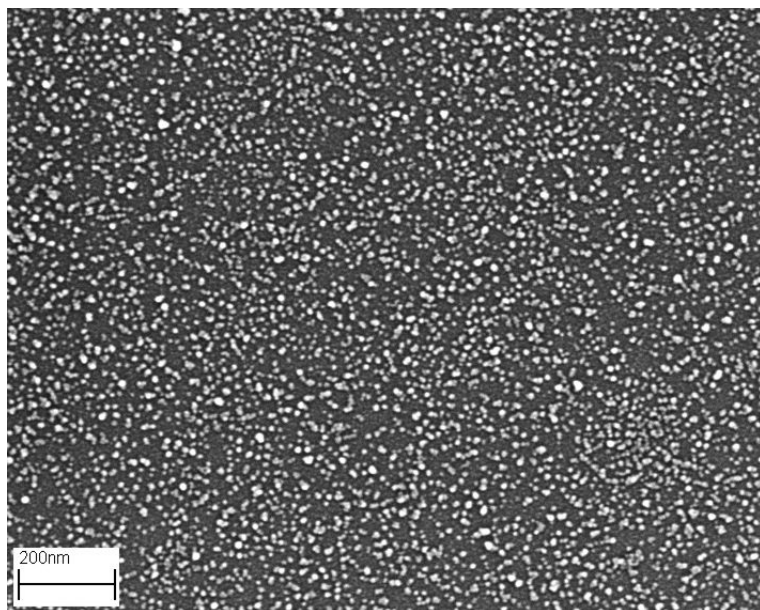


Figure 56. SEM image of as-prepared $\text{CeO}_2:\text{Gd}$ nanocrystals in DEG.

Characteristic SEM images reveal as-prepared $\text{CeO}_2:\text{Gd}$ particles to be practically non-agglomerated and of spherical and very uniform morphology (Figure 56). SEM images were also used for a statistical evaluation of particle diameter and size distribution. To this end, the mean diameter was deduced based on 6200 particles and amounts to 14(1) nm. This value is in good agreement with DLS analysis, especially considering the close arrangement of particles in the SEM sample. In addition, nitrogen absorption measurements of powder samples were performed according to the BET type of method. Herein, a specific surface of $88.1 \text{ m}^2\text{g}^{-1}$ was measured. Assuming spherical and non-porous gadolinium-doped cerium oxide particles with a density of bulk CeO_2 (7.7 gcm^{-3}),^[45] this value corresponds to a particle diameter of 9 nm, which is again in accordance with SEM and DLS analysis. Thus, due to the finely dispersed, non-agglomerated particles, it is expected that as-prepared suspensions can be applied to form homogeneous, compact layers. Moreover, the crystallinity of as-prepared $\text{CeO}_2:\text{Gd}$ was evidenced based on X-ray powder diffraction (Figure 57).

XRD evidences the presence of cubic CeO_2 , i.e. powder samples crystallize with a CaF_2 - type structure (Figure 57).^[143] Thus, oxidation of Ce^{III} present in the introduced precursor to Ce^{IV} present in the formed cerium oxide was successful. In addition, there are no visible peaks of other compounds such as e.g. gadolinium oxide, in the powder diffractogram of $\text{CeO}_2:\text{Gd}$. Thus, it can be concluded that the sample is phase pure. Via Scherrer's formula (see Equation (9)), powder diffraction patterns can also be used to calculate the crystallite size. From the three most intensive Bragg diffraction peaks – (111), (220), and (311) – an average crystallite size of 6 nm was obtained. This value is slightly lower than the particle sizes obtained via SEM, DLS, and BET analysis. However, the crystallite size is considered to be in sufficient agreement with other analytical tools, which implies that the particles are single crystalline.

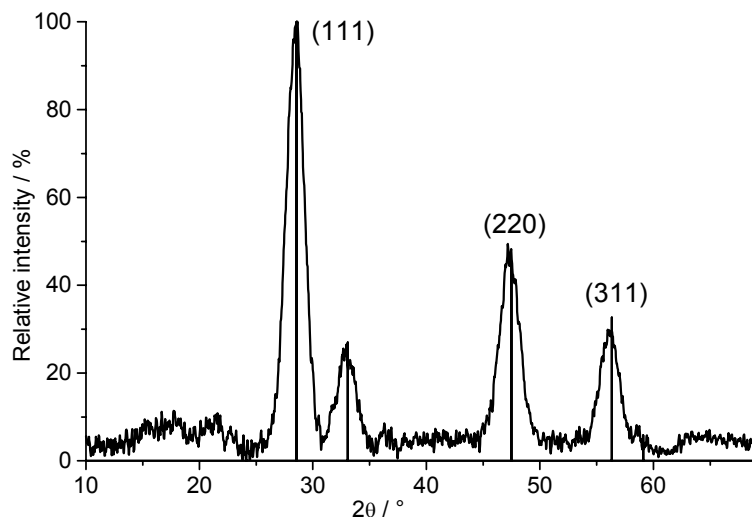


Figure 57. XRD pattern of as-prepared nanocrystalline $\text{CeO}_2:\text{Gd}$ (reference: CeO_2 – ICDD No. 1071-4199) with diffraction peaks (111), (220), and (311) denoted.

The particle sizes obtained via investigations based on DLS, SEM, BET, and XRD are summarized in Table 11. Here, it can be seen that the investigations of particles sizes based on several analytical tools result in a good agreement. Furthermore, the concentration of build-in gadolinium dopants in cerium oxide was studied via energy-dispersive X-ray analysis. In addition to the $\text{CeO}_2:\text{Gd}$ (10 mol-%) sample, a sample with an introduced Gd:Ce molar ratio of 2 % was also analyzed. A comparison between introduced and evidenced molar ratios is presented in Table 12.

Table 11. Comparison of particle sizes of as-prepared $\text{CeO}_2:\text{Gd}$ evidenced with various analytical tools.

DLS	SEM	BET	XRD
11 nm	14 nm	9 nm	6 nm

Table 12. Gd:Ce molar ratios of as-prepared gadolinium-doped cerium oxide samples: introduced and evidenced via EDX.

introduced	EDX
2 %	2.7 %
10 %	9.0 %

EDX investigations evidence gadolinium to be incorporated in the cerium oxide particles in about the same amounts as was introduced during synthesis. It is interesting to compare these results with the investigation of Al:Zn doping concentration in AZO samples (see section 4.1.2). For AZO samples in which the introduced doping concentration was higher than about 1 mol-%, the evidenced built-in concentration was significantly lower, whereas for $\text{CeO}_2:\text{Gd}$ samples, the introduced and incorporated doping concentrations are about the same for introduced Gd:Ce molar ratios as high as 10 %. The difference in evidenced doping concentrations in AZO and $\text{CeO}_2:\text{Gd}$ samples are too large to be explained by the relatively poor measurement accuracy of EDX. The higher amount of dopants present in $\text{CeO}_2:\text{Gd}$ can be explained in terms of ionic radii. Thus, the difference in radius between Ce^{4+} and Gd^{3+} ions

is relatively small (Table 13) whereas Zn^{2+} and Al^{3+} exhibit a large difference in ionic radii (Table 4).

Table 13. Radii of metal ions in doped CeO_2 .^[45]

ion	CN	radius
Ce^{4+}	8	0.97 Å
Gd^{3+}	8	1.05 Å

Hence, the similar size of Ce^{4+} and Gd^{3+} ions allows incorporation of large amounts of gadolinium in the cerium oxide lattice. The incorporation of Gd^{3+} in cerium oxide is known to initiate oxygen vacancies, which cause a high oxygen ion conductivity,^[136] but the ionic conductivity of prepared gadolinium-doped cerium oxide has not been investigated. The electrical conductivity was investigated via four-point probing, analogue to the previously presented n-doped transparent conductive oxides. Measurements were carried out on as-prepared samples, as well as samples treated in air (500 °C, 1 h) and in forming gas (500 °C, 2 h). However, none of the investigated samples showed any measurable electrical conductivity at all.

Thus, in summary, microwave-assisted polyol synthesis of gadolinium-doped cerium oxide resulted in nanoscale particles of around 10 nm in size according to dynamic light scattering, scanning electron microscopy, Brunauer-Emmett-Teller analysis, and X-ray powder diffraction. The various methods show good agreement regarding particle size. According to XRD measurements, as-prepared particles were crystalline. It is expected that as-prepared suspensions can be readily applied to form homogeneous compact layers due to the presence of non-agglomerated particles of small size. The incorporation of gadolinium in the cerium oxide particles was evidence via EDX and showed that the built-in Gd:Ce molar ratio was the same as the introduced ratio. However, no investigation of the ionic conductivity of the samples was carried out.

4.1.5 Lanthanum hydroxide

Lanthanum hydroxide is of interest e.g. due to its catalytic properties; $La(OH)_3$ has been used as support for metal catalysts such rhodium and platinum that are active for different reactions.^[144] Another application is as precursor for lanthanum-containing compounds. To this concern, nanoscale lanthanide oxysulfide (La_2O_2S), which is a phosphor, has been successfully prepared via a $La(OH)_3$ gel.^[145] However, in this work, neither particle size nor crystallinity of lanthanum hydroxide particles was investigated.^[145] Most works concerned with preparation of nanoscale crystalline $La(OH)_3$ have focused on nanowires and other relatively large structures.^[146-149] However, few works have evidenced synthesis of small nanoparticles consisting of crystalline lanthanum hydroxide. To this end, Djerdj *et al.* synthesized crystalline $La(OH)_3$ in the form of nanorods of different lengths via sol-gel synthesis while applying lanthanum alkoxide as precursor.

Here, suspensions of $La(OH)_3$ particles were prepared in diethylene glycol (DEG) via microwave irradiation. In a typical recipe, 2.3 mmol $La(NO_3)_3 \cdot 6 H_2O$ was dissolved in 50 ml DEG. At 80 °C, 5.75 ml of a 2 M aqueous NaOH solution was added, whereby precipitation of a colorless solid occurred. The suspensions were heated at 200 °C in a laboratory microwave oven (Ar atmosphere, magnetic stirring). To improve material crystallinity, the temperature was maintained for 30 min. Subsequent to centrifugation and drying, as-prepared lanthanum hydroxide can be separated from the suspension and was yielded as a white powder in quantities of 70 %. The yield is thus higher than the yield obtained for cerium

4.1.5 Lanthanum hydroxide

oxide but still lower than for ITO, ZnO, and SnO₂. The size and size distribution of as-prepared La(OH)₃ suspensions were quantified by dynamic light scattering. According to DLS measurements, the average diameter of as-prepared gadolinium-doped cerium oxide particles in DEG amounts to 26(1) nm (Figure 58). Thus, nanoscale particles with a near monodisperse size distribution have formed. In addition, scanning electron microscopy of diluted DEG suspensions was applied to obtain a direct view of as-prepared lanthanum hydroxide particles.

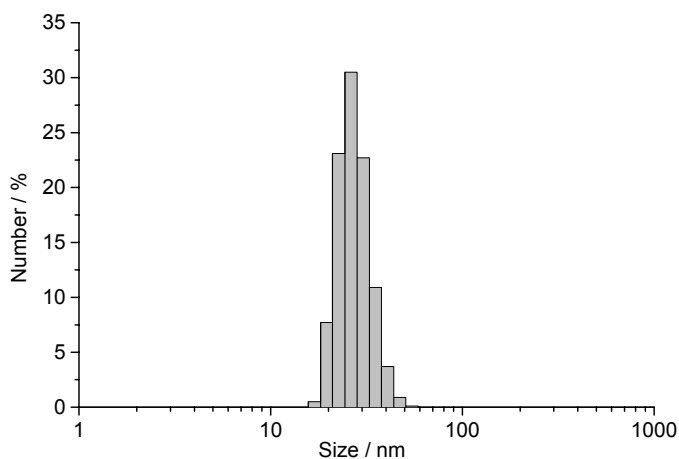


Figure 58. DLS measurement of particle size distribution of as-prepared La(OH)₃ nanocrystals in DEG.

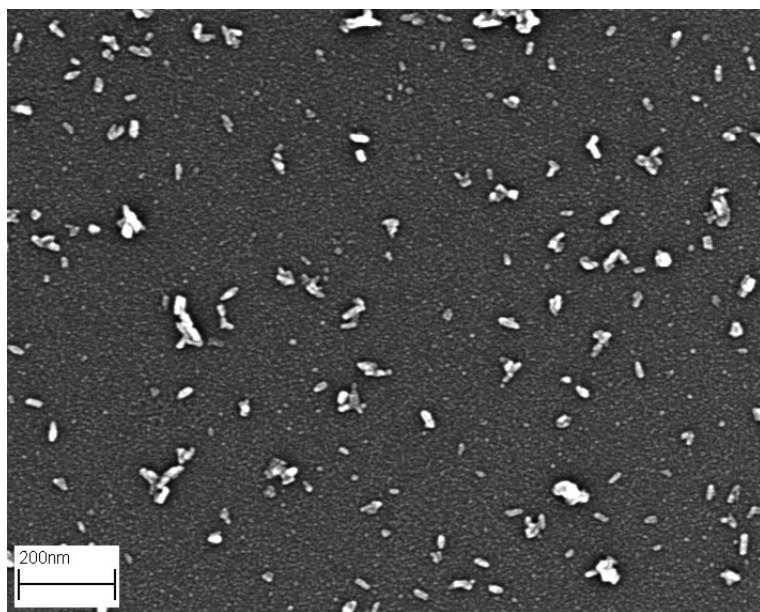


Figure 59. SEM image of as-prepared La(OH)₃ nanocrystals in DEG.

Characteristic SEM images exhibit as-prepared La(OH)₃ particles of uniform morphology formed into small aggregates (Figure 59). SEM images were also used for a statistical evaluation of particle diameter and size distribution. To this end, the mean diameter was deduced based on 730 particles and amounts to 22(1) nm. This value is in very good agreement with DLS analysis, considering an enlarged hydrodynamic diameter in the latter case. In addition, nitrogen absorption measurements of powder samples were performed

according to the BET type of method. Herein, a specific surface of $121.9 \text{ m}^2\text{g}^{-1}$ was measured. Assuming spherical and non-porous lanthanum hydroxide particles with a density of bulk $\text{La}(\text{OH})_3$ (4.4 gcm^{-3}),^[150] this value corresponds to a particle diameter of 11 nm, which is considerably smaller than the particle size obtained via DLS and SEM analysis. Thus, it is assumed that the particle sizes resulting from DLS and SEM analysis correspond to small agglomerates, or alternatively, that short nanorods have formed. Moreover, the crystallinity of as-prepared lanthanum hydroxide was investigated via X-ray powder diffraction (Figure 60).

XRD evidences the presence of hexagonal $\text{La}(\text{OH})_3$.^[150] There are no visible peaks of other compounds in the powder diffractogram. Thus, it can be concluded that the sample consists of phase pure lanthanum hydroxide. Via Scherrer's formula (see Equation (9)), powder diffraction patterns can also be used to calculate the crystallite size. From the two most intensive individually separable Bragg diffraction peaks – (100) and (201) – an average crystallite size of 7 nm was obtained. The estimated crystallite size is significantly smaller than the particle sizes obtained via SEM and DLS analysis, but agrees well with the results of BET analysis, from which it was concluded that either the sample contains small agglomerates, or short nanorods have been formed. It is expected that transmission electron microscopy could be applied in order to differentiate between these two cases.

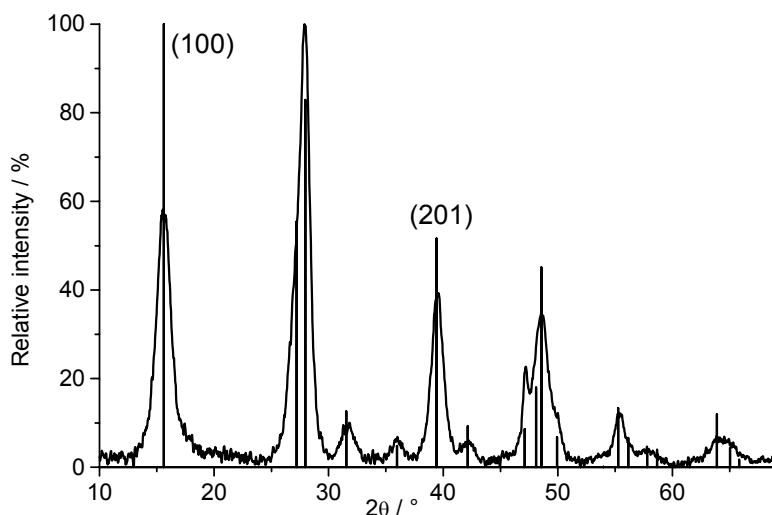


Figure 60. XRD pattern of as-prepared nanocrystalline $\text{La}(\text{OH})_3$ (reference: $\text{La}(\text{OH})_3$ – ICCD No. 83-2034 with diffraction peaks (100) and (201) denoted).

In summary, microwave-assisted polyol synthesis of lanthanum hydroxide resulted in crystalline, nanoscale particles while employing lanthanum nitrate as a precursor. The sample was investigated via dynamic light scattering, scanning electron microscopy, Brunauer-Emmett-Teller analysis, and X-ray powder diffraction. According to XRD measurements, as-prepared particles were crystalline. The various methods exhibit certain disagreement regarding particle size. According to DLS and SEM analysis, the particle diameter is around 25 nm, whereas BET and XRD analysis resulted in particle sizes of around 10 nm. Thus, the sample is either slightly agglomerated in the liquid phase, or alternatively, short nanorods have formed. TEM investigations are expected to determine the exact morphology of lanthanum hydroxide nanocrystals.

4.2 Ternary oxides

Binary oxides have been thoroughly studied considering their application as TCO materials. Aiming at entirely new TCO materials with improved conductivities, multicomponent oxide systems are being studied and are regarded as promising alternatives to ITO.^[3] To this concern, ternary and quaternary oxides containing at least one of the metals Zn, Cd, In, and Sn have exhibited high conductivities.^[3] With the intention to prepare low-cost, non-toxic TCO materials, the focus of the following studies is zinc-containing oxides. Thus, here the possibility of preparing nanoscale zinc-containing ternary oxides via microwave-assisted polyol synthesis will be investigated.

4.2.1 Zinc aluminium oxide

Liquid phase preparation of nanoscale zinc aluminium oxide has been carried out in microemulsions and with the sol-gel method.^[151-153] In these works, however, heating at temperatures between 400 and 800 °C was necessary in order to obtain crystalline ZnAl₂O₄ particles. To this end, Zawadzki prepared crystalline undoped ZnAl₂O₄ particles, 2.4 nm in size, while utilizing a microwave-assisted hydrothermal method.^[154] On the other hand, the electrical conductivity of as-prepared or post-treated ZnAl₂O₄ samples was not investigated in any of these works.^[151-154]

Here, suspensions of nanoscale ZnAl₂O₄ were prepared in diethylene glycol (DEG) via microwave irradiation. With the intention to achieve conductive materials, In³⁺, Sn⁴⁺ and Ti⁴⁺ dopants were introduced. The choice of dopants is motivated by the similarity in ionic radii (Table 14).

Table 14. Radii of metal ions in doped ZnAl₂O₄.^[45]

ion	CN	radius
Zn ²⁺	4	0.60 Å
In ³⁺	4	0.62 Å
Al ³⁺	6	0.54 Å
Sn ⁴⁺	6	0.69 Å
Ti ⁴⁺	6	0.61 Å

In a typical recipe, 1.0 mmol Zn(CH₃COO)₂ · 2 H₂O and 2.0 mmol AlCl₃ · 6 H₂O were dissolved in 25 ml DEG. The dopant precursors were introduced in amounts of 0.05 mmol (InCl₃ · 4 H₂O) and 0.10 mmol (SnCl₄ · 5 H₂O and Ti(OCH(CH₃)₂)₄) and were dissolved together with the previously prepared solution. At 80 °C, the solution was added to a solution of 25 ml DEG containing 10.0 mmol N(CH₃)₄OH · 5 H₂O and 1 ml deionized H₂O. Upon adding the solutions, precipitation of a colorless solid occurred. The suspensions were then heated at 200 °C in a laboratory microwave oven (Ar atmosphere, magnetic stirring) for 1 h, whereby the color did not change.

As-prepared samples were analyzed via dynamic light scattering, scanning electron microscopy, and X-ray powder diffraction. According to these analytical tools, ZnAl₂O₄:In, ZnAl₂O₄:Sn, and ZnAl₂O₄:Ti samples exhibit similar results regarding particle size and crystallinity, independent of the introduced dopant precursor. As a representative example, analytic data of ZnAl₂O₄:In are presented. First, particle size and size distribution of as-prepared suspensions were measured via DLS (Figure 61).

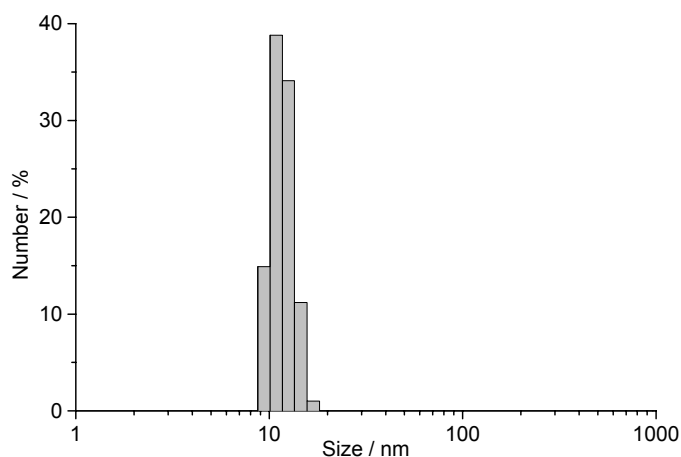


Figure 61. DLS measurement of particle size distribution of as-prepared $\text{ZnAl}_2\text{O}_4:\text{In}$ in DEG.

According to DLS analysis, the mean hydrodynamic diameter of $\text{ZnAl}_2\text{O}_4:\text{In}$ in DEG amounts to 10(1) nm (Figure 61). Thus, nanoscale particles with a near monodisperse particle size distribution have been formed. Furthermore, scanning electron microscopy of as-prepared suspensions diluted with DEG is applied in order to obtain a direct view of as-prepared nanoparticles (Figure 62).

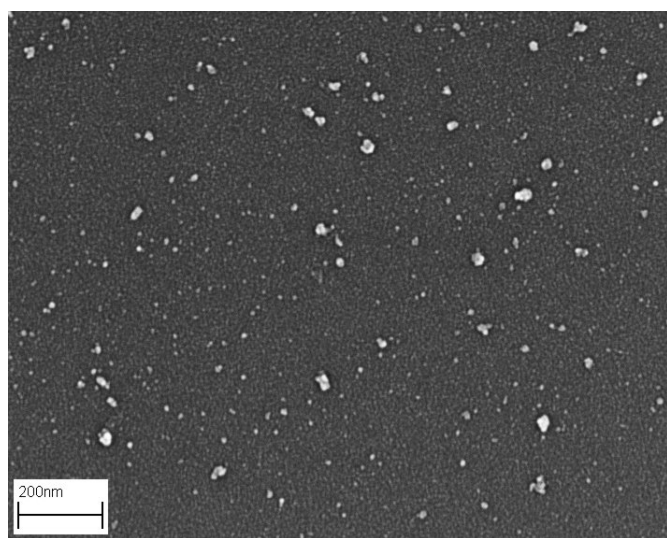


Figure 62. SEM image of as-prepared $\text{ZnAl}_2\text{O}_4:\text{In}$ in DEG.

Characteristic SEM images of as-prepared $\text{ZnAl}_2\text{O}_4:\text{In}$ show particles to be spherical and of uniform morphology (Figure 62). The sample contains primary particles, 10-15 nm in size, as well as small aggregates, all clearly below 100 nm in size. Thus, the primary particle size obtained via SEM analysis is in good agreement with the particle size obtained via DLS analysis.

The crystallinity of as-prepared zinc aluminium oxide powders, obtained via centrifugation and washing with ethanol, was evidenced via X-ray powder diffraction. According to XRD measurements, all as-prepared samples were amorphous. Thus, although microwave heating in DEG turned out to be advantageous concerning the crystallinity of binary oxides, it was not successful with regard to preparing crystalline zinc aluminium oxide. In order to obtain

crystalline materials, samples were post-treated in air at 600 °C for 1 h. Subsequent to post-treatment, powder patterns were again recorded via XRD (Figure 63).

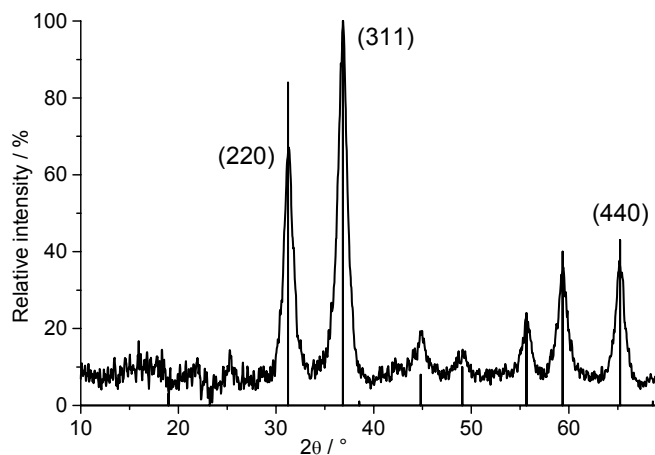


Figure 63. XRD pattern of $\text{ZnAl}_2\text{O}_4:\text{In}$ heated in air (600 °C, 1 h) (reference: ZnAl_2O_4 – ICDD No. 5-669) with diffraction peaks (220), (311), and (440) denoted.

XRD measurements evidence samples heated in air (600 °C, 1 h) to crystallize in the cubic gahnite-type spinel structure (Figure 63).^[155] Thus, the chosen post-treatment temperature and time were suitable for obtaining crystalline materials. There are no visible traces of other compounds, e.g. zinc oxide or aluminium oxide in the powder diffractogram. Thus, post-treated ZnAl_2O_4 powder samples are phase pure. In addition, the crystallite size was calculated from the peak width of the powder diffraction pattern via Scherrer's formula (see Equation (9)). From the three most intensive Bragg diffraction peaks – (220), (311), and (440) – an average crystallite size of 11 nm was obtained. Thus, the samples are still nanocrystalline, although a temperature as high as 600 °C was applied. The crystallite size obtained via XRD analysis is in good agreement with the particle size data obtained via DLS and SEM analysis. This implies that zinc aluminium oxide samples heated in air (600 °C, 1 h) consist of nanoscale, crystalline particles. To verify this view, scanning electron microscopy of post-treated ZnAl_2O_4 powders redispersed in ethanol via ultrasound without the addition of any surface stabilizers was conducted (Figure 64).

Characteristic SEM images of post-treated ZnAl_2O_4 exhibit primary particles 10-15 nm in size as well as aggregates of various sizes (Figure 64). The primary particles are of the same size as those observed in SEM images of as-prepared samples (Figure 62) and the aggregates clearly have an internal structure, consisting of smaller particles. Thus, post-treated ZnAl_2O_4 particles do not appear to be melted together. Hence, SEM analysis confirms the results of XRD analysis: subsequent to a suitable post-treatment – heating in air at 600 °C for 1 h – the formation of nanoscale, crystalline ZnAl_2O_4 is observed. In addition, post-treated samples are expected to exhibit a better redispersibility if surface stabilizers are added. In this way, stable suspensions of nanoscale, crystalline ZnAl_2O_4 could be prepared.

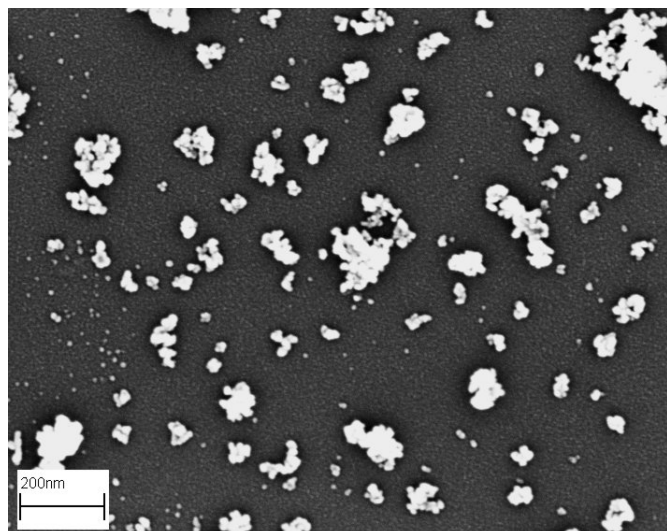


Figure 64. SEM image of $\text{ZnAl}_2\text{O}_4:\text{In}$ heated in air (600 °C, 1 h); powders redispersed in EtOH.

Furthermore, the conductivities of pellets of as-prepared samples and samples heated in air (600 °C, 1 h) were investigated via four-point probing. However, none of the samples exhibited any measurable conductivity. With the intention to improve the conductivity, samples were processed in forming gas, which in previous studies resulted in highly conductive doped ZnO and SnO_2 powders (see section 4.1.2 and 4.1.3). Thus, zinc aluminium oxide samples heated in air were subsequently treated in forming gas at 500 °C for 2 h. However, even after treatment in forming gas at a relatively high temperature, none of the samples exhibited any measurable conductivity, according to four-point probing of pellets. The concentration of dopants in ZnAl_2O_4 was studied via energy-dispersive X-ray analysis. EDX evidenced dopants to be present in the samples in about the same amounts as introduced during synthesis. However, as has been seen in earlier studies presented in this thesis, the presence of dopants in the samples does not necessarily mean that they are inserted in the crystalline lattice and thereby contribute to conductivity.

Thus, in summary, microwave-assisted polyol synthesis of doped ZnAl_2O_4 resulted in particles of around 10-15 nm in size according to DLS and SEM analysis. As-prepared particles are amorphous according to XRD measurements. Subsequent to a suitable post-treatment, namely, heating in air at 600 °C for 1 h, XRD evidenced samples to consist of phase pure crystalline ZnAl_2O_4 with an average crystallite size of 11 nm. SEM analysis verified that post-treated samples still consist of nanoscale particles. Thus, stable suspensions of nanoscale, crystalline zinc aluminium oxide are expected to be in reach with the addition of suitable surface stabilizers. In addition, subsequent to heating in air doped ZnAl_2O_4 powders were processed in forming gas at 500 °C for 2 h in order to improve the conductivity. However, according to four-point probing of pellets of as-prepared samples, samples heated in air, as well as samples processed in forming gas, no measureable conductivity was obtained for any of the sample, although dopants were evidenced to be present in the samples.

4.2.2 Zinc gallium oxide

Zinc gallium oxide has been reported to be a transparent, conductive material.^[156] Omata *et al.* prepared ZnGa_2O_4 by sintering ZnO and Ga_2O_3 powders at 1300 °C and obtained conductive samples with a resistivity of $3 \cdot 10^{-2} \Omega\text{cm}$ by annealing in H_2 atmosphere at 700 °C.^[156] Liquid phase preparation of nanoscale zinc gallium oxide has been carried out utilizing sol-gel and hydrothermal methods.^[157-159] For example, Sung *et al.* synthesized crystalline ZnGa_2O_4

particles, around 3 nm in size, via sol-gel synthesis.^[159] However, in the works concerned with liquid phase preparation of zinc gallium oxide, the electrical conductivity of as-prepared or post-treated ZnGa_2O_4 samples was not evaluated.^[157-159]

Here, suspensions of nanoscale ZnGa_2O_4 doped with Sn^{4+} and Ti^{4+} were prepared in diethylene glycol (DEG) via microwave irradiation. The choice of dopants is motivated by the similarity in ionic radii of gallium, tin, and titanium (Table 15).

Table 15. Radii of metal ions in doped ZnGa_2O_4 .^[45]

ion	CN	radius
Ga^{3+}	6	0.62 Å
Sn^{4+}	6	0.69 Å
Ti^{4+}	6	0.61 Å

In a typical recipe, 1.4 mmol $\text{Zn}(\text{CH}_3\text{COO})_2 \cdot 2 \text{H}_2\text{O}$ and 2.8 mmol $\text{Ga}(\text{NO}_3)_3 \cdot \text{H}_2\text{O}$ were dissolved in 50 ml DEG. The dopant precursors – $\text{SnCl}_4 \cdot 5 \text{H}_2\text{O}$ and $\text{Ti}(\text{OCH}(\text{CH}_3)_2)_4$ – were introduced in the amount of 0.1 mmol and were dissolved together with the previously prepared solution. At 80 °C, the solution was added to a solution of 50 ml DEG containing 14.0 mmol $\text{N}(\text{CH}_3)_4\text{OH} \cdot 5 \text{H}_2\text{O}$ and 2 ml deionized H_2O . Upon adding the solutions, precipitation of a colorless solid occurred. The suspensions were then heated at 200 °C in a laboratory microwave oven (Ar atmosphere, magnetic stirring) for 1 h, whereby the color did not change.

As-prepared samples were analyzed via dynamic light scattering, scanning electron microscopy, and X-ray powder diffraction. According to these analytical tools, $\text{ZnGa}_2\text{O}_4:\text{Sn}$ and $\text{ZnGa}_2\text{O}_4:\text{Ti}$ exhibit similar results regarding particle size and crystallinity, independent of the introduced dopant precursor. As an illustrative example, analytic data of $\text{ZnGa}_2\text{O}_4:\text{Sn}$ are presented. First, particle size and size distribution of as-prepared suspensions were measured via DLS (Figure 65).

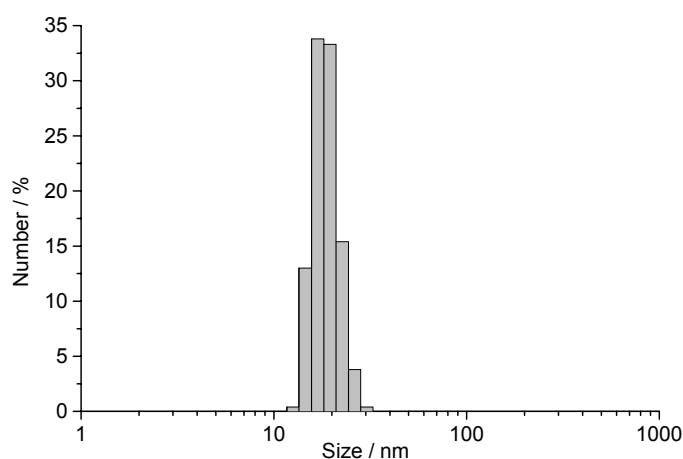


Figure 65. DLS measurement of particle size distribution of as-prepared $\text{ZnGa}_2\text{O}_4:\text{Sn}$ in DEG.

According to DLS analysis, the mean hydrodynamic diameter of $\text{ZnGa}_2\text{O}_4:\text{Sn}$ in DEG amounts to 17(1) nm (Figure 65). Thus, nanoscale particles with a near monodisperse particle size distribution have been formed. Furthermore, scanning electron microscopy of as-prepared

suspensions diluted with DEG is applied in order to obtain a direct view of as-prepared nanoparticles (Figure 66).

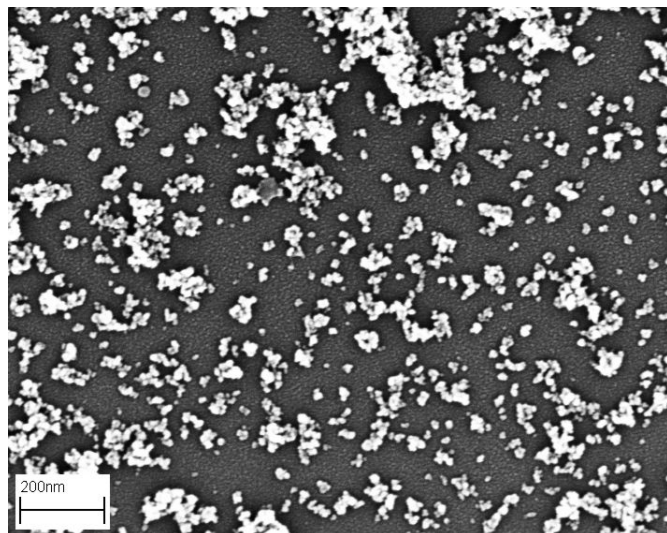


Figure 66. SEM image of as-prepared $\text{ZnGa}_2\text{O}_4:\text{Sn}$ in DEG.

The crystallinity of as-prepared zinc gallium oxide powders, obtained via centrifugation and washing with ethanol, was evidenced via X-ray powder diffraction. According to XRD measurements, both as-prepared samples were amorphous, which was also the case for the previously presented ZnAl_2O_4 . In order to crystallize the samples, the same post-treatment as for ZnAl_2O_4 was chosen, since it proved successful for preparing crystalline ZnAl_2O_4 (see section 4.2.1). Thus, subsequent to post-treatment (heating in air at $600\text{ }^\circ\text{C}$ for 1 h), powder patterns of zinc gallium oxide samples were again recorded via XRD (Figure 67).

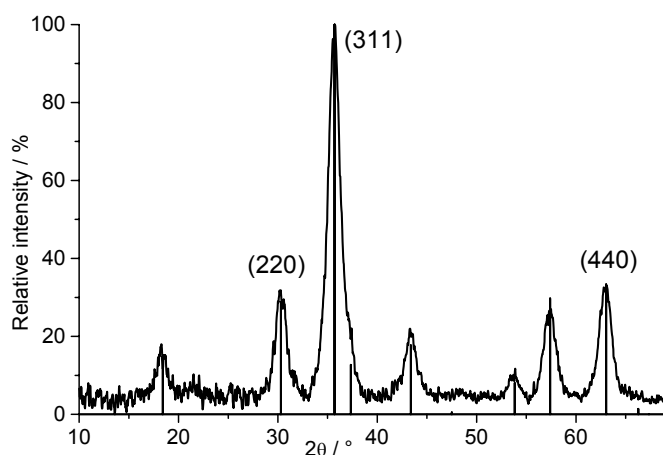


Figure 67. XRD pattern of $\text{ZnGa}_2\text{O}_4:\text{Sn}$ heated in air ($600\text{ }^\circ\text{C}$, 1 h) (reference: ZnGa_2O_4 – ICDD No. 1086-415) with diffraction peaks (220), (311), and (440) denoted.

XRD measurements of samples heated in air ($600\text{ }^\circ\text{C}$, 1 h) evidence the presence of crystalline cubic ZnGa_2O_4 with spinel-type structure (Figure 67).^[160] There are no visible traces of other compounds, e.g. zinc oxide or gallium oxide in the powder diffractogram. Thus, post-treated ZnGa_2O_4 powder samples are phase pure. In addition, the crystallite size was calculated from the peak width of the powder diffraction pattern via Scherrer's formula (see Equation (9)). From the three most intensive Bragg diffraction peaks – (220), (311), and

(440) – an average crystallite size of 7 nm was obtained. Thus, the samples are still nanocrystalline, although a temperature as high as 600 °C was applied. The crystallite size obtained via XRD analysis is regarded to be in sufficient agreement with the particle sizes that were obtained via DLS and SEM analysis. This implies that zinc gallium oxide samples heated in air (600 °C, 1 h) consist of nanoscale, crystalline particles. To verify this view, scanning electron microscopy of post-treated ZnGa_2O_4 powders redispersed in ethanol via ultrasound without the addition of any surface stabilizers was conducted (Figure 68).

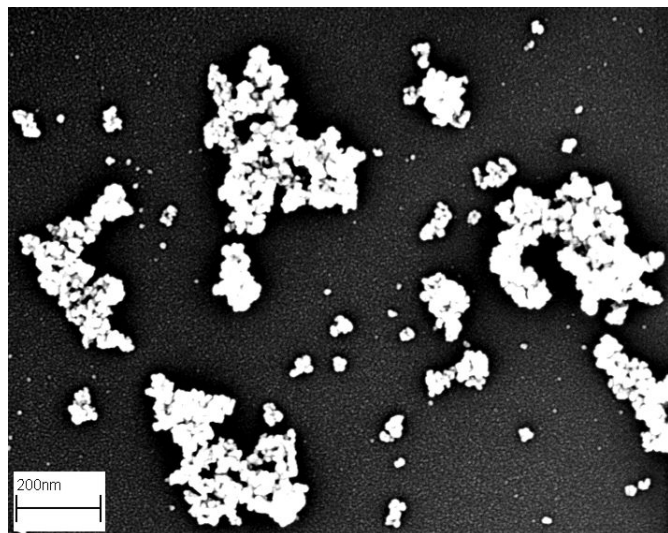


Figure 68. SEM image of $\text{ZnGa}_2\text{O}_4:\text{Sn}$ heated in air (600 °C, 1 h); powders redispersed in EtOH.

Characteristic SEM images of post-treated ZnGa_2O_4 exhibit primary particles 15-20 nm in size as well as aggregates of various sizes (Figure 68). The primary particles are of the same size as those observed in SEM images of as-prepared samples (Figure 66) and the aggregates clearly have an internal structure, consisting of smaller particles. Thus, post-treated ZnGa_2O_4 particles do not appear to be melted together. Hence, SEM analysis confirms the results of XRD analysis: subsequent to a suitable post-treatment – heating in air at 600 °C for 1 h – the formation of nanoscale, crystalline ZnGa_2O_4 is observed. In addition, post-treated samples are expected to exhibit a better redispersibility if surface stabilizers are added. In this way, stable suspensions of nanoscale, crystalline ZnGa_2O_4 could be prepared.

Furthermore, the conductivities of pellets of as-prepared samples and samples heated in air (600 °C, 1 h) were investigated via four-point probing. However, none of the samples exhibited any measurable conductivity. Analogous to doped ZnAl_2O_4 samples (see section 4.2.1), doped ZnGa_2O_4 samples were also treated in forming gas (500 °C, 2 h) with the intention to achieve conductive samples. However, also here, none of the samples exhibited any measurable conductivity subsequent to post-treatment in forming gas, according to four-point probing of pellets. The concentration of dopants in ZnAl_2O_4 was studied via energy-dispersive X-ray analysis. EDX evidenced dopants to be present in the samples in about the same amounts as introduced during synthesis. However, as has been seen in earlier studies presented in this thesis, the presence of dopants in the samples does not necessarily mean that they are inserted in the crystalline lattice and thereby contribute to conductivity.

Thus, in summary, microwave-assisted polyol synthesis of doped ZnGa_2O_4 resulted in particles of around 15-20 nm in size according to DLS and SEM analysis. As-prepared particles are amorphous according to XRD measurements. Subsequent to a suitable post-treatment, namely heating in air at 600 °C for 1 h, XRD evidenced samples to consist of phase

pure crystalline ZnGa_2O_4 with an average crystallite size of 7 nm. SEM analysis verified that post-treated samples still consist of nanoscale particles. Thus, stable suspensions of nanoscale, crystalline zinc gallium oxide are expected to be achievable with the addition of suitable surface stabilizers. In addition, doped ZnGa_2O_4 powders were, subsequent to heating in air, processed in forming gas at 500 °C for 2 h in order to improve the conductivity. However, according to four-point probing of pellets of as-prepared samples, samples heated in air as well as samples processed in forming gas, no measureable conductivity was obtained for any of the samples, although dopants were evidenced to be present in the samples.

4.2.3 Zinc indium oxide

As opposed to the zinc aluminium oxide and zinc gallium oxide systems, which contain only one known compound, namely the spinel, many different compounds are known in the zinc indium oxide system. In 1967, Kasper described a new class of oxides with a general formula $\text{Zn}_k\text{In}_2\text{O}_{k+3}$, where k is a natural number equal to or higher than 2.^[161] He synthesized bulk $\text{Zn}_k\text{In}_2\text{O}_{k+3}$ homologous compounds with $k=2, 3, 4, 5,$ and 7 by sintering mixtures of ZnO and In_2O_3 powders at temperatures between 1050-1550 °C and also tried to synthesize the $\text{Zn}_k\text{In}_2\text{O}_{k+3}$ homologous compound with $k=1$, namely the spinel ZnIn_2O_4 , but did not succeed. Further bulk compounds of this oxide class were prepared in the nineties via sintering mixtures of ZnO and In_2O_3 powders by Nakamura *et al.*^[162] ($k=3-11,$ and 13) and Moriga *et al.*^[163] ($k=3-7, 9, 11, 13,$ and 15). Interestingly, the conductivity and transparency of the $\text{Zn}_k\text{In}_2\text{O}_{k+3}$ compounds were found to increase as the k value decreased.^[163]

Nanoscale thin films of $\text{Zn}_k\text{In}_2\text{O}_{k+3}$ homologous compounds have been prepared by vapor phase methods.^[164-166] Naghavi *et al.* prepared undoped thin films with varying Zn:In ratios and found the conductivity to be at maximum for the film with a $\text{Zn}_2\text{In}_2\text{O}_5$ crystal structure.^[164] Minami *et al.* reported that the resistivity of an undoped $\text{Zn}_2\text{In}_2\text{O}_5$ thin film was $4 \cdot 10^{-4} \Omega\text{cm}$ and its band gap was estimated to 2.9 eV.^[165] Phillips *et al.* reported that an improved conductivity could be achieved by introducing Sn^{4+} dopants.^[166] In addition, a few groups have succeeded with liquid phase preparation of thin films with $\text{Zn}_k\text{In}_2\text{O}_{k+3}$ structure by utilizing the sol-gel method.^[167-169] Also here, the minimum resistivity ($2 \cdot 10^{-3} \Omega\text{cm}$) was found for a film with $\text{Zn}_2\text{In}_2\text{O}_5$ crystal structure.^[168] No determination of particle size in the liquid phase was carried out in these works.^[167-169]

Based on the results of other groups presented above, the main interest in this study is the preparation of nanoscale tin-doped $\text{Zn}_k\text{In}_2\text{O}_{k+3}$ homologous compounds with low k values. The possibility of preparing these compounds via microwave-assisted polyol synthesis will be investigated and the resulting substances will in particular be compared with the compounds prepared by Kasper.^[161]

Thus, suspensions of tin-doped zinc indium oxides were prepared in diethylene glycol (DEG).^[84,170] Samples were prepared with different molar ratios between the zinc and indium precursors – $\text{Zn}(\text{CH}_3\text{COO})_2 \cdot 2 \text{H}_2\text{O}$ and $\text{InCl}_3 \cdot 4 \text{H}_2\text{O}$. The introduced molar ratios were equal to 2:1 (corresponding to a $\text{Zn}_k\text{In}_2\text{O}_{k+3}$ with $k=4$), 3:2 ($k=3$), 1:1 ($k=2$), and 1:2 (corresponding to the theoretical spinel ZnIn_2O_4 , $k=1$), respectively. In order to improve the conductivity, samples were doped with Sn^{4+} . Furthermore, an undoped zinc indium oxide sample Zn:In = 1:2 was prepared as a reference. In a typical recipe for $k=1$, 1.4 mmol $\text{Zn}(\text{CH}_3\text{COO})_2 \cdot 2 \text{H}_2\text{O}$, 2.8 mmol $\text{InCl}_3 \cdot 4 \text{H}_2\text{O}$, and 0.14 mmol $\text{SnCl}_4 \cdot 5 \text{H}_2\text{O}$ were dissolved in 50 ml DEG. At 80 °C, the solution was added to a solution of 50 ml DEG containing 14.0 mmol $\text{N}(\text{CH}_3)_4\text{OH} \cdot 5 \text{H}_2\text{O}$ and 2 ml deionized H_2O . Upon adding the solutions, precipitation of a colorless solid occurred. The suspensions were then heated at 200 °C in a laboratory microwave oven (Ar atmosphere, magnetic stirring) for 2 h.

In order to study what compounds have formed, as prepared samples were examined via X-ray powder diffraction. According to XRD measurements, the crystallinity of the samples was poor directly after synthesis (Figure 69).

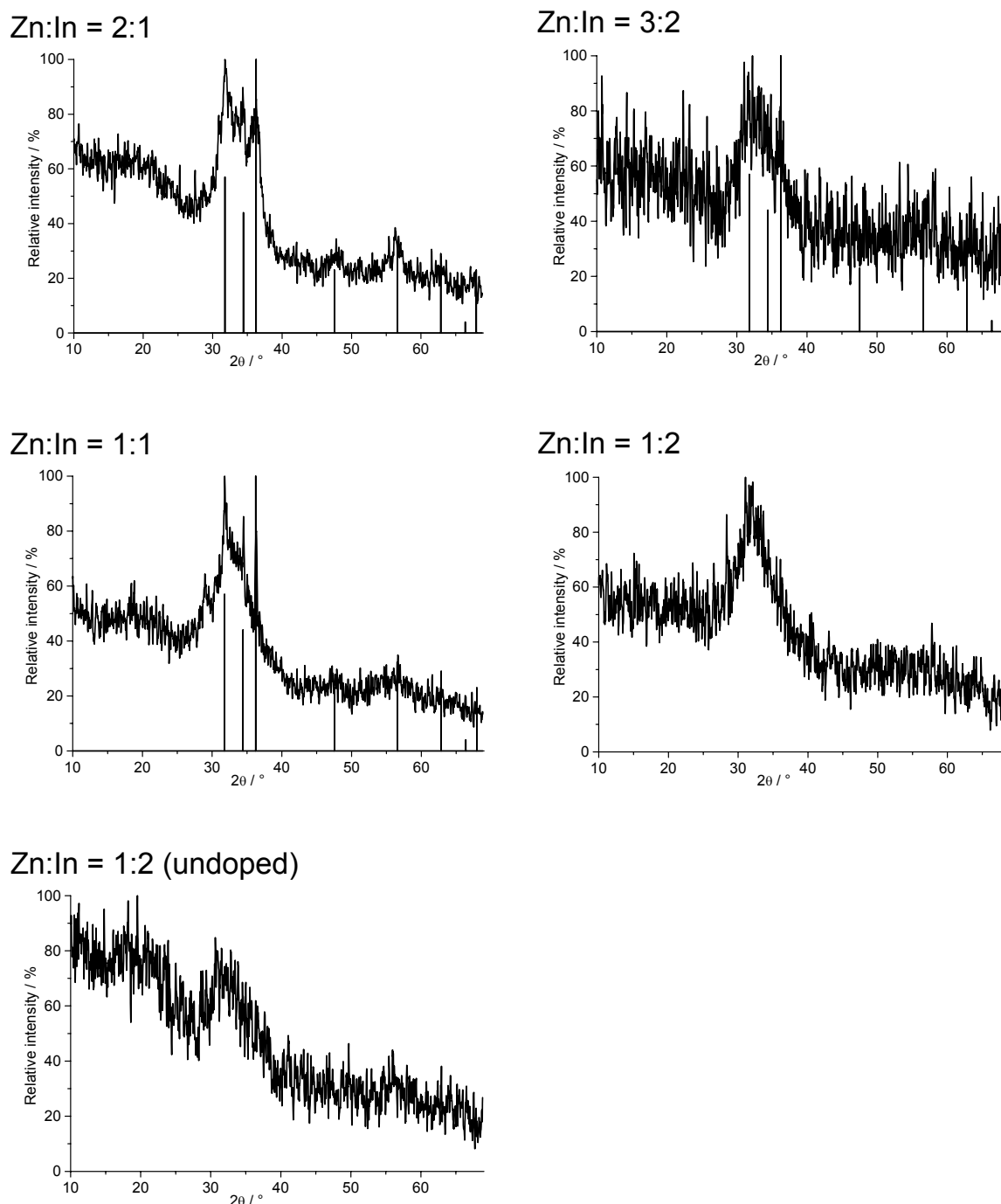


Figure 69. XRD patterns of as-prepared tin-doped zinc indium oxides with Zn:In molar ratios 2:1, 3:2, 1:1, 1:2, and as-prepared undoped zinc indium oxide with Zn:In = 1:2 (reference: ZnO – ICDD No. 36-1451).

Figure 69 shows the powder pattern of as-prepared tin-doped zinc indium oxides with Zn:In molar ratio of 2:1, 3:2, 1:1, and 1:2, corresponding to the homologous compounds $Zn_kIn_2O_{k+3}$ with $k = 4, 3, 2,$ and $1,$ respectively. In addition, the XRD pattern of undoped zinc indium

oxide with Zn:In = 1:2 ($k = 1$) is shown. For the samples with Zn:In = 2:1, 3:2, and 1:1, weak Bragg diffraction peaks of hexagonal ZnO can be observed.^[101] In addition, the sample with Zn:In = 1 exhibits other weak, unidentified peaks. The samples with Zn:In = 1:2 do not exhibit any peaks from ZnO; the tin-doped sample shows weak, unidentified peaks, whereas the crystallinity of the undoped sample is very poor. Thus, it is again observed that crystalline ternary oxides cannot be successfully prepared via the investigated microwave-assisted polyol process.

In order to obtain crystalline materials, samples were post-treated by heating in air at 600 °C for 1 h. Subsequent to this post-treatment, sample crystallinity was again evaluated via XRD.

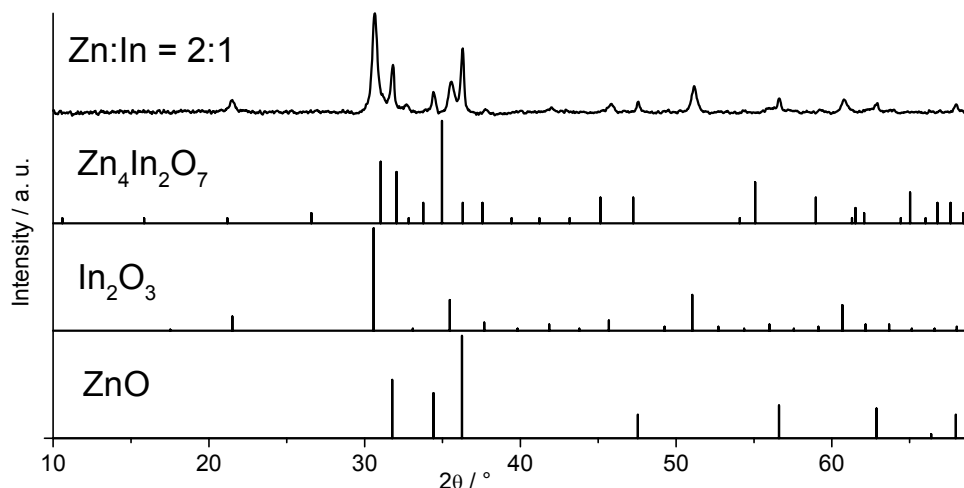


Figure 70. XRD pattern of post-treated tin-doped zinc indium oxide; Zn:In = 2:1 (references: $Zn_4In_2O_7$ – ICCD No. 20-1438, In_2O_3 – ICCD No. 6-416, ZnO – ICCD No. 36-1451).

Subsequent to post-treatment (air, 600 °C, 1 h), the sample with Zn:In = 2:1 is highly crystalline according to XRD measurements (Figure 70). There are no visible traces of Bragg diffraction peaks of the corresponding compound $Zn_4In_2O_7$, as described by Kasper,^[161] in the powder diffractogram. On the other hand, all peaks observable in the powder pattern fit either hexagonal ZnO^[101] or cubic In_2O_3 .^[85] The two compounds seem to be present in about the same amounts, considering that the peaks are of similar intensities. Thus, preparation of a sample with a Zn:In molar ratio of 2:1 resulted in the formation of two phases; zinc oxide and indium oxide. Because of this, the sample was not further characterized.

XRD patterns of samples with Zn:In = 3:2 (Figure 71), 1:1 (Figure 72), and 1:2 (Figure 73) also do not show any visible traces of Bragg diffraction peaks of the corresponding homologous compounds $Zn_kIn_2O_{k+3}$ as described by Kasper.^[161] However, due to the large differences in synthesis temperature applied by Kasper and in this study, it is not unexpected that the resulting compounds are different. Interestingly, all three samples exhibit diffraction peaks that could not be identified with any known crystal phase of zinc indium oxide, zinc oxide, indium oxide, or any other compound in the ICCD data base. The unidentified peaks occur at the same angles for all three samples, indicating that the same compound has formed in all cases. In addition to the unidentified peaks, the powder patterns of the samples with Zn:In = 3:2 (Figure 71) and 1:1 (Figure 72) evidence the presence of ZnO.^[101] The sample with Zn:In = 1:2 (Figure 73) do not exhibit any diffraction peaks of ZnO, which is in accordance with XRD measurements of as-prepared samples (Figure 69). However, the

powder pattern of evidence the presence of cubic In_2O_3 (Figure 73).^[85] The samples in which the unidentified phase is most clearly present are those with Zn:In molar ratios of 1:1 and 1:2, considering the intensity of the unidentified peaks. The differences and similarities of the samples with Zn:In molar ratios equal to 1:1 and 1:2 can be seen more clearly in Figure 74.

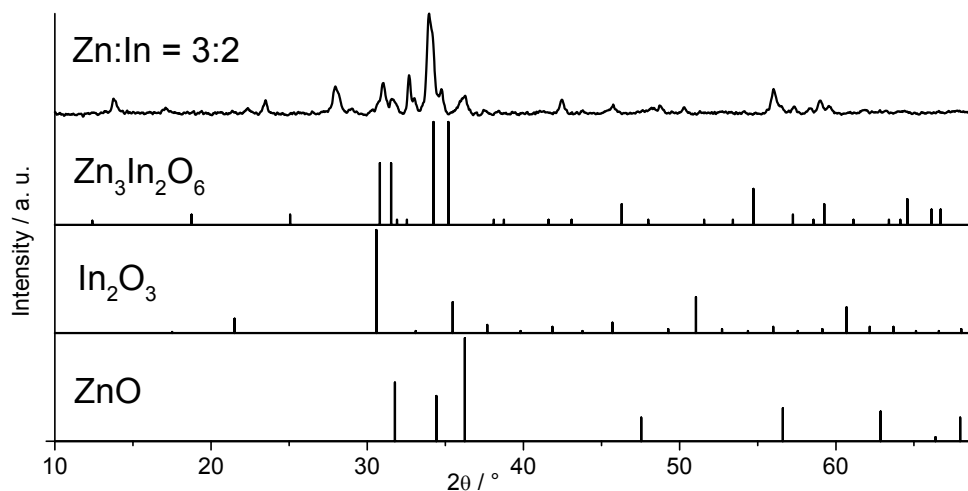


Figure 71. XRD pattern of post-treated tin-doped zinc indium oxide; Zn:In = 3:2 (references: $\text{Zn}_3\text{In}_2\text{O}_6$ – ICCD No. 20-1439, In_2O_3 – ICCD No. 6-416, ZnO – ICCD No. 36-1451).

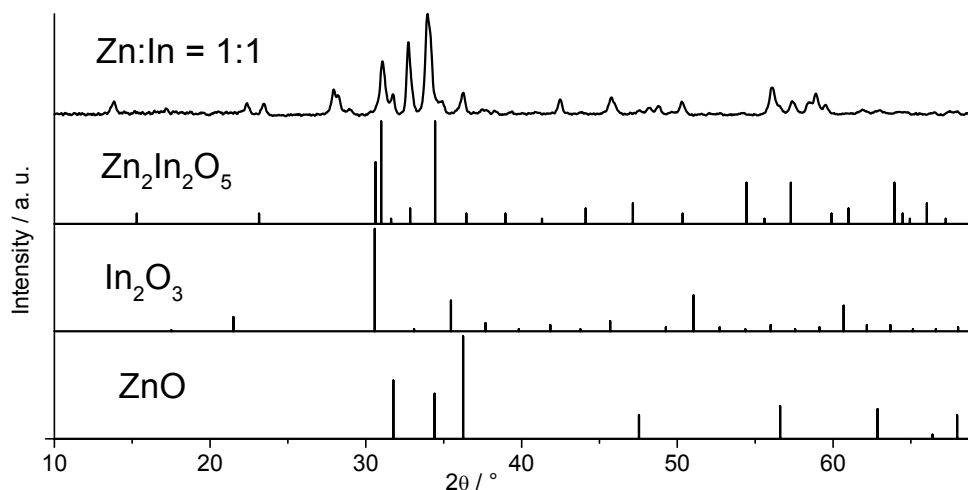


Figure 72. XRD pattern of post-treated tin-doped zinc indium oxide; Zn:In = 1:1 (references: $\text{Zn}_2\text{In}_2\text{O}_5$ – ICCD No. 20-1442, In_2O_3 – ICCD No. 6-416, ZnO – ICCD No. 36-1451).

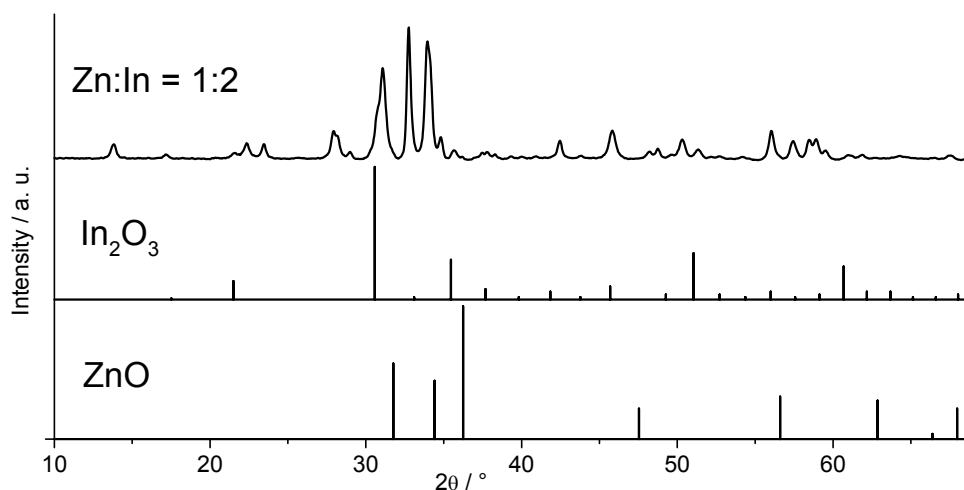


Figure 73. XRD pattern of post-treated tin-doped zinc indium oxide; Zn:In = 1:2 (references: In_2O_3 – ICCD No. 6-416, ZnO – ICCD No. 36-1451).

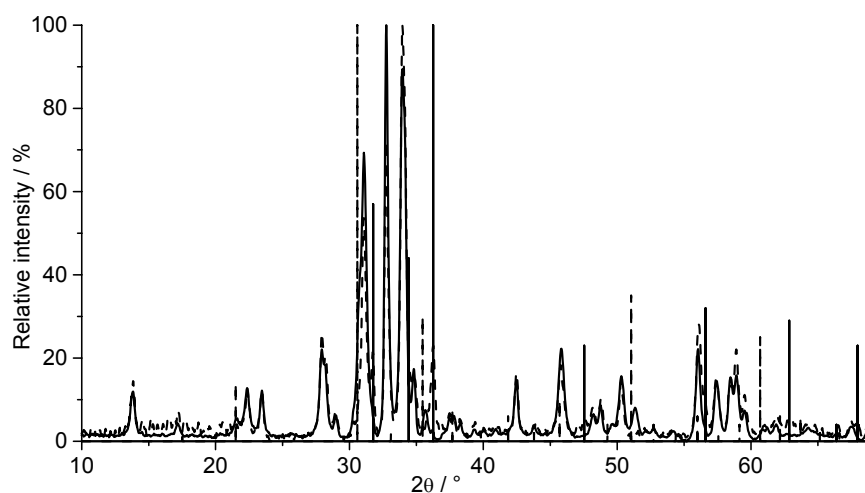


Figure 74. Powder patterns of post-treated tin-doped zinc indium oxide with Zn:In molar ratios of 1:2 (solid) and 1:1 (dashed) (references: ZnO – ICCD No. 36-1451, solid and In_2O_3 – ICCD No. 6-416, dashed).

Furthermore, the tin-doped and undoped zinc indium oxide samples with an Zn:In molar ratio of 1:2 were compared. In Figure 75, it can be seen that the powder patterns of tin-doped and undoped zinc indium oxide samples with are similar. The peak positions are in principle the same, whereas some peaks have different intensities. The peak intensity difference between tin-doped and undoped samples proved to be reproducible. Thus, it can be concluded that the introduction of Sn^{4+} dopants has an influence on the crystal structure of the samples.

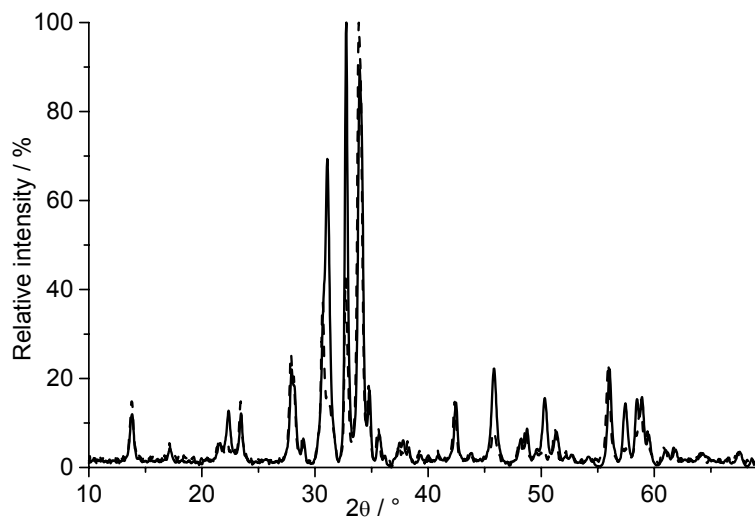


Figure 75. XRD patterns of post-treated tin-doped (solid) and undoped (dashed) zinc indium oxide; Zn:In = 1:2).

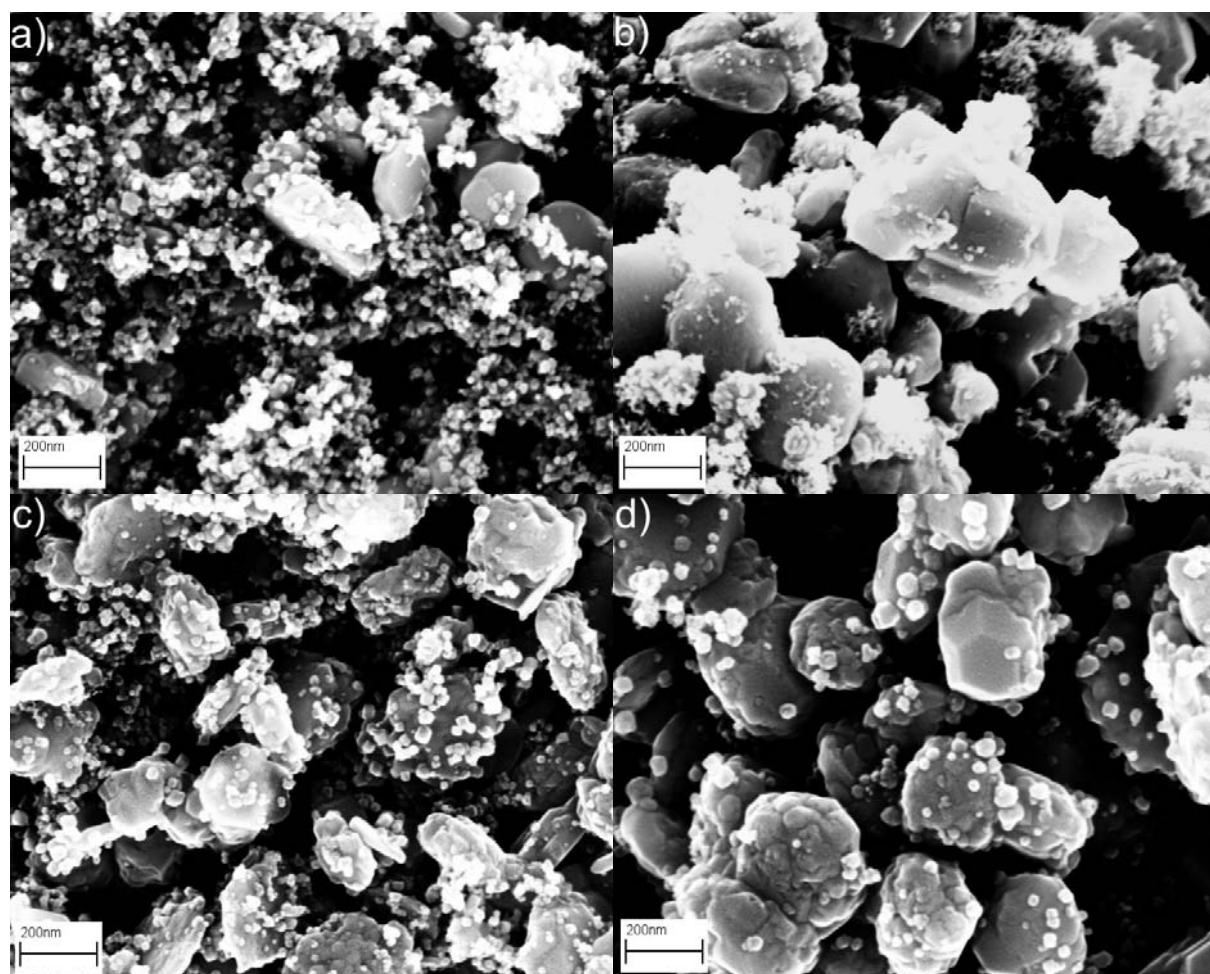


Figure 76. SEM image of post-treated zinc indium oxide with different Zn:In molar ratios: a) 3:2 tin-doped, b) 1:1 tin-doped, c) 1:2 tin-doped, and d) 1:2 undoped; powders redispersed in EtOH.

In addition, post-treated powders with Zn:In molar ratios of 3:2, 1:2 and 1:2 were redispersed in ethanol with ultrasound and investigated via scanning electron microscopy (Figure 76). Characteristic SEM images of post-treated zinc indium oxide powders show that all samples exhibit relatively small particles, 20-50 nm in size, as well as larger formations of various shapes, around 300 nm in size. These larger formations exhibit no internal structure and thus appear to be melted together. Comparing SEM images of post-treated zinc indium oxide samples (Figure 76) with SEM images of zinc aluminium oxide (Figure 64) and zinc gallium oxide (Figure 68) samples that were post-treated at the same temperature and time (air, 600 °C, 1 h), it is clear that zinc indium oxides show a much higher tendency of sintering. The larger aggregates present in $ZnAl_2O_4$ and $ZnGa_2O_4$ samples clearly consist of smaller particles, whereas they do not have an internal structure in the zinc indium oxide samples.

Post-treated tin-doped zinc indium oxide with Zn:In molar ratios of 3:2, 1:1, and 1:2 were analyzed also via energy-dispersive X-ray analysis (Table 16).

Table 16. Zn:In molar ratios of post-treated zinc indium oxide samples; introduced during synthesis and evidenced via EDX.

k	Zn:In (introduced)	Zn:In (EDX)
3	3:2 (0.60)	0.79
2	1:1 (0.50)	0.67
1	1:2 (0.33)	0.46

A comparison between the Zn:In molar ratios introduced during synthesis and the molar ratios evidenced via EDX indicate that the actually present Zn:In molar ratio is significantly higher than the ratio introduced during synthesis for all three investigated samples. This implies that the rest of the indium that was introduced during synthesis remains in solution. Interestingly, the relationship between introduced and evidenced Zn:In ratios is more or less the same for all samples. Investigations with X-ray powder diffraction showed that the two samples with the highest amount of the unidentified crystalline phase also contained small amounts of ZnO ($k = 2$) and In_2O_3 ($k = 1$), respectively. This implies that the Zn:In molar ratio of the unknown zinc indium oxide phase should be between 0.46 and 0.67.

Furthermore, the two samples with the highest amount of the unidentified crystalline phase (Zn:In=1:1 and 1:2) were processed in forming gas at 300 °C for 2 h in order to achieve conductive materials. XRD measurements of samples treated in forming gas evidenced the crystal structure of the substances to remain exactly the same. This was expected due to the low temperature applied in forming gas processing in comparison to the temperature applied while heating in air (300 °C). The sheet resistances of pellets of powders processed in forming gas (300 °C, 2 h) were then evaluated via four-point probing. As a result, tin-doped zinc indium oxide with a Zn:In molar ratio of 1:1 exhibited a sheet resistance of 15.1 $\Omega\Box$, whereas the sheet resistance of tin-doped zinc indium oxide with a molar ratio of 1:2 was measured to 3.3 $\Omega\Box$. Comparing these values with the results of previous studies of ITO, (see section 4.1.1) it is obvious that the prepared zinc indium oxides may present an interesting alternative to ITO. Pellets of as-prepared ITO of similar thickness exhibited a sheet resistance of 4.0 $\Omega\Box$. Although no post-treatment was necessary to achieve low resistance ITO samples, the reduced amount of indium needed in the synthesis of tin-doped zinc indium oxides constitutes a clear advantage of the prepared tin-doped zinc indium oxides over ITO.

In order to realize a useful nanoscale TCO material, particles with a narrow size distribution and of homogenous morphology are needed. In addition, a high optical transmittance is

imperative. To this concern, the particle size and morphology, as well as the optical properties of the sample with the lowest measured resistance ($\text{Zn:In} = 1:2$) were investigated.

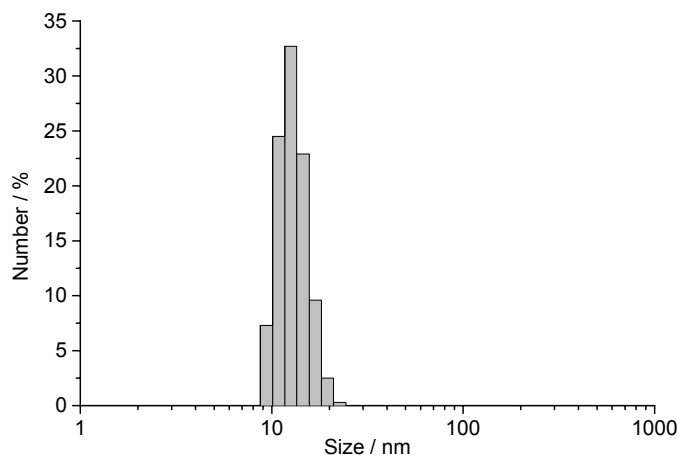


Figure 77. DLS measurement of particle size distribution of as-prepared tin-doped zinc indium oxide with a Zn:In molar ratio of 1:2 in DEG.

First, the as-prepared sample was analyzed via dynamic light scattering and scanning electron microscopy. The particle size and size distribution were measured via DLS and are presented in Figure 77. According to DLS measurements, the mean hydrodynamic diameter of tin-doped zinc indium oxide with a Zn:In molar ratio of 1:2 amounts to 12(1) nm (Figure 77). Thus, as-prepared samples contain nanoscale particles with a near monodisperse particle size distribution. In order to obtain a direct view of as-prepared particles, as-prepared suspensions diluted with DEG were analyzed via scanning electron microscopy (Figure 78).

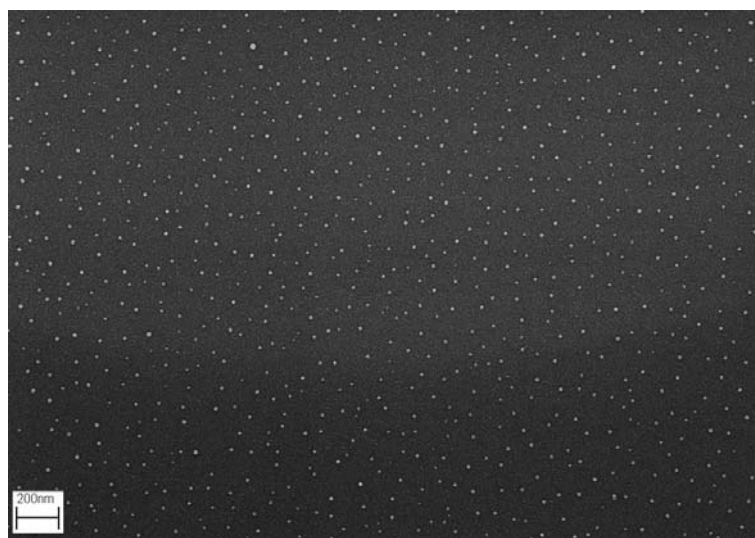


Figure 78. SEM image of as-prepared tin-doped zinc indium oxide with a Zn:In molar ratio of 1:2.

Characteristic SEM images of as-prepared tin-doped zinc indium oxide with a Zn:In molar ratio of 1:2 show spherical, non-agglomerated particles of very uniform morphology. SEM images were also used for statistical evaluation of particle size. Calculations based on 1030 particles resulted in a mean particle size of 17(1) nm which is in good agreement with particle size data obtained via DLS analysis. Thus, according to DLS and SEM analysis, as-prepared

samples are evidenced to consist of homogeneous, nanoscale particles with a near monodisperse size distribution. Based on these results, it is expected that conductive thin layers of tin-doped zinc indium oxide can be formed subsequent to post-treatment of applied as-prepared suspensions.

For optical characterization of tin-doped zinc indium oxide, the reflectance of post-treated powders with a Zn:In molar ratio of 1:2 was measured via UV-Vis spectroscopy (Figure 79).

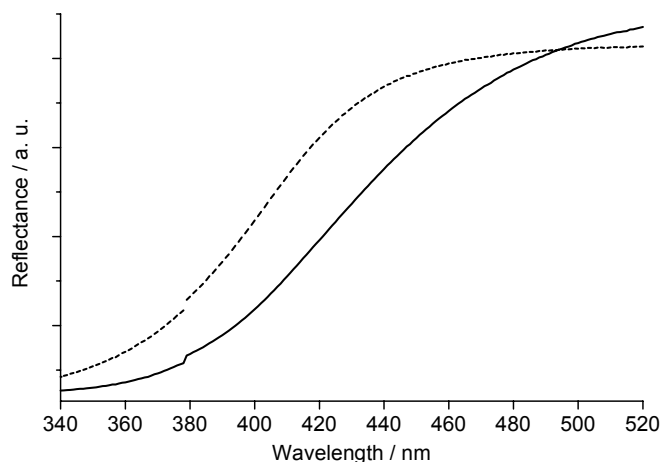


Figure 79. UV-Vis spectra of tin-doped zinc indium oxide with a Zn:In molar ratio of 1:2: heated in air (600 °C, 1 h, solid) and processed in forming gas (300 °C, 2 h, dashed).

Based on measured UV-Vis spectra, the bandgap was calculated as the energy corresponding to the wavelength where the first derivative of the reflectance is at maximum as described for zinc oxide (see section 4.1.2).^[104,105] For tin-doped zinc indium oxide heated in air, this resulted in a wavelength of 429 nm (Figure 79) and a bandgap energy of 2.89 eV. For tin-doped zinc indium oxide treated in forming gas, the first derivative of the reflectance is at maximum at 407 nm, which corresponds to a bandgap of 3.05 eV. Thus, a bandgap shift of +0.16 eV between insulating oxidized samples and conductive reduced samples occurs. This finding is in accordance with the expectation and ascribed to the higher concentration of free charge carriers in reduced samples. The resulting partial filling of the conduction band is well-known as the Moss-Burstein effect.^[106,107] Hence, post-treated conductive tin-doped zinc indium oxide is transparent in the main part of the visible wavelength interval, which, again, indicates its potential application as a TCO material. Comparing these results with previous results concerning zinc oxide band gaps (see section 4.1.2), the bandgap of doped zinc oxide and doped zinc indium oxide heated in air are of similar values, whereas the bandgap shift after treatment in forming gas is smaller for zinc indium oxide. However, the bandgap of the here synthesized conductive reduced tin-doped zinc indium oxide is higher than the bandgap of an undoped $Zn_2In_2O_5$ thin film (2.9 eV) prepared by Minami *et al.*^[165] In addition, the bandgap of a thin film is expected to be larger than a bulk powder of the same substance. Thus, the synthesized substance in the form of a thin film is expected to be transparent in a yet broader wavelength interval than the investigated powder sample.

Finally, with the intention to identify the formed unknown phase, experiments were made to obtain single crystals via hydrothermal processing of post-treated powders of tin-doped zinc indium oxide with a molar ratio of 1:2. The powder was redispersed in H_2O with ultrasounds and heated in an autoclave for 6 days at a temperature of 200 °C and a pressure of 14 bar. This treatment proved successful; after hydrothermal processing, a few transparent, colorless,

single crystals were formed (Figure 80). Measurements of an obtain crystal were conducted on a four-circle single crystal diffractometer. In Table 17, the obtained lattice parameters are presented.

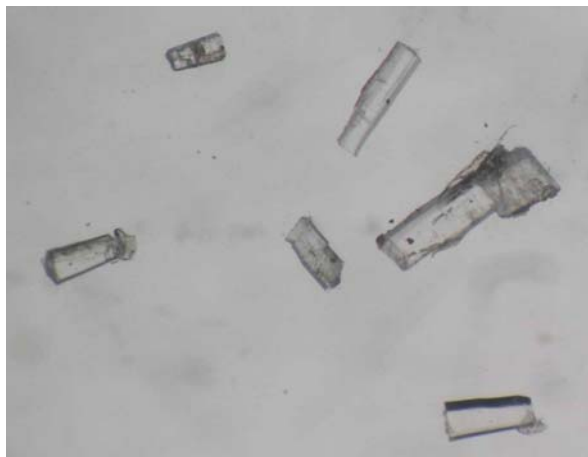


Figure 80. Crystals obtained from hydrothermal processing of tin-doped zinc indium oxide powders with a Zn:In molar ratio of 1:2.

Table 17. Lattice parameters obtained for crystals formed by hydrothermal processing of tin-doped zinc indium oxide with a Zn:In molar ratio of 1:2.

$a (= b)$	c	c/a	$\alpha (= \beta)$	γ	V_{UC}
7.033 Å	9.543 Å	1.36	90°	120°	408.8 Å ³

The unit cell volume, V_{UC} , is calculated according to the formula

$$V_{EC} = a \cdot b \cdot c \cdot \sin \gamma \quad (48)$$

Now, the obtained unit cell volume is compared with the V_{UC} of ZnO (47.6 Å³)^[101] and In₂O₃ (1035.8 Å³).^[85] The number of atoms per unit cell (Z) are also taken into account ($Z(\text{ZnO}) = 2$; $Z(\text{In}_2\text{O}_3) = 16$). It is found that

$$3 \left(3 \frac{V_{EC}(\text{ZnO})}{Z(\text{ZnO})} + \frac{V_{EC}(\text{In}_2\text{O}_3)}{Z(\text{In}_2\text{O}_3)} \right) = 408.4 \text{ Å}^3$$

Thus, the obtained unit cell volume fits very well with the structural formula Zn₃In₂O₆. The prepared single crystal hence has a Zn:In molar ratio of 0.6. This is in agreement with EDX investigations on powders from which it was concluded that the actual present Zn:In molar ratio is higher than the introduced molar ratio and that the molar ratio of the unidentified crystalline phase is between 0.46 and 0.67. A complete structure determination of the measured crystal has unfortunately not yet succeeded since the compound obviously crystallizes as a *Drilling* (triplet). However, calculations are still in progress. For comparison, the lattice parameters of the first three Zn_kIn₂O_{k+3} homologous compounds ($k = 2-4$) as described by Kasper are given in Table 18.^[161]

4.2.3 Zinc indium oxide

Table 18. Lattice parameters of $Zn_kIn_2O_{k+3}$ homologous compounds with $k = 2, 3,$ and 4 according to Kasper.^[161]

k	compound	a	c	c/a	V_{UC}
4	$Zn_4In_2O_7$	3.339 Å	33.520 Å	10.04	323.6 Å ³
3	$Zn_3In_2O_6$	3.355 Å	42.515 Å	12.67	414.5 Å ³
2	$Zn_2In_2O_5$	3.376 Å	23.154 Å	6.86	228.5 Å ³

The a and c parameters, which were determined by Kasper via indexing of recorded powder patterns,^[161] are very different from the lattice parameters obtained from measurements on here synthesized crystals of tin-doped zinc indium oxide. The c/a quotient determined for synthesized tin-doped zinc indium oxide is low, whereas it for the compounds prepared by Kasper is more than five times larger for all compounds. However, considering the unit cell volumes, the compound $Zn_3In_2O_6$ as described by Kasper has a similar volume as that obtained from X-ray single crystal diffraction measurements in this study. Hence, it is likely that the prepared single crystal has the same structure as $Zn_3In_2O_6$ as described by Kasper and that the differences in the a and c parameters arise from the different determination methods applied. Interestingly, the unit cell volume obtained from X-ray single crystal diffraction represents a better fit with the structural formula $Zn_3In_2O_6$ obtained from calculations with the cell volumes of ZnO and In_2O_3 . Alternatively, the structures of the single crystal and the compound prepared by Kasper could be similar, but with slight distortions. If the powder pattern of the post-treated tin-doped zinc indium oxide sample with a Zn:In molar ratio of 1:2 is compared with the compound $Zn_3In_2O_6$ as described by Kasper, it is seen that they are not the same (Figure 81). However, it is not yet clarified if the differences arise from the possible distortions of the structure, or if a different crystal structure is formed during hydrothermal treatment of the sample.

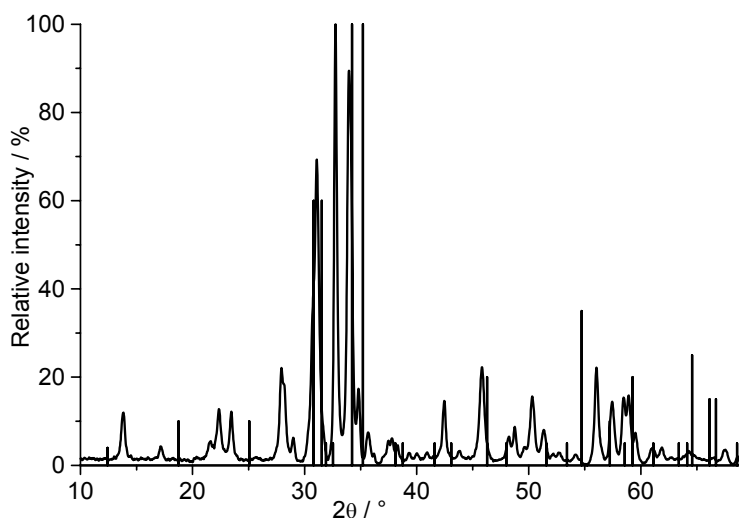


Figure 81. XRD pattern of post-treated tin-doped zinc indium oxide; Zn:In = 1:2 (reference: $Zn_3In_2O_6$ – ICCD No. 20-1439).

In summary, a series of zinc indium oxides samples have been prepared in order to investigate the possibility to synthesize $Zn_kIn_2O_{k+3}$ homologous compounds via a microwave-assisted polyol method. Samples were prepared with Zn:In molar ratios corresponding to the four first $Zn_kIn_2O_{k+3}$ homologous compounds – 2:1 ($k = 4$), 3:2 ($k = 3$), 1:1 ($k = 2$), and 1:2 ($k = 1$).

According to XRD measurements, all as-prepared samples show poor crystallinity, however, with indications of beginning crystallization where all as-prepared samples apart from those with a Zn:In molar ratio of 1:2 exhibited weak peaks of ZnO. After post-treatment in air (600 °C, 1 h), all samples were highly crystalline. It turned out that none of the $Zn_kIn_2O_{k+3}$ homologous compounds as described by Kasper^[161] were formed, which is probably due to the large difference in applied synthesis temperature. The sample with Zn:In = 2:1 consisted solely of ZnO and In_2O_3 after heating in air, whereas the powder patterns of the other samples showed the presence of an unidentified crystalline phase, together with diffraction peaks of ZnO (samples with Zn:In = 3:2 and 1:1) and In_2O_3 (samples with Zn:In = 1:2). EDX investigations showed that the Zn:In molar ratio present in the unidentified crystalline phase should be between 0.46 and 0.67. Single crystals were successfully prepared via hydrothermal processing of powders with Zn:In = 1:2. Their crystal structure has not yet been fully determined, whereby however in a first stage, the unit cell volume fits very well with the structural formula $Zn_3In_2O_6$. The two samples in which the highest amounts of the new crystalline phase were present ($k = 2$ and 1) were processed in forming gas (300 °C, 2 h) in order to increase their conductivities. Four-point probing of pellets of post-treated powders resulted in sheet resistances of $15.1 \Omega \square$ ($k = 2$) and $3.3 \Omega \square$ ($k = 1$). The lowest resistance is comparable to the resistance of ITO pellets of similar thickness ($4.0 \Omega \square$) of as-prepared powders synthesized in the same way as the presented zinc indium oxides. Calculations based on UV-Vis measurements of powders of the sample with the lowest resistance ($k = 1$) resulted in a bandgap energy of 3.05 eV. DLS and SEM analysis of as-prepared tin-doped zinc indium oxide resulted in an average particle size of about 15 nm. Thus, it is expected that homogeneous thin layers of this material can be prepared. Hence, nanoparticles of a substance that exhibits a high conductivity and is transparent in the visible wavelength interval have been synthesized. This obviously makes it a very interesting TCO material and the fact that its indium content is lower than in ITO presents a cost-effective alternative to ITO.

4.3 Elementary metals

4.3.1 Indium

A possible application of metal nanoparticles is as precursors for nanoscale compounds containing the metal in question. One example is the synthesis of nanoscale III-V semiconductors; to this end, nanoparticles of elementary indium have been applied as precursors in the synthesis of InAs and InP semiconducting nanorods.^[171,172] Synthesis of In⁰ nanoparticles was carried out via thermal decomposition of organometallic compounds^[171] and reduction of indium chloride in TOP/TOPO,^[172] respectively. Highly water and air free environments were employed in order to avoid contaminations of e.g. In₂O₃. Recently, Chou *et al.* prepared In⁰ nanocrystals 80 nm in size, which were reported to be redispersible in ethanol at ambient conditions, via reduction in isopropanol – however, no determination of particle size in the liquid phase was conducted.^[173]

Here, suspensions of nanoscale indium particles were prepared in a water-containing environment.^[174] First, analogue to all previously presented substances, synthesis was carried out in diethylene glycol (DEG). Elementary indium was obtained via reduction of indium chloride with sodium borohydride as reducing agent. Synthesis was carried out in an open system where the starting solution was stored in a three-neck flask vented with nitrogen gas. The colorless starting solution contained 0.5 mmol InCl₃ · 4 H₂O dissolved in 25 ml DEG. At a temperature of 50 °C, a solution containing 5.0 mmol NaBH₄ dissolved in 25 ml DEG was rapidly added to the starting solution. A dark brown precipitate was formed within minutes. The suspension then was further heated to 90 °C with a heating mantle and the temperature kept for 5 min.

As-prepared indium suspensions in DEG exhibit a turbid appearance (Figure 82 a). The particle size and size distribution of as-prepared suspensions were evaluated via dynamic light scattering. First, DLS results were plotted to show the particle size as a function of particle number (Figure 82 b). Here, the average hydrodynamic diameter of the particles amounts to 38(2) nm. Moreover, the particle size was plotted as a function of particle volume (Figure 83). Here, it is obvious that even diluted suspensions contain considerable amounts of larger aggregates, as opposed to all samples previously presented in this thesis. This is in accordance with the fact that suspensions exhibit a turbid appearance although their solids contents are relatively low (<0.5 wt-%, Figure 82 a).

Subsequently, as-prepared suspensions diluted with DEG were investigated via scanning electron microscopy in order to obtain a direct view of as-prepared nanoparticles (Figure 84). Characteristic SEM images of indium nanoparticles in DEG show spherical, homogeneous particles formed into small aggregates. SEM images of In⁰ in DEG were also used for statistical evaluation of particle size. Calculations based on 780 particles resulted in a mean particle size of 27(1) nm. Here, the mean size obtained via SEM analysis is smaller than the mean size resulting from DLS analysis, which implies that the particles are more agglomerated in the liquid phase.

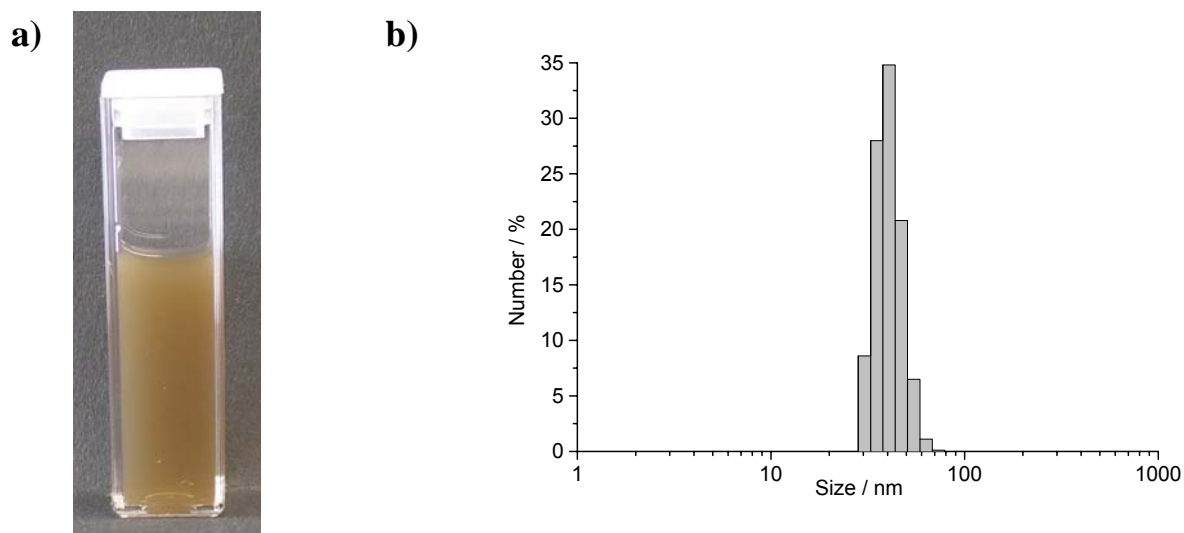


Figure 82. a) Photograph of as-prepared In^0 nanoparticles in DEG and b) particle size distribution thereof measured via DLS; plotted as a function of particle number.

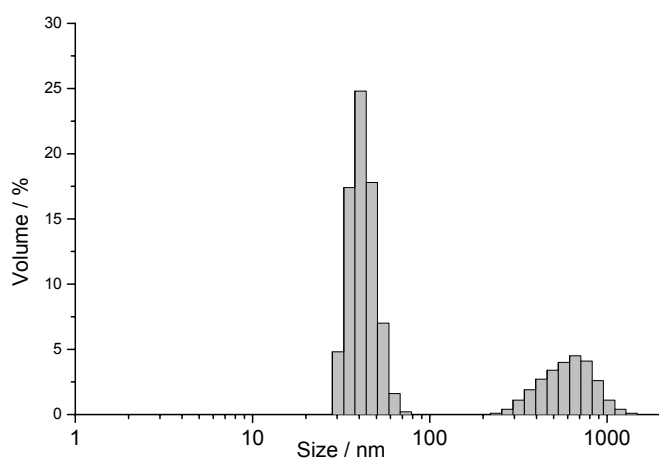


Figure 83. DLS measurement of particle size distribution of as-prepared In^0 nanoparticles in DEG; plotted as a function of particle volume.

In order to obtain powders, suspensions were first centrifuged and washed in EtOH in air at ambient conditions. Thereafter, EtOH was removed under vacuum at room temperature with the intention to avoid contamination of indium oxide, which could form when powders dry in air. The dried samples were slightly viscous and thus not completely solidified. Nevertheless, the crystallinity of as-prepared samples dried in vacuum was evaluated via X-ray powder diffraction. Sample preparation was carried out in a glove box with Ar atmosphere. For comparison, elementary indium dried in air was also examined via XRD.

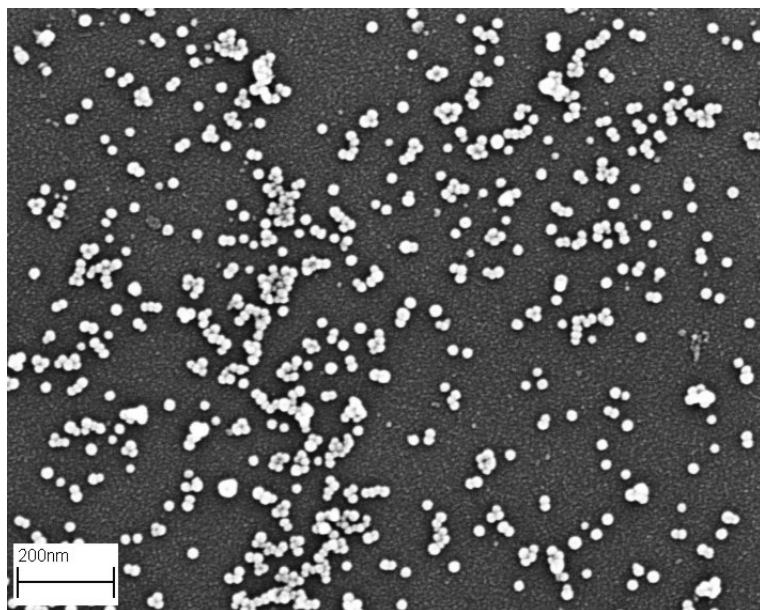


Figure 84. SEM image of as-prepared In^0 nanoparticles in DEG.

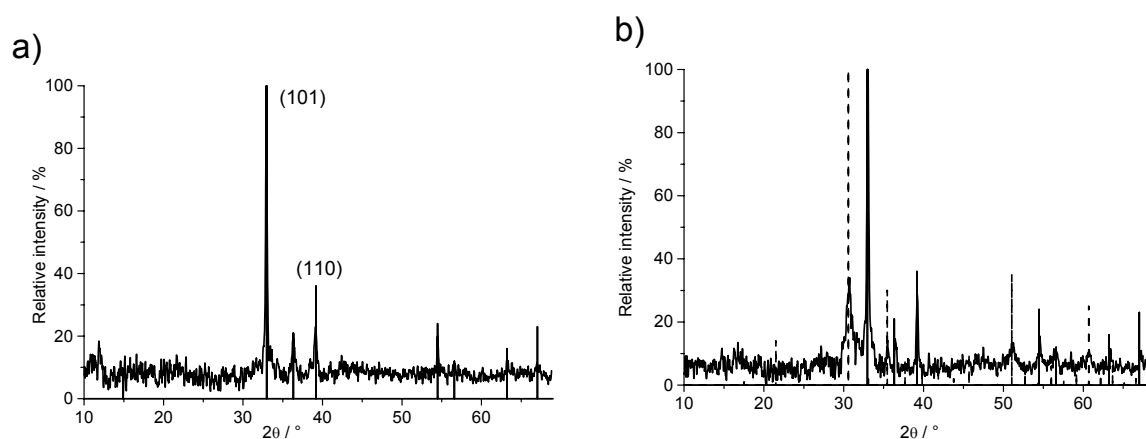


Figure 85. XRD pattern of In^0 nanoparticles synthesized in DEG, washed with EtOH, and dried in a) vacuum and b) air (references: In – ICCD No. 5-642, solid and In_2O_3 – ICCD No. 6-416, dashed) with diffraction peaks (101) and (110) denoted.

XRD measurements of In^0 particles prepared in DEG and dried in vacuum evidence the presence of crystalline tetragonal indium (Figure 85 a).^[155] The powder diffractogram exhibit no traces of other peaks from e.g. indium oxide, which indicates that the sample is phase pure. It is still possible that amorphous In_2O_3 has formed, which cannot be evidenced via XRD. However, the dark color of the sample indicates that there is no indium oxide present. Furthermore, the powder diffractogram of the sample dried in air (Figure 85 b) clearly shows the presence of In_2O_3 ^[85] in addition to elementary indium.^[155] The clear difference between the powder patterns of the samples dried in vacuum and air indicates that indium oxide was formed by drying in air and not during synthesis. Thus, it was possible to avoid formation of indium oxide although the synthesis was carried out in a water-containing environment. In addition, the crystallite size was calculated from the peak width of the powder diffraction pattern via Scherrer's formula (see Equation (9)). From the two most intensive Bragg diffraction peaks – (101) and (110) – an average crystallite size of 34 nm was obtained. The crystallite size obtained from XRD analysis of In^0 particles prepared in DEG is in agreement

with particle size data obtained via DLS and SEM analysis of the same sample, which implies that particles are single crystalline.

Moreover, a phase transfer of In^0 particles from DEG into dodecane was carried out. Here, the same starting solution was used as in the previously presented synthetic route. Here, 25 ml of dodecane was added to the starting solution, whereby two separate colorless, clear phases were formed. As vigorous stirring was employed, the two phases formed an emulsion, which was heated to 100 °C with a heating mantle. Subsequently, a solution containing 5.0 mmol NaBH_4 as reducing agent and 1 ml oleylamine as surface stabilizer dissolved in 25 ml DEG was rapidly added to the emulsion. Oleylamine is solvable in dodecane as well as in DEG and is applied in order to initiate a phase transfer. Within minutes, the emulsion turned dark brown. After 5 min, vigorous stirring was ended and the emulsion separated into two phases. The dark brown precipitate was found to be located in the polar, lower DEG phase. The phase transfer into the nonpolar, upper dodecane phase occurred very slowly; however, after a few days, the polar DEG phase was completely clear and colorless, whereas the dark brown precipitate was located in the nonpolar dodecane phase (Figure 86 a). Thus, a suspension of In^0 particles in dodecane could be obtained.

The In^0 suspension in dodecane exhibits a transparent appearance (Figure 86 b) and turned out to be stable for months. The suspensions were stored in air at ambient conditions, whereas no sedimentation occurred, nor was any change in color observable. Thus, the introduced stabilizing agent oleylamine proved successful concerning making a phase transfer possible and achieving a suspension of surface protected elementary indium nanoparticles, which is stable during storage in air.

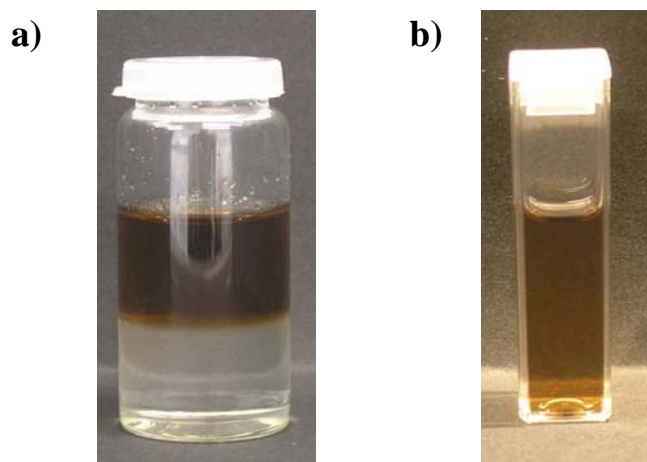


Figure 86. Photographs of as-prepared In^0 nanoparticles in dodecane / DEG: a) both phases and b) the separated dodecane phase.

The particle size and size distribution of as-prepared In^0 suspensions in dodecane were evaluated via dynamic light scattering and scanning electron microscopy. According to DLS measurements of as-prepared indium suspensions diluted with dodecane, the mean hydrodynamic diameter of In^0 particles in dodecane amounts to 18(1) nm (Figure 87). Thus, nanoscale particles with a near monodisperse size distribution have formed. The particle size obtained here is much smaller than the particle size of indium particles in DEG resulting from DLS analysis (38 nm). If the particle size is plotted as a function of particle volume instead of as a function of particle number, it is seen that no peaks corresponding to large agglomerates are present (figure not shown here), in contrast to suspensions in DEG (Figure 83) The small

particle size and the fact that no large agglomerates are present are in accordance with the transparency and excellent stability of suspensions in dodecane.

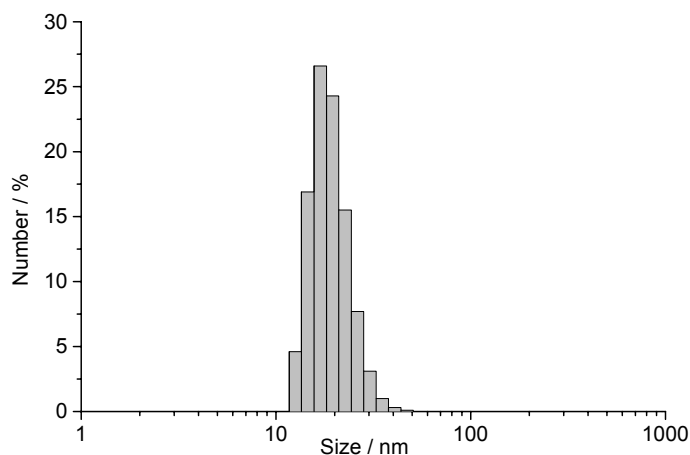


Figure 87. DLS measurement of particle size distribution of as-prepared In^0 nanoparticles transferred into dodecane.

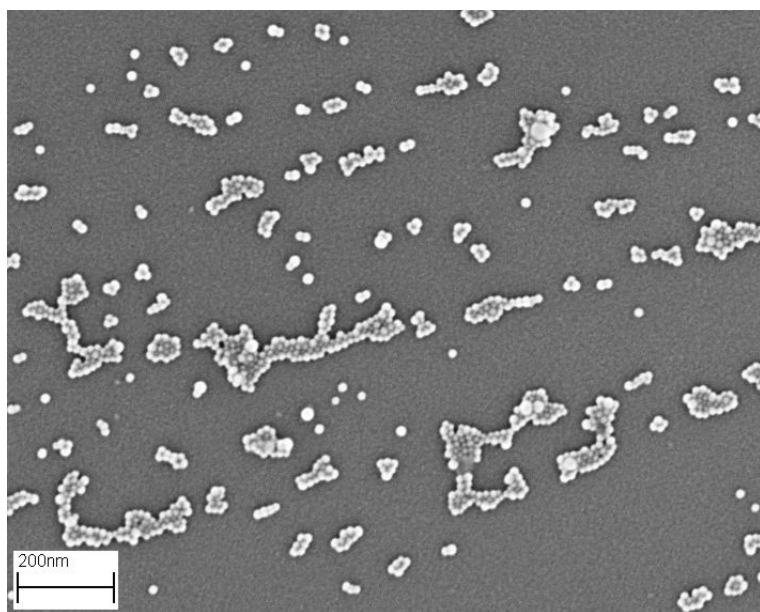


Figure 88. SEM image of as-prepared In^0 nanoparticles transferred into dodecane.

In addition, diluted as-prepared In^0 suspensions in dodecane were analyzed via SEM in order to obtain a direct view of as-prepared nanoparticles (Figure 88). Characteristic SEM images of indium nanoparticles in dodecane show spherical, homogeneous particles formed into small aggregates. SEM images were also used for statistical evaluation of particle size. Calculations based on 400 particles resulted in an average particle size of 27(1) nm. Thus, as opposed to the oxide samples previously presented in this thesis, SEM analysis of elementary indium resulted in a larger particle size than that obtained via DLS analysis of the same sample. Apparently, when indium suspensions in dodecane are applied on heated SEM sample carriers, the particles tend to form small aggregates, whereas it is assumed that they can move individually while they are located in the liquid phase, taking the smaller particle size obtained via DLS analysis into account. Coincidentally, the average particle size deduced

from SEM analysis of indium transferred into dodecane is exactly the same as the average size obtained from SEM analysis of elementary indium in DEG.

Powders of indium transferred into dodecane were obtained as previously described for the indium prepared in DEG – via centrifugation, washing with EtOH in air in ambient conditions, and drying in vacuum. In this case, samples were even more viscous and thus not completely solidified. Thereafter, the crystallinity of as-prepared samples dried in vacuum was evaluated via X-ray powder diffraction. Sample preparation was carried out in a glove box with Ar atmosphere. XRD measurements evidence indium particles transferred into dodecane and dried in vacuum to exhibit a poor crystallinity (Figure 89), which could be due to the viscous nature of the samples. Nevertheless, the (101) Bragg diffraction peak of tetragonal indium could be clearly identified.^[155] In addition, there are no other visible peaks of e.g. indium oxide visible, which implies that samples are phase pure. However, due to the poor crystallinity of the sample, the presence of small amounts of other compounds cannot be completely ruled out. In addition, no calculation of crystallite size from the peak width via Scherrer's formula could be conducted.

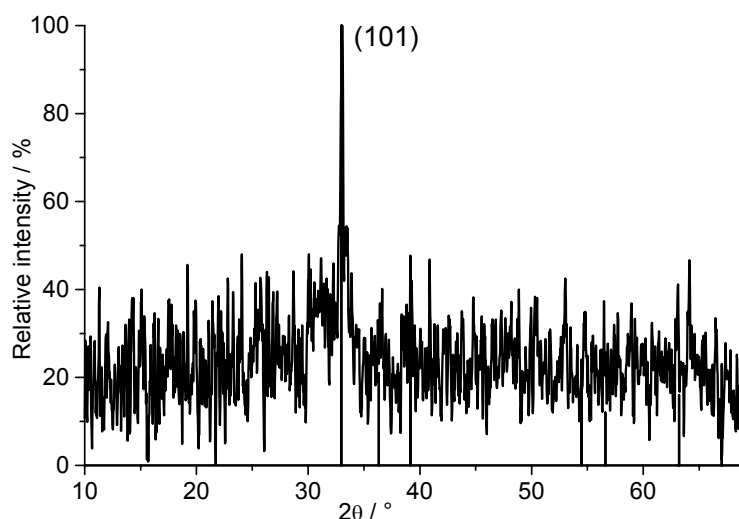


Figure 89. XRD pattern of In^0 nanoparticles transferred into dodecane, washed with EtOH, and dried in vacuum (reference: *In* – ICCD No. 5-642) with diffraction peak (101) denoted.

Furthermore, the size and crystallinity of as-prepared indium particles were evaluated via transmission electron microscopy. In order to obtain suspensions in a highly volatile solvent and to, thereby, facilitate TEM investigations, indium particles were transferred into pentane instead of dodecane. In this case, 1 ml oleylamine was added to an indium suspension in DEG. Subsequent to cooling to ambient temperature, 25 ml of pentane was added. The nonpolar pentane phase turned dark brown over night. Suspensions in pentane turned out to be stable for approximately one week; thereafter sedimentation could be observed. However, only a part of the formed indium particles were transferred into the nonpolar pentane phase, as the polar DEG phase did not become colorless.

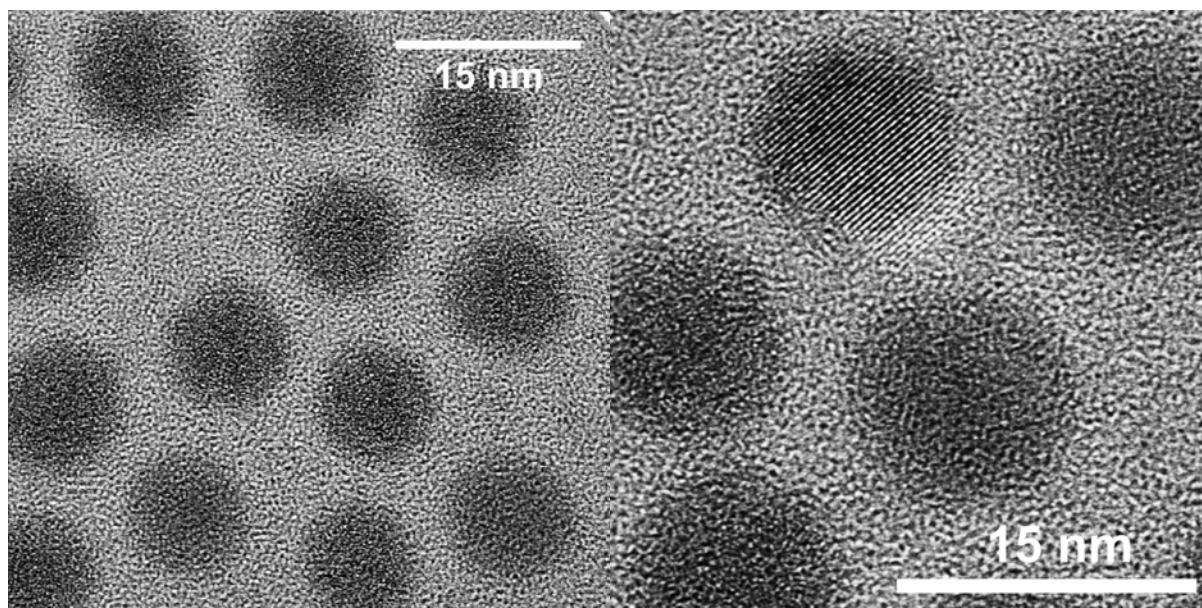


Figure 90. TEM images of In^0 nanoparticles transferred into pentane.

Suspensions of In^0 nanoparticles in pentane proved useful for preparation of TEM samples. Characteristic TEM images of indium in pentane exhibit spherical, non-agglomerated particles of a very uniform morphology (Figure 90). This again verifies the successful surface stabilization that is achieved by applying oleylamine, which makes it possible to prepare non-agglomerated particles in the liquid phase. Since pentane suspensions easily evaporated from TEM sample carriers, the particles obviously remained non-agglomerated. The particle diameters of indium particles in pentane were measured to be between 9.5 and 10.7 nm. Thus, surprisingly, the particle size obtained via TEM analysis is considerably smaller than the particle sizes obtained via SEM analysis. This could simply be an effect of sample preparation: apparently, the particles tend to agglomerate more when they are applied as drops on heated SEM sample carriers than when they are nebulized on TEM sample carriers at room temperature. In addition, the particle sizes obtained via TEM analysis is in relatively good agreement with the results of DLS analysis of indium transferred into dodecane. This would imply that the main difference concerning particle size between elementary indium particles prepared in DEG and particles transferred into dodecane lies in the formation of aggregates in the liquid phase, which also, as noted earlier, affects the stability of the suspensions.

Furthermore, considering the crystallinity of as-prepared In^0 particles, TEM images mostly show particles that do not exhibit any lattice fringes. This could indicate that they are amorphous, or that they are oriented in an unfortunate way. Another possibility is that the particles were initially crystalline but turned amorphous when exposed to the high-energetic electron beam. However, a few crystalline particles could also be observed (Figure 90). From the crystalline particle in Figure 90, a lattice plane distance of $2.96 \pm 0.12 \text{ \AA}$ was identified. The lattice plane of tetragonal indium that fits best to this distance is the (101) lattice plane, for which the plane distance amounts to 2.72 \AA .^[155] Thus, the agreement with tetragonal indium is rather poor. However, for the lattice plane (222) in cubic In_2O_3 , the plane distance is 2.92 \AA .^[85] Thus, indium oxide presents a better fit with the measured lattice plane distance than elementary indium. Hence, according to TEM analysis, most particles do not show crystallinity, whereas a few exhibit a crystalline structure of indium oxide. The formation of indium oxide probably occurs as some particle come into contact with air. However, TEM analysis of indium transferred into pentane does not agree with XRD analysis of particles synthesized in DEG. According to XRD analysis, the sample was highly crystalline with an

average size of 34 nm. Even though estimation of crystallite size via Scherrer's formula is only approximate, the obtained crystallite size is still more than three times larger than particles seen in TEM, which, in addition, are not highly crystalline. This raises the question of how representative these TEM images in fact are. In addition, it can be concluded that in order to clarify what the true particle sizes of elementary indium prepared in DEG and transferred into dodecane are, further TEM investigations are needed.

Thus, in summary, elementary indium nanoparticles have been successfully prepared in dodecane / DEG via reduction of indium chloride using sodium borohydride as a reducing agent. Preparation was carried out according to two different synthetic routes; in the first route, indium particles were prepared in DEG without applying any surface stabilizer. In the second route, a phase transfer from DEG into dodecane while applying oleylamine as a surface stabilizer was demonstrated. XRD measurements verified the presence of crystalline indium for samples prepared via both routes. Samples prepared in DEG exhibited higher crystallinity than those transferred into dodecane; the reason for this remains to be investigated. According to SEM analysis, the particle sizes – or alternatively aggregate sizes – of samples prepared in DEG and transferred into dodecane were very similar: spherical particles with an average diameter of 27 nm were found for both routes. Via DLS analysis, the mean hydrodynamic diameters of the suspensions were 18 nm for indium particles transferred into dodecane and 38 nm for In^0 prepared in DEG. In addition, suspensions in dodecane were transparent, whereas suspensions prepared in DEG exhibited a turbid appearance. Thus, considering the optical appearance and DLS particle size data, In^0 particles transferred into dodecane were much less agglomerated than particles prepared in DEG. Hence, the application of oleylamine as a surface stabilizer made a successful phase transfer of non-agglomerated indium nanoparticles into dodecane possible. Finally, TEM investigations of indium particles transferred into pentane evidenced particles of about 10 nm in size. Thus, further TEM investigations are needed in order to determine the true particle size of particles prepared in DEG and transferred into dodecane.

5 Conclusions

5.1 Summary

The focus of this work was the preparation of suspensions containing transparent conductive oxide (TCO) nanoparticles. TCO materials are typically applied as transparent electrodes in e.g. solar cells or flat panel displays. In order to apply coating or printing techniques, which are significantly cheaper than standard gas-phase deposition processes, suspensions of TCO nanoparticles are required. The goal of the studies presented in this thesis was the synthesis of crystalline, non-agglomerated, redispersible TCO nanoparticles with a narrow particle size distribution. To this end, the approach to utilize a microwave-assisted polyol synthetic route turned out to be successful.

Initially, suspensions of a number of well-known n-doped TCO materials were synthesized: indium tin oxide (ITO), doped zinc oxide, and doped tin oxide. Microwave-assisted heating turned out to be beneficial regarding material crystallinity. As a result, as-prepared ITO particles were highly conductive. On the other hand, synthesized ZnO and SnO₂ particles were conductive only after a certain post-treatment was carried out, although they were crystalline and the insertion of dopants was evidenced. As a proof of concept, transparent conductive thin layers of ITO as well as doped ZnO were prepared. In addition to standard TCO materials, other binary and ternary oxides were achieved on the nanoscale. Tin-doped zinc indium oxide was revealed to be transparent and with a conductivity similar to ITO, despite its considerably lower indium content. Furthermore, in this work solid state NMR was applied for the first time as an analytical tool for the investigation of TCO nanoparticles. The results of the studies of the local structure of dopants in the host lattices are expected to lead to enhancement of synthesis and thereby improved conductivities. Finally, the scope of the study was extended from oxides to less noble elementary metals. To this end, nanoscale, crystalline elementary indium particles were prepared and a phase transfer of synthesized metal particles was demonstrated.

Via microwave-assisted heating, transparent, blue, colloiddally stable suspensions of ITO were prepared in diethylene glycol (DEG). Nanoscale ITO was realized with a high yield and analytical methods showed a very good agreement concerning a particle size of 15-19 nm. The particles were practically non-agglomerated and with a narrow particle size distribution. As-prepared ITO powders were highly crystalline due to the advantageous effect of microwave-assisted heating, in contrast to experiments where a heating mantle was employed. As a result, as-prepared ITO particles exhibited a low resistivity ($1.1 \cdot 10^{-2} \Omega\text{cm}$) and a high reflectivity in the infrared. As a proof of concept, a simple layer formation process via direct deposition of as-prepared ITO suspensions on glass plates was carried out. Due to the incompactness of these layers, thermal post-treatment was necessary in order to increase particle-to-particle contacts. Post-treated layers were with a visible transmittance similar to the uncoated glass substrate and a low resistivity ($1.2 \cdot 10^{-2} \Omega\text{cm}$).

Colloiddally stable aluminium- and indium-doped zinc oxide as well as fluorine- and tantalum-doped tin oxide suspensions were also prepared in DEG via microwave polyol synthesis. The average diameter of as-prepared doped zinc oxide particles was determined to be 10 to 15 nm by several independent analytical tools. ZnO:In (IZO) samples were practically non-agglomerated while ZnO:Al (AZO) samples exhibited a low degree of agglomeration. On the other hand, as-prepared doped SnO₂ particles were 3-4 nm in diameter and formed into small aggregates. All samples were non-conductive directly after synthesis, despite that they were crystalline and the insertion of dopants was evidenced. However, after a suitable post-treatment, resistivities of $2.0 \cdot 10^{-1} \Omega\text{cm}$ and $5.7 \cdot 10^{-1} \Omega\text{cm}$ were obtained for IZO and AZO

powder samples. Analogous to ITO, thin layers were prepared from as-prepared IZO and AZO suspensions. Subsequent to thermal treatment, the resulting layers exhibited a visible transmittance of about 80 % and a comparably low resistivity (IZO: $2.1 \cdot 10^{-1} \Omega\text{cm}$, AZO: $2.6 \cdot 10^{-1} \Omega\text{cm}$). Post-treated tin oxide powders exhibited resistivities of $1.5 \cdot 10^0 \Omega\text{cm}$ (tantalum-doped) and $1.9 \cdot 10^{-1} \Omega\text{cm}$ (fluorine-doped). Investigations concerning doping concentration showed that an increased amount of introduced dopants caused the conductivity of $\text{SnO}_2\text{:F}$ (FTO) to increase, whereas the conductivity of AZO declined. All particles were coated with large amounts of DEG, which causes a low conductivity of as-prepared samples.

In addition, suspensions of cerium oxide, lanthanum hydroxide, zinc aluminium oxide, zinc gallium oxide and zinc indium oxide were prepared in DEG via microwave-assisted heating. As-prepared CeO_2 , and $\text{La}(\text{OH})_3$ were crystalline, whereas the ternary oxides were amorphous directly after synthesis and thus had to be tempered to crystallize. In general, as-prepared particles were 10 to 20 nm in diameter. Although most samples were non-conductive even after post-treatment, it was discovered that a synthesized tin-doped zinc indium oxide sample exhibited a conductivity comparable to ITO subsequent to thermal treatment. In addition, the estimated bandgap of zinc indium oxide showed that it was transparent in the visible wavelength interval. Thus, in addition to binary transparent conductive oxides, the preparation of a ternary TCO material proved to be successful. The crystal structure of the prepared substance has not yet been fully determined. Nevertheless, considering that tin-doped zinc indium oxide exhibited a conductivity comparable to ITO and contains a significantly lower amount of indium, this substance represents a very interesting alternative TCO material.

In this work, solid state NMR was applied for the first time as an analytical tool for the investigation of TCO nanomaterials, in particular AZO and FTO. NMR provides a unique opportunity for understanding how dopants are inserted in host lattices, which is highly relevant for the conductivity of TCO materials. Although DEG coating is obviously a factor which could hinder particle-to-particle conductivity, NMR investigations revealed that even the AZO and FTO particles themselves were non-conductive directly after synthesis. In addition, for AZO it was discovered that only a certain amount of dopants were inserted in the crystalline core of the particle whereas additionally introduced dopants were added to an amorphous shell. Apparently, if too much Al was added, the amorphous shell caused the particle conductivity to decline. On the other hand, NMR analysis of fluorine-doped tin oxide revealed that all F^- ions were incorporated in the SnO_2 lattice at O^{2-} sites and were located in a Sn^{II} environment. However, only about a tenth of the introduced dopants were evidenced to be actually present in the sample. Furthermore, Mössbauer spectroscopy showed that post-treated conductive $\text{SnO}_2\text{:F}$ contained a few percent divalent tin.

Finally, the scope of study was extended from oxides to less noble elementary metals. As a case study, elementary indium particles were synthesized. In contrast to previous works concerned with more noble metals, in which polyols were applied as reducing agents as well as solvents, here the introduction of an additional reducing agent was necessary. As-prepared particles were nanoscale and crystalline. However, suspensions prepared in DEG turned out to be turbid and agglomerated. Thus, DEG did not prove to be a sufficient stabilizer of metal particle surfaces. In order to obtain transparent, stable suspensions of elementary metals, an additional surface stabilizer was applied. In addition, this made a phase transfer of metal particles into a nonpolar phase possible.

Thus, according to the studies presented in this thesis, microwave-assisted polyol synthesis was shown to be a versatile method for the preparation of suspensions of nanoscale transparent conductive oxides and other functional materials. The polyol method is a facile, low-cost process, in which less harmful chemicals and solvents are applied throughout. In

particular, polyol-mediated synthesis has great potential for industrial application. Due to the high boiling point of the solvent, crystalline materials can be synthesized at ambient pressure. There is thus no need for a closed high-pressure chamber, which naturally reduces production expenses. Another cost advantage is that synthesis is not carried out under vacuum conditions. These factors imply that an open system can be utilized, in which samples are simply vented with protective gas in order to prohibit oxidation of the solvent. All syntheses were carried out with precursors – mainly simple metal salts – purchasable from standard chemical manufacturers which do not need further refinement. In principle, the prepared nanomaterials are realizable in large quantities and obtainable via industrial continuous processes.

5.2 Outlook

The microwave-assisted polyol synthesis turned out to be a successful route for the preparation of nanoscale transparent conductive oxides. Future research goals can be divided into short-term and long-term goals. On a short-term basis, the materials that were prepared and presented in this thesis can certainly be enhanced concerning the conductivity of thin layers as well as that of powders. Long-term goals are e.g. the preparation of new TCO materials – possibly in new forms – and the application of them in devices.

For thin layers, optimization of parameters such as viscosity, solids content, type of solvent, or substrate preconditioning as well as application of professional printing techniques and enhanced post-treatment are expected to result in significantly improved conductivities. In terms of improving the conductivities of powders, synthesis parameters such as inserted doping concentration, applied precursors, heating time and temperature can be further optimized. Concerning doping concentration, improvements are expected e.g. for fluorine-doped tin oxide by introducing an amount of dopants higher than the investigated 10 mol-%. For aluminium-doped zinc oxide, the opposite applies. Here, an introduced doping concentration lower than the tested 1 mol-% is expected to enhance the conductivity. In addition, it is anticipated that further investigations via solid state NMR spectroscopy of these and other substances can shed more light on how dopants are inserted into host lattices.

An example of how the applied precursors can result in increased conductivities is given by FTO. Since post-treated conductive tin oxide powders contain a few percent of divalent tin and fluorine is located in a Sn^{II} environment, SnF₂ seems a logical choice for a precursor which hopefully can be incorporated to a higher degree in the lattice. Furthermore, especially for dopants that are difficult to insert in the host lattice in question, longer heating times and/or higher heating temperatures could improve the degree of dopant insertion, and thereby also material conductivity. For example, it is easier to insert Sn⁴⁺ dopants in the In₂O₃ lattice than it is to insert Al³⁺ dopants in the ZnO lattice. However, ITO suspensions were heated for 2 h at 200 °C, whereas ZnO suspensions were heated for 30 min at the same temperature. Thus, it will certainly be worthwhile to investigate if longer heating times and/or higher heating temperatures could improve the conductivities of doped zinc oxide.

Considering the highly conductive ternary tin-doped zinc indium oxide, work still needs to be done in order to realize a phase pure material. This is expected to be achievable via systematic variation of the Zn:In molar ratio between 1:1 and 1:2. In addition, since a relatively large part of the introduced indium was found not to take part in any reaction, finding a way to obtain a better yield, possibly with the application of other precursors, would be beneficial. More importantly, however, the crystal structure of the prepared material needs to be determined. Regarding this issue, calculations are still in progress.

As ternary oxides represent an interesting option for finding new TCO materials with improved conductivities, it will definitely be worthwhile to explore this area in more detail.

Important here would be finding a way of preparing crystalline ternary oxides without the need for additional tempering. Possibly, this could be achieved via reactions under high pressure. Alternatively, thin layers could be prepared of as-prepared amorphous ternary oxides which could crystallize during post-treatment. Furthermore, research on ternary TCO materials is relatively new and it is expected that new combinations of elements giving rise to further improved conductivities can still be found.

Elementary metals were here only synthesized as a case study concerning the possibility to prepare metal nanoparticles of elements for which the reducing properties of the solvent are not strong enough to reduce the metal precursor in question. Therefore, in this work an additional reducing agent was introduced. It can be assumed that yet many more elementary metals can be synthesized in a similar way. In the future, these metals could be applied as precursors for the synthesis of nanoscale compounds containing the metal in question. In addition, elementary metals prepared via polyol-mediated synthesis might also be applied as catalysts.

As stated earlier, the motivation behind the preparation of suspensions with application as printable inks is reducing the waste of material while creating a certain pattern. In addition, other ways of reducing the needed TCO material can be considered. To this end, it would be possible to reduce the amount of TCO material present in the individual particles. Preparation of hollow spheres of transparent conductive oxides would result in particles that mainly consist of air, which naturally implies tremendous material savings. However, if post-treatment is necessary, hollow spheres may not be hard enough for a prepared thin layer to remain continuous and thereby conductive. In order to solve this problem, a core/shell structure could be conceived. Here, the shell would consist of a highly conductive TCO material such as ITO, whereas the core, from which the main part of the particle is made up of, would consist of a cheaper material, e.g. SnO₂. A core/shell structure would result in considerable material cost reductions, while hopefully maintaining a high conductivity.

Moreover, the TCO materials synthesized in this work were all well-known n-conductive substances. It would certainly be an interesting challenge to prepare p-doped materials with the polyol method. In particular, the realization of a material for which a good conductivity is achievable both via n-dopants and p-dopants would lead to many technical advantages. Such a material would namely be beneficial with respect to the preparation of p-n junctions, for which it is important that the bandgaps of the n and p materials are not too different. Thus, finally, when the conductivity of materials as well as the deposition techniques have been optimized, prepared suspensions could be tested for practical use in real devices.

Combing the concepts of the two previous paragraphs, a core/shell structure consisting of one p-doped and one n-doped material could be conceived. In this way, each single particle would itself constitute a p-n junction. The assembly of these miniature p-n junctions into two- or three-dimensional structures could certainly lead to interesting electrical and optical properties as well as new devices.

6 Acknowledgements

This work was carried out in cooperation with Evonik Degussa GmbH, Marl: projects of the Science-to-Business Center Nanotronics are financially supported by the state of North-Rhine-Westphalia in Germany and are co-financed by the European Union. The Center for Functional Nanostructures (CFN) of the Deutsche Forschungsgemeinschaft (DFG) at the University of Karlsruhe (TH) is also acknowledged for financial support.

My supervisor Prof. Dr Claus Feldmann is thanked for giving me the opportunity to work in his group on this interesting subject, for his support, interest, and many fruitful suggestions and discussions, for the good working conditions in his group, for taking the risk of letting a non-chemist candidate for a doctor's degree in chemistry, and for introducing me to chemical synthesis.

Dr. Anna Prodi-Schwab, Dr. Detlef Thölmann, and Rita Fügemann have been responsible for the project on behalf of Evonik Degussa GmbH and are thanked for their support, for many fruitful discussions and for a nice cooperation.

Yamini Avadhut and Dr. Jörn Schmedt auf der Günne in the research group of Prof. Dr. W. Schnick, Department of Chemistry and Biochemistry, Munich University (LMU) are thanked for measuring and interpreting the solid state NMR spectra presented in this thesis, for answering all my questions about NMR and for a nice cooperation.

I. Schellenberg and Prof. Dr. R. Pöttgen, Institut für Anorganische und Analytische Chemie, Universität Münster are thanked for measuring and interpreting the Mössbauer spectrum presented in this thesis.

The TEM images presented in this thesis were taken by Dipl. Phys. W. Send (ITO and SnO₂:F) and Dr. R. Popescu (ZnO:In and In) in the research group of Prof. Dr. D. Gerthsen, Laboratory for Electron Microscopy, University of Karlsruhe (TH).

The four-point probe measuring station was constructed by Dr.-Ing. A. Weber in the research group of Prof. Dr.-Ing. E. Ivers-Tiffée, Institute of Materials for Electrical Engineering, University of Karlsruhe (TH).

Dr. Helmut Goesmann is thanked for X-ray single crystal measurements.

Sabine Lude, my laboratory assistant for one year, has contributed a lot to this work and has been of invaluable help. Ich danke dir!

Dominic Freudenmann and Eva Eisenhauer, chemistry students, have conducted practical training in my laboratory for six weeks each and are thanked for their contributions to this work.

Zum Schluss möchte ich alle meine Kollegen für eure Freundschaft und für die schöne Zeit, die wir zusammen verbracht haben, danken!

7 References

- [1] C. G. Granqvist, A. Hultaker, *Thin Solid Films* **2002**, *411*, 1.
- [2] K. L. Chopra, S. Major, D. K. Pandya, *Thin Solid Films* **1983**, *102*, 1.
- [3] T. Minami, *Semicond. Sci. Technol.* **2005**, *20*, S35.
- [4] D. S. Ginley, C. Bright, *MRS Bull.* **2000**, *25*, 15.
- [5] B. G. Lewis, D. C. Paine, *MRS Bull.* **2000**, *25*, 22.
- [6] R. G. Gordon, *MRS Bull.* **2000**, *25*, 52.
- [7] J. Ederth, P. Heszler, A. Hultaker, G. A. Niklasson, C. G. Granqvist, *Thin Solid Films* **2003**, *445*, 199.
- [8] R. A. Street, W. S. Wong, S. E. Ready, M. L. Chabinyk, A. C. Arias, S. Limb, A. Salleo, R. Lujan, *Materials Today* **2006**, *9*, 32.
- [9] D.-H. Lee, Y.-J. Chang, G. S. Herman, C.-H. Chang, *Adv. Mater.* **2007**, *19*, 843.
- [10] Y. Xia, B. Gates, Y. Yin, Y. Lu, *Adv. Mater.* **2000**, *12*, 693.
- [11] B. L. Cushing, V. L. Kolesnichenko, C. J. O'Connor, *Chem. Rev.* **2004**, *104*, 3893.
- [12] J. Park, J. Joo, S. G. Kwon, Y. Jang, T. Hyeon, *Angew. Chem., Int. Ed.* **2007**, *46*, 4630.
- [13] D. Shi, *Functional Thin Films and Functional Materials: New Concepts and Technologies*, Springer, **2003**.
- [14] Z. Ma, S. Dai, *Mater. Technol.* **2008**, *23*, 81.
- [15] P. C. Stair, *J. Chem. Phys.* **2008**, *128*, 182507/1.
- [16] T. Trindade, P. O'Brien, N. L. Pickett, *Chem. Mater.* **2001**, *13*, 3843.
- [17] A. P. Alivisatos, *Science* **1996**, *271*, 933.
- [18] K. J. Klabunde, *Nanoscale Materials in Chemistry*, John Wiley & Sons, **2001**.
- [19] L. M. Liz-Marzan, P. V. Kamat, *Nanoscale Materials*, Kluwer Academic Publishers, **2003**.
- [20] G. Ozin, A. Arsenault, *Nanochemistry: A Chemistry Approach to Nanomaterials*, Royal Society of Chemistry, **2005**.
- [21] C. N. R. Rao, A. Mueller, A. K. Cheetham, *Nanomaterials Chemistry: Recent Developments and New Directions*, Wiley-VCH, **2007**.
- [22] M. A. Aegerter, M. Mennig, *Sol-Gel Technologies for Glass Producers and Users*, Kluwer Academic Publishers, **2004**.
- [23] J. Livage, M. Henry, C. Sanchez, *Prog. Solid State Chem.* **1988**, *18*, 259.
- [24] J. D. MacKenzie, E. P. Bescher, *Acc. Chem. Res.* **2007**, *40*, 810.
- [25] C. Destree, J. B. Nagy, *Adv. Colloid Interface Sci.* **2006**, *123-126*, 353.
- [26] K. Byrappa, T. Adschiri, *Prog. Cryst. Growth Charact. Mater.* **2007**, *53*, 117.
- [27] G. Demazeau, *J. Mater. Sci.* **2008**, *43*, 2104.
- [28] F. Fievet, J. P. Lagier, M. Figlarz, *MRS Bull.* **1989**, *14*, 29.
- [29] P. Toneguzzo, G. Viau, O. Acher, F. Guillet, E. Bruneton, F. Fievet-Vincent, F. Fievet, *J. Mater. Sci.* **2000**, *35*, 3767.
- [30] D. Jezequel, J. Guenot, N. Jouini, F. Fievet, *J. Mater. Res.* **1995**, *10*, 77.
- [31] C. Feldmann, *Adv. Funct. Mater.* **2003**, *13*, 101.
- [32] C. Feldmann, H.-O. Jungk, *Angew. Chem., Int. Ed.* **2001**, *40*, 359.
- [33] C. Feldmann, C. Metzmacher, *J. Mater. Chem.* **2001**, *11*, 2603.
- [34] C. Feldmann, M. Roming, K. Trampert, *Small* **2006**, *2*, 1248.
- [35] X. Jiang, Y. Wang, T. Herricks, Y. Xia, *J. Mater. Chem.* **2004**, *14*, 695.
- [36] A. Mueller, O. Heim, M. Panneerselvam, M. Willert-Porada, *Mater. Res. Bull.* **2005**, *40*, 2153.
- [37] C. Feldmann, *Solid State Sci.* **2005**, *7*, 868.
- [38] C. Feldmann, *Scr. Mater.* **2001**, *44*, 2193.

-
- [39] O. Palchik, R. Kerner, A. Gedanken, A. M. Weiss, M. A. Slifkin, V. Palchik, *J. Mater. Chem.* **2001**, *11*, 874.
- [40] S. Komarneni, D. Li, B. Newalkar, H. Katsuki, A. S. Bhalla, *Langmuir* **2002**, *18*, 5959.
- [41] M. Tsuji, N. Miyamae, M. Hashimoto, M. Nishio, S. Hikino, N. Ishigami, I. Tanaka, *Colloids Surf., A* **2007**, *302*, 587.
- [42] Z. Liu, Z. Sun, B. Han, J. Zhang, J. Huang, J. Du, S. Miao, *J. Nanosci. Nanotechnol.* **2006**, *6*, 175.
- [43] G. Buehler, D. Thoelmann, C. Feldmann, *Adv. Mater.* **2007**, *19*, 2224.
- [44] G. Buehler, C. Feldmann, *Angew. Chem., Int. Ed.* **2006**, *45*, 4864.
- [45] D. R. Lide, *CRC Handbook of Chemistry and Physics*, 86th ed., CRC Press, **2005**.
- [46] I. Pastoriza-Santos, L. M. Liz-Marzan, *Langmuir* **2002**, *18*, 2888.
- [47] D. M. P. Mingos, D. R. Baghurst, *Chem. Soc. Rev.* **1991**, *20*, 1.
- [48] C. Gabriel, S. Gabriel, E. H. Grant, E. H. Grant, B. S. J. Halstead, D. M. P. Mingos, *Chem. Soc. Rev.* **1998**, *27*, 213.
- [49] P. J. Goodhew, J. Humphreys, R. Beanland, *Electron Microscopy and Analysis*, 3rd ed., Taylor & Francis, **2001**.
- [50] L. Reimer, *Scanning Electron Microscopy*, 2nd ed., Springer, **1998**.
- [51] L. Reimer, *Transmission Electron Microscopy: Physics of Image Formation and Microanalysis*, 4th ed., Springer, **1997**.
- [52] A. R. West, *Solid State Chemistry and its Applications*, John Wiley & Sons, **1984**.
- [53] W. Clegg, *Crystal Structure Determination*, Oxford University Press, **2004**.
- [54] W. Massa, *Crystal Structure Determination*, 2nd ed., Springer, **2004**.
- [55] I. D. Morrison, S. Ross, *Colloidal Dispersions: Suspensions, Emulsions, and Foams*, Wiley-Interscience, **2002**.
- [56] E. Kissa, *Dispersions: characterization, testing, and measurement*, Dekker, **1999**.
- [57] N. De Jaeger, H. Demeyere, R. Finsy, R. Sneyers, J. Vanderdeelen, P. Van der Meeren, M. Van Laethem, *Part. Part. Syst. Charact.* **1991**, *8*, 179.
- [58] R. Finsy, N. De Jaeger, R. Sneyers, E. Gelade, *Part. Part. Syst. Charact.* **1992**, *9*, 125.
- [59] B. J. Berne, R. Pecora, *Dynamic Light Scattering: with Applications to Chemistry, Biology, and Physics*, Wiley-Interscience, **1975**.
- [60] H. C. van de Hulst, *Light Scattering by Small Particles*, Dover, **1982**.
- [61] P. W. Atkins, *Physical Chemistry*, 6th ed., Oxford University Press, **1998**.
- [62] S. Brunauer, P. H. Emmett, E. Teller, *J. Am. Chem. Soc.* **1938**, *60*, 309.
- [63] S. Brunauer, L. S. Deming, W. E. Deming, E. Teller, *J. Am. Chem. Soc.* **1940**, *62*, 1723.
- [64] D. Myers, *Surfaces, Interfaces, and Colloids: Principles and Applications*, VCH, **1991**.
- [65] P. J. Haines, Editor, *Principles of Thermal Analysis and Calorimetry*, Royal Society of Chemistry, **2002**.
- [66] D. K. Schroder, *Semiconductor Materials and Device Characterization*, 2nd ed., John Wiley & Sons, **1998**.
- [67] S. M. Sze, *Semiconductor Devices: Physics and Technology*, 2nd ed., John Wiley & Sons, **2001**.
- [68] L. B. Valdes, *Proc. IRE* **1954**, *42*, 420.
- [69] H. Günzler, H.-U. Gremlich, *IR spectroscopy: An Introduction*, Wiley-VCH, **2002**.
- [70] M. Hesse, H. Meier, B. Zeeh, *Spectroscopic Methods in Organic Chemistry*, Thieme, **1995**.
- [71] J. Sole, L. Bausa, D. Jaque, *An Introduction to the Optical Spectroscopy of Organic Solids*, Wiley, **2005**.

- [72] J. Tauc, R. Grigorovici, A. Vancu, *Phys. Status Solidi* **1966**, *15*, 627.
- [73] E. D. Becker, *High Resolution NMR: Theory and Chemical Applications*, 3rd ed., Academic, **1999**.
- [74] D. D. Laws, H.-M. L. Bitter, A. Jerschow, *Angew. Chem., Int. Ed.* **2002**, *41*, 3096.
- [75] R. V. Parish, *NMR, NQR, EPR, and Mössbauer spectroscopy in inorganic chemistry*, Ellis Horwood, **1990**.
- [76] I. Hamberg, C. G. Granqvist, *J. Appl. Phys.* **1986**, *60*, R123.
- [77] D.-W. Kim, S.-G. Oh, J.-D. Lee, *Langmuir* **1999**, *15*, 1599.
- [78] H. Xu, G. Zhu, H. Zhou, A. Yu, *J. Am. Ceram. Soc.* **2005**, *88*, 986.
- [79] J.-S. Lee, S.-C. Choi, *J. Eur. Ceram. Soc.* **2005**, *25*, 3307.
- [80] D. Fattakhova-Rohlfing, T. Brezesinski, J. Rathousky, A. Feldhoff, T. Oekermann, M. Wark, B. Smarsly, *Adv. Mater.* **2006**, *18*, 2980.
- [81] J. Ba, D. Fattakhova Rohlffing, A. Feldhoff, T. Brezesinski, I. Djerdj, M. Wark, M. Niederberger, *Chem. Mater.* **2006**, *18*, 2848.
- [82] R. Bel Hadj Tahar, T. Ban, Y. Ohya, Y. Takahashi, *J. Appl. Phys.* **1997**, *82*, 865.
- [83] E. Hammarberg, A. Prodi-Schwab, C. Feldmann, *Thin Solid Films* **2008**, *516*, 7437.
- [84] C. Feldmann, E. Hammarberg, D. Thölmann, *Patent Application* **2007**, DE 102006015540.
- [85] H. E. Swanson, N. T. Gilfrich, G. M. Ugrinic, *Natl. Bur. Stand. Circ.* **1955**, *539*, 75.
- [86] W. Ostwald, *Z. Phys. Chem.* **1879**, *22*, 289.
- [87] C. Feldmann, *Z. Anorg. Allg. Chem.* **2004**, *630*, 2473.
- [88] C. Feldmann, S. Matschulo, S. Ahlert, *J. Mater. Sci.* **2007**, *42*, 7076.
- [89] I. Hamberg, C. G. Granqvist, *Appl. Opt.* **1985**, *24*, 1815.
- [90] C. Klingshirn, *ChemPhysChem* **2007**, *8*, 782.
- [91] U. Ozgur, Y. I. Alivov, C. Liu, A. Teke, M. A. Reshchikov, S. Dogan, V. Avrutin, S. J. Cho, H. Morkoc, *J. Appl. Phys.* **2005**, *98*, 041301/1.
- [92] M. Hilgendorff, L. Spanhel, C. Rothenhäusler, G. Müller, *J. Electrochem. Soc.* **1998**, *145*, 3632.
- [93] T. Schuler, M. A. Aegerter, *Thin Solid Films* **1999**, *351*, 125.
- [94] J.-H. Lee, B.-O. Park, *Thin Solid Films* **2003**, *426*, 94.
- [95] V. Musat, B. Teixeira, E. Fortunato, R. C. C. Monteiro, P. Vilarinho, *Surf. Coat. Technol.* **2004**, *180-181*, 659.
- [96] E. J. Luna-Arredondo, A. Maldonado, R. Asomoza, D. R. Acosta, M. A. Melendez-Lira, M. de la L. Olvera, *Thin Solid Films* **2005**, *490*, 132.
- [97] Z. Q. Xu, H. Deng, Y. Li, Q. H. Guo, Y. R. Li, *Mater. Res. Bull.* **2006**, *41*, 354.
- [98] K.-m. Lin, P. Tsai, *Thin Solid Films* **2007**, *515*, 8601.
- [99] M. Niederberger, *Acc. Chem. Res.* **2007**, *40*, 793.
- [100] E. Hammarberg, A. Prodi-Schwab, C. Feldmann, *submitted*.
- [101] W. L. Bragg, *Philos. Mag.* **1920**, *39*, 647.
- [102] P. Y. Emelie, J. D. Phillips, B. Buller, U. D. Venkateswaran, *J. Electron. Mater.* **2006**, *35*, 525.
- [103] G. A. Parks, *Chem. Rev.* **1965**, *65*, 177.
- [104] R. E. Marotti, P. Giorgi, G. Machado, E. A. Dalchiele, *Sol. Energy Mater. Sol. Cells* **2006**, *90*, 2356.
- [105] T. Ren, H. R. Baker, K. M. Poduska, *Thin Solid Films* **2007**, *515*, 7976.
- [106] E. Burstein, *Phys. Rev.* **1954**, *93*, 632.
- [107] T. S. Moss, *Proc. Phys. Soc., London* **1954**, *67B*, 775.
- [108] Z. Q. Li, D. X. Zhang, J. J. Lin, *J. Appl. Phys.* **2006**, *99*, 124906/1.
- [109] R. K. Shukla, A. Srivastava, A. Srivastava, K. C. Dubey, *J. Cryst. Growth* **2006**, *294*, 427.

-
- [110] B. Joseph, P. K. Manoj, V. K. Vaidyan, *Bull. Mater. Sci.* **2005**, *28*, 487.
- [111] G. Machado, D. N. Guerra, D. Leinen, J. R. Ramos-Barrado, R. E. Marotti, E. A. Dalchiele, *Thin Solid Films* **2005**, *490*, 124.
- [112] M. A. Lucio-Lopez, M. A. Luna-Arias, A. Maldonado, M. de la L. Olvera, D. R. Acosta, *Sol. Energy Mater. Sol. Cells* **2006**, *90*, 733.
- [113] R. A. Andrievski, *J. Mater. Sci.* **1994**, *29*, 614.
- [114] Y. Avadhut, J. Schmedt auf der Guenne, E. Hammarberg, C. Feldmann, *in preparation*.
- [115] K. J. D. MacKenzie, M. E. Smith, *Multinuclear Solid-State Nuclear Magnetic Resonance of Inorganic Materials*, Pergamon, **2002**.
- [116] A. Gamard, O. Babot, B. Jousseume, M.-C. Rascle, T. Toupance, G. Campet, *Chem. Mater.* **2000**, *12*, 3419.
- [117] D. Boegeat, B. Jousseume, T. Toupance, G. Campet, L. Fournes, *Inorg. Chem.* **2000**, *39*, 3924.
- [118] A. N. Banerjee, R. Maity, S. Kundoo, K. K. Chattopadhyay, *Phys. Status Solidi A* **2004**, *201*, 983.
- [119] P. K. Biswas, L. Dua, A. De, T. Chaudhuri, *Mater. Sci.* **2006**, *24*, 367.
- [120] A. Kurz, K. Brakecha, J. Puetz, M. A. Aegerter, *Thin Solid Films* **2006**, *502*, 212.
- [121] G. J. McCarthy, J. M. Welton, *Powder Diffr.* **1989**, *4*, 156.
- [122] Y. Avadhut, J. Schmedt auf der Guenne, E. Hammarberg, C. Feldmann, I. Schellenberg, R. Poettgen, *in preparation*.
- [123] P. E. Lippens, *Phys. Rev. B* **1999**, *60*, 4576.
- [124] P. E. Lippens, J. Olivier-Fourcade, J. C. Jumas, *Hyperfine Interact.* **2000**, *126*, 137.
- [125] T. Birchall, G. Denes, K. Ruebenbauer, J. Pannetier, *J. Chem. Soc., Dalton Trans.* **1981**, 2296.
- [126] T. Birchall, G. Denes, K. Ruebenbauer, J. Pannetier, *Hyperfine Interact.* **1986**, *29*, 1327.
- [127] G. Denes, E. Laou, *Hyperfine Interact.* **1994**, *92*, 1013.
- [128] L. Fournes, J. Grannec, C. Mirambet, B. Darriet, P. Hagenmuller, *Z. Anorg. Allg. Chem.* **1991**, *601*, 93.
- [129] J. K. Lees, P. A. Flinn, *J. Chem. Phys.* **1968**, *48*, 882.
- [130] P. A. Flinn, *in: Mössbauer Isomer Shifts*, G. K. Shenoy, F. E. Wagner (eds.), **1978**, pp 593.
- [131] R. Tala-Ighil, M. Boumaour, M. S. Belkaid, A. Maallemi, K. Melhani, A. Iratni, *Sol. Energy Mater. Sol. Cells* **2006**, *90*, 1797.
- [132] C. Jagadish, A. L. Dawar, S. Sharma, P. K. Shishodia, K. N. Tripathi, P. C. Mathur, *Mater. Lett.* **1988**, *6*, 149.
- [133] C. Cossement, J. Darville, J. M. Gilles, J. B. Nagy, C. Fernandez, J. P. Amoureux, *Magn. Reson. Chem.* **1992**, *30*, 263.
- [134] J. S. Knyrim, F. M. Schappacher, R. Poettgen, J. Schmedt auf der Guenne, D. Johrendt, H. Huppertz, *Chem. Mater.* **2007**, *19*, 254.
- [135] W. H. Baur, *Acta Crystallogr.* **1956**, *9*, 515.
- [136] B. C. H. Steele, *Solid State Ionics* **2000**, *129*, 95.
- [137] M. Hirano, M. Inagaki, *J. Mater. Chem.* **2000**, *10*, 473.
- [138] A. I. Y. Tok, L. H. Luo, F. Y. C. Boey, *Mater. Sci. Eng., A* **2004**, *A383*, 229.
- [139] X. D. Zhou, W. Huebner, H. U. Anderson, *Chem. Mater.* **2003**, *15*, 378.
- [140] H. Yang, C. Huang, A. Tang, X. Zhang, W. Yang, *Mater. Res. Bull.* **2005**, *40*, 1690.
- [141] T. Taniguchi, T. Watanabe, N. Sakamoto, N. Matsushita, M. Yoshimura, *Cryst. Growth Des.* **2008**, *8*, 3725.

- [142] M. J. Godinho, R. F. Goncalves, L. P. S. Santos, J. A. Varela, E. Longo, E. R. Leite, *Mater. Lett.* **2007**, *61*, 1904.
- [143] D. Taylor, *Br. Ceram. Trans. J.* **1984**, *83*, 32.
- [144] S. Irusta, L. M. Cornaglia, E. A. Lombardo, *Mater. Chem. Phys.* **2004**, *86*, 440.
- [145] Y. Jiang, Y. Wu, Y. Xie, Y.-T. Qian, *J. Am. Ceram. Soc.* **2000**, *83*, 2628.
- [146] X. Wang, Y. Li, *Angew. Chem., Int. Ed.* **2002**, *41*, 4790.
- [147] X. Wang, Y. Li, *Chem. Eur. J.* **2003**, *9*, 5627.
- [148] X. Ma, H. Zhang, Y. Ji, J. Xu, D. Yang, *Mater. Lett.* **2004**, *58*, 1180.
- [149] C. Hu, H. Liu, W. Dong, Y. Zhang, G. Bao, C. Lao, Z. L. Wang, *Adv. Mater.* **2007**, *19*, 470.
- [150] G. W. Beall, W. O. Milligan, H. A. Wolcott, *J. Inorg. Nucl. Chem.* **1977**, *39*, 65.
- [151] S. Mathur, M. Veith, M. Haas, H. Shen, N. Lecerf, V. Huch, S. Hufner, R. Haberkorn, H. P. Beck, M. Jilavi, *J. Am. Ceram. Soc.* **2001**, *84*, 1921.
- [152] A. E. Giannakas, T. C. Vaimakis, A. K. Ladavos, P. N. Trikalitis, P. J. Pomonis, *J. Colloid Interface Sci.* **2003**, *259*, 244.
- [153] X. Duan, D. Yuan, Z. Sun, C. Luan, D. Pan, D. Xu, M. Lu, *J. Alloys Compd.* **2005**, *386*, 311.
- [154] M. Zawadzki, *Solid State Sci.* **2006**, *8*, 14.
- [155] H. E. Swanson, R. K. Fuyat, *Natl. Bur. Stand. Circ.* **1953**, *539*, 65.
- [156] T. Omata, N. Ueda, K. Ueda, H. Kawazoe, *Appl. Phys. Lett.* **1994**, *64*, 1077.
- [157] M. Hirano, N. Sakaida, *J. Am. Ceram. Soc.* **2002**, *85*, 1145.
- [158] S.-h. Wu, H.-C. Cheng, *J. Electrochem. Soc.* **2004**, *151*, H159.
- [159] K. Sung, T.-M. Chung, C. G. Kim, *Mater. Lett.* **2007**, *61*, 1011.
- [160] M. Wendschuh-Josties, H. S. C. O'Neill, K. Bente, G. Brey, *Neues Jahrb. Mineral., Monatsh.* **1995**, 273.
- [161] H. Kasper, *Z. Anorg. Allg. Chem.* **1967**, *349*, 113.
- [162] M. Nakamura, N. Kimizuka, T. Mohri, *J. Solid State Chem.* **1990**, *86*, 16.
- [163] T. Moriga, D. D. Edwards, T. O. Mason, G. B. Palmer, K. R. Poeppelmeier, J. L. Schindler, C. R. Kannewurf, I. Nakabayashi, *J. Am. Ceram. Soc.* **1998**, *81*, 1310.
- [164] N. Naghavi, C. Marcel, L. Dupont, A. Rougier, J.-B. Leriche, C. Guery, *J. Mater. Chem.* **2000**, *10*, 2315.
- [165] T. Minami, H. Sonohara, T. Kakumu, S. Takata, *Jpn. J. Appl. Phys.* **1995**, *34*, L971.
- [166] J. M. Phillips, R. J. Cava, G. A. Thomas, S. A. Carter, J. Kwo, T. Siegrist, J. J. Krajewski, J. H. Marshall, W. F. Peck, Jr., D. H. Rapkine, *Appl. Phys. Lett.* **1995**, *67*, 2246.
- [167] D. Charoenkul, D. D. Edwards, *J. Met., Mater. Miner.* **1999**, *9*, 9.
- [168] S.-Y. Lee, B.-O. Park, *Thin Solid Films* **2005**, *484*, 184.
- [169] A. Kurz, M. A. Aegerter, *Thin Solid Films* **2008**, *516*, 4513.
- [170] E. Hammarberg, A. Prodi-Schwab, C. Feldmann, *in preparation*.
- [171] J. M. Nedeljkovic, O. I. Micic, S. P. Ahrenkiel, A. Miedaner, A. J. Nozik, *J. Am. Chem. Soc.* **2004**, *126*, 2632.
- [172] S. Kan, A. Aharoni, T. Mokari, U. Banin, *Faraday Discuss.* **2004**, *125*, 23.
- [173] N. H. Chou, X. Ke, P. Schiffer, R. E. Schaak, *J. Am. Chem. Soc.* **2008**, *130*, 8140.
- [174] E. Hammarberg, C. Feldmann, *Chem. Mater.* **2009**, *in press*.

8 Index of tables and figures

8.1 Index of tables

Table 1. Some examples of spin quantum numbers of nuclei.....	28
Table 2. Comparison of particle sizes of as-prepared ITO evidenced with various analytical tools.....	38
Table 3. Comparison of particle sizes of IZO and AZO evidenced with various analytical tools.....	43
Table 4. Radii of metal ions in doped ZnO. ^[45]	46
Table 5. Mean diameters of as-prepared and post-treated AZO samples with varying Al:Zn molar ratios deduced via SEM, XRD, and BET analysis.....	52
Table 6. Al:Zn molar ratios of AZO samples treated in air and forming gas: introduced and evidenced via EDX and quantitative analysis.....	56
Table 7. Mean particle diameters of as-prepared FTO (1 mol-%) and FTO (10 mol-%) suspensions measured via dynamic light scattering.....	64
Table 8. Mean diameters of as-prepared and post-treated FTO (1 mol-%) and FTO (10 mol-%) samples deduced via SEM, XRD, and BET analysis.....	70
Table 9. Resistance and resistivity of post-treated doped and undoped tin oxide samples according to four-point probing measurements.....	70
Table 10. F:Sn molar ratios of FTO samples treated in air and forming gas: introduced and evidenced via quantitative analysis.....	71
Table 11. Comparison of particle sizes of as-prepared CeO ₂ :Gd evidenced with various analytical tools.....	80
Table 12. Gd:Ce molar ratios of as-prepared gadolinium-doped cerium oxide samples: introduced and evidenced via EDX.....	80
Table 13. Radii of metal ions in doped CeO ₂ . ^[45]	81
Table 14. Radii of metal ions in doped ZnAl ₂ O ₄ . ^[45]	85
Table 15. Radii of metal ions in doped ZnGa ₂ O ₄ . ^[45]	89
Table 16. Zn:In molar ratios of post-treated zinc indium oxide samples; introduced during synthesis and evidenced via EDX.....	98
Table 17. Lattice parameters obtained for crystals formed by hydrothermal processing of tin-doped zinc indium oxide with a Zn:In molar ratio of 1:2.....	101
Table 18. Lattice parameters of Zn _k In ₂ O _{k+3} homologous compounds with k = 2, 3, and 4 according to Kasper. ^[161]	102

8.2 Index of figures

Figure 1. Experimental set-up of microwave-assisted polyol synthesis.....	4
Figure 2. Interaction processes between the incident electron beam and the sample.....	8
Figure 3. Sample, objective lens, and back focal and image plane in TEM.....	9
Figure 4. Some of the allowed transitions resulting in emission of characteristic X-rays.....	11
Figure 5. Diffraction of electromagnetic radiation according to Bragg's law.....	13
Figure 6. Diffraction pattern from a) single crystal and b) polycrystalline powder.....	14
Figure 7. Schematic set-up of a powder diffractometer.....	16
Figure 8. Schematic set-up of the four-point probing method.....	23
Figure 9. Possible electronic transitions that can be detected with UV-Vis spectroscopy.....	27
Figure 10. A $\pi/2$ pulse rotates \mathbf{M} from the z-axis with 90°	30
Figure 11. Magic angle spinning of sample in solid state NMR.....	31
Figure 12. a) Photograph of ITO nanocrystals in DEG (solids content: 0.62 wt-%), and b) Particle size distribution thereof, measured with dynamic light scattering.....	36

Figure 13. SEM image of as-prepared ITO nanocrystals.....	36
Figure 14. XRD pattern of as-prepared nanocrystalline ITO (reference: In ₂ O ₃ – ICDD No. 6-416) with diffraction peaks (222), (400), and (440) denoted.....	37
Figure 15. HRTEM image of as-prepared ITO nanocrystal with lattice plane distances denoted, where a corresponds to 10 lattice planes with a distance of 2.93 Å and b to 10 lattice planes with a distance of 2.54 Å.....	38
Figure 16. FT-IR spectra of ITO powder sample: as-prepared (solid), after thermal treatment in air at 500 °C (dashed), and after reduction with forming gas at 300 °C (dotted).	39
Figure 17. TG analysis of as-prepared ITO powder.....	39
Figure 18. UV-Vis spectra of ITO-coated (solid) and uncoated glass plate (dashed).	41
Figure 19. a) Photograph of AZO-I nanocrystals in DEG (solids content: 10 wt-%), and b) Particle size distribution thereof, measured with dynamic light scattering.	42
Figure 20. a) Photograph of IZO-I nanocrystals in DEG (solids content: 10 wt-%), and b) Particle size distribution thereof, measured with dynamic light scattering.	43
Figure 21. SEM images of as-prepared nanocrystals of a) IZO-I, b) AZO-I, c) IZO-II, and d) AZO-II.	44
Figure 22. TEM images of as-prepared IZO nanocrystals: a) overview image and b) HRTEM image.	45
Figure 23. a) XRD patterns of as-prepared nanocrystalline AZO (solid) and IZO (dashed) (reference: ZnO – ICDD No. 36-1451), and b) magnification of the three most intensive diffraction peaks (100), (002), and (101).	45
Figure 24. FT-IR spectra of AZO powder: as-prepared (cross) and after thermal treatment (circle).	47
Figure 25. TG analysis of as-prepared AZO (solid) and IZO (dashed).	47
Figure 26. Zeta Potential of as-prepared AZO (solid) and IZO (dashed) redispersed in water.	48
Figure 27. a) UV-Vis spectra and b) bandgap energy of powders of AZO (solid) and IZO (dotted): as-prepared (cross), after annealing in air (400 °C, 30 min, triangle), and after forming gas process (400 °C, 60 min, circle) in comparison to as-prepared ZnO (square).	49
Figure 28. SEM Images of thin layers of a) IZO and b) AZO on glass plates.....	49
Figure 29. a) UV-Vis spectra of AZO (solid) and IZO (dotted) layers on glass plates and b) estimation of the bandgap of these layers.	50
Figure 30. XRD patterns of as-prepared AZO samples with introduced Al:Zn molar ratios of 1 % (solid), 5 % (dashed), and 20 % (dotted).	51
Figure 31. SEM images of as-prepared AZO samples with Al:Zn molar ratios of a) 1 %, b) 5 %, and c) 20 %; powders redispersed in ethanol.	53
Figure 32. XRD patterns of AZO (1 mol-%): as-prepared (dashed), after heating in air and forming gas at 400 °C (dotted), and after heating in air at 800 °C (solid).	54
Figure 33. SEM images of thermally treated AZO powders redispersed in ethanol: AZO (1 mol-%) at a) 400 °C and b) 800 °C; AZO (20 mol-%) at c) 400 °C and d) 800 °C.	55
Figure 34. 1D ²⁷ Al single pulse NMR spectra of AZO (5 mol-%); as-prepared, oxidized by heating in air (400 °C, 30 min), and reduced via forming gas processing (400 °C, 60 min).	57
Figure 35. Core-shell model of AZO particles consisting of a single crystalline core with fourfold coordinated Al ³⁺ ions inserted in the ZnO lattice and an amorphous shell with sixfold coordinated Al ³⁺	58
Figure 36. 2D ²⁷ Al- ¹ H NMR spectrum of AZO (5 mol-%) heated in air (400 °C, 30 min).....	59

Figure 37. ^{27}Al NMR spectra of as-prepared and post-treated a) AZO (1 mol-%), and b) AZO (5 mol-%) using echo experiment.....	60
Figure 38. ^{27}Al NMR spectra of AZO samples with Al:Zn molar ratios of 1 %, 5 %, and 20 % reduced in forming gas (400 °C, 60 min) using echo experiment.....	61
Figure 39. a) Particle size distribution of as-prepared $\text{SnO}_2\text{:Ta}$ in DEG measured with dynamic light scattering and b) photograph of $\text{SnO}_2\text{:Ta}$ in DEG (solids content: 1 wt-%).	63
Figure 40. a) SEM image and b) XRD pattern of as-prepared $\text{SnO}_2\text{:Ta}$ (reference: SnO_2 – ICCD No. 41-1445).....	63
Figure 41. DLS measurement of particle size distribution of FTO (1 mol-%): reaction suspension (solid), redispersed in DEG (dashed), and redispersed in EtOH (dotted).	64
Figure 42. a) DLS measurement of particle size distribution of FTO (10 mol-%): reaction suspension (solid), redispersed in DEG (dashed), and redispersed in EtOH (dotted) and b) photograph of FTO (10 mol-%) suspension in DEG (solids content: 1 wt-%).	64
Figure 43. SEM images of as-prepared a) FTO (1 mol-%) and b) FTO (10 mol-%) redispersed in ethanol.	65
Figure 44. XRD patterns of as-prepared FTO (1 mol-%) (solid) and FTO (10 mol-%) (dotted) (reference: SnO_2 – ICCD No. 41-1445).....	66
Figure 45. HRTEM images of as-prepared FTO (10 mol-%) in ethanol.	67
Figure 46. TG analysis of as-prepared FTO (5 mol-%).	67
Figure 47. XRD patterns of post-treated FTO (1 mol-%) processed in air (500 °C, dashed), in air (500 °C) and forming gas (250 °C, dotted), and in air (800 °C, solid).	69
Figure 48. SEM images of FTO (1 mol-%) processed in a) air 500 °C and forming gas 250 °C and b) air 800 °C; powders redispersed in ethanol.....	69
Figure 49. Experimental and simulated ^{119}Sn Mössbauer spectra of FTO (10 mol-%) processed in air (500 °C, 2 h) and forming gas (250 °C, 1 h).....	72
Figure 50. 1D ^{119}Sn NMR spectrum of as-prepared FTO (10 mol-%).	74
Figure 51. 1D ^{19}F NMR spectrum of as-prepared FTO (10 mol-%).....	74
Figure 52. ^{119}Sn - ^{19}F CP-MAS NMR spectra of FTO (10 mol-%) measured with contact times 15.0 ms and 1.0 ms, respectively.	75
Figure 53. 2D ^{19}F exchange NMR spectrum of as-prepared FTO (10 mol-%) measured with mixing time 100 ms.....	76
Figure 54. Model of FTO particles consisting of single crystalline SnO_2 in which F^- ions are inserted on oxygen sites and a partial reduction of some Sn^{4+} ions to Sn^{2+} has taken place.	77
Figure 55. DLS measurement of particle size distribution of as-prepared $\text{CeO}_2\text{:Gd}$ nanocrystals in DEG.....	78
Figure 56. SEM image of as-prepared $\text{CeO}_2\text{:Gd}$ nanocrystals in DEG.	79
Figure 57. XRD pattern of as-prepared nanocrystalline $\text{CeO}_2\text{:Gd}$ (reference: CeO_2 – ICCD No. 1071-4199 with diffraction peaks (111), (220), and (311) denoted).....	80
Figure 58. DLS measurement of particle size distribution of as-prepared $\text{La}(\text{OH})_3$ nanocrystals in DEG.....	82
Figure 59. SEM image of as-prepared $\text{La}(\text{OH})_3$ nanocrystals in DEG.	82
Figure 60. XRD pattern of as-prepared nanocrystalline $\text{La}(\text{OH})_3$ (reference: $\text{La}(\text{OH})_3$ – ICCD No. 83-2034 with diffraction peaks (100) and (201) denoted).	83
Figure 61. DLS measurement of particle size distribution of as-prepared $\text{ZnAl}_2\text{O}_4\text{:In}$ in DEG.	86
Figure 62. SEM image of as-prepared $\text{ZnAl}_2\text{O}_4\text{:In}$ in DEG.....	86
Figure 63. XRD pattern of $\text{ZnAl}_2\text{O}_4\text{:In}$ heated in air (600 °C, 1 h) (reference: ZnAl_2O_4 – ICCD No. 5-669) with diffraction peaks (220), (311), and (440) denoted.	87

Figure 64. SEM image of ZnAl ₂ O ₄ :In heated in air (600 °C, 1 h); powders redispersed in EtOH.....	88
Figure 65. DLS measurement of particle size distribution of as-prepared ZnGa ₂ O ₄ :Sn in DEG.	89
Figure 66. SEM image of as-prepared ZnGa ₂ O ₄ :Sn in DEG.	90
Figure 67. XRD pattern of ZnGa ₂ O ₄ :Sn heated in air (600 °C, 1 h) (reference: ZnGa ₂ O ₄ – ICCD No. 1086-415) with diffraction peaks (220), (311), and (440) denoted.	90
Figure 68. SEM image of ZnGa ₂ O ₄ :Sn heated in air (600 °C, 1 h); powders redispersed in EtOH.....	91
Figure 69. XRD patterns of as-prepared tin-doped zinc indium oxides with Zn:In molar ratios 2:1, 3:2, 1:1, 1:2, and as-prepared undoped zinc indium oxide with Zn:In = 1:2 (reference: ZnO – ICCD No. 36-1451).	93
Figure 70. XRD pattern of post-treated tin-doped zinc indium oxide; Zn:In = 2:1 (references: Zn ₄ In ₂ O ₇ – ICCD No. 20-1438, In ₂ O ₃ – ICCD No. 6-416, ZnO – ICCD No. 36-1451).	94
Figure 71. XRD pattern of post-treated tin-doped zinc indium oxide; Zn:In = 3:2 (references: Zn ₃ In ₂ O ₆ – ICCD No. 20-1439, In ₂ O ₃ – ICCD No. 6-416, ZnO – ICCD No. 36-1451).	95
Figure 72. XRD pattern of post-treated tin-doped zinc indium oxide; Zn:In = 1:1 (references: Zn ₂ In ₂ O ₅ – ICCD No. 20-1442, In ₂ O ₃ – ICCD No. 6-416, ZnO – ICCD No. 36-1451).	95
Figure 73. XRD pattern of post-treated tin-doped zinc indium oxide; Zn:In = 1:2 (references: In ₂ O ₃ – ICCD No. 6-416, ZnO – ICCD No. 36-1451).	96
Figure 74. Powder patterns of post-treated tin-doped zinc indium oxide with Zn:In molar ratios of 1:2 (solid) and 1:1 (dashed) (references: ZnO – ICCD No. 36-1451, solid and In ₂ O ₃ – ICCD No. 6-416, dashed).	96
Figure 75. XRD patterns of post-treated tin-doped (solid) and undoped (dashed) zinc indium oxide; Zn:In = 1:2).	97
Figure 76. SEM image of post-treated zinc indium oxide with different Zn:In molar ratios: a) 3:2 tin-doped, b) 1:1 tin-doped, c) 1:2 tin-doped, and d) 1:2 undoped; powders redispersed in EtOH.	97
Figure 77. DLS measurement of particle size distribution of as-prepared tin-doped zinc indium oxide with a Zn:In molar ratio of 1:2 in DEG.	99
Figure 78. SEM image of as-prepared tin-doped zinc indium oxide with a Zn:In molar ratio of 1:2.	99
Figure 79. UV-Vis spectra of tin-doped zinc indium oxide with a Zn:In molar ratio of 1:2: heated in air (600 °C, 1 h, solid) and processed in forming gas (300 °C, 2 h, dashed).	100
Figure 80. Crystals obtained from hydrothermal processing of tin-doped zinc indium oxide powders with a Zn:In molar ratio of 1:2.	101
Figure 81. XRD pattern of post-treated tin-doped zinc indium oxide; Zn:In = 1:2 (reference: Zn ₃ In ₂ O ₆ – ICCD No. 20-1439).	102
Figure 82. a) Photograph of as-prepared In ⁰ nanoparticles in DEG and b) particle size distribution thereof measured via DLS; plotted as a function of particle number.	106
Figure 83. DLS measurement of particle size distribution of as-prepared In ⁰ nanoparticles in DEG; plotted as a function of particle volume.	106
Figure 84. SEM image of as-prepared In ⁰ nanoparticles in DEG.	107
Figure 85. XRD pattern of In ⁰ nanoparticles synthesized in DEG, washed with EtOH, and dried in a) vacuum and b) air (references: In – ICCD No. 5-642, solid and In ₂ O ₃ – ICCD No. 6-416, dashed) with diffraction peaks (101) and (110) denoted.	107
Figure 86. Photographs of as-prepared In ⁰ nanoparticles in dodecane / DEG: a) both phases and b) the separated dodecane phase.	108
Figure 87. DLS measurement of particle size distribution of as-prepared In ⁰ nanoparticles transferred into dodecane.	109

Figure 88. SEM image of as-prepared In ⁰ nanoparticles transferred into dodecane.....	109
Figure 89. XRD pattern of In ⁰ nanoparticles transferred into dodecane, washed with EtOH, and dried in vacuum (reference: In – ICCD No. 5-642) with diffraction peak (101) denoted.	110
Figure 90. TEM images of In ⁰ nanoparticles transferred into pentane.	111

9 Appendix

9.1 Curriculum vitae

Personal

Name	Elin Hammarberg
Date of birth	03.03.1977
Place of birth	Uppsala, Sweden
Citizenship	Swedish
Marital status	single

Education

01/2005-	Doctoral Degree in Natural Sciences, Institute of Inorganic Chemistry University of Karlsruhe (TH) Doctoral thesis under the supervision of Prof. Dr. Claus Feldmann: “ <i>Nanoscale Transparent Conductive Oxides via Microwave-assisted Polyol Synthesis</i> ”
08/1996-01/2002	Master of Science Degree in Engineering Physics, Uppsala University Master thesis under the supervision of Prof. Dr. Arne Roos: “ <i>Antireflective Coatings on Float-glass and Low-emitting Glass</i> ”
08/1993-06/1996	Upper secondary school, Fyrisskolan, Uppsala

Professional experience

09/2002-02/2004	Research engineer, Optical Calibration Laboratory, STFI-Packforsk, Stockholm
03/2002-08/2002	Research assistant, Division of Solid State Physics, Department of Engineering Sciences, Uppsala University

9.2 Publications

- E. Hammarberg, A. Roos, *Thin Solid Films* **2003**, 442, 222.
- E. Hammarberg, D. Thölmann, C. Feldmann, *Z. Anorg. Allg. Chem.* **2006**, 632, 2120.
- C. Feldmann, E. Hammarberg, D. Thölmann, *Patent Application* **2007**, DE 102006015540.
- E. Hammarberg, A. Prodi-Schwab, C. Feldmann, *Thin Solid Films* **2008**, 516, 7437.
- E. Hammarberg, C. Feldmann “In⁰ Nanoparticle Synthesis Assisted by Phase-Transfer Reaction”, *Chem. Mater.* **2009**, *in press*.
- E. Hammarberg, A. Prodi-Schwab, C. Feldmann, “Microwave-assisted Polyol Synthesis of Aluminium- and Indium-doped ZnO Nanocrystals”, *submitted*.
- Y. Avadhut, J. Schmedt auf der Günne, E. Hammarberg, C. Feldmann, I. Schellenberg, R. Pöttgen, “Study of the Defects in SnO₂:F Nanoparticles by Solid State NMR”, *in preparation*.
- Y. Avadhut, J. Schmedt auf der Günne, E. Hammarberg, C. Feldmann, “Study of the Insertion of Al Dopants in ZnO:Al Nanoparticles by Solid State NMR”, *in preparation*.
- E. Hammarberg, A. Prodi-Schwab, C. Feldmann, “Synthesis and characterization of a ternary Zn-In-O TCO nanomaterial”, *in preparation*.

Conference contributions

- A. Roos, E. Hammarberg, A. Werner, M-L. Persson and J. Karlsson, Eurosun 2002, Bologna, Italy, June 2002 (Poster).
- K. Gelin, E. Hammarberg, A. Roos and F. Geotti-Bianchini, 4th International Conference on Coatings on Glass, Braunschweig, Germany, November 2002 (Poster).
- E. Hammarberg, D. Thölmann, C. Feldmann, Summerschool Science to Business Nanotronics 2006, Evonik Degussa GmbH, Marl, September 2006 (Poster).
- E. Hammarberg, A. Prodi-Schwab, C. Feldmann, MC8: Advancing Materials by Chemical Design, London, UK, July 2007 (Poster).
- E. Hammarberg, A. Prodi-Schwab, C. Feldmann, Summerschool Science to Business Nanotronics 2007, Evonik Degussa GmbH, Marl, September 2007 (Oral talk).
- E. Hammarberg, A. Prodi-Schwab, C. Feldmann, International Karlsruhe Nanoscience Workshop: Metal-rich Compounds, Karlsruhe, Germany, October 2007 (Poster).
- E. Hammarberg, A. Prodi-Schwab, C. Feldmann, Particles 2008, Orlando, USA, May 2008 (Poster).
- Y. Avadhut, J. Schmedt auf der Günne, E. Hammarberg, C. Feldmann, I. Schellenberg, R. Pöttgen, 30th Trinational Annual Discussion Meeting, Magnetic Resonance in Biology and Chemistry, Regensburg, Germany, September 2008 (Poster).